PACIFIC EARTHQUAKE ENGINEERING
RESEARCH CENTER

Empirical Characterization of Site Conditions on Strong Ground Motion

Jonathan P. Stewart
Yoojoong Choi
University of California, Los Angeles

and

Robert W. Graves
URS Corporation
Pasadena, California

PEER 2005/01
JUNE 2005

Empirical Characterization of Site Conditions on Strong Ground Motion

Jonathan P. Stewart
Yoojoong Choi
Department of Civil and Environmental Engineering
University of California, Los Angeles

and

Robert W. Graves
URS Corporation, Pasadena, California

PEER Report 2005/01
Pacific Earthquake Engineering Research Center
College of Engineering
University of California, Berkeley

June 2005

ABSTRACT

Empirical relationships are developed to predict amplification factors for 5% damped response spectral acceleration as a function of site condition. Amplification factors are evaluated as residuals between ground motion recordings and predictions from modified rock attenuation relationships.

Both shallow and deep characteristics of site condition are considered to identify those parameters that are most effective from the standpoint of bias and dispersion reduction. The parameterization of shallow site condition is based on (1) surface geology, (2) NEHRP classification, (3) geotechnical site categories, and (4) average shear wave velocity in upper 30 m of site (V_{s-30}). Also considered are parameters that reflect the relatively deep sedimentary structure at many of the strong motion sites, including depth to the 1.5 km/s shear wave isosurface ($z_{1.5}$) as well as the location of the source inside or outside of the basin in which the site is located. Sites located in a basin overlaying the source are denoted as having coincident source and site basin locations (CBL) and are differentiated from distinct source and site basin locations (DBL).

It is found that standard deviation is minimized with the use of detailed surface geology or V_{s-30} as the site parameter for shallow site condition. The V_{s-30}-based amplification model has several innovative features, including V_{s-30}-dependent nonlinearity and standard deviation and quantification of the reference velocity for a number of rock attenuation relationships. For all site categories, standard deviation was found to increase with period, being as much as 0.3 larger at long periods than short periods.

The work on basin parameters utilized residuals calculated with respect to ground motion predictions derived using rock attenuation relations coupled with amplification factors for shallow site condition. Models relating amplification to $z_{1.5}$ were developed for the CBL and DBL data groups. The results indicate that the use of basin models is generally worthwhile for periods $T \geq 0.75$ s. At those long periods, residuals are significantly sensitive to $z_{1.5}$ for CBL but not for DBL when shallow site condition is parameterized based on V_{s-30}. Standard deviation is also reduced at long periods, such that the increase with period is significantly reduced.

ACKNOWLEDGMENTS

This work was supported by the Earthquake Engineering Research Centers Program of the National Science Foundation under award number EEC-9701568 through the Pacific Earthquake Engineering Research (PEER) Center.

Any opinions, findings, and conclusions or recommendations expressed in this material are those of the authors and do not necessarily reflect those of the National Science Foundation.

Many individuals assisted the authors during this study. We would especially like to thank Caroline Wang, Annie Kwok, Andrew Liu, and Mehmet Baturay for their assistance. We are also grateful to Rie Von Eyben and Xiao Chen who provided valuable consultation regarding the statistical analyses. We would like to extend our thanks to Dr. Kenneth Campbell for his assistance in compiling distance parameters for strong motion stations.

CONTENTS

LIST OF FIGURES

LIST OF TABLES

1 Introduction

1.1 STATEMENT OF THE PROBLEM

Ground motion attenuation relationships are used in seismic design practice to estimate probabilistic distributions of ground motion intensity measures (*IMs*), such as 5% damped response spectral acceleration, conditional on magnitude, site-source distance, and parameters representing site condition and style of faulting. Ground motion data are often log-normally distributed, in which case the distribution can be represented by a median and standard deviation, σ (in natural logarithmic units).

Site condition is generally characterized in attenuation relations as broadly defined categories (i.e., rock or soil), and hence, estimates from attenuation relationships necessarily represent averaged values across the broad range of possible site conditions within the "rock" or "soil" categories. Accordingly, ground motion estimates for site conditions that are different from the average of the sites considered in development of the attenuation relationships could be inaccurate.

The objective of this study is to evaluate the degree to which more detailed information on site condition can improve ground motion predictions relative to what is obtained with attenuation relationships. Information on both shallow and relatively deep site characteristics is considered. The "improvement" in ground motion prediction generally involves (1) removing potential bias in median ground motion estimates that might be present for a particular site condition and (2) reducing the uncertainty in ground motion estimates, as measured by standard error term, σ.

Amplification factors are derived for individual ground motion recordings using a non-reference site method in which 5% damped response spectral accelerations from recorded ground motions are normalized by reference motions derived from modified rock attenuation relationships for active regions. Statistical analyses are performed to develop amplification models that relate amplification to various parameters. The amplification models provide estimates of the median *IM* for the site condition. Standard deviation (σ) is estimated from the data residuals.

The first suite of analyses involve the development of amplification models derived with respect to various metrics of shallow site condition and the amplitude of shaking on the reference (soft rock) site condition. These analyses are useful to define the characteristics of ground shaking for various site categories, variations of standard deviation across site categories, and the method of site classification that minimizes the standard deviation of predicted ground motions. The minimization of standard deviation is desirable because low standard deviation implies that the method of computation is capturing site-to-site variations in ground motion attributable to site condition, which is the underlying purpose of using site factors. The parameterization of shallow site condition is based on (1) surface geologic categories (age only, age + depositional environment, age + sediment texture); (2) categories within a so-called NEHRP classification scheme, which is based on average shear wave velocity in the upper 30 m (V_{s-30}); (3) geotechnical site categories that consider soil stiffness and depth (although the range of depths differentiated by the method are shallow and do not enable parameterization of deep basin structure); and (4) direct use of V_{s-30} as a site parameter.

The second suite of analyses utilizes residuals between data and predictions from attenuation relationships modified with amplification factors for shallow site conditions. Statistical analyses are performed to relate those residuals to basin-related parameters such as sediment thickness as parameterized by depth to the 1.5 km/s shear wave isosurface ($z_{1.5}$) as well as the location of the source inside or outside of the basin in which the site is located. The site/source location consideration is an original feature of this research; sites located in a basin overlying the source are denoted as having <u>c</u>oincident source and site <u>b</u>asin <u>l</u>ocations (CBL) and are differentiated from <u>d</u>istinct source and site <u>b</u>asin <u>l</u>ocations (DBL).

1.2 ORGANIZATION OF THE REPORT

Two databases were used in this research and are described in Chapter 2. The first is a database of ground motions recordings with information on magnitude, rupture mechanism, and site-source distance. The second is a database of site conditions containing the aforementioned shallow and deep characteristics of site condition. Also described in Chapter 2 are the results of an extensive effort to validate and improve our site database through systematic comparisons to databases developed by others.

In Chapter 3, amplification factor models are developed with respect to various site categories defined on the basis of shallow site condition. Engineering models of site amplification and standard deviation are provided for each category. An important result of the work is an assessment of the effectiveness of the various site classification schemes, as measured by an intercategory standard deviation. Based on those results, recommendations for practical application of the amplification factors are provided.

In Chapter 4, amplification factor models are developed as a continuous function of V_{s-30}. The models have innovative features such as V_{s-30}-dependent nonlinearity and intra-event standard deviation. Variations of dispersion with magnitude and distance are also investigated. The results of the work are used to investigate the accuracy of existing site factors in building codes (e.g., BSSC, 2001).

Chapter 5 relates to ground motion amplification as a function of basin geometry. The physics underlying basin response are reviewed, and the results of previous studies utilizing simulated and empirical data are discussed. Ground motion amplification factors from a large, recent simulation exercise by others are then utilized to identify site/source parameters that seem to correlate with ground motion amplification in basins. Parameters that appear promising based on those analyses include basin depth ($z_{1.5}$) and the CBL/DBL characterization of source and site basin locations. These parameters form the basis of statistical analyses of basin response effects using ground motion recordings from basins. The results provide insight into the types of *IMs* and site conditions for which it is worthwhile to apply basin models as a further correction to the shallow site models. Recommendations for application of the basin amplification factors are provided.

The report concludes with Chapter 6, in which tasks undertaken in this research are reviewed, the important findings from this study are compiled, and recommendations for further research are provided.

2 Data Resources

As described in Chapter 1, the objective of this study is to evaluate empirically the effects of site conditions on strong ground motion. This is accomplished by drawing out site effects from strong motion recordings through statistical analysis of data. Accordingly, the databases used in this study are the cornerstone of the research, and every effort was made to ensure that the data reflect the most current available information.

The data utilized in this study include strong motion data and site data. The site data fall into two categories, one representing shallow site conditions and the other representing deep basin structure. The process of collecting and organizing the data for this study is described in this chapter. Separate sections are provided for each of the following databases:

- strong motion
- shallow site condition
- deep basin structure parameters

It should be emphasized that the data collection and synthesis effort utilized in this research occurred in two principal phases. The first occurred in 1999–2001 and was documented by Stewart et al. (2001). The databases compiled during that effort represented the best available information on strong motion and shallow site condition before the large data collection effort undertaken as part of Next Generation Attenuation (NGA) project sponsored by the Pacific Earthquake Engineering Research (PEER) Center's Lifelines Program. The second phase occurred coincident with the NGA project, and involved updates to the strong motion and shallow site condition databases and the addition of information on deep basin structure. Given that this data collection effort occurred within a collaborative environment involving many researchers, it is certainly not solely the work of the authors. Acknowledgments of the various participants are made in the sections that follow.

2.1 STRONG MOTION DATABASE

The phase I database of strong motions (Stewart et al., 2001) consisted largely of the 2001 version of the PEER strong motion database compiled by Dr. Walter Silva of Pacific Engineering and Analysis. This PEER database consisted of worldwide shallow crustal earthquakes near active plate margins, and included the 1999 Kocaeli, Turkey; 1999 Chi Chi, Taiwan; and 1999 Düzce, Turkey, earthquakes. Subduction and intraplate events were excluded. Additional events and individual recordings that were largely missing from the PEER database at that time were added to form the complete phase I database described by Stewart et al. (2001) (e.g., Northridge aftershock recordings, 1999 Hector Mine earthquake recordings, most of 1992 Big Bear recordings).

The phase I database contains a total of 1828 recordings from 154 earthquakes. Event dates range from the 1933 Long Beach, California, earthquake to the 1999 Düzce, Turkey, earthquake. Removed from the data set for this study were recordings from events with poorly defined magnitude or focal mechanism, recordings for which site-source distances are poorly constrained because of the lack of a finite source model, and recordings for which problems were detected with one or more components. These removals reduced the data set to 1032 recordings from 51 events, which are distributed in magnitude-distance space as shown in Figure 2.1. Characteristics of the events are listed in Table 2.1, which shows that the events are principally from California, Turkey, and Japan. Note that the attenuation with distance observed during the recent Turkey earthquakes and the Kobe, Japan, earthquake was found to be similar to that predicted by attenuation relations derived principally from California recordings (Rathje et al., 2000; EERC, 1995), which justifies the inclusion of those data in the database. The data from the 1999 Chi Chi, Taiwan, earthquake were not used because of the general lack of high quality site data for the strong motion stations and the lack of agreement within the seismological community whether that earthquake is more properly classified as being associated with active tectonic regions or a subduction zone.

Since 2001, the PEER database has been updated as part of the NGA project to include events that had previously been excluded (Northridge aftershocks, Hector Mine, most of Big Bear, 5 Chi Chi aftershocks), to include recordings from recent events [such as the 2002 Nenana Mountain and Denali earthquakes in Alaska and nine small magnitude (4.8–5.7) events in or near California], to include four additional events in extensional regions (M 5.7 1994 Little Skull

Mountain earthquake, three NW China earthquakes, M=5.7–6.0), and to include more recordings at large distance (up to 200 km). The NGA-updated PEER database (as of 2003) comprises what is referred to here as the "phase II database." This database has 3524 recordings from 175 events. The vast majority of the additional recordings are from the Chi Chi, Taiwan, aftershocks. Besides the addition of Chi Chi data, the phase II database is not substantially different from the modified phase I database.

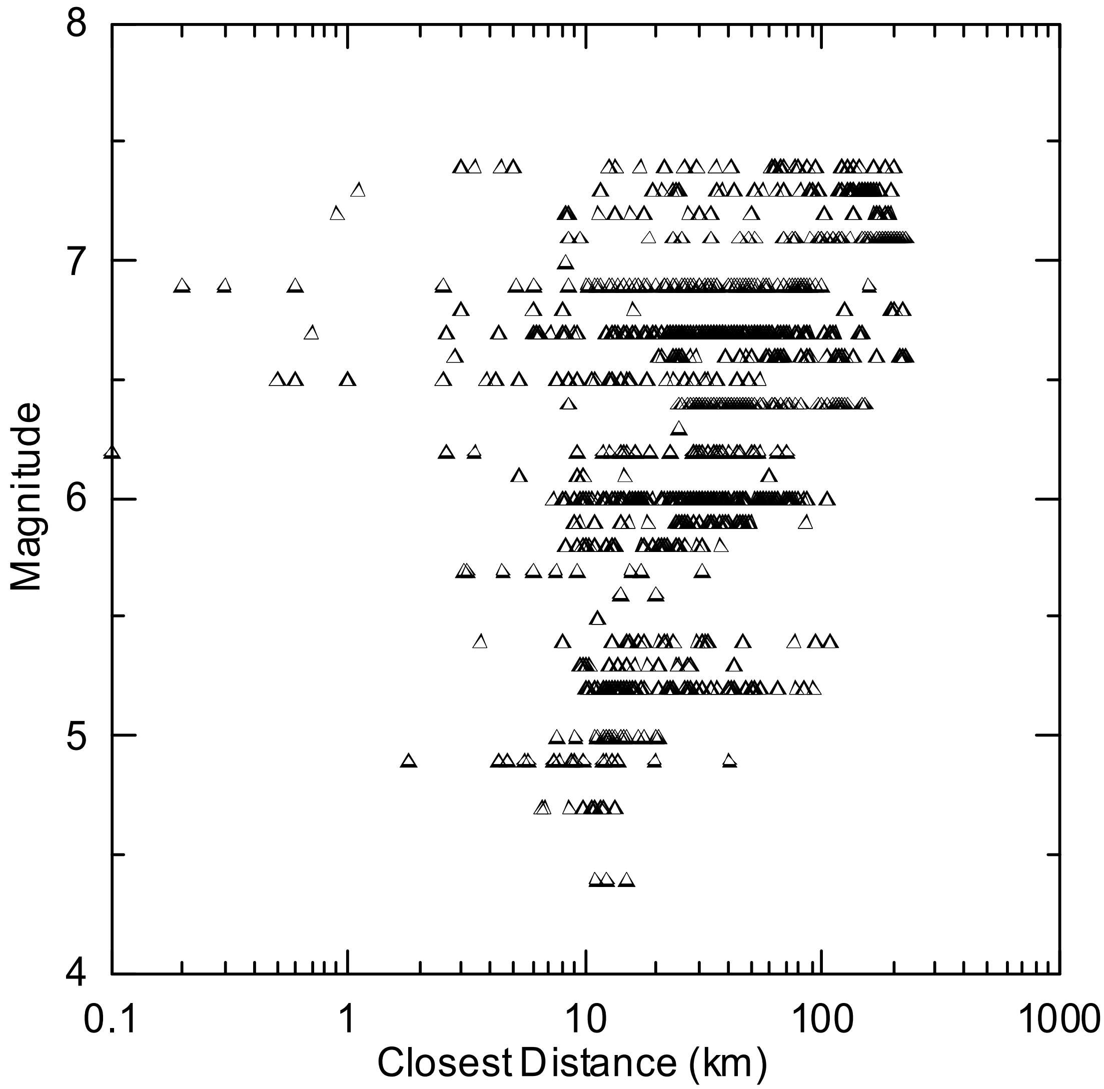

Fig. 2.1 Inventory of strong motion recordings utilized in phase I database

Table 2.1 Earthquakes included in phase I database (after removal of events with poorly defined source and site parameters)

Event	Year	Mo-Day	Time	Magnitude
Imperial Valley	1940	519	437	7.0
Kern County	1952	721	1153	7.4
San Francisco	1957	322	1944	5.3
Parkfield	1966	628	426	6.1
Borrego Mtn	1968	409	230	6.8
Lytle Creek	1970	912	1430	5.4
Hollister	1974	1128	2301	5.2
Oroville	1975	801	2020	6.0
Oroville	1975	802	2022	5.0
Oroville	1975	802	2059	4.4
Oroville	1975	808	700	4.7
Santa Barbara	1978	813		6.0
Tabas, Iran	1978	916		7.4
Coyote Lake	1979	806	1705	5.7
Imperial Valley	1979	1015	2316	6.5
Imperial Valley	1979	1015	2319	5.2
Imperial Valley	1979	1016	658	5.5
Livermore	1980	124	1900	5.8
Livermore	1980	127	233	5.4
Mammoth Lakes	1980	527	1901	4.9
Mammoth Lakes	1980	531	1516	4.9
Mammoth Lakes	1980	611	441	5.0
Westmoreland	1981	426	1209	5.8
Coalinga	1983	502	2342	6.4
Coalinga	1983	509	249	5.0
Coalinga	1983	611	309	5.3
Coalinga	1983	709	740	5.2
Coalinga	1983	722	239	5.8
Morgan Hill	1984	424	2115	6.2
Bishop (Rnd Val)	1984	1123	1912	5.8
Hollister	1986	126	1920	5.4
N. Palm Springs	1986	708	920	6.0
Chalfant Valley	1986	720	1429	5.9
Chalfant Valley	1986	721	1442	6.2
Chalfant Valley	1986	721	1451	5.6
Chalfant Valley	1986	731	722	5.8
Whittier Narrows	1987	1001	1442	6.0
Whittier Narrows	1987	1004	1059	5.3
Superstition Hills (A)	1987	1124	514	6.3
Superstition Hills (B)	1987	1124	1316	6.7
Loma Prieta	1989	1018	5	6.9
Cape Mendocino	1992	425	1806	7.1
Landers	1992	628	1158	7.3
Big Bear	1992	628	1506	6.4
Northridge	1994	117	1231	6.7
Northridge Aftershock	1994	117	431	5.9
Northridge Aftershock	1994	320	1320	5.2
Kobe, Japan	1995	116	2046	6.9
Kocaeli, Turkey	1999	817		7.4
Hector Mine	1999	1016	946	7.1
Duzce, Turkey	1999	1112		7.2

The ground motion intensity measure for which amplification factors are derived in this study is 5% damped response spectral acceleration (S_a). The spectral periods considered range from T = 0.01 to 5 s. It should be noted that spectral ordinates with frequencies of less than $f = 1.25 \times f_{HP}$ are not used, where f_{HP} = high-pass frequency used during data processing. However, the spectral ordinates at frequencies higher than the low-pass frequency (f_{LP}) are used because of the saturation of S_a at high frequency. Sources of strong motion recordings for the western U.S. include the California Strong Motion Instrumentation Program (CSMIP), the U.S. Geological Survey (USGS), the University of Southern California (USC), the California Division of Mines and Geology (CDMG), and the Los Angeles Department of Water and Power (LADWP). Additional data were obtained for the 1999 Kocaeli and Düzce, Turkey, earthquakes from the Kandilli Observatory and Earthquake Engineering Research Institute of Boğaçizi University (Kandilli), the Earthquake Research Department of the General Directorate of Disaster Affairs (ERD), and Istanbul Technical University (ITU). Most of the time histories used in this study can be obtained at the website of the Pacific Earthquake Engineering Research Center (**www.peer.berkeley.edu**).

2.2 SHALLOW SITE CONDITION DATABASE

The site characterization schemes that are employed in this study to describe the geological and geotechnical characteristics of the near-surface materials include:

- surface geology
- near-surface shear wave velocity (V_{s-30} : average shear wave velocity to depth of 30m)
- geotechnical data

The work involved in classifying sites according to these three schemes is described in the following subsections.

2.2.1 Surface Geology

Stewart et al. (2001) developed the phase I database of surface geologic classifications at strong motion sites. The geologic maps used in the development of that database were:

- 1:24,000-scale digital geologic maps prepared as part of the Southern California Aerial Mapping Project (SCAMP) covering 7.5′ quadrangles in Los Angeles and Orange counties (provided by Charles Real, California Geological Survey, *personal communication*)

- 1:100,000-scale geologic maps by Morton et al. (1999) prepared as part of the Southern California Aerial Mapping Project (SCAMP) covering Santa Ana 30′ x 60′ quadrangle
- 1:24,000-scale geologic maps (so-called Diblee maps) for the Los Angeles area published by the Diblee Geological Foundation
- 1:250,000-scale geologic maps prepared by the California Division of Mines and Geology (CDMG, 1959–1998), which provide coverage of the entire state of California

The digitalized SCAMP maps are the most detailed of the available geologic maps, providing basic information on the texture of Quaternary deposits (e.g., coarse/fine/mixed), and detailed information on depositional environment. In assigning a surface geologic classification to a particular site, priority was always given to maps at large scale (i.e., 1:24,000 SCAMP maps and Diblee maps) and surface geologic classifications established from site visits (by the authors or reported in Geomatrix, 1993). Surface geologic classifications of all strong motion stations used in phase I work are reported in Appendix A of Stewart et al. (2001). The phase I database of Stewart et al. (2001) has been modified over time to incorporate sites that had previously been omitted. Those 35 added sites are listed in Table 2.2 along with their classifications.

Additional data on surface geologic classifications at strong motion stations have become available recently as part of the NGA project. These additional data include:

- statewide surface geologic classifications by Christopher Wills of the California Geological Survey (based on small-scale, statewide maps)
- geologic classifications in the San Francisco and Los Angeles areas by Roger Borcherdt of the U.S. Geological Survey (based on the best available information from small-scale or large-scale maps, but not including SCAMP data, supplemented in some cases by site visits)
- geologic classifications throughout California by Yousef Bozorgnia and Kenneth Campbell compiled in support of GEOCODE site classifications used in their attenuation relationship (Campbell and Bozorgnia, 2003)

Table 2.2 Sites added to phase I database (to form modified phase I database)

Location	Station Name	Agency	Station #	Age	Grain Size	Depositional History	Reference[1]	Boring Dist.	Geot. Class.	Vs (m/s)	Vs Index[2]	NEHRP	Vs Dist.[3]	Reference
Bear Valley	Stn. 10; Webb Residence	USGS	1479	Holocene		Alluvium	DOC	A	C2	304	0	D	A	USGS OFR 94-552*
Bear Valley	Stn. 12; Williams Ranch	USGS	1481	Holocene		Alluvial Fan	DOC	A	D1C	331	0	D	A	USGS OFR 94-552*
Bear Valley	Stn. 5; Callens Ranch	USGS	1474	Pleistocene			DOC	A	C2	391	0	C	A	USGS OFR 94-552*
Berkeley	UCB-Haviland Hall (bsmt)	USGS	1006	Tertiary			Boring	A	B	1266	0	B	A	USGC OFR 03-191, AA 9225-6427
Calaveras	Calaveras Resevoir S.	USGS	1687	Holocene		Alluvium	DOC, Geomatrix	A	D2S	478	0	C	A	USGS OFR 94-552*
Cholame *	Temblor II	CIT	97	Pleistocene			DOC, Geomatrix	A	C1	528	0	C	A	USGS OFR 82-407*, NGA
El Centro	Array 12 - 907 Brockman Rd	USGS	931	Holocene	Fine	Lacustrine	DOC, Geomatrix	A	D	198	0	D	A	Stoke, USGS OFR 84-562
El Centro	Array 6 - Huston Rd	USGS	942/5158	Holocene	Fine	Lacustrine	DOC, Geomatrix	A	E	203	0	D	A	USGS OFR 84-562*, NGA, Stoke
Emeryville	6363 Christie Ave. - gnd. Site. S.	USGS	1662	Holocene		Alluvial Valley	DOC, Geomatrix	A	E	199	0	E	A	USGS OFR 94-222*, NGA
Foster City	APEEL 1; Redwood Shores	CSMIP	58375	Holocene	Fine	Fill	DOC, Geomatrix	A	E	113	0	E	A	USGS OFR 93-376*, NGA
Gilroy	Gilroy 4; San Ysidro School	CSMIP	57382	Holocene	Aggregate	Alluvial Fan	DOC, Geomatrix	A	D1	222	0	D	A	USGS OFR 82-407*, NGA, USGS OFR 91-311
Indio	County Services Bldg Grounds	CSMIP	12543	Holocene			DOC	A		250	0.5	D	A	UCB EERC 97/01
Irvine	2603 Main Street	USGS	5466	Holocene	Fine	Alluvial Fan	SCAMP	A	C3-D	268	0	D	A	Law/Crandall 84145
LA	1955 1/2 Purdue Ave (bsmt)	USGS	5284	Holocene	Fine	Alluvial Valley	SCAMP	B	D2	285	0	D	B	Law/Crandall 84280
LA	Bulk Mail Facility	USGS	5129	Holocene	Coarse	Alluvial Fan	SCAMP, Geomatrix	A	D2	302	0	D	A	ROSRINE
LA	Griffith Observatory	USGS	141	Mesozoic			SCAMP, Geomatrix	A	B	958	0	B	A	ROSRINE
LA	Wadsworth VA Hospital (N gnd)	USGS	5082	Pleistocene		Alluvial Valley	SCAMP	A	C3	421	0	C	A	ROSRINE
LA	Wadsworth VA Hospital (S gnd)	USGS	5082	Pleistocene		Alluvial Valley	SCAMP	A	D2	391	0	C	A	ROSRINE
LA County	Leona Valley - Fire Station	USGS	5029	Holocene		Alluv	Borcherdt	C		327	0	D	C	USGS OFR 82-833*
Larkspur	Ferry Teminal	USGS	1590	Holocene	Fine	Marine	DOC	A	E1	170	0	E	A	USGS OFR 94-222*, NGA
Loma Linda	VA Hospital, North Ground site	USGS	5229	Holocene		Alluvium	DOC	A	D	273	0	D	A	UCB EERC 97/01
Loma Linda	VA Hospital, South Ground site	USGS	5229	Holocene		Alluvium	DOC	A	D	273	0	D	A	UCB EERC 97/01
Long Beach	VA Hospital Ground site	USGS, VA	5106	Pleistocene		Marine	SCAMP	A	C3-D	366	0	C	A	USGS OFR 80-378*
Martinez	VA Hospital (bsmt)	USGS	1448	Tertiary			DOC	A	C3	384	0	C	A	USGS OFR 03-191, AA 9225-6427
Menlo Park	VA Hospital, Bldg.37	USGS	1230	Holocene	Medium	Alluvial Valley	DOC, Geomatrix	A	D2C	267	0	D	A	USGS OFR 03-191, AA 9225-6427
Milpitas	Industrial Bldg. (2-story)	CSMIP	57502	Holocene	Aggregate		DOC, Geomatrix	A	D?	229	0.5	D	A	UCB EERC-97/01(Est)
Palo Alto	VA Hospital, Bldg.1 (bsmt)	USGS	1227	Pleistocene	Fine		Geomatrix	A	D1	352	0	D	A	USGS OFR 92-287*
Pasadena	NASA, JPL Bldg. 230	USGS	5412	Holocene		Alluvial Fan	SCAMP	A	D2	488	0	C	A	NUREG/CR-0055, V2
Pasadena	USGS/NSMP Office	USGS	5296	Pleistocene		Alluvial Fan	SCAMP	A	D	411	0	C	A	NUREG-0029, V2
Rancho Cucamonga	Deer Canyon	CSMIP	23598	Mesozoic			DOC			822	1	B	E_NGA	NGA
San Bernadino	County Bldg. Grounds	USGS	5245	Holocene			DOC	A	D	326	0	D	N/A	USGS OFR 01-506*
San Jose	Santa Teresa Hills	CSMIP	57563	Mesozoic			DOC	A	C1	648	0	C	A	ROSRINE
Santa Cruz	BRAN	UCSC	13	Tertiary			Wills			376	1	C	E_NGA	NGA
Santa Cruz	UCSC	UCSC	15	Mesozoic			DOC	A	C1	713	0	C	A	AA 9225-6427
Vasquez Rocks Park		CSMIP	24047	Tertiary			Wills			996	0	B	A	NGA, Stoke

Note: [1] DOC - 1:250:000 scale geologic maps by the California Division of Mines and Geology

[1] SCAMP - Geologic maps prepared as part of the Southern Californai Aerial Mapping Project (SCAMP)

[1] Borcherdt - geologic classifications by Roger Borcherdt as part of NGA project

[1] Wills - geologic classifications by Christopher Wills as part of NGA project

[1] Geomatrix - geologic classifications by Geomatrix Consultants (1993)

[2] Vs Index: 0 for Vs based on on-site geophysical measurement, 0.5 for Vs based on the site specific estimation, 1 for Vs estimated by geology

[3] E_NGA - Vs estimated based on geology, Boore - Vs calculated by Boore

Comparisons of surface geologic classifications from the modified phase I database of Stewart et al. (2001) and the NGA-classifications of Wills, Borcherdt, and Bozorgnia/Campbell were performed. The objective of this comparison exercise was to identify conflicts in the site classifications, and resolve those conflicts with a re-review of available site data (including site visits, examination of boring logs, and re-examination of geologic maps).

Of the 460 California sites in the modified phase I database, no conflict was found for 372 of those sites. Conflicts were resolved by changing the original classifications of Stewart et al. (2001) in the following cases:

- Phase I classification was based on small-scale maps (i.e., the statewide maps), whereas NGA classifications by Borcherdt are based on site visits or large-scale geologic maps (typically 1;24,000), often with corroborating classifications by Bozorgnia and Campbell. The rationale for making those changes to the phase I classifications is that the NGA classifications are based on better, higher-resolution data. This affected nine sites.
- Phase I classification was based on small-scale maps. No NGA classification by Borcherdt is available, but NGA classifications by Wills from small-scale maps are available. These conflicts generally occurred for sites near boundaries of geologic units. The rationale for changing the phase I classifications is that the NGA classifications by Wills utilized digitized maps, whereas phase I classifications were based on the less precise process of plotting coordinates on hard copies. This affected 48 sites.

Table 2.3 lists sites whose geologic classifications were changed since the modified phase I study, and provides the rationale for those changes. In most cases, the changes involved only adjusting the geologic age of the material.

Several sites in the NGA database were not included in the modified phase I database or were included but were unclassified. In those cases, the NGA classifications were used. Some of the sites not included in the phase I database had actually been previously classified in Appendix B of Stewart et al. (2001); classifications for those sites were checked against NGA classifications, and the results are included in Tables 2.3 and 2.4, as applicable.

A number of sites were identified where it is believed that the NGA geologic classifications may be in error. Those sites are listed in Table 2.4. In most cases, the discrepancy is associated with one of the following situations:

Table 2.3 Sites with conflicts in geologic classification in which NGA classification was adopted

				Modified Phase I Classification				New Classification			
Location	Station Name	Agency	Station #	Age	Grain Size	Depositional History	Reference [2]	Age	Grain Size	Depositional History	Reference
Anacapa Island		CSMIP	25169	Tertiary			DOC	Mesozoic			Borcherdt
Angeles Nat. Forest	Big Tujunga	USC	90061	Mesozoic			DOC	Holocene	Coarse	Alluv	Borcherdt
Barstow	Vineyard & H St.	CSMIP	23559	Holocene			Geomatrix	Pleistocene		Alluvium	Wills
Castaic	Old Ridge Route #	CSMIP	24278	Mesozoic			Geomatrix	Tertiary			Wills, Boring
Cholame *	Temblor pre 1969	CDMG	1438	Pleistocene			DOC	Mesozoic			Wills
Cholame Array	Cholame-Limb Station 12W	CDMG	36229	Holocene	Coarse		Geomatrix	Pleistocene		Alluvium	Wills
Cholame Array	Fault Zone Station 11	CDMG	36453	Pleistocene	Coarse		DOC, Geomatrix	Tertiary	Coarse		Wills
Cholame Array	Fault Zone Station 14	CDMG	36456	Pleistocene	Coarse	Alluvial Fan	DOC, Geomatrix	Holocene		Alluv	Wills
Cholame Array	Fault Zone Station 15	CDMG	36445	Pleistocene	Coarse		DOC, Geomatrix	Tertiary	Coarse		Wills
Cholame Array	Fault Zone Station 3	CDMG	36408	Holocene	Aggregate	Alluvium	DOC, Geomatrix	Pleistocene		Alluvium	Wills
Cholame Array	Fault Zone Station 8	CDMG	36449	Pleistocene	Aggregate		DOC, Geomatrix	Tertiary			Wills
Cholame Array	Fault Zone Station 9	CDMG	36443	Holocene	Aggregate	Non-marine	DOC, Geomatrix	Pleistocene			Wills
Cholame Array	Gold Hill Limb Station 2E	CDMG	36421	Pleistocene	Aggregate	Alluvium	DOC, Geomatrix	Holocene		Alluvium	Wills
Cholame Array	Gold Hill Limb Station 2W	CDMG	36416	Pleistocene	Aggregate	Marine	DOC, Geomatrix	Tertiary			Wills
Cholame Array	Stone Corral Limb Station 2E	CDMG	36422	Pleistocene	Aggregate		DOC, Geomatrix	Tertiary			Wills
Cholame Array	Stone Corral Limb Station 3E	CDMG	36437	Pleistocene	Aggregate		DOC, Geomatrix	Tertiary			Wills
Cholame Array	Stone Corral Limb Station 4E	CDMG	36438	Pleistocene	Aggregate		DOC, Geomatrix	Tertiary			Wills
Cholame Array	Vineyard Canyon Limb Station 1W	CDMG	36448	Pleistocene	Coarse	Marine	DOC, Geomatrix	Tertiary			Wills
Cholame Array	Vineyard Canyon Limb Station 2W	CDMG	36447	Pleistocene	Coarse	Alluvial Fan	DOC, Geomatrix	Holocene		Alluvium	Wills
Cholame Array	Vineyard Canyon Limb Station 4W	CDMG	36446	Holocene	Coarse	Marine	DOC, Geomatrix	Tertiary			Wills
Cogswell Resevoir	Cogswell Dam	CSMIP	23210	Holocene		Fill	DOC	Mesozoic			Wills
Fortuna	701 S. Fortuna Blvd.	CSMIP	89486	Holocene			DOC, Geomatrix	Pleistocene		Alluvium	Wills
Gilroy	Gilroy 6; San Ysidro	CSMIP	57383	Tertiary			DOC, Geomatrix	Mesozoic			Wills
Gorman*	Oso Pumping Plant	CIT/USGS	52/994	Holocene	Coarse		Geomatrix	Pleistocene		Alluvium	Wills
Hayward	APEEL 3E-CSUH Stadium Grounds	CSMIP	58219	Mesozoic			DOC	Tertiary			Borcherdt
Hesperia	4th and Palm	CSMIP	23583	Pleistocene		Alluvium		Holocene	Coarse	Alluvium	Wills
Hollister	City Hall	USGS	1028	Holocene	Aggregate		DOC, Geomatrix	Pleistocene		Alluvium	Wills
Hollister	Hollister Airport-differential Array	USGS	1656	Pleistocene	Aggregate	Alluvial Valley	DOC, Geomatrix	Tertiary			Wills
Hollister	South & Pine	CSMIP	47524	Holocene	Aggregate		DOC, Geomatrix	Pleistocene		Alluvium	Wills
LA	Stone Canyon #	MWD	78	Tertiary			DOC	Pleistocene			Wills
LA	Temple & Hope #	CSMIP	24611	Pleistocene			DOC	Tertiary			Borcherdt
La Crescenta	New York	USC	90060	Pleistocene			Dibblee Map	Holocene	Coarse	Alluv	Borcherdt
Lake Crowley	Long Valley Dam (left abutment)	CSMIP	54214	Mesozoic			DOC, Geomatrix	Pleistocene			Wills
Lake Crowley	Shehorn Residence	CSMIP	54T03	Mesozoic			DOC	Holocene		Alluv	Wills
Leona Valley	#1	CSMIP	24305	Pleistocene			RM	Mesozoic			Wills
Leona Valley	#2	CSMIP	24306	Holocene			RM	Pleistocene	Coarse	Alluv	Borcherdt
Leona Valley	#6	CSMIP	24309	Holocene			RM	Pleistocene	Coarse	Alluv	Borcherdt
Mammoth Lakes	Sheriff Substation	CSMIP	54T04	Tertiary			DOC	Pleistocene			Wills
Oakland	Title & Trust Bldg.. (2-story)	CSMIP	58224	Holocene	Coarse	Aeolian	DOC	Pleistocene	Coarse		Radbruch map
Oroville	Johnson Ranch	CDMG	1493	Tertiary			DOC	Pleistocene			Wills
Oroville	Medical Center	CIT	1544	Tertiary			DOC	Pleistocene			Wills
Oroville	Pacific Heights	CDMG	1549	Pleistocene			DOC	Holocene	Coarse	Alluv	Wills
Pasadena	CIT Athenaeuem	CDMG/USGS	80053/0475	Holocene	Coarse		Geomatrix	Pleistocene		Alluvium	Wills
Pearblossom	Pallet Creek	CSMIP	23584	Holocene	Coarse		DOC	Mesozoic			Wills
Petrolia		CSMIP	89156	Holocene	Fine		DOC, Geomatrix	Mesozoic			Wills
San Bernadino	Mill Creek Ranger Station	UGSS	5076	Holocene		Alluvium	DOC_YC	Pleistocene		Alluv	Wills
San Martin	Coyote Lake Dam (abutment)	CSMIP	57217	lolo/Mesoz 12/14/0	Coarse	Landslide	DOC, Geomatrix	Mesozoic			Campbell
San Onofre*	Nuclear Power Plant	CIT	280	Tertiary			DOC_YC	Pleistocene		Alluv	Wills
Santa Barbara	Courthouse	USGS	283	Holocene	Aggregate		Geomatrix	Pleistocene		Alluvium	Wills
Santa Clara County	Anderson Dam (downstream)	USGS	1652	Pleistocene	Aggregate		DOC	Tertiary			Wills
Santa Clara County	Anderson Dam (left abutment)	USGS	1652	Mesozoic			DOC, Geomatrix	Tertiary			Wills
Seal Beach	Office Bldg #	CSMIP	14578	Pleistocene			DOC	Holocene	Fine	Alluv	Borcherdt
Tracy	Sewage Plant	CSMIP	57458, 57063 ?	Pleistocene		Marine	DOC	Holocene		Alluv	Wills
Tracy	Sewage Plant	CSMIP	63	Pleistocene		Marine	DOC	Holocene		Alluv	Wills
Vasquez Rocks Park		CSMIP	24047	Mesozoic			DOC_YC	Tertiary			Wills
	McGee Creek	USC	52	Holocene				Mesozoic			Wills
	WAHO	UCSC	14	Holocene		Marine	DOC	Tertiary			Wills
Alhambra[1]	900 South Fremont Ave	USGS/CIT	482	Holocene	Coarse		Geomatrix	Pleistocene			Wills
Sunol[1]	Calaveras Array - Fire Stn.	USGS	1688	Pleistocene			DOC, Geomatrix	Holocene		Alluv	Wills

Note: (1) Sites from Table B in Stewart et al. (2001b)
(2) RM - Rodriguez-Marek et al. (1999)

Table 2.4 Sites with conflicts in geologic classification in which NGA classification is likely in error

				Modified Phase I Classification						
Location	Station Name	Agency	Station #	Age	Grain Size	Depositional History	Reference	Borcherdt Geologic Symbol	Wills Geologic Symbol	Campbell & Bozorgnia - Geologic Description
	San Justo Dam	USGS	1655	Pleistocene	Aggregate		DOC, Geomatrix		J metamorphic	THIN SOIL/PLIOCENE SANDSTONE
Lake Hughes	#9 - Warm Springs Camp	CDMG/(USGS/CIT)	24272/127	Holocene	Coarse		Boring	sgn	pCg	FILL(3M)/GNEISS
Altadena	Eaton Canyon Park	CSMIP	24402	Holocene	Coarse	Alluvial Fan	SCAMP, Geomatrix		Qoa	ALLUVIUM
Brea	Carbon Canyon Dam (left abut	ACOE/CIT	108	Holocene	Coarse	Alluvial Fan	SCAMP, Geomatrix		Tss	PLIOCENE MARINE SEDIMENTS
Brea	Carbon Canyon Dam (right abu	ACOE/CIT	108	Holocene	Coarse	Alluvial Fan	SCAMP, Geomatrix		Tss	PLIOCENE MARINE SEDIMENTS
Brea	S. Flower Ave	USC	90087	Pleistocene		Alluvial Valley	SCAMP	Qym	Qoa	PLEISTOCENE NONMARINE
Inglewood	LAX	USGS	5399	Holocene	Coarse	Aeolian	SCAMP		Qoa	
LA	Baldwin Hills#	CSMIP	24157	Holocene		Fill	SCAMP, Geomatrix	Qom	Tsh	FILL(IM)/PLIOCENE SHALE AND SANDSTONE
LA	LA Dam	USGS/LADWP	2141	Tertiary			SCAMP		Qal, deep	
LA	N Faring Rd	USC	90016	Mesozoic			SCAMP	Qom	Qoa	UPPER JURASSIC MARINE
LA	N Westmoreland	USC	90021	Holocene		Alluvial Valley	SCAMP	Tpsl	Qoa	PLEISTOCENE NONMARINE
LA	N. Figueroa St.	USC	90032	Holocene		Alluvium	Dibblee Map	Qom	Tsh	PLEISTOCENE NONMARINE
La Habra	Briarcliff	USC	90074	Holocene			SCAMP	Qof	Qoa	PLEISTOCENE NONMARINE
Lancaster	15th & J, Hospital Grounds	CSMIP	24526	Holocene		Alluvium	DOC	Qpl	Qal, deep	ALLUVIUM
Lancaster	Fox Airfield	CSMIP	24475	Holocene		Alluvium	DOC	Qpl	Qal, deep	ALLUVIUM
Manhattan Beach	Manhattan	USC	90046	Holocene	Coarse	Aeolian	SCAMP	Qom	Qoa	DUNE SAND
Monterey Park	Garvey Resevoir (abutment bui	MWD	709	Tertiary			SCAMP, Geomatrix		Qoa	PLIOCENE ROCK
Newport Beach	Newport Blvd. & Coast Highwa	CSMIP	13610	Holocene	Coarse	Aeolian	SCAMP	Qof	Qoa	SEDIMENTARY ROCK
Northridge	17645 Saticoy St	USC	90003	Pleistocene		Alluvial Fan	SCAMP	Qym	Qal, deep	ALLUVIUM
Pacific Palisades	Sunset Blvd	USC	90049	Tertiary			SCAMP	Qyc	Tsh	OLIGOCENE NONMARINE
Palos Verdes*	Estates - Via Tejon	USGS/CIT	411	Pleistocene	Coarse	Aeolian	SCAMP		Tsh	
Pasadena	CIT Keck Lab	CDMG	80049	Holocene		Alluvial Fan	SCAMP		Qoa	
Playa Del Rey	Saran	USC	90047	Holocene	Coarse	Aeolian	SCAMP	Qom	Qoa	PLEIST. MARINE AND MARINE TERR. DEPOSITS
Rinaldi	Receiving Station	DWP	5968 (77)	Pleistocene	Coarse	Alluvial Fan	SCAMP	Qym	Qal, deep	RECENT ALLUVIUM
Rosamond	Aiport	CSMIP	24092	Holocene		Alluvium	DOC	Qpl	Qal, coarse	ALLUVIUM
Rosamond	Godde Ranch	CSMIP	24274	Holocene		Alluvium	DOC	Qpl	Qal, deep	ALLUVIUM
Sylmar	Converter Station East	DWP	75	Holocene	Coarse	Alluvial Fan	SCAMP	Ts	Qal, thin	PLIO-PLEISTOCENE MARINE
Torrance	W 226th St	USC	90038	Holocene		Alluvial Valley	SCAMP		Qoa	DUNE SAND
LA	Obregon Park #	CSMIP	24400	Holocene		Alluvial Valley	Dibblee Map	Qom	Qoa	HOLOCENE ALLUVIUM
Richmond	City Hall Parking Lot	CSMIP	58505	Holocene	Fine	Marine/Lacustrine	Boring, Site Visit by UCLA	QTs	Qal, deep	PLIO-PLEISTOCENE ALLUVIUM
Santa Monica	City Hall	CSMIP	24538	Holocene		Alluv	Dibblee Map	Qom	Qoa	PLEISTOCENE TERRACE DEPOSITS
Ferndale(1)	City Hall	USGS	1023	Pleistocene		Alluvial Valley	SCAMP, Geomatrix		Qal,thin	RECENT ALLUVIUM (>60M)
Pasadena(1)	NASA, JPL Bldg. 179	USGS	5410	Holocene		Alluvial Fan	SCAMP		Qoa	
San Francisco(1)	1295 Shafter, Fire Station	USGS	1675	Mesozoic			USGS OFR 91-311(2)		Qal,thin	FRANCISCAN CHERT
Santa Ana(1)	Diemer Filter Plant - administr	USGS	698	Holocene		Fill	SCAMP	Tpsc	Tsh	PLIOCENE MARINE

Note: (1) Sites from Table B in Stewart et al. (2001b)
(2) Based on Preliminary Geologic Map (scale 1:24,000) by M.G. Bonilla

- The recommended classifications are based on site data apparently unavailable to the NGA team. These include proprietary boring logs or site visits by the authors or their co-workers.
- The site is very near a geologic boundary. The recommended classifications are based on precise site locations established by consultation with staff at the California Strong Motion Instrumentation Program, whereas the NGA classifications are believed to be based on relatively crude site locations based on published geodetic coordinates.

The phase I geologic classification database was updated as described above. The updated database is referred to as the “phase II database”. In the phase II database, as in that of phase I, sites are classified by geologic age, age + depositional environment, and age + material texture. Table 2.5 lists the major categories of classification and the number of sites in each category. A complete listing of the phase II site classifications and the references used for each site, is provided at the Ground Motions Research web page of Professor Jonathan Stewart (**http://cee.ea.ucla.edu/faculty/jstewart/groundmotions.htm**).

Table 2.5 Criteria for surface geology classifications (and no. of sites)

Age	Depositional Environment	Sediment Texture
Holocene (531)	Holocene alluvium (329)	Holocene Coarse (90)
Pleistocene (138)	Pleistocene alluvium (83)	Pleistocene Coarse (19)
	H. lacustrine/marine (36)	Holo. Fine-Mixed (75)
	P. lacustrine/marine (9)	Pleist. Fine-Mixed (18)
	Aeolian (6)	
	Artificial Fill (12)	
Tertiary (132)		
Mesozoic + Igneous (82)		

2.2.2 Near-Surface Shear Wave Velocity

The average shear wave velocity of shallow sediments is commonly represented by parameter V_{s-30}, which is calculated as the ratio of 30 m to the vertical shear wave travel time through the upper 30 m of the site. Based on empirical studies by Borcherdt and Glassmoyer (1994), Borcherdt (1994) recommended V_{s-30} as a means of classifying sites for building codes, and similar site categories were selected for the NEHRP seismic design provisions for new buildings (Martin, 1994; Dobry et al., 2000). The V_{s-30}-based site classification scheme in the NEHRP provisions is presented in Table 2.6. An exception to the V_{s-30} criteria is made for soft clays (defined as having undrained shear strength < 24 kPa, plasticity index > 20, and water content > 40%), for which category E is assigned if the thickness of soft clay exceeds 3 m regardless of $V_{s\text{-}30}$.

Table 2.6 Site categories in NEHRP provisions (Martin, 1994; Dobry et al., 2000)

NEHRP Category	Description	Mean Shear Wave Velocity to 30 m
A	Hard Rock	> 1500 m/s
B	Firm to hard rock	760-1500 m/s
C	Dense soil, soft rock	360-760 m/s
D	Stiff soil	180-360 m/s
E	Soft clays	< 180 m/s
F	Special study soils, e.g., liquefiable soils, sensitive clays, organic soils, soft clays > 36 m thick	

It should be noted that shear wave velocity has been found to be well correlated to detailed surface geology (age + texture for soil, age + weathering/fracture spacing for rock) by Fumal (1978). The $V_{s\text{-}30}$ parameter has been correlated with surface geology by Wills and Silva (1998), and this information has been used to generate state-wide maps of $V_{s\text{-}30}$ by Wills et al. (2000).

A phase I database of $V_{s\text{-}30}$ parameters was compiled for strong motion sites by Stewart et al. (2001). That database was based solely on on-site geophysical measurements using one of the following techniques: downhole measurements in boreholes or CPT soundings, suspension logging, SASW techniques (generally by Kenneth Stokoe and co-workers), and cross-hole testing. Borings and geophysical measurements were paired with strong motion stations using a GIS database containing the locations of both strong motion stations and boreholes in California. Each strong motion station location was checked with instrument owners (USGS and CSMIP) or against published reports (USC—Anderson et al., 1981), to optimize accuracy. Borehole locations were generally obtained from maps in reports. The borehole database was similar to that of Wills and Silva (1998), but also contained additional Caltrans boreholes, boreholes from selected consulting geotechnical engineers, and data recently compiled in the ROSRINE program (**http://geoinfo.usc.edu/rosrine/**). The quality of site data pairings with strong motion site was judged as follows: A = 0–150 m, B = 150–450 m, C = 450–1600 m. Matches were assigned only if the borehole and strong motion site were on similar mapped surface geology.

If more than one set of site data is available for a given strong motion station (e.g., Fig. 2.2), $V_{s\text{-}30}$ values were generally assigned using the closest measurements to the strong motion station. If multiple measurements are available at close distance, the most recent set of measurements were generally used (e.g., ROSRINE sites given preference over USGS downhole sites). Additional factors considered in such situations included depth of geophysical measurements (larger depths preferred) and the depth where velocity data begin (shallow depths, implying less need for extrapolation, are preferred).

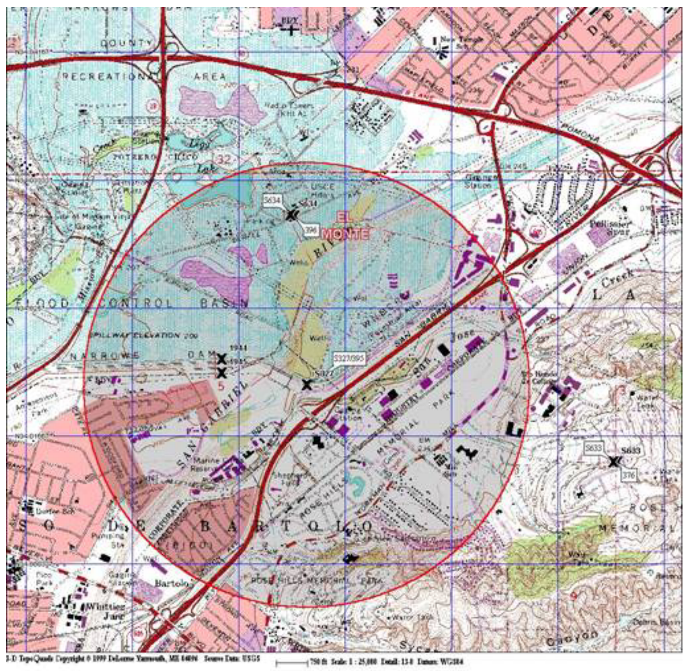

Fig. 2.2 An example of matching borehole/geophysical measurement and strong motion station

The phase I database of Stewart et al. (2001) has been continuously updated as additional data have become available. Sites added to the database appear in Table 2.2 (31 of which have measured $V_{s\text{-}30}$ values). Major sources of data since 2001 have included SASW data at both the Los Angeles and Imperial Valley strong motion stations by Stokoe and co-workers (Kenneth Stokoe, *personal communication*) and re-analyzed downhole velocity profiles from USGS boreholes by Boore (2003). As a result of those new data, $V_{s\text{-}30}$ values for many sites have changed.

An additional database of $V_{s\text{-}30}$ values and NEHRP site classifications at strong motion sites has been compiled as part of the NGA project. NGA protocols call for $V_{s\text{-}30}$ values to be assigned based on site-specific V_s measurements if the measured V_s profile depths are deeper than 20 m (applied in all but 14 sites, where shallower profiles were used) and the separation distance between the strong motion site and the boring/geophysical measurement is ≤ 300 m. Otherwise, $V_{s\text{-}30}$ values are estimated based on classified surface geology by Borcherdt and co-worker (e.g., Borcherdt and Glassmoyer, 1994; Borcherdt, 2002), Wills, or Geomatrix site categories. It should be noted that NEHRP categories assigned by NGA are based solely on $V_{s\text{-}30}$ values (i.e., shear strength criteria are not considered for soft clay sites).

The $V_{s\text{-}30}$ values in the modified phase I database have been compared to those in the NGA database that are based on on-site geophysical measurements. The objective of this comparison exercise was to identify conflicts in the $V_{s\text{-}30}$ values and resolve those conflicts with a re-review of available boring logs and geophysical data. For the purpose of these comparisons, conflicts are defined as difference > 10% (i.e., the ratio of UCLA/NGA $V_{s\text{-}30}$ values is less than 0.9 or larger than 1.1).

Of the 234 sites in the modified phase I database, 166 were classified by NGA using local geophysical data. NGA researchers were notified of the sites missing from their database in written correspondence. Of those 166 sites, no conflict was found for 153. Of the 13 sites with a conflict, re-checks of the geophysical logs indicate that $V_{s\text{-}30}$ values from the modified phase I database were correctly interpreted from the logs, are based on data sources generally regarded as being high quality, and involve small separation distances between the strong motion station and the location of geophysical measurements/borehole. Those sites are listed in Table 2.7. In some of those cases, it is possible that NGA $V_{s\text{-}30}$ values are in error. In most cases it is suspected that the deviations arise from different assumptions about velocities in the upper few meters (which are generally not measured with suspension or downhole logging techniques). In other cases different geophysical logs from the same site may have been used.

There are 10 unclassified sites in the modified phase I database that were classified by NGA based on on-site geophysical data. In those cases, the NGA classifications were adopted. Those sites are listed in Table 2.8. In addition, there are 36 sites classified by NGA based on on-site geophysical data that were not in the modified phase I database. Those sites were added to the phase II database, and are classified using NGA $V_{s\text{-}30}$ values. Of those 36 sites, 7 have previous classifications that appear in Appendix B of Stewart et al. (2001). NGA $V_{s\text{-}30}$ values for those sites were checked, and no conflicts were identified.

Table 2.7 Sites with conflicts in V_{s-30} values in which NGA value may be in error

				Modified Phase I			NGA
Location	Station Name	Agency	Station #	V_{s-30} (m/s)	Distance Code	Phase I Source	V_{s-30} (m/s)
Gilroy	Gilroy 3; Sewage Plant	CSMIP	47381	309	A	USGS OFR 82-407*	350
Joshua Tree	Fire Station	CSMIP	22170	343	A	ROSRINE	379
LA	Obregon Park #	CSMIP	24400	449	A	ROSRINE	349
Rancho Palos Verdes	Luconia	USC	90044	1054	A	ROSRINE	509
Rinaldi	Receiving Station	DWP	5968 (77)	333	A	USGS OFR 99-446*	282
Salton Sea	Salton Sea Wildlife Refuge	USGS	5062	167	A	USGS OFR 84-562*	191
San Francisco	International Airport	CSMIP	58223	225	A	USGS OFR 92-287*	190
Tarzana	Cedar Hill Nursery	CSMIP	24436	300	A	ROSRINE	257
Treasure Island	Naval Base Fire Station	CSMIP	58117	172	A	USGS OFR 92-287*	155
Turkey	Arcelik ARGE Lab.	Kandilli		430	A	Rathje et al. (2003)	523
Turkey	Bolu Bayindirlik ve Iskan Mudurlugu	ERD		290	A	Rathje et al. (2003)	326
Turkey	Lam1060	Lamont		650	A	Rathje et al. (2003)	782
Yerba Buena Island	USCG Foghorn Bldg.	CSMIP	58163	572	A	USGS OFR 92-287*	660

* Velocities from this source updated by Boore (2003)

Table 2.8 Sites not classified in modified phase I database but classified by NGA based on on-site geophysical data

Location	Station Name	Agency	Station #	V_{s-30} (m/s)	Source
Arcadia	Campus Dr.	USC	90093	368	NGA
Hyoken-Nanbu	Port Island 0m	CEOR		198	NGA
LA County	Whittier Narrows Dam (upstream)	ACOE	289	299	NGA
Leona Valley	#6	CSMIP	24309	327	NGA
San Martin	Coyote Lake Dam (downstream)	CSMIP	57504	295	NGA
San Onofre*	Nuclear Power Plant	CIT	280	443	NGA
Santa Clara County	Anderson Dam (left abutment)	USGS	1652	489	NGA
Santa Fe Springs	E. Joslin	USC	90077	339	NGA
Tabas	Tabas		9101	767	NGA
Wheeler Ridge*	Tejon Hills oil Field	CIT	102/1102	348	NGA

Even for sites where the modified phase I V_{s-30} values and NGA V_{s-30} values are similar, discrepancies in NEHRP categories occurred for some soft soil sites. This occurred because the NGA classification is based strictly on V_{s-30}, whereas the present classifications utilize the full NEHRP criteria that consider the thickness and shear strength of soft soil layers. All sites affected by this situation have a D classification in NGA and E classification in the present database. Those sites are San Francisco International Airport (CSMIP 58223), Alameda Naval Air Station (US Navy), Palo Alto—1900 Embarcadero (CSMIP 58264), and El Centro Array 11 (USGS 5058).

The modified phase I V_{s-30} values database was updated as described above. The updated database is referred to as the phase II database. The phase II database contains a total of 280 strong motion stations paired to boreholes with geophysical measurements and/or paired to geophysical measurements without boreholes (i.e., SASW data). The distribution of V_{s-30} values is presented in Figure 2.3. The phase II database of V_{s-30} parameters can be found at the Ground Motions Research website of Prof. Jonathan Stewart (**http://cee.ea.ucla.edu/faculty/jstewart/groundmotions.htm**).

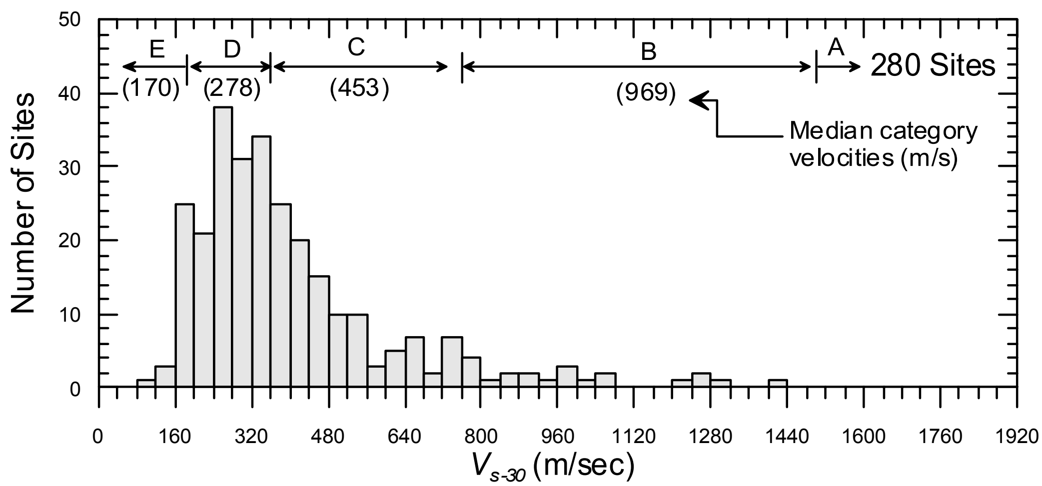

Fig. 2.3 Distribution of V_{s-30} utilized in phase II database (measured V_{s-30} only)

2.2.3 Geotechnical Data

Geotechnical engineers have developed site classification schemes that are intended to aide in the estimation of response spectra as a function of site condition. Early work on this topic is summarized in Seed and Idriss (1982), who recommended the following site classification scheme:

1. Rock sites
2. Stiff soil sites (< 60 m deep)
3. Deep cohesionless soil sites (> 75 m deep)
4. Sites underlain by soft to medium stiff clays

Dickenson (1994) and Chang (1996) proposed new site categories based on additional data gathered from the 1985 Mexico City, 1989 Loma Prieta, and 1994 Northridge earthquakes. A feature that differentiates those geotechnical schemes from other schemes discussed previously is the incorporation of information on sediment depth. However, these schemes generally do not directly consider sediment age nor a direct quantification of stiffness.

The most recent of the geotechnical classification schemes is shown in Table 2.9, and was proposed by Rodriguez-Marek et al. (2001) based on event-specific regressions of Loma Prieta and Northridge earthquake recordings. Rodriguez-Marek et al. (2001) recommend use of their classification scheme over the $V_{s\text{-}30}$ scheme, since they found intracategory standard error terms for these two earthquakes to be minimized through the use of the geotechnical scheme.

Table 2.9 Geotechnical site categories proposed by Rodriguez-Marek et al. (2001)

Site	Description	Comments
A	Hard Rock	Crystalline Bedrock; $V_s \geq 1500$ m/s
B	Competent Bedrock	$V_s \geq 760$ m/s or < 6 m of soil. Most "unweathered" California Rock cases
C1	Weathered Rock	$V_s \approx 360$ m/s increasing to > 700 m/s, weathering zone > 6 m and < 30 m
C2	Shallow Stiff Soil	Soil depth > 6 m and < 30 m
C3	Intermediate Depth Stiff Soil	Soil depth > 30 m and < 60 m
D1	Deep Stiff Holocene Soil	Depth > 60 m and < 200 m
D2	Deep Stiff Pleistocene Soil	Depth > 60 m and < 200 m
D3	Very Deep Stiff Soil	Depth > 200 m
E1	Medium Thickness Soft Clay	Thickness of soft clay layer 3-12 m
E2	Deep Soft Clay	Thickness of soft clay layer > 12 m
F	Potentially Liquefiable Sand	Holocene loose sand with high water table ($z_w \leq 6$ m)

An effort was made during the development of the phase I database to classify strong motion stations according to the scheme in Table 2.9 (Stewart et al., 2001). Sites were classified according to the geotechnical scheme using data from boreholes matched to strong motion stations (using the matching system described in Section 2.2.2). Geotechnical classifications were developed for all sites with a matched borehole. Developing the classification was straightforward if the borehole reached rock. If depth to rock was not known but the site is located in an area with known deep sediments, D classifications were given. If the depth to rock was not known and the sediment thickness could reasonably be expected to fall within several of the depth categories in Table 2.9, a range of possible classifications was given (e.g., C2–C3). The lower end of this depth range was constrained by the minimum known depth of sediments from the borehole (e.g., a site with a 30-m borehole that encounters only sediments must be C3 or D, and cannot be C2). Geotechnical classifications were not made in the absence of borehole data with the exception of sites known from field mapping to be near outcropping rock, in which case B-C1 classifications were generally assigned. Classifications were obtained in this way for 205 sites, with the classifications presented in Appendix A of Stewart et al. (2001).

An additional database of geotechnical classifications at strong motion sites has been compiled as part of the NGA project. NGA geotechnical classifications are based on borehole or geophysical site-specific data where available, and for other sites are based on correlation relationships with other types of site classifications. NGA site classifications using site-specific data drew upon previous classifications by others (Rathje et al., 2003 for selected Turkey sites; Rodriguez-Marek et al., 2001 for selected sites that recorded the Loma Prieta and Northridge earthquakes; Stewart et al., 2001 for California sites with boreholes). For sites without site-specific borehole/geophysical data, NGA geotechnical classifications are based on correlation relationships with other classification schemes as follows:

- For Taiwan sites, correlations with geology-based classifications by Lee et al. (2001), as shown in Table 2.10.
- For sites in extensional regions, correlations with geotechnical-type classifications by Spudich et al. (1999), as shown in Table 2.11.
- For other areas, corrections with Geomatrix site classifications were used, as shown in Table 2.12.

Note that for NGA sites classified by the above process, the geotechnical classifications would be expected to be highly correlated with surface geology-based classifications.

Table 2.10 Correlation relationship between geology-based classification by Lee et al. (2001) and geotechnical categories

Lee et al. (2001) Classification	Geotech. Category
Miocene and Old Strata, limestone, igneous rocks, and metamorphic rocks, etc	B
Pliocene and Pleistocene strata, conglomerates, pyroclastic rocks, etc, and geomorphologic lateritic terraces	C
Late Pleistocene and Holocene strata, geomorphologic flurial terrace, and stiff clays and sandy soils with average SPT N > 15 in the upper 30m	D
Holocene deposits and Fills, etc., with average SPT N < 15 in the upper 30m	E

Table 2.11 Correlation relationship between geotechnical-type classification by Spudich et al. (1999) and geotechnical categories

Spudich et al. (1999) Classification	Geotech. Category
Hard Rock	B
Soft Rock	C
Deep Soil	D
Shallow Soil	C

Table 2.12 Correlation relationship between Geomatrix classification and geotechnical categories

Geomatrix Classification	Geotech. Category
A	B
B	C
C,D	D
E	E

As noted previously, the phase I database has been modified over time with the addition of the sites in Table 2.2 (30 of which have geotechnical classifications). Consequently, the modified phase I database has a total of 235 sites.

The geotechnical classifications in the modified phase I database have been compared to those in the NGA database. The objective of this comparison exercise was to identify conflicts and to resolve those conflicts with a re-review of available boring logs and geophysical data. In addition, NGA classifications were added for 10 sites in Turkey that were unclassified in the modified phase I database.

Of the 235 sites in the modified phase I database, no conflict was found for 208 of those sites. Conflicts were resolved by re-reviewing available site-specific data and by considering whether site visits had been performed (this is especially important for distinguishing rock and soil sites, i.e., resolving geotechnical categories B–C or C1–C2). Based on this re-review, of the 27 conflicts, classifications of nine sites originally classified by Stewart et al. (2001) were changed to match NGA classifications. Those sites are listed in Table 2.13.

Table 2.13 Sites with conflicts in geotechnical classifications in which NGA classification was adopted

Location	Station Name	Agency	Station #	Mod. Phase I Geot.	NGA Geot.
Belmont	Envirotech Bldg. (2 story)	CSMIP	58262	B	C
Gilroy	Gilroy 1; Gavilian Coll. Water Tank	CSMIP	47379	A	B
Gilroy	Gilroy 6; San Ysidro	CSMIP	57383	B	C
LA	Brentwood VA Hospital	USGS	638	C3	D
LA	LA Dam	USGS/LADWP	2141	B	C
Lake Hughes	#12 - Elizabeth Lake	CSMIP/CIT	24607	B	C
San Francisco	Presidio	CSMIP	58222	B	C
Santa Cruz	UCSC/ Lick Obs. Elect. Lab	CSMIP	58135	B	C
Sylmar	Converter Station East	DWP	75	C2	D

A number of sites were identified where a discrepancy exists, but a re-check of the site data does not providing compelling evidence for changing the modified phase I classifications. Those sites are listed in Table 2.14. In most cases, the discrepancy arises in the absence of definitive data indicating sediment depth (i.e., there is an on-site borehole, but it does not reach firm bedrock), and different assumptions regarding sediment depth were made in the absence of such data. Many of those sites are near basin edges, where it is difficult to judge sediment depths. In other cases, the authors and their co-workers had access to proprietary borehole data that may not have been available to other investigators, which likely caused the discrepancy. Finally, the authors and their co-workers have visited many of the sites, and those visits have influenced our interpretations in several cases —again, these are data that may not have been available to those providing NGA classifications.

There are many sites that either did not appear in the modified phase I database or that did appear in the database but lacked geotechnical classifications. Some of those sites have geotechnical classifications in the NGA database. In general, those NGA classifications were not adopted because it is believed that they were developed with correlation relationships (i.e., Tables 2.10–2.12) and not site-specific data. However, classifications based on borehole data are available for 7 of those NGA sites in Appendix B of Stewart et al. (2001). Those classifications were checked against NGA classifications, and any resulting conflicts are presented in Tables 2.13–2.14.

Table 2.14 Sites with geotechnical classification discrepancy between modified phase I database and NGA database

				Modified Phase I			NGA
Location	Station Name	Agency	Station #	Geot.	Boring/SiteVisit	Source	Geot.
Gorman*	Oso Pumping Plant	CIT/USGS	52/994	C3	boring	USGS OFR 84-681	D
Tehachapi*	Pumping Plant	CIT	27/1027	C1	boring	USGS OFR 84-681	B
	Santa Felicia Dam (Outlet)	CIT	285	C2	boring	NUREG/CR-0055, V2, LC 8'	B
Lake Hughes	#4 - Camp Mendenhall	CSMIP/CIT	24469	C	boring	USGS OFR 82-833	B
Newhall	LA County Fire Station	CSMIP	24279	C3	boring/site visit	ROSRINE	D
San Marino	SW Academy	CSMIP	24401	D	boring	Law/Crandall 85240	C
Sylmar	Converter Station	DWP	74	C3	boring	ROSRINE	D
Hollister	SAGO-South	CSMIP	47189	C1	boring	AA 9225-6427	B
LA	Saturn St	USC	90091	D	boring	ROSRINE	F
Lake Hughes	#1 - Fire Station #78	CSMIP/CIT	24271	C2	boring	USGS OFR 82-833	D
Lake Hughes	#4B - Camp Mendenhall	CSMIP	24523	C2	boring	USGS OFR 82-833	B
Palmdale	Hotel free field	CSMIP	24521	D	boring/site visit	USGS OFR 82-833, UCB EI	C
Palos Verdes*	Estates - Via Tejon	USGS/CIT	411	C2	boring	USGS OFR 84-681	D
San Bernadino	CSUSB Grounds	CSMIP	23672	C?	boring/site visit	UCB EERC-97/01:estimatior	D
Santa Barbara	UCSB Goleta	CSMIP	25091	D	boring/site visit	Law/Crandall 80172	C
Santa Susana	ETEC, Freefield	USGS	5108	B	boring/site visit	ROSRINE	C
Superstition Mtn	USAF Camera Site	USGS/CIT	286	C1	boring	ROSRINE	B
El Centro	Array 6 - Huston Rd	USGS	942/5158	E	boring/SASW	USGS OFR 84-562	D
Fairmont Resevoir(1)	Fairmont Dam Right Abut.	CSMIP	24270	C1	boring	Nureg/CR-0055	B

Note: (1) Sites from Table B in Stewart et al. (2001b)

There are 12 sites that (a) did not appear in the modified phase I database, (b) are present in the NGA database but without geotechnical classifications, and (c) are classified in Appendix B of Stewart et al. (2001). Those sites were added to the phase II database using the previous classifications of Stewart et al. (2001).

The modified phase I geotechnical classifications database was updated as indicated above. The updated database is referred to as the "phase II database," and contains a total of 264 classified sites. The distribution of sites among geotechnical categories is presented in Figure 2.4. The phase II database of classified sites is presented at the Ground Motions Research website of Professor Jonathan Stewart (**http://cee.ea.ucla.edu/faculty/jstewart/groundmotions.htm**).

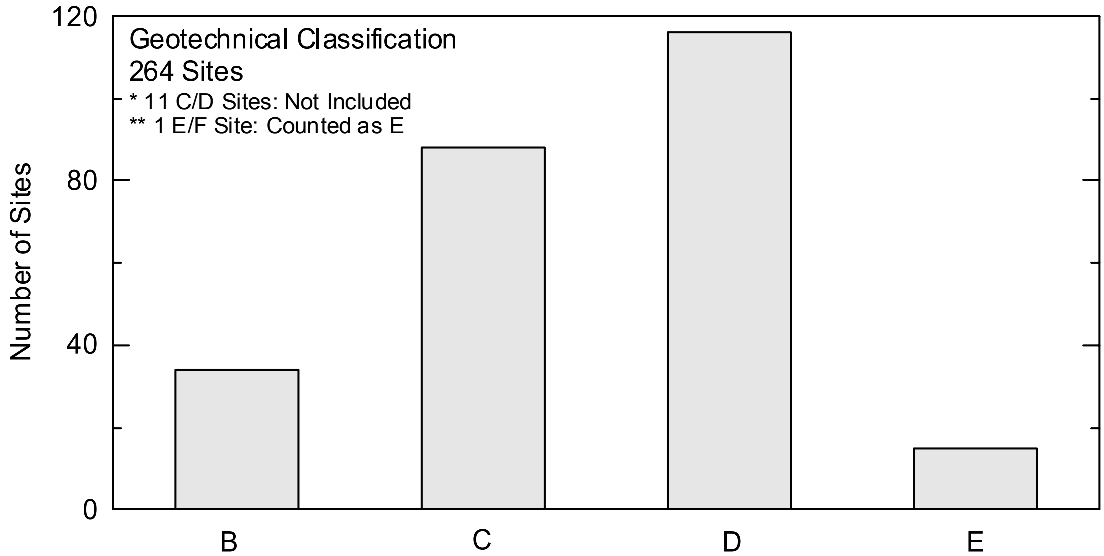

Fig. 2.4 Data breakdown for classification scheme based on geotechnical data

2.3 DEEP BASIN STRUCTURE PARAMETER DATABASE

2.3.1 Introduction

The overall "site effect" inherent to a given strong motion recording would be expected to be influenced by both shallow sediments and deeper basin structure. For convenience of terminology, the effects of shallow sediments are referred to as "local ground response," and the influence of deeper basin structure is referred to as "basin effects." Accordingly, local ground response refers to the influence of relatively shallow geologic materials on (nearly) vertically propagating waves. The term "basin effects" refers to the influence of two- or three-dimensional sedimentary basin structures on ground motions, including critical body wave reflections and surface wave generation at basin edges. An effort was made in this study to parameterize basin structure using available models. The models and basin parameters utilized in this work are described in the following sections.

2.3.2 Available Basin Models

Models of basin structure are available for the following areas within active tectonic regions:

- Southern California (Los Angeles area): Magistrale et al. (2000)
- San Francisco Bay Area: Hole et al. (2000)

- Kanto (Tokyo region): Sato et al. (1999)
- Kobe (Osaka region): Pitarka et al. (1998)
- Taipei: Wen and Peng (1998)

As the focus is on ground motions associated with shallow crustal earthquakes in active tectonic regions, the models for northern and southern California are utilized here. These models are described further in the paragraphs below.

(a) Southern California Basin Model

Magistrale et al. (2000) developed a 3D seismic velocity model for southern California. The model consists of detailed, rule-based representations of the major southern California basins embedded in a 3D crust and overlying a variable depth Moho (i.e., boundary between crust and upper mantle). The location map of this model is shown in Figure 2.5. The geometry of the basins within the model is represented by the contour maps in Figure 2.6. The basins are parameterized as *objects* (constructed from data) and *rules* for (1) estimation of real-valued parameters based on object properties and for (2) interpolation of those quantities between objects. Outside of the basins, the model crust is based on regional tomographic results.

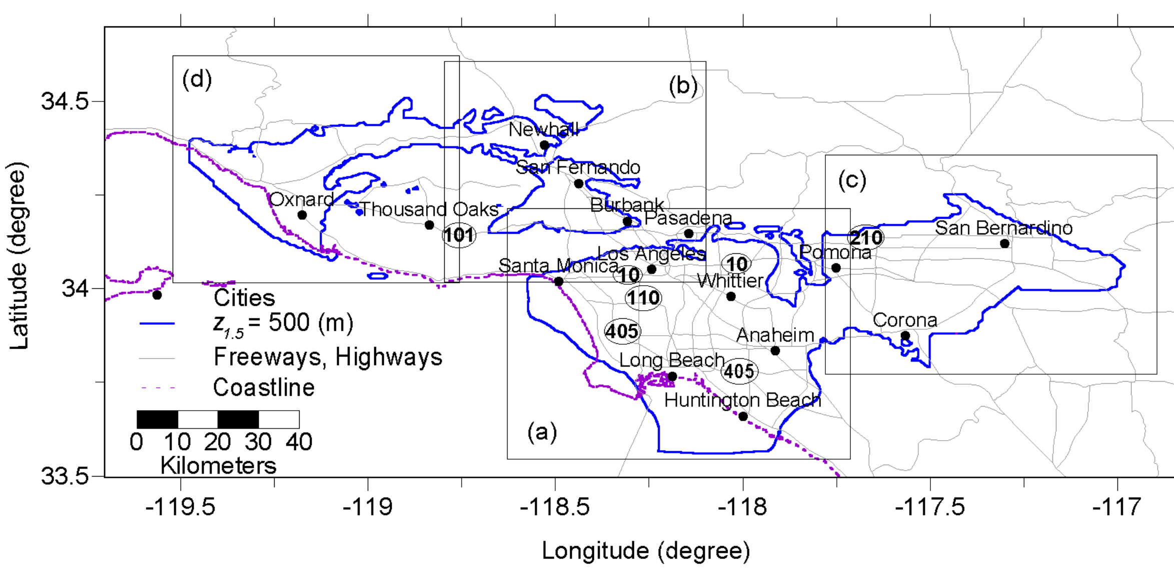

Fig. 2.5 Location map for southern California basins, with basin boundaries defined as contour of $z_{1.5}$ = 500 m (where $z_{1.5}$ is defined as depth to 1.5 km/s shear wave isosurface). Results shown are based on Magistrale et al. (2000) basin models for southern California. Detail maps for individual basins given in Figures 2.6(a)–(d).

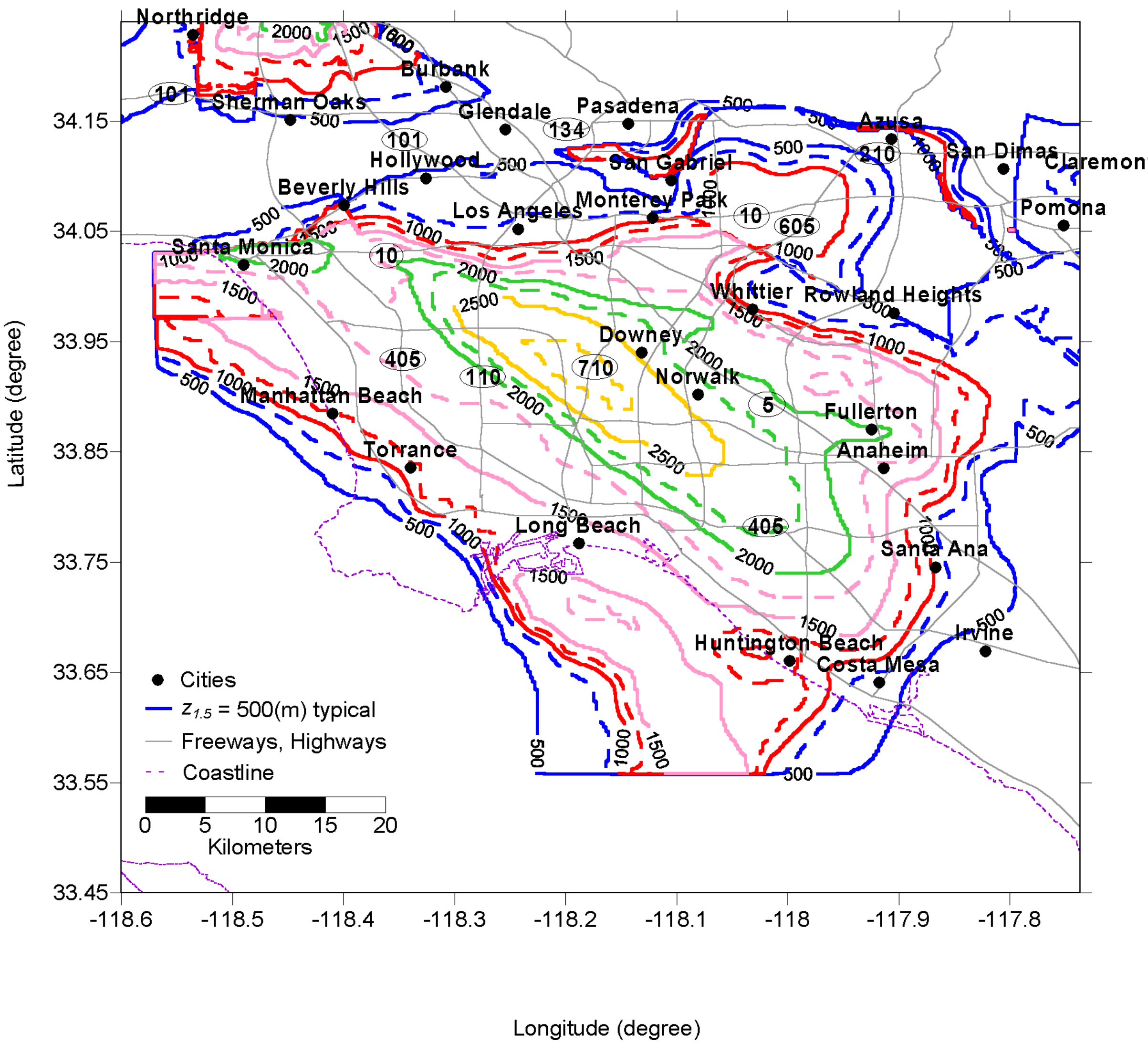

Fig. 2.6(a) Contour map of depth to 1.5 km/s shear wave isosurface ($z_{1.5}$) for Los Angeles basin, based on model of Magistrale et al. (2000)

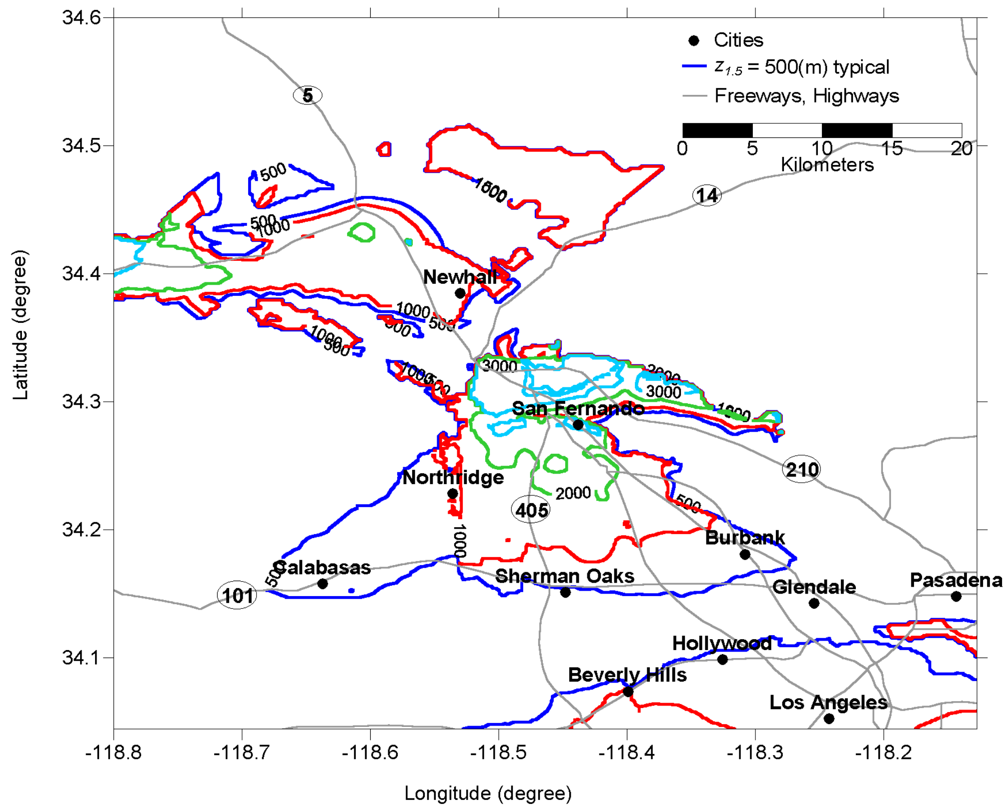

Fig. 2.6(b) Contour map of depth to 1.5 km/s shear wave isosurface ($z_{1.5}$) for San Fernando basin, based on model of Magistrale et al. (2000)

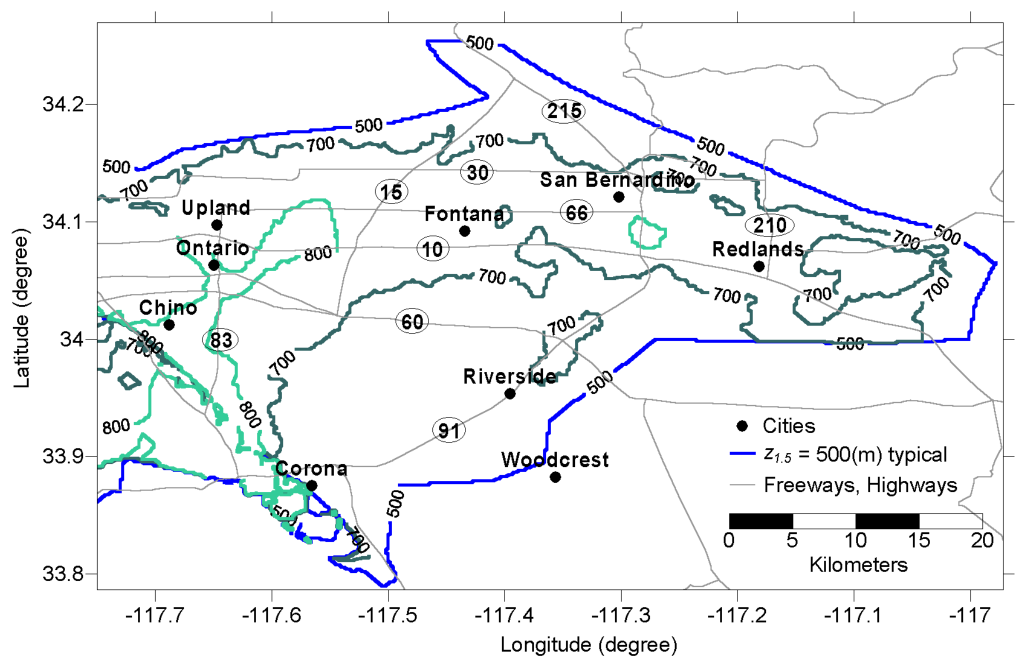

Fig. 2.6(c) Contour map of depth to 1.5 km/s shear wave isosurface ($z_{1.5}$) for San Bernardino-Chino basin, based on model of Magistrale et al. (2000)

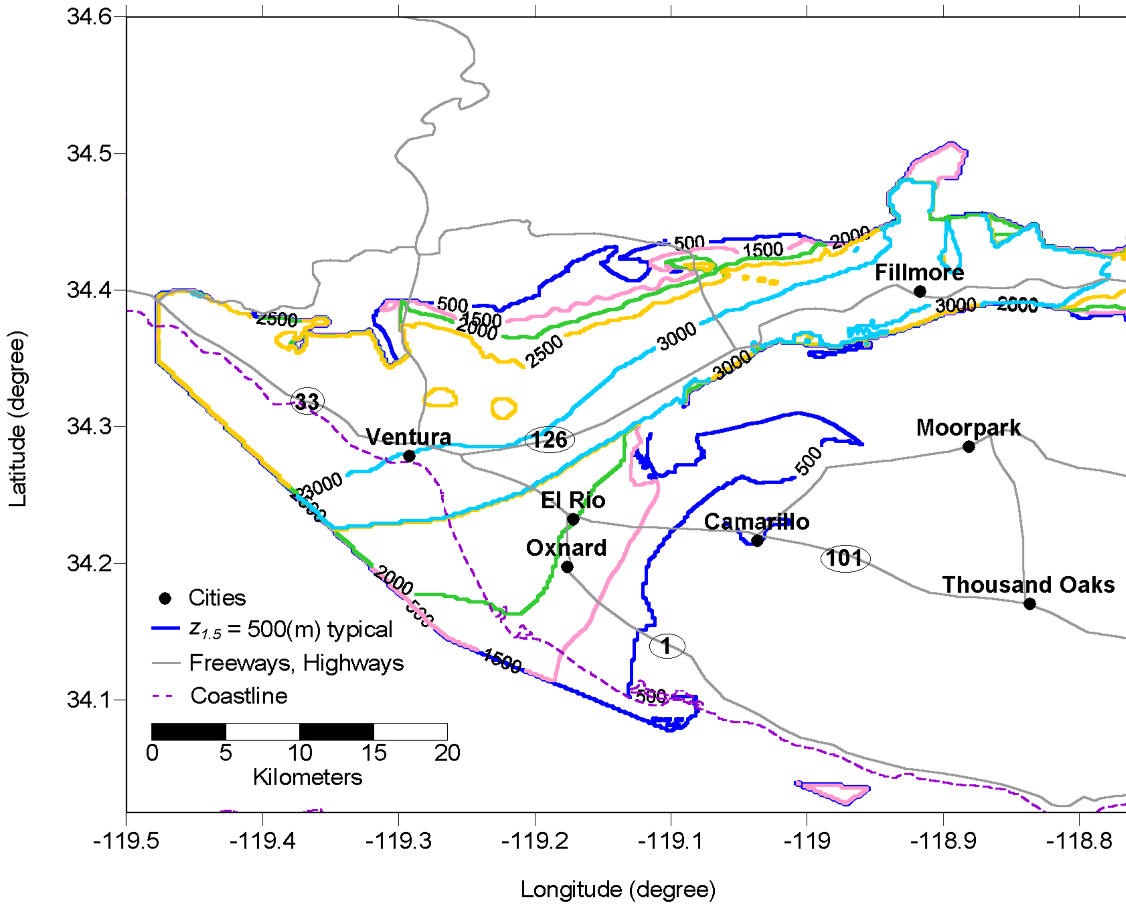

Fig. 2.6(d) Contour map of depth to 1.5 km/s shear wave isosurface ($z_{1.5}$) for Ventura basin, based on model of Magistrale et al. (2000)

The *objects* consist of reference surfaces within basins having known depth and age. The depth and age data for the objects are based on structural geologic cross sections and maps developed from oil and water exploration activities and other geologic studies. The reference surfaces correspond to stratigraphic horizons, sediment-basement contacts, and faults.

Rules used in the development of the velocity model include (1) an empirical relationship to estimate V_p from depth and age (which, in turn, are established from objects or interpolation between objects) and (2) empirical relationships between V_p and density and between density and Poisson's ratio, υ. The V_p-depth-age relationship is an empirical model by Faust (1951) that is based on about 500 seismic well surveys in the U.S. and Canada in sand and shale:

$$V_p = k(da)^{1/6} \tag{2.1}$$

where d = burial depth of sediments and a = age. Parameter k is an empirical constant that was taken as 197 by Magistrale et al. (2000) for the calculation of V_p at two regional biostratigraphic surfaces (base of Repetto and Mohnian; Wright, 1991) and the top of the crystalline basement (McCulloh, 1960; Yerkes et al., 1965). The above value of k is based on seven oil well sonic logs in the Los Angeles basin and four logs in the San Fernando basin along with seismic refraction survey results. Velocities are calculated for any position in a basin by interpolating between reference surfaces.

Density (ρ) was derived from velocity V_p using the relation of Nafe and Drake (1960), which is shown in Figure 2.7. Poisson's ratio (υ) was derived from density using the relation of Ludwig et al. (1970), which is shown in Figure 2.8. Shear wave velocity V_s was then estimated from V_p and υ as follows:

$$V_S = V_P \times \sqrt{\frac{1-2\upsilon}{2-2\upsilon}} \tag{2.2}$$

Properties of shallow sediments (depth < 300 m) within basins were separately established from geotechnical borehole data grouped into the five $V_{s\text{-}30}$-based categories of Wills et al. (2000). Generic velocity-depth profiles for each category were established and were coupled with surface mapping of $V_{s\text{-}30}$ by Wills et al. (2000) to estimate shallow velocity profiles for locations not near boreholes. For locations near boreholes, shallow velocities were based directly on the borehole data.

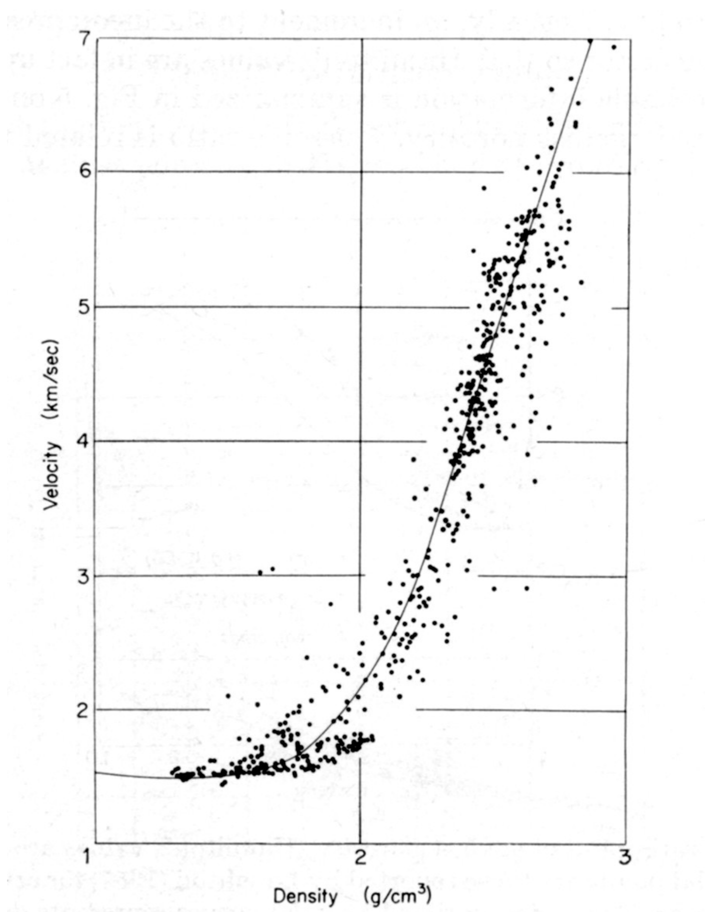

Fig. 2.7 Relationship between velocity V_p and density (Nafe and Drake, 1960)

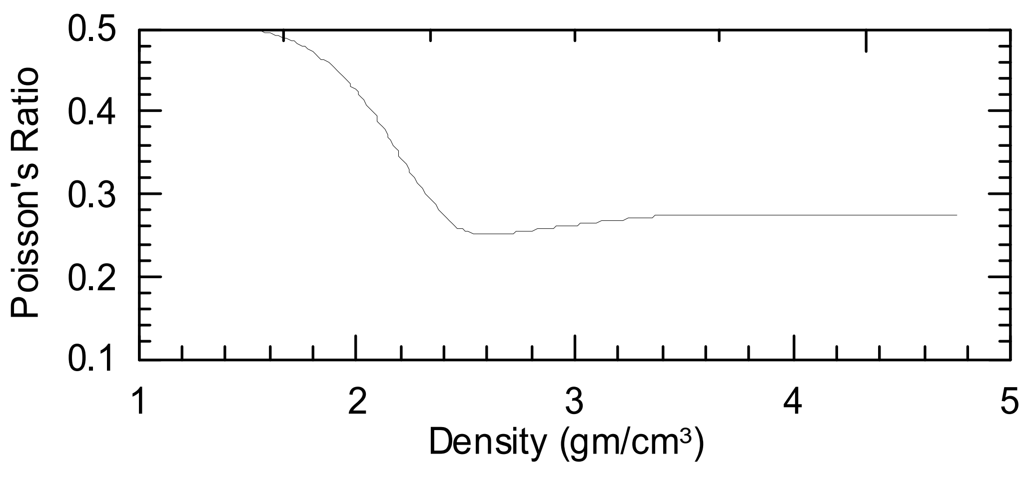

Fig. 2.8 Relationship between density and Poisson's ratio (after Ludwig et al., 1970)

(b) *Northern California Basin Model*

Hole et al. (2000) developed a 3D seismic velocity model for the San Francisco Bay Area. The model covers an area 130 by 220 km and vertical positions that vary from 3 km above sea level to 30 km below sea level. The model area is shown in Figure 2.9. The model provides p- and s-wave velocities at grid points at 125 m spacing (Graves, 2002, *personal communication*). The geometry of the basins within the model is represented by the contour map in Figure 2.10.

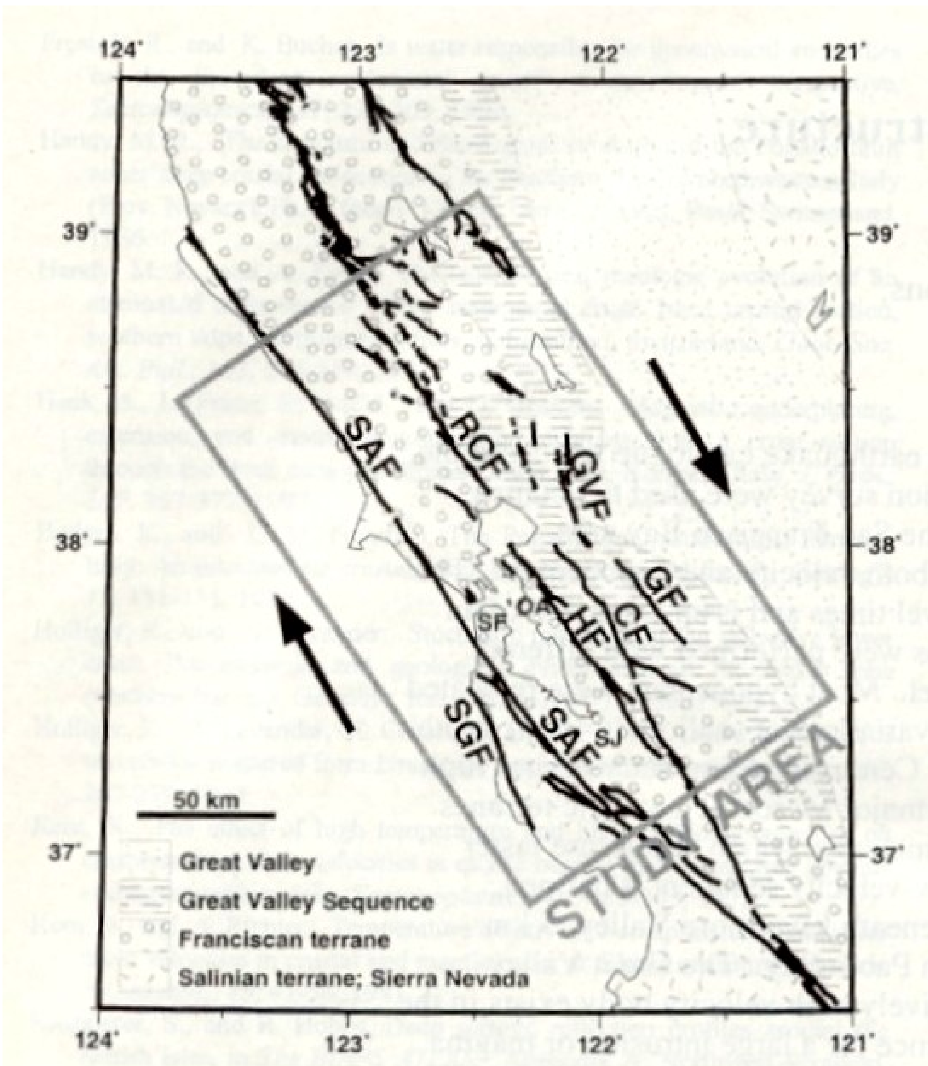

Fig. 2.9 Location map of San Francisco Bay Area basin model (Hole et al., 2000)

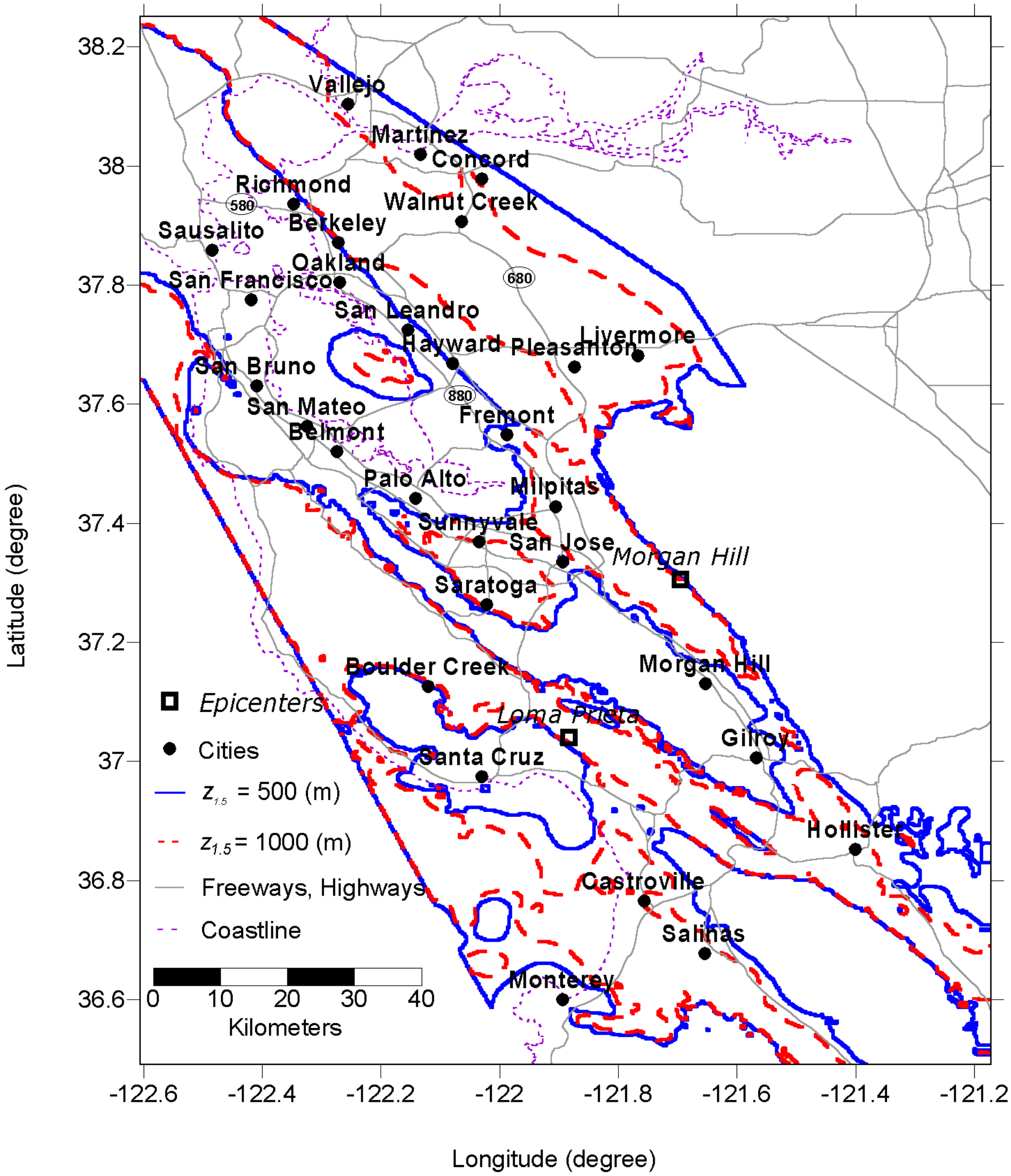

Fig. 2.10 Contour map showing depth to V_s = 1.5 km/s isovelocity surface in Hole et al. (2000) basin model for San Francisco Bay Area

The 3D velocity model is based on nonlinear tomography. Tomography is a process by which recorded waveforms are used in an inversion process to estimate both source locations and source-surface velocity structure. The process is complicated by the fact that the source location and origin time may not be known (i.e., in the case of an earthquake source), and thus have to be determined from the same set of recordings (i.e., the estimation of velocity structure and source characteristics is a coupled problem). Moreover, the paths along which seismic waves travel will bend, refract, and reflect at velocity contrasts; hence such contrasts influence the travel times not only directly but also indirectly (this is referred to as a problem of nonlinearity in the inversion). Seismologists have developed sophisticated numerical inversion techniques to solve these problems and simultaneously estimate source characteristics and velocity structure (e.g., Hole, 1992; Vidale, 1990; Toomey and Foulger, 1989).

Hole et al. (2000) employed nonlinear tomographic inversion techniques to establish the velocity structure within the study area shown in Figure 2.9. The data include earthquake travel times for well-recorded and well-located earthquakes with M > 2, as well as recordings derived from air gun shot recordings from the Bay Area Seismic Imaging Experiment (BASIX, Brocher and Pope, 1994). More weight was given to velocities inferred from BASIX data because of the known source locations. Earthquake data are abundant near faults, and velocities in the model are significantly influenced by seismic sources in those areas. In intermediate areas velocities are more significantly controlled by the BASIX data.

We generally have greater confidence in the relatively shallow velocity structure (i.e., corresponding to an s-wave isosurface of 1.0–1.5 km/s) than in deeper velocity structure (2.5 km/s shear wave isosurface). This is because the deeper isosurfaces are horizontal between the Bay Area's major strike-slip faults, which would appear to be an oversimplification. Confidence in seismic velocities estimated by tomographic inversion generally decreases with depth, so the above outcome is not surprising.

2.3.3 Parameterization of Basin Geometry

A number of parameters are used to describe basin geometry for ground motion studies. The motivation and justification for the use of these parameters is described in Chapter 5. The parameters that are used consist of the following:

- *Basin Depth (as parameterized by depth to shear wave isosurface)*: The value of this parameter that is considered is $z_{1.5}$ (depth to 1.5 km/s shear wave isosurface). This parameter was selected by a committee of basin modeling experts as the consensus depth parameter for basin studies.

- *Source-Site Basin Location*: We distinguish data with coincident source and site basin locations (CBL) from data with distinct source and site basin locations (DBL). The basin edge is defined as the $z_{1.5}$ = 500 m contour ($z_{1.5}$ < 500 m is outside basin, $z_{1.5}$ > 500 m is inside basin). If the surface projection of any portion of the fault plane lies within the basin boundary, "CBL" is assigned, whereas if no portion of the surface projection of the fault is within the basin, "DBL" is assigned.

These parameters were estimated for strong motion sites based on source locations developed by Dr. Walter Silva, as part of the NGA project and the basin models described above.

2.3.4 Uncertainty in Basin Depths

One of the most critical basin parameters is basin depth, as defined by the depth to a particular shear wave isosurface. Accordingly, an effort was undertaken to compare depth parameters obtained from the SCEC southern California (Los Angeles area) basin model of Magistrale et al. (2000) with an independent set of velocity measurements from sonic logs.

A large inventory of sonic log data was compiled by Süss and Shaw (2003), who used these data to develop an independent model of the p-wave seismic velocity structure in a portion of the Los Angeles basin. The model was based on more than 150 sonic logs and 7000 stacking velocities from industry reflection data. In comparing the sonic log velocities with those predicted by the SCEC model (Magistrale et al., 2000), Süss and Shaw (2003) found that the bulk average of estimated SCEC velocities are within about 100 m/s of the measured sonic log velocities. However, the standard deviation of the residuals was about 440 m/s, which is about 20% of the modeled velocities. Moreover, Süss and Shaw found that discrepancies between the two models are not evenly distributed across the basin, but that SCEC velocities are generally overestimated near basin borders and underestimated near the basin center. Those systematic discrepancies were attributed to significant lateral variations in SCEC velocities in cross sections drawn normal to the basin edge that are not observed in the sonic log data.

For the present study, a subset of the sonic log data of Süss and Shaw (2003) that was provided by Shaw (2002, *personal communication*) were utilized. The data subset consisted of 102 measured sonic log profiles in the Los Angeles basin at the locations shown in Figure 2.11. The SCEC model was queried for each sonic log location, and estimated V_p profiles were obtained.

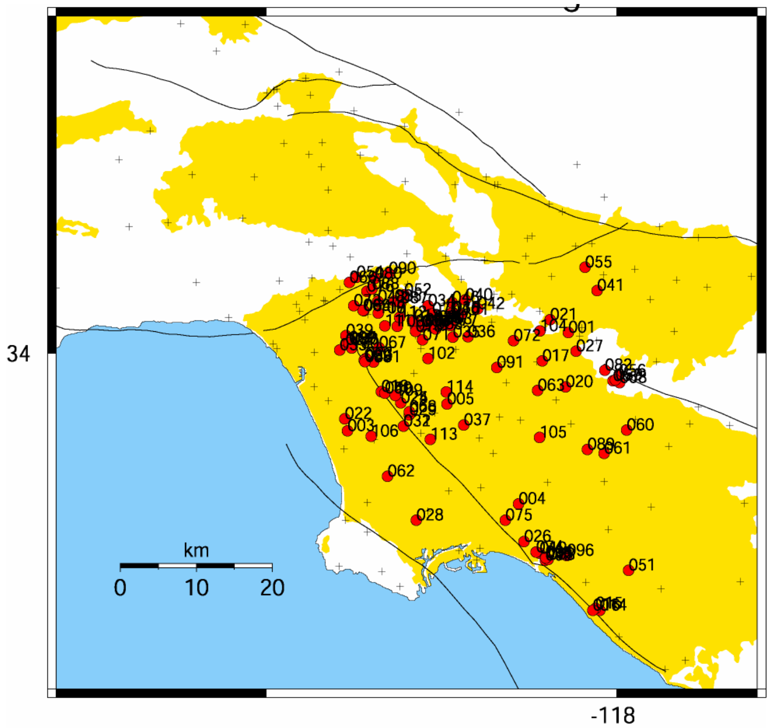

Fig. 2.11 Sonic log locations in Los Angeles basin (Shaw, 2002, personal communication)

Figure 2.12 shows a comparison of average V_p profiles from sonic logs as compared to predictions from the SCEC model. In order to quantify the location-specific discrepancies identified by Süss and Shaw (2003), the sonic-SCEC comparisons are performed for two geographic regions—one having $z_{1.5}$ < 1550 m and the other having $z_{1.5}$ > 1550 m (based on SCEC model). The 1550 m depth was chosen because it is the depth threshold that generally separates positive and negative residuals in the sonic-SCEC data. The results confirm Süss and Shaw's observation that SCEC velocities are high near basin margins and low near basin center. In both depth regions, the velocity gradient from SCEC is steeper (i.e., more rapid increase of velocity with depth) than observed in the sonic logs in the upper 2–3 km.

The location dependence of the sonic-SCEC velocity residuals affects depths to the 1.5 km/s velocity isosurface. Figure 2.13 maps residuals by locations and shows that the SCEC model generally underpredicts this depth parameter near basin margins and overpredicts it near the basin center.

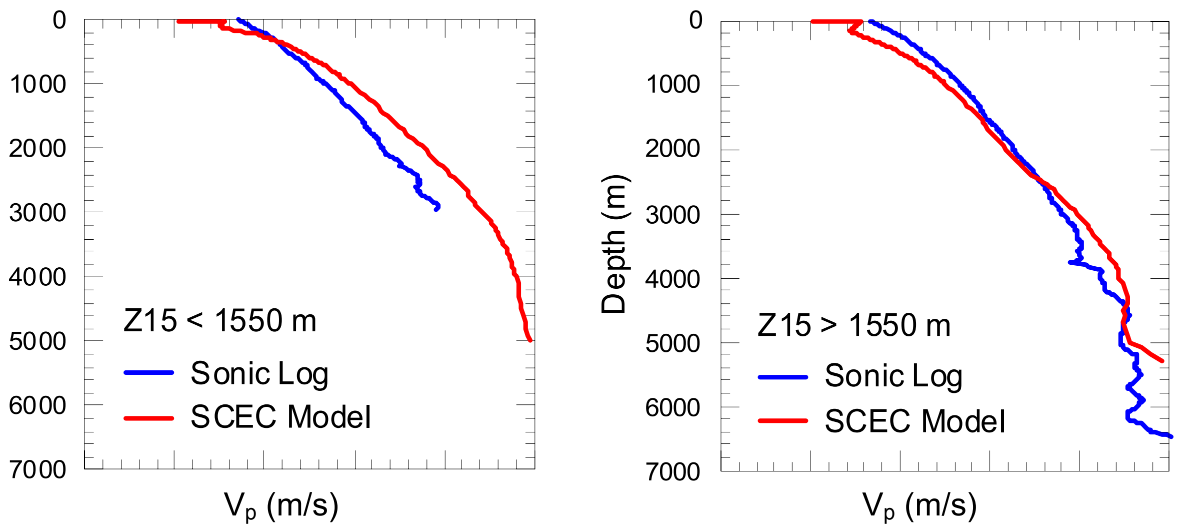

Fig. 2.12 Comparison of average p-wave velocity profiles from sonic log and SCEC model

The analysis of uncertainty in basin depth parameters estimated using the SCEC model takes into consideration the regional dependencies of residuals discussed above. Residuals for subsets of sonic logs with $z_{1.5}$ < 1550 m and $z_{1.5}$ > 1550 m are compiled and analyzed separately. In addition, residuals for a combined group of all data are analyzed.

Residuals are calculated for depth parameters $z_{1.0}$, $z_{1.5}$, and $z_{2.5}$. These are evaluated using corresponding p-wave velocities isosurfaces of 2.41 km/s (matching V_s=1.0 km/s), 3.07 km/s (matching V_s=1.5 km/s), and 4.41 km/s (matching V_s=2.5 km/s), respectively. Only 6 of the 102 sonic logs have profiles that extend to V_p = 4.41 km/s. Accordingly, comparisons are only possible for the depths to V_p = 2.41 km/s (102 logs available) and 3.07 km/s (83 logs available).

Figure 2.14 (a)–(d) show residuals plotted against SCEC model predictions, histograms of residuals, normalized residuals vs. SCEC depths, and histograms of normalized residuals for depth parameter $z_{1.0}$ and $z_{1.5}$. The SCEC model is seen to generally underestimate isosurface depths at locations with $z_{1.5}$ < 1550 m and to overestimate isosurface depths at locations with z_{15} > 1550 m, which is consistent with the findings described above. The combined data set has a negligible average residual (-50 m and 107m for $z_{1.0}$ and $z_{1.5}$, respectively). The standard deviation of residuals for the combined data set (e.g., 408 m for $z_{1.5}$) is significantly higher than the standard deviation of the partitioned data sets (approximately 280 m for both).

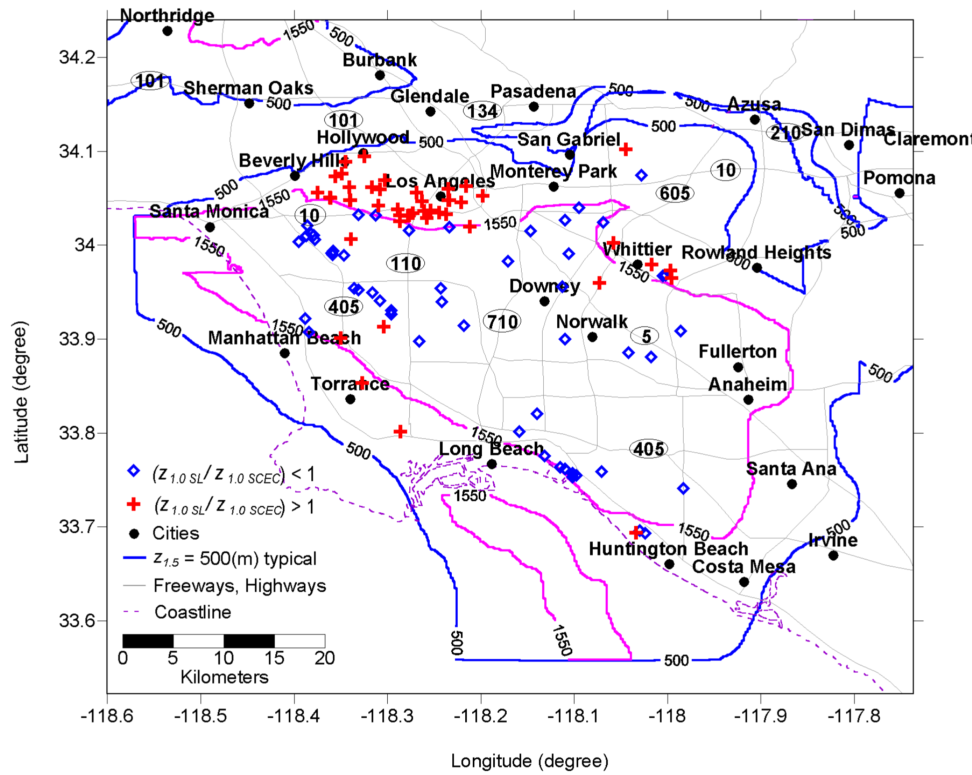

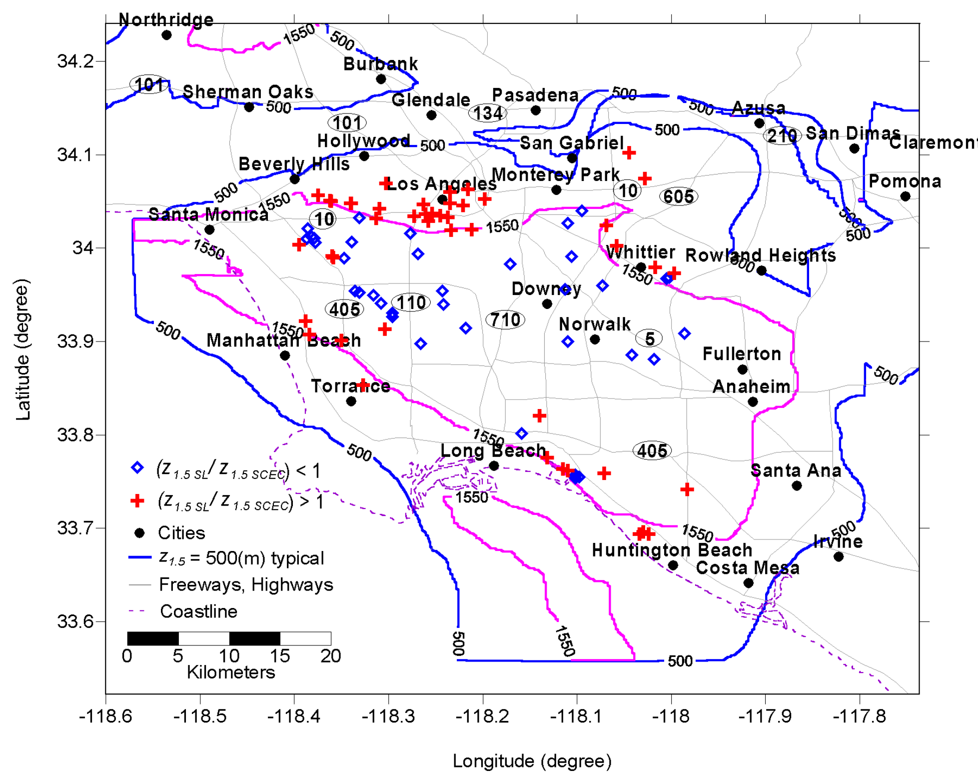

Fig. 2.13 Spatial distribution of ratios of over- and underprediction biases in SCEC model predictions

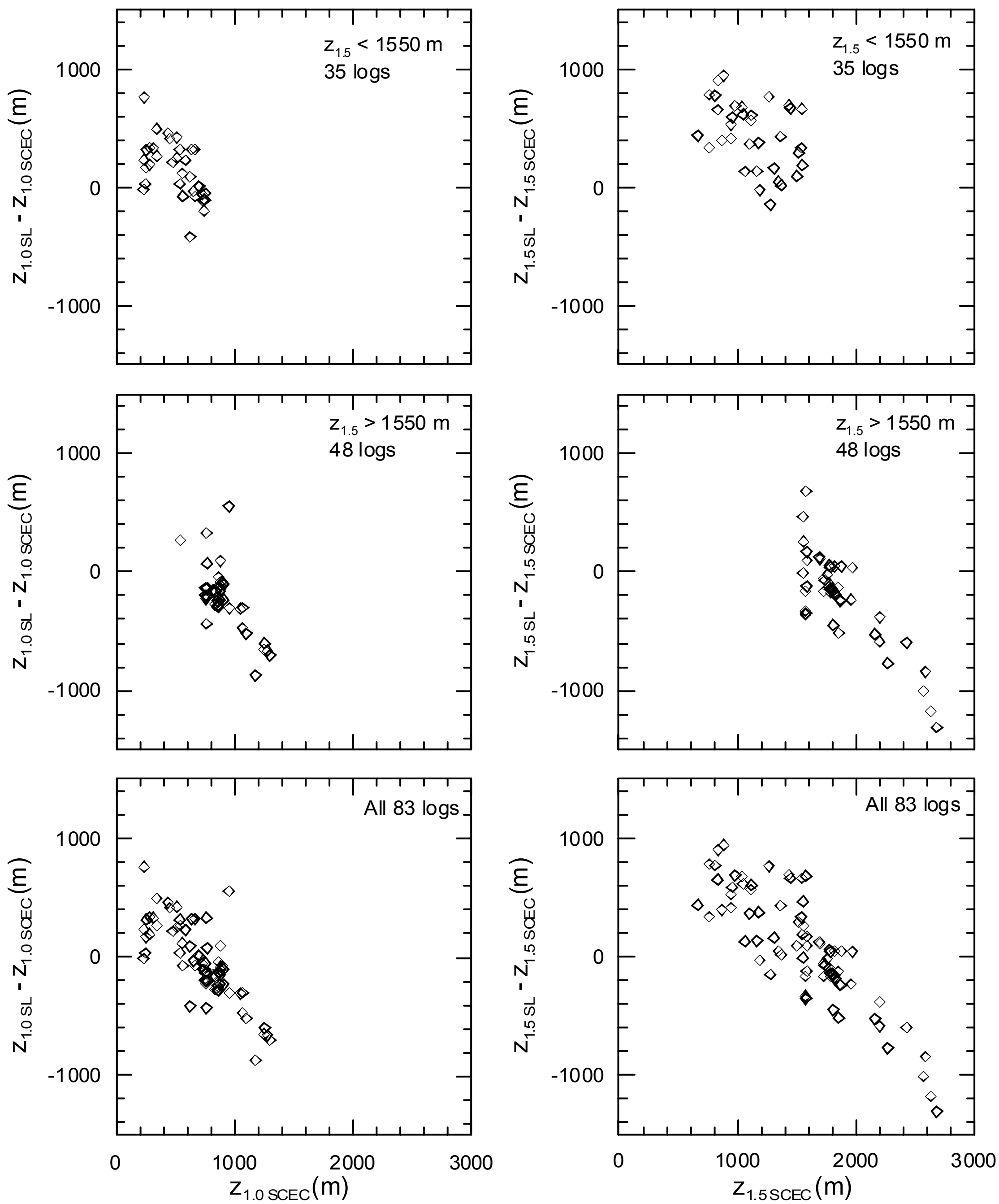

Fig. 2.14(a) Residuals of SCEC model with respect to sonic log data ($z_{1.0}$ and $z_{1.5}$)

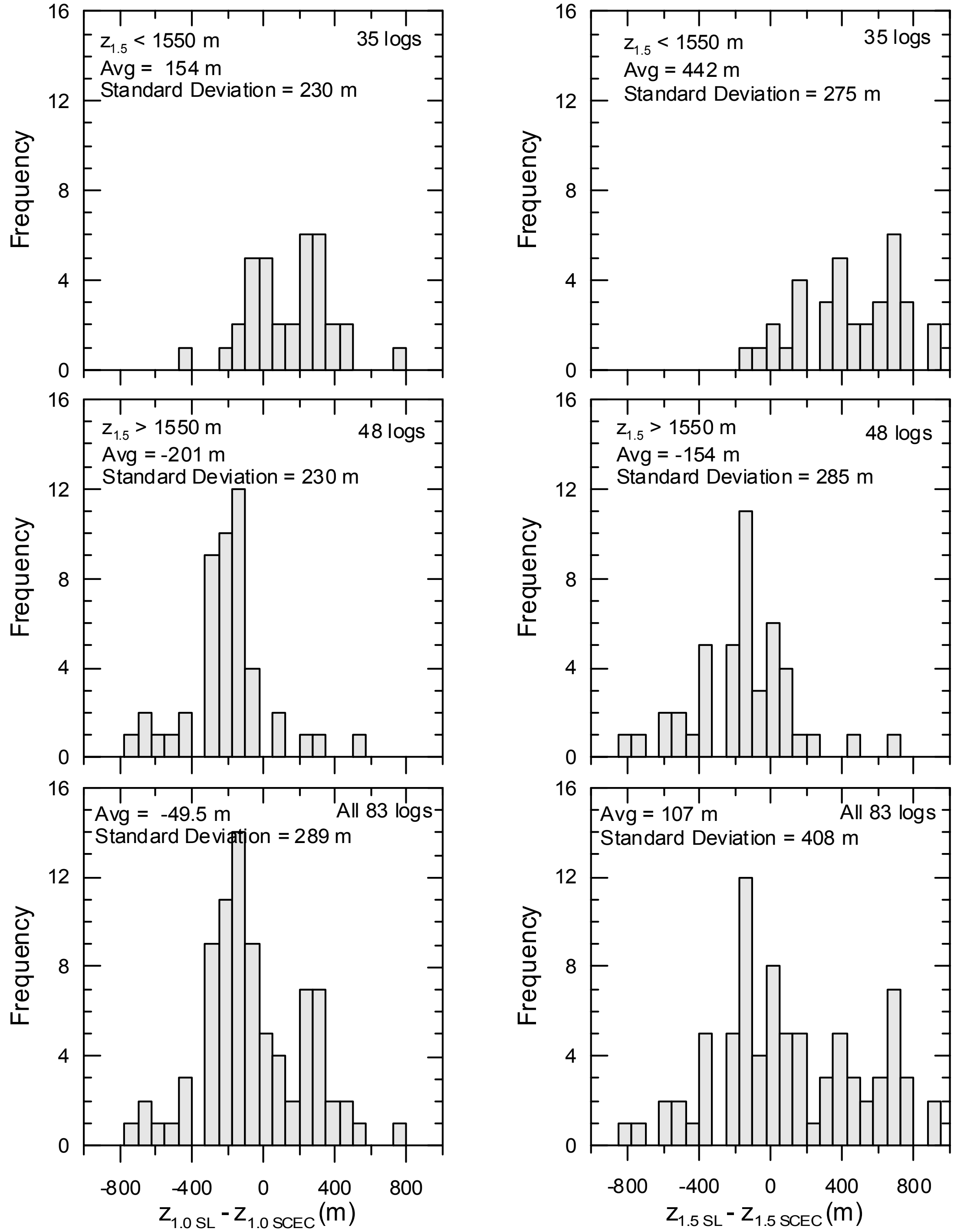

Fig. 2.14(b) Histogram of residuals of SCEC model with respect to sonic log data ($z_{1.0}$ and $z_{1.5}$)

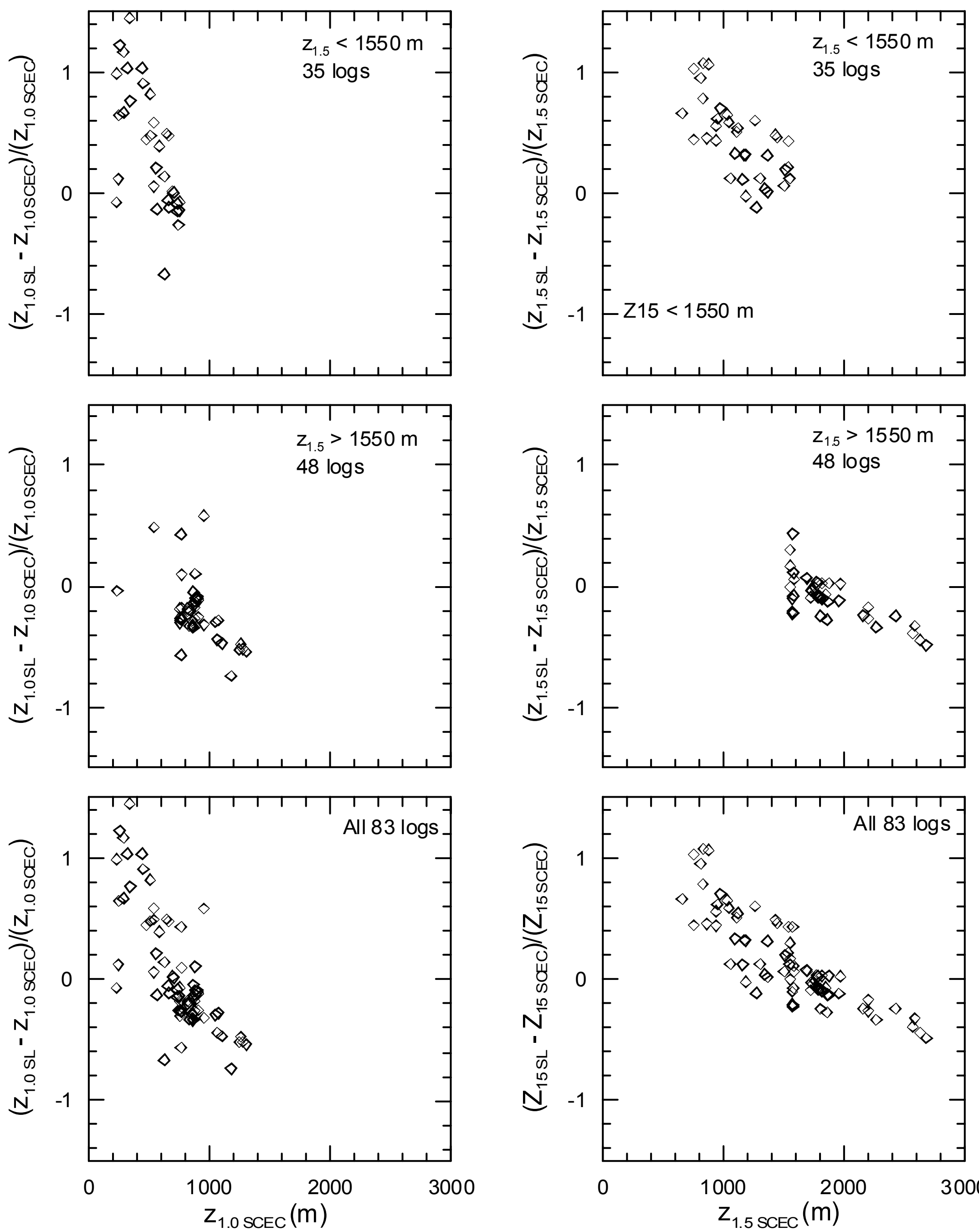

Fig. 2.14(c) Normalized residuals of SCEC model with respect to sonic log data (*$z_{1.0}$* and *$z_{1.5}$*)

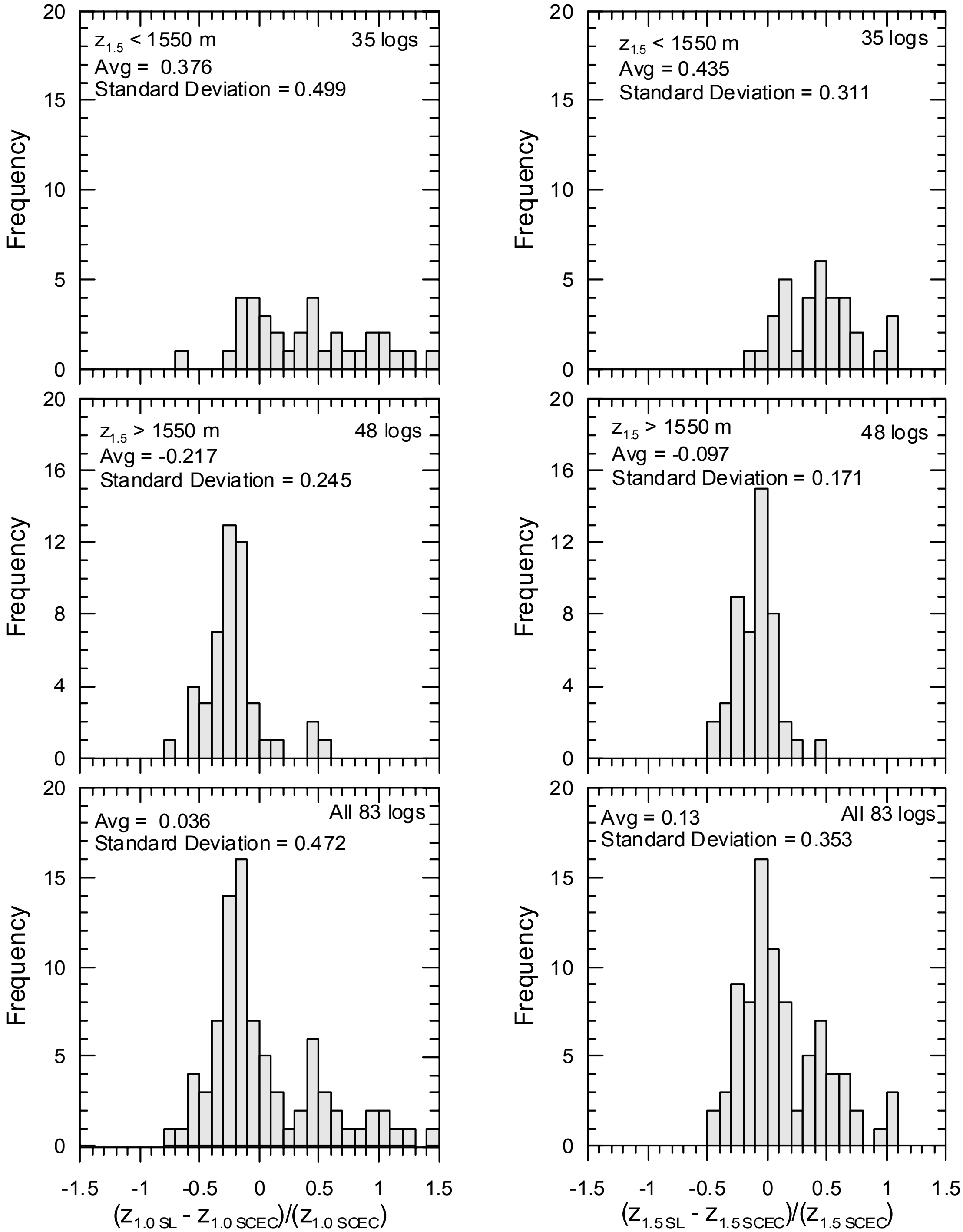

Fig. 2.14(d) Histogram of normalized residuals of SCEC model with respect to sonic log data (*$z_{1.0}$* and *$z_{1.5}$*)

3 Ground Motion Amplification Factors for Various Classification Schemes

3.1 INTRODUCTION

Ground motion attenuation relationships are used in seismic hazard analyses to provide a probabilistic distribution of a particular ground motion intensity measure (*IM*), such as 5% damped response spectral acceleration, conditional on magnitude, site-source distance, and parameters representing site condition and style of faulting. Ground motion data are often log-normally distributed, in which case the distribution can be represented by a median and standard deviation, σ (in natural logarithmic units). Site condition is often characterized in attenuation relations as either rock or soil. Actual conditions at strong motion recording sites are variable with respect to local site conditions and underlying basin structure, and hence estimates from attenuation relationships necessarily represent averaged values across the range of possible site conditions within the "rock" or "soil" categories. Ground motion amplification factors provide a means by which more detailed information on site conditions can be used to improve ground motion predictions relative to what is obtained with attenuation relationships. This "improvement" in ground motion prediction generally involves (1) removing potential bias in median ground motion estimates that might be present for a particular site condition and (2) reducing the uncertainty in ground motion estimates, as measured by standard error term, σ.

Amplification factors represent the ratio of an observed *IM* to a reference value of that *IM* for a particular site condition (e.g., intact rock or rock-average for active regions). Since ground motion recordings are affected by source, path, and site effects, the evaluation of amplification factors from recorded motions requires the removal of source and path effects. This can be accomplished by comparing, for a given earthquake, *IM*s from sites with various geologic conditions to *IM*s from "reference" (usually firm rock) sites, with appropriate corrections for distance variations between the sites. A number of variations on this so-called reference site approach are described by Field and Jacob (1995), and the approach has been widely used (e.g., Boatwright et al., 1991; Borcherdt and Glassmoyer, 1994; Harmsen, 1997; Hartzell et al., 2000; and Borcherdt, 2002a).

The second category of approaches for evaluating site amplification effects does not require the presence of a reference site. Field and Jacob (1995) review several variations on non-reference site approaches. A non-reference site approach in which amplification is evaluated by normalizing the spectra of recorded motions by a reference (rock) spectrum obtained from an attenuation relationship was adopted. This approach has been applied to specific basins by Sokolov (1997) and Sokolov et al. (2000) using locally derived attenuation functions for Fourier amplitude spectra, and for the southern California region using attenuation relations for spectral acceleration (Field, 2000; Lee and Anderson, 2000; Steidl, 2000). Two significant advantages to this approach are that (1) relatively large amounts of strong motion data can be utilized and (2) amplification factors derived from attenuation residuals can be readily incorporated into conventional hazard analyses (i.e., the amplification factors provide straight-forward modifications to the median and standard error from attenuation relations).

The objectives of the work reported in this chapter are (1) to develop empirical amplification factors for 5% damped response spectral acceleration (period range T = 0.01–5 s) using a comprehensive strong motion database for active regions, (2) to classify the strong motion stations based on geologic and geotechnical classification schemes using recently developed data resources not available to previous investigators, and (3) to investigate the relative effectiveness of various site classification schemes in terms of their ability to minimize *IM* dispersion levels and to delineate distinct amplification levels between categories. The relatively large size of the strong motion database and the opportunity to compare results for various alternative site classification schemes represent significant new features of the present study. The results are considered applicable to active tectonic regions (i.e., areas near plate boundaries but from non-subduction earthquakes) because the data used in the study are derived from such regions/earthquakes. It is possible that the amplification factors derived from these data are also applicable to other tectonic regimes, although this should be verified with data in future studies.

In the following section, the site classification schemes used in the study and the strong motion/borehole databases are described. The classification schemes considered herein are all based on characteristics of near-surface geologic materials, i.e., the effects of deep basin structure are not considered. Such effects are considered subsequently in Chapter 5. Then, the processes used to interpret the data through the example of a relatively simple, age-based geologic classification scheme are described. Included in the interpretation are statistical tests for the nonlinearity of amplification factors and the level of distinction between site categories. Then, the results for each classification scheme are reviewed, and the classification schemes that minimize the dispersion of prediction residuals are identified. The cumulative results of the study provide insight into the "optimal" classification schemes for defining empirical amplification factors (with the constraint that the schemes are all based on characteristics of near-surface materials). Recommendations for practical application of the amplification factors are also provided. The findings presented in this chapter have been previously presented by Stewart et al. (2003).

3.2 DATABASES

3.2.1 Strong Motion Data

The ground motion database used in this study consists of the modified phase I database described previously in Section 2.1.

The distance measure used here is the closest distance to the rupture plane, which can include a vertical component for dipping source zones and buried strike-slip source zones. Magnitude is taken as moment magnitude where available, and is otherwise taken as surface wave magnitude for $m > 6$ and local magnitude for $m < 6$.

3.2.2 Site Classifications

(a) Surface Geology

The surface geologic classifications for California sites used in this study are from the modified phase I database described in Section 2.2.1. Additional (non-California) sites include 21 stations near Kobe, Japan (classified by Fukushima et al., 2000), 8 stations near Tabas, Iran (classified by Shoja-Taheri and Anderson, 1978), 7 stations in northern Mexico (classified by Geomatrix, 1993), and 30 stations in Turkey (classified in this study). Attempts were made to classify each site according to the three geologic classification schemes shown in Table 3.1, which are based on geologic age-only (493 classified sites, 900 motions), age + depositional environment (259 sites, 495 motions), and age + material texture (179 sites, 334 motions).

Table 3.1 Criteria for surface geology classifications (and no. of sites)

Age	Depositional Environment	Sediment Texture
Holocene (286)	Holocene alluvium (159)	Holocene Coarse (70)
Pleistocene (88)	Pleistocene alluvium (37)	Pleistocene Coarse (19)
	H. lacustrine/marine (36)	Holo. Fine-Mixed (72)
	P. lacustrine/marine (9)	Pleist. Fine-Mixed (18)
	Aeolian (6)	
	Artificial Fill (12)	
Tertiary (59)		
Mesozoic + Igneous (60)		

(b) Near-Surface Shear Wave Velocity

The average shear wave velocity of shallow sediments is commonly represented by parameter V_{s-30}, which is calculated as the ratio of 30 m to the vertical shear wave travel time through the upper 30 m of the site. The V_{s-30}-based site classification scheme in the NEHRP provisions is presented in Table 2.6. An exception to the V_{s-30} criteria is made for soft clays (defined as having undrained shear strength < 24 kPa, plasticity index > 20, and water content > 40%), for which category E is assigned if the thickness of soft clay exceeds 3 m regardless of V_{s-30}.

The classification of strong motion sites according to the V_{s-30} parameter was performed as described in Section 2.2.2. The database actually used in the present study corresponds to the modified phase I database described in that section.

(c) Geotechnical Data

Section 2.2.3 reviews the historical development of geotechnical classification schemes and the characteristics of a recently proposed scheme by Rodriguez-Marek et al. (2001). That scheme is summarized by Table 2.9. Sites were classified according to that geotechnical scheme as described in Section 2.2.3. The version of the database used in the work described here was the modified phase I database.

3.3 DATA ANALYSIS

3.3.1 Amplification Factors from Individual Recordings

The amplification factor for ground motion j within site category i, F_{ij}, is evaluated from the geometric mean of 5% damped acceleration response spectra for the two horizontal components of shaking, S_{ij}, and the reference ground motion for the site, $(S_r)_{ij}$, as follows:

$$F_{ij}(T) = S_{ij} / (S_r)_{ij} \tag{3.1}$$

where T = spectral period. In Equation 3.1, S_{ij} and $(S_r)_{ij}$ are computed at the same spectral period, which is varied from 0.01 to 5 s. Amplification factors are not evaluated for $T > 1/(f_{hp} \times 1.25)$ where f_{hp} = high-pass corner frequency. Reference motion parameter $(S_r)_{ij}$ is taken as the median spectral acceleration calculated from the Abrahamson and Silva (1997) attenuation relationship for rock sites, with modifications for event terms and rupture directivity effects. The rock attenuation estimate is a function of moment magnitude (m), closest site-source distance (r), rupture mechanism, and location of the site on or off the hanging wall of dip-slip faults. For well-recorded events, the event term represents the period-dependent average residual between motions from a given event and the general attenuation model. These terms are evaluated during the development of attenuation models with a random effects regression procedure (Abrahamson and Youngs, 1992). The rupture directivity correction is made for sites near the seismic source using the empirical model by Somerville et al. (1997), later modified by Abrahamson (2000).

By evaluating reference motion parameters through the use of a rock attenuation relationship, the site condition associated with this reference motion is vaguely defined. This is because many site conditions are present at the recording sites represented within the "rock" category. Some sites have fresh, relatively hard rock, but most consist of deeply weathered, relatively soft rock. The median V_{s-30} values for these rock sites has been assessed as 520 and 620 m/s from compilations of borehole geophysical data by Silva et al. (1997) and Boore et al. (1997), respectively. Ambiguity in the reference site condition can be smaller when amplification factors are derived using reference site approaches (e.g., Borcherdt, 2002). However, for practical purposes, what is most important is that the reference site condition is one for which attenuation relationships can be readily defined and one for which attenuation estimates of *IMs* are stable over time (i.e., as more earthquakes are added to the regression data set). Both criteria are satisfied through the approach taken here. First, use of the broad "rock" category provides ample recordings from which attenuation relations have previously been developed. Second, the use of event terms for well-recorded events provide stability because when coupled with the rock attenuation estimate of *IMs*, event terms for a given event define the rock average for that event, which would not be expected to change significantly over time.

The ground motion amplification provided by Equation 3.1 is subject to error as a result of the uncertainty associated with reference motion $(S_r)_{ij}$. Because S_{ij} is known, the standard error of the ground motion amplification for a particular site, $(\sigma_f)_{ij}$, is equivalent to the standard error of the reference motion estimate, $(\sigma_r)_{ij}$, i.e.,

$$(\sigma_f)_{ij} = (\sigma_r)_{ij} \tag{3.2}$$

Standard error terms from attenuation relationships are fairly large (≈0.4–0.9), and hence the uncertainty in individual estimates of amplification is also large. However, the central limit theorem in statistical theory (e.g., Ang and Tang, 1975) suggests that statistical moments (i.e., mean, standard deviation) estimated from *large* data populations are relatively insensitive to the probability density function associated with individual data points in the population. Accordingly, the errors in point estimates of amplification can be accepted when relations for amplification factors are regressed upon using a large database. As discussed further subsequently in the paper, confidence intervals around regressed amplification functions are calculated to quantify the degree to which the database is sufficiently large for a particular site category.

Finally, it is acknowledged that the evaluation of amplification factors in terms of response spectral ordinates is less physically based than Fourier amplitude ratios, which have been used in some previous studies. The use of response spectral ratios was prompted by two factors (1) state-of-the-art procedures for evaluating reference motions in terms of response spectral ordinates are more maturely developed than those for Fourier spectral ordinates, and (2) seismic hazard analyses are typically performed in terms of response spectral ordinates, and hence amplification factors expressed in term of spectral ordinates will have greater practical application.

3.3.2 Regression Procedure

Amplification factors computed using Equation 3.1 were sorted into site categories defined by the schemes in Tables 2.6, 2.9, and 3.1. For a particular scheme, within a given category *i*, regression analyses were performed to relate amplification factors, F_{ij}, to ground motion amplitude as follows:

$$\ln(F_{ij}) = a_i + b_i \ln(G_{ij}) + \varepsilon_{ij} \tag{3.3a}$$

where a_i and b_i are regression coefficients specific to category i, G_{ij} is a parameter representing the amplitude of the reference ground motion for site j, and ε_{ij} is an error. This same regression equation has been used by Youngs (1993) and Bazzuro (1998), with G_{ij} taken as PHA_r (subscript "r" indicates the reference site condition). Abrahamson and Silva (1997) also took G_{ij} as PHA_r, but added a constant term to G_{ij} as shown below.

$$\ln(F_{ij}) = a_i + b_i \ln(G_{ij} + c) + \varepsilon_{ij} \tag{3.3b}$$

where c = 0.03g independent of period. This form of the regression equation was also investigated here, but was not found to decrease data dispersion, and so the c term was dropped.

We considered the use of several G_{ij} parameters for evaluating amplification, including PHA_r, spectral acceleration at the same period used in the evaluation of F_{ij}, and peak velocity (calculated using the attenuation relation by Campbell, 1997, 2000, 2001). As reported in Stewart and Liu (2000), G_{ij} parameters other than PHA_r did not reduce data dispersion relative to those for PHA, and so in the following we take G_{ij} as PHA_r.

Due to the incorporation of event terms into the reference motions for spectral acceleration, systematic variations of amplification factors across events are not expected. Accordingly, least-squares regression analyses are performed (which give equal weight to all points) in lieu of a random effects model such as that of Abrahamson and Youngs (1992).

Residuals (ε_{ij}) between the amplification "prediction" of Equation 3a and $\ln(F_{ij})$ values were evaluated [$\varepsilon_{ij} = \ln(F_{ij})_{data} - \ln(F_{ij})_{model}$] for all data in category i to enable evaluation of the mean residual, ε_i, and the standard deviation of the residual, σ_i.

$$\varepsilon_i = \frac{1}{N_i}\sum_{j=1}^{N_i}\varepsilon_{ij} \tag{3.4a}$$

$$\sigma_i = \sqrt{\frac{\sum_{j=1}^{N_i}\left(\varepsilon_{ij} - \varepsilon_i\right)^2}{N_i - df_i}} \tag{3.4b}$$

where N_i = number of data points in category i and df_i = number of degrees of freedom in the regression equation for category i (two in this case). The mean residual is always zero, i.e., ε_i =

0. Well-defined site categories would be expected to have smaller values of σ_i than relatively broad categories.

3.3.3 Example Results and Statistical Testing of Results

In this section, we present example results for the age-only geologic classification scheme, and describe the statistical tests performed on the data. For each age category, we plot in Figure 3.1 the spectral amplification at four periods—peak horizontal acceleration (PHA), T = 0.3, 1.0, and 3.0 s. Also plotted are results of regression analyses performed according to Equation 3.3a (solid lines), ± 95% confidence intervals on the median amplification (dotted lines), and median regression ± standard error, σ (dashed lines). The regression coefficients and standard error terms are listed in Table 3.2(a). The estimation error terms for parameters a_i and b_i in Table 3.2(a) are the half-widths of the ±95% confidence intervals on the parameters.

Table 3.2(a) Regression coefficients for S_a amplification factors, age only classification scheme

Geology	Period	a	b	σ	Rejection confidence for b=0 model (%)
Holocene (H)	PHA	-0.24 ± 0.14	-0.17 ± 0.05	0.54	100
	0.3 s	-0.18 ± 0.13	-0.15 ± 0.05	0.53	100
	1.0 s	0.24 ± 0.15	-0.05 ± 0.06	0.57	91
	3.0 s	0.36 ± 0.19	-0.05 ± 0.08	0.64	82
Pleistocene (P)	PHA	0.14 ± 0.27	0.02 ± 0.10	0.47	29
	0.3 s	0.22 ± 0.27	0.07 ± 0.10	0.48	80
	1.0 s	0.21 ± 0.32	-0.02 ± 0.12	0.52	23
	3.0 s	-0.03 ± 0.37	-0.19 ± 0.14	0.51	99
Tertiary (T)	PHA	0.23 ± 0.35	-0.02 ± 0.14	0.62	21
	0.3 s	0.09 ± 0.37	-0.05 ± 0.14	0.65	49
	1.0 s	0.09 ± 0.34	-0.05 ± 0.14	0.58	55
	3.0 s	0.10 ± 0.45	-0.06 ± 0.18	0.69	48
Mesozoic + Igneous	PHA	-0.13 ± 0.30	-0.08 ± 0.12	0.52	78
(M + I)	0.3 s	-0.46 ± 0.33	-0.14 ± 0.13	0.57	96
	1.0 s	-0.45 ± 0.46	-0.12 ± 0.19	0.75	78
	3.0 s	-0.74 ± 0.63	-0.22 ± 0.27	0.79	89

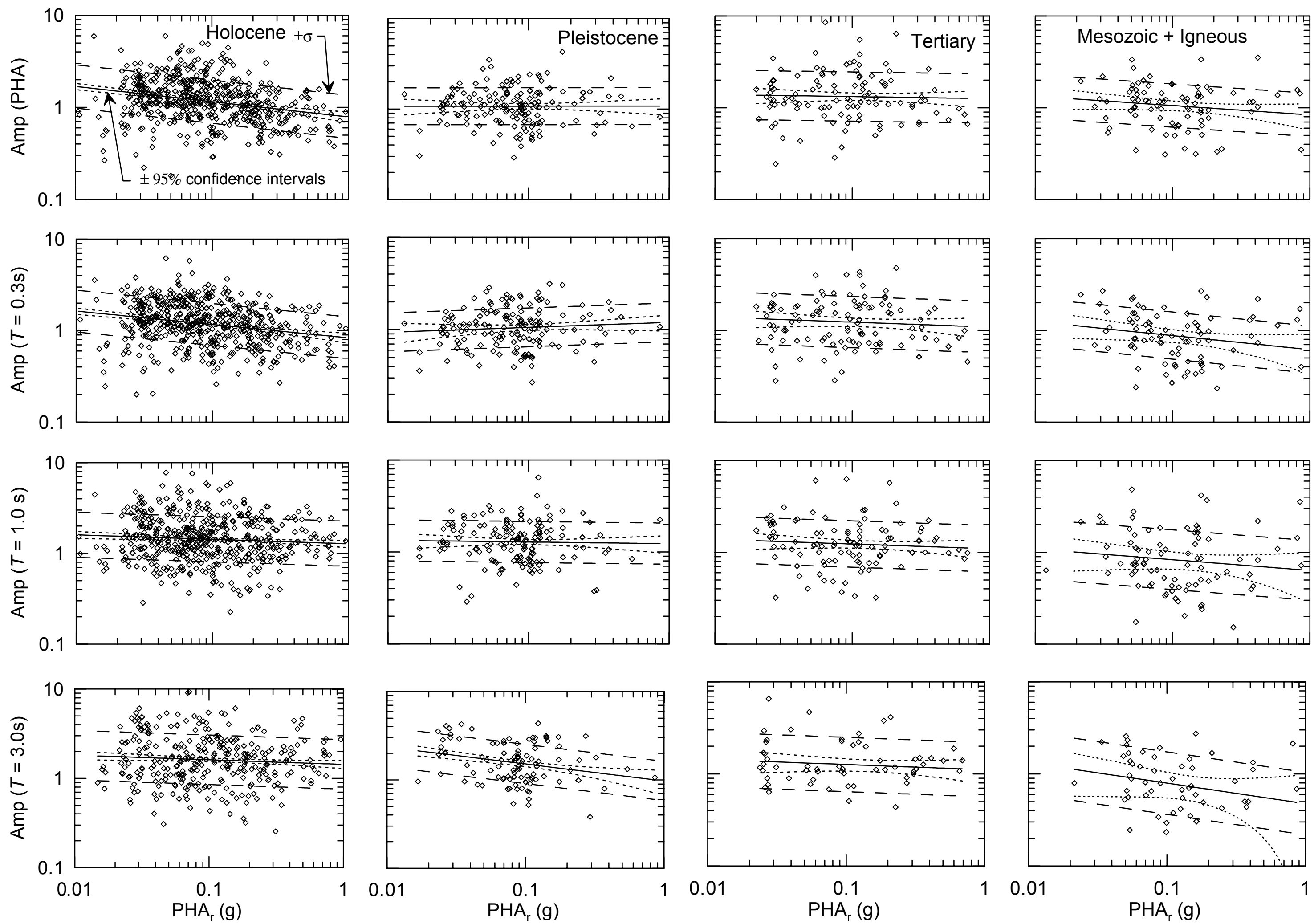

Fig. 3.1 Spectral acceleration amplification factors for categories in age-only geologic classification scheme. PHA$_r$ refers to peak horizontal acceleration of reference motion.

Reductions of amplification factors with increasing PHA_r are taken as evidence of sediment nonlinearity. This nonlinearity is quantified by the b_i parameter for each category *i*. The statistical significance of the PHA_r dependence of amplification factors is assessed two ways. The first significance test consists of comparing the absolute value of b_i to the estimation error for b_i (both indicated in Table 3.2a). When $|b_i|$ exceeds the estimation error, the nonlinearity is considered significant. Secondly, sample "t" statistics are compiled to test the null hypothesis that b_i=0 and a_i = overall data median. This statistical testing provides a significance level = α that the null hypothesis cannot be rejected. For clarity of expression, we tabulate in Table 3.2(a) values of 1-α, which is referred to as a "rejection confidence for a *b*=0 model." Large rejection confidence levels (i.e., > 95%) suggest significant PHA_r dependence in amplification factors. These results are also shown in Table 3.2(a).

The results in Table 3.2(a) indicate for Holocene sediments statistically significant PHA_r dependence of amplification functions at small to intermediate periods (i.e., T < ~1.0 s). At short periods (PHA, T = 0.3 s), the rejection confidence for the *b*=0 model is nearly 100%, and the estimated values of $|b_i|$ exceed their prediction errors. Amplification occurs for PHA_r < 0.2g, and de-amplification occurs for PHA_r >~0.2g. At longer periods (T = 1.0, 3.0 s), the nonlinearity is less statistically significant and amplification occurs across the full range of PHA_r. Nonlinearity is generally not statistically significant for age categories other than Holocene.

A key issue when interpreting regression results for different site categories is the degree to which the data for different categories are distinct. This is evaluated using statistical F-tests (Cook and Weiberg, 1999), which compare submodels with a full model. For example, a pair of submodels could be the regression results in Figure 3.1 and Table 3.2(a) for Holocene (H) and Pleistocene (P). The full model in this example would consist of a regression through all data in the H and P categories. The F-test is performed by calculating the residual sum of squares (based on misfit from the median model prediction) for the submodels (RSS_1 and RSS_2) and the full model (RSS_f). Since *RSS* measures lack of fit, the submodels and full model are compared by examining the difference $RSS_f-(RSS_1+RSS_2)$. If this difference is "small," then the submodels and full model fit the data about equally well. For well-populated submodel data spaces, this would imply that the submodels do not describe distinct data sets.

For normally distributed data sets, the F-statistic is calculated as

$$F = \frac{\left(RSS_f - \left(RSS_1 + RSS_2\right)\right) / \left(\left(df_1 + df_2\right) - df_f\right)}{\hat{\sigma}^2} \tag{3.5}$$

where df_i refers to the degree of freedom of regression fit i (two in this case), and

$$\hat{\sigma}^2 = \frac{RSS_1 + RSS_2}{N_f - \left(df_1 + df_2\right)} \tag{3.6}$$

where N_f = number of data points in the full model. This F statistic can be compared to the F distribution to evaluate a significance level (p) for the test. Large values of p (e.g., $p > 0.05$) are often taken to imply that the submodels are not distinct.

We compile the F statistic and significance level (p) for the category pairs of Holocene-Pleistocene, Pleistocene-Tertiary, and Tertiary-Mesozoic. These statistics are compiled in Table 3.2(b) for the geologic age-only classification scheme. We judge the distinction between categories to be "significant" for $p < 0.05$, "moderate" for $0.05 < p < 0.15$, and "insignificant" for $p > 0.15$.

Table 3.2(b) F-statistics indicating distinction between site categories, age only classification scheme

	PHA		*T* = 0.3 s		*T* = 1.0 s		*T* = 3.0 s	
Categories	**F**	**p**	**F**	**p**	**F**	**p**	**F**	**p**
H-P	6.4	0.002	10.5	0.000	2.6	0.076	1.3	0.266
P-T	4.3	0.014	3.4	0.035	0.9	0.424	2.9	0.061
T-M+I	4.0	0.020	7.8	0.001	9.7	0.000	6.4	0.002

Significantly distinct values of short-period amplification factors (PHA and 0.3 s) are observed between Holocene and Pleistocene sediments. Short-period Pleistocene amplification is significantly distinct from Tertiary, which has larger amplification factors. Compilations of median borehole velocity profiles by geologic unit by Silva et al. (1999) suggest that the velocity gradient (i.e., increase of velocity with depth) in Tertiary sediments is greater than old alluvium (which is interpreted as analogous to Pleistocene). This higher gradient may explain the larger short-period amplification factors in Tertiary. Medium- to long-period (T = 1.0 and 3.0 s) amplification levels for Holocene-Pleistocene and Pleistocene-Tertiary sediments are moderately or insignificantly distinct. The Tertiary and Mesozoic + Igneous (M+I) categories (i.e., the categories encompassing the materials that would generally be considered "rock") have significantly distinct amplification levels at all periods, with T amplification exceeding M+I.

3.4 RESULTS

3.4.1 Synthesis of Results for Each Classification Scheme

The data analysis procedures described in the previous section were repeated for data grouped according to the classification schemes listed in Tables 2.6, 2.9, and 3.1. we identify here the distinct categories within each scheme that emerged from the analyses, and discuss variations in the amplification factors across categories. Regression results for many individual periods are presented in Appendix A for recommended categories. Some minor adjustments to the coefficients have been made to smooth the variations between periods. Note that in some cases, non-zero b-values given in the appendix are not statistically significant, as discussed in the preceding section and further below.

Table 3.3 presents F statistics and significance levels (p) for category pairs associated with the detailed surface geology, NEHRP, and geotechnical data schemes. Table 3.4 presents regression results, standard error terms, and hypothesis test results for distinct categories. Regression results for recommended categories are plotted against data in Figures 3.2–3.5 for periods $T = 0.3$ and 1.0 s (which were chosen to represent results at short and mid periods).

Table 3.3 F-statistics indicating distinction between site categories

	PHA		T = 0.3 s		T = 1.0 s		T = 3.0 s	
Categories	F	p	F	p	F	p	F	p
Geology, Depositional Environment								
Hlm-Ha	6.2	0.002	1.2	0.293	2.1	0.119	2.0	0.138
Ha-Pa	0.9	0.421	3.0	0.052	0.7	0.504	0.3	0.731
Hlm-Qa	7.3	0.001	1.8	0.175	2.4	0.089	2.2	0.114
Qa-T	3.1	0.044	0.6	0.571	3.0	0.049	3.3	0.037
Geology, Material Texture								
Hc-Hm	6.5	0.002	3.7	0.025	2.1	0.121	2.1	0.121
Hc-Pc	0.7	0.499	0.1	0.886	0.7	0.499	0.6	0.561
Pc-Pm	0.2	0.851	0.3	0.748	2.9	0.061	0.3	0.756
Hm-Pm	3.6	0.028	1.1	0.328	1.7	0.178	1.2	0.308
NEHRP								
B-C	0.3	0.774	2.8	0.064	4.6	0.011	1.3	0.288
C-D	5.2	0.006	5.7	0.004	8.6	0.000	12.4	0.000
D-E	6.8	0.001	6.2	0.002	10.5	0.000	4.2	0.016
Geotechnical Data								
B-C	4.5	0.012	14.4	0.000	15.2	0.000	2.3	0.101
C-D	0.3	0.777	0.8	0.442	3.8	0.023	8.5	0.000
D-E	10.8	0.000	10.6	0.000	11.2	0.000	2.3	0.106

Table 3.4 Regression coefficients for amplification factors and hypothesis test results

Category	PHA				0.3 s				1.0 s				3.0 s			
	a	b	σ	Rej C.	a	b	σ	Rej C.	a	b	σ	Rej C.	a	b	σ	Rej C.
Hlm	-0.59	-0.39	0.47	100	-0.39	-0.25	0.44	100	0.02	-0.22	0.45	100	0.29	-0.19	0.48	98
Qa	-0.15	-0.13	0.52	100	-0.10	-0.11	0.51	100	0.20	-0.06	0.58	89	0.14	-0.14	0.65	99
Hc	-0.11	-0.10	0.52	96	-0.08	-0.08	0.53	90	0.13	-0.06	0.57	71	0.00	-0.17	0.64	97
Hm	-0.50	-0.33	0.51	100	-0.33	-0.24	0.46	100	0.10	-0.14	0.56	98	0.38	-0.09	0.55	80
NEHRP B	0.09	0.05	0.48	21	-0.16	0.08	0.44	33	-0.71	-0.13	0.78	32	-1.57	-0.54	0.36	99
NEHRP C	-0.06	-0.05	0.55	65	-0.22	-0.09	0.64	89	0.07	-0.03	0.74	36	-0.01	0.00	0.90	2
NEHRP D	0.08	-0.07	0.57	89	0.11	-0.04	0.54	68	0.38	-0.02	0.48	32	0.44	-0.01	0.55	16
NEHRP E	-0.60	-0.50	0.46	100	-0.49	-0.43	0.54	99	-0.24	-0.46	0.48	100	0.47	-0.18	0.46	77
Geot. B	0.07	0.07	0.55	51	-0.02	0.15	0.66	78	0.24	0.25	0.73	91	-0.41	-0.06	0.77	27
Geot. C	0.11	-0.04	0.60	51	-0.10	-0.12	0.62	97	0.04	-0.08	0.72	73	0.01	-0.03	0.83	28
Geot. D	-0.02	-0.08	0.56	94	0.08	-0.04	0.51	67	0.41	-0.01	0.49	21	0.42	-0.03	0.59	45
Geot. E	-0.82	-0.63	0.40	100	-0.89	-0.60	0.36	100	-0.27	-0.49	0.45	100	0.54	-0.13	0.48	64

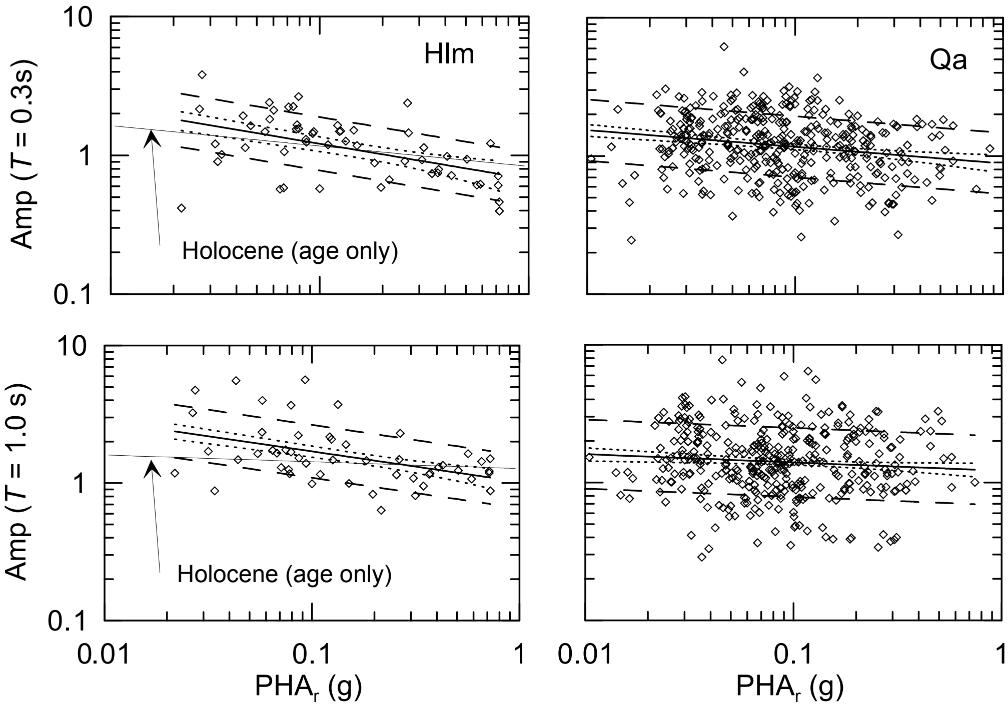

Fig. 3.2 Spectral acceleration amplification factors for categories in age + depositional environment classification scheme

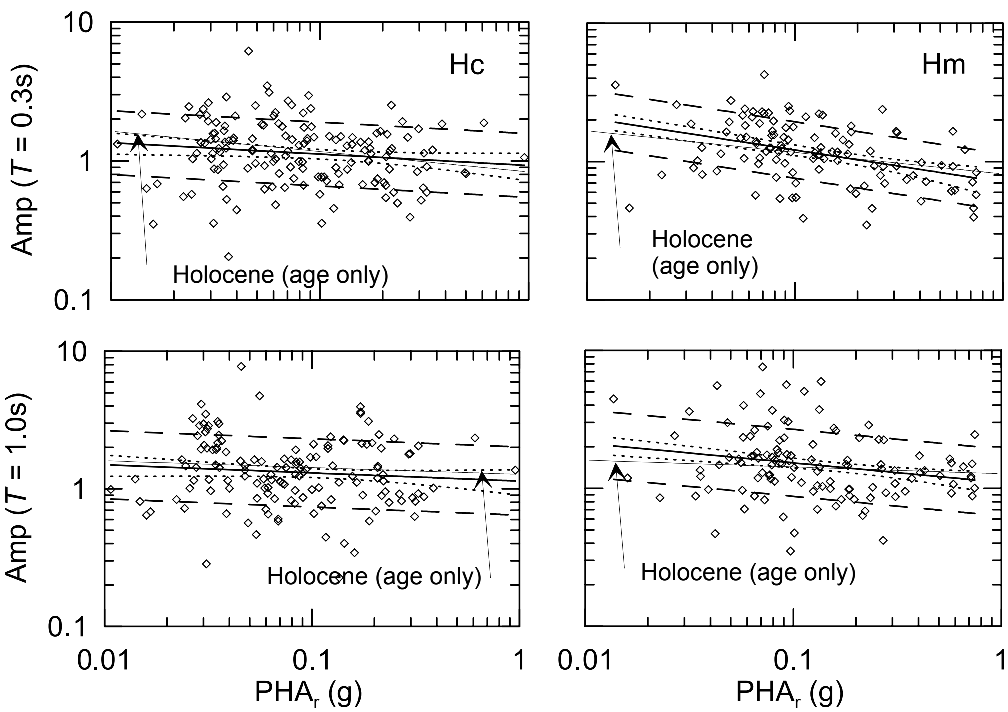

Fig. 3.3 Spectral acceleration amplification factors for categories in age + material texture classification scheme

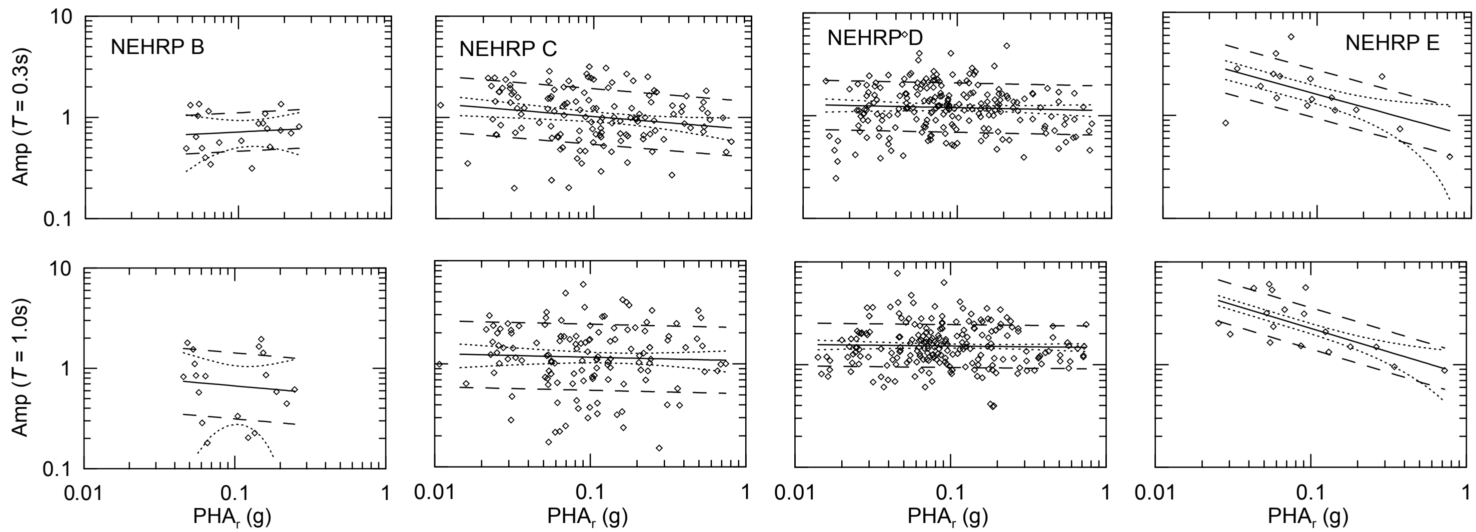

Fig. 3.4 Spectral acceleration amplification factors for NEHRP categories B-E

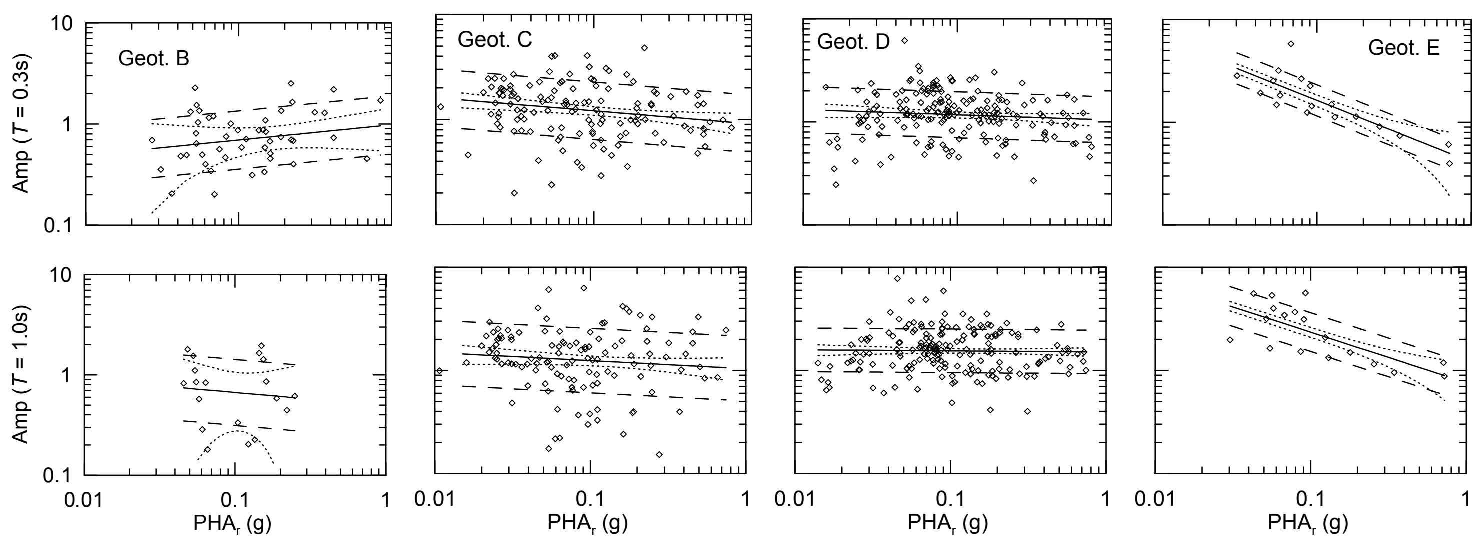

Fig. 3.5 Spectral acceleration amplification factors for geotechnical categories B–E

For the age + depositional environment geologic classification scheme, regression analyses were performed for the Holocene lacustrine/marine (Hlm), Holocene alluvium (Ha), Pleistocene alluvium (Pa), and Quaternary alluvium (Qa = Ha + Pa) categories. Regression analyses for other categories listed in Table 3.1 were not performed due to sparse data. The lack of distinction between Ha and Pa amplification levels shown in Table 3.4 motivated the use of the Qa category. Qa is significantly distinct from Hlm and Tertiary (T) for PHA, but the distinction is reduced at longer periods. Regression results for the Hlm and Qa categories are presented in Figure 3.2. Levels of amplification and nonlinearity in the Hlm category, which includes a significant number of sites from Imperial Valley, and San Francisco bayshore locations are large at small periods and decrease gradually with increasing period. However, nonlinearity for Hlm is statistically significant across the full period range considered (T = 0.01−5 s). Levels of nonlinearity in the Qa category are less than Hlm, but are statistically significant.

For the age + material texture geologic classification scheme, regression analyses were performed within the Holocene and Pleistocene age groups for coarse and fine/mixed sediments (denoted "Hc," "Pc," "Hm," and "Pm"). As shown in Table 3.4, Pleistocene categories Pc and Pm are insignificantly distinct at nearly all periods, and hence we considered subdivision of Pleistocene according to material texture to not be justified. The Hm category has significantly distinct variations from Hc at short period (PHA and 0.3 s), but the subcategories are insignificantly distinct at longer periods ($T \geq 1.0$ s). Regression results for the Hm and Hc categories are presented in Figure 3.3 for periods of 0.3 and 1.0 s. category Hm exhibits higher levels of weak-motion amplification and short- to moderate-period nonlinearity than Hc.

Regression results for NEHRP categories B–E (defined in Table 2.6) are presented in Figure 3.4 for T = 0.3 and 1.0 s. Regression analyses for category A were not performed due to sparse data. The data are also fairly sparse for categories B and E, and thus the confidence intervals on the amplification function are relatively wide. However, the results are considered sufficiently statistically robust to enable comparisons of amplification levels across site categories. Amplification levels for categories B–C are not distinct for some individual periods (PHA, 3.0 s), but are distinct at midperiods (0.3, 1.0 s), with C amplification exceeding B. The PHA_r dependence of amplification in NEHRP B is generally statistically insignificant. For C, the PHA_r dependence is moderate at short periods (PHA, 0.3 s), and insignificant for $T > \sim 0.3$ s. Amplification levels for NEHRP categories C−D are significantly distinct at all periods, with the amplification being larger for NEHRP D than for C. The NEHRP D category has moderate nonlinearity at short periods (PHA, 0.3 s), but no significant nonlinearity for T > ~0.3 s. Amplification levels for NEHRP categories D–E are significantly distinct at all periods. category E generally has the most significant PHA_r dependence of amplification factors and the largest weak motion amplification. Nonlinearity for category E has only moderate statistical significance for $T > 1.0$ s. These trends for category E are based on a small number of recordings (18) and are therefore tentative.

The amplification factors for NEHRP categories do not exactly match those for surface geology categories because there is not a one-to-one correspondence between $V_{s\text{-}30}$ and surface geology. NEHRP B amplification factors are generally smaller than Mesozoic, which likely occurs because many of the Mesozoic geology sites in the database have $V_{s\text{-}30}$ smaller than the lower-bound NEHRP B threshold of 760 m/s (e.g., among the 26 Mesozoic sites with NEHRP classifications, 13 are C, 10 are B, and 3 are A). The results for NEHRP C sites are generally intermediate between results for the geologic Pleistocene and Tertiary categories. Results for NEHRP D sites are generally intermediate between those for Holocene and Pleistocene sediments. Results for NEHRP E sites demonstrate more low-period nonlinearity and higher weak-motion amplification than any geologic category, including Hlm.

Regression results for categories B-E in the Geotechnical Data classification scheme (Table 2.9) are presented in Figure 3.5. Regression analyses for category A were not performed due to sparse data. category B (intact rock) has substantial de-amplification that is significantly distinct from category C at low- to moderate-periods ($T \leq 1.0$ s). De-amplification factors for B do not vary significantly with PHA_r, and are generally lower than those for the Mesozoic + Igneous category in the age-only geology classification scheme. For categories C and D, short-period amplification levels ($T = 0.01$ and 0.3 s) are not distinct, while intermediate to long-period amplification factors are significantly distinct with D exceeding C. This result is a reversal of trends discussed above in which intercategory distinction was generally greater at smaller period, and may be associated with a sediment depth effect on long-period spectral ordinates (the geotechnical scheme is the only one that incorporates depth in the definition of the site categories, even though the depths considered in the scheme are much smaller than typical basin dimensions). The general levels of C and D amplification at small periods are comparable to those for Quaternary alluvial sediments. Nonlinearity is generally modest to weak in categories C and D at small period ($T \leq 0.3$ s) and weak at longer periods. Data for category E indicate much larger weak-motion amplification and nonlinearity than C or D; however E nonlinearity is of only moderate statistical significance for $T > 1.0$ s. As with the NEHRP E category, the trends for Geotechnical category E are based on a small number of recordings (18) and are therefore tentative.

3.4.2 Comparison to Previous Studies

Several previous studies have developed amplification factors suitable for comparison to the results of this study. In Figures 3.6a–c we compare the results of this study for geologic categories to those of Steidl (2000), which were derived using a non-reference site approach similar to that employed here [Steidl's amplification factors are derived relative to the Sadigh (1993) attenuation relationship for rock, which produces reference motions similar to those from Abrahamson and Silva (1997) attenuation (Abrahamson and Shedlock, 1997)]. The Qa amplification factors (Fig. 3.6a) of this study are similar to those of Steidl for the Q (all Quaternary) and Qy (young Quaternary) categories. For Tertiary sites (Fig. 3.6b), the results of this study indicate similar levels of amplification to those of Steidl, although a lower degree of short-period nonlinearity. For Mesozoic materials, the results of this study show comparable overall amplification levels and degrees of apparent nonlinearity to those of Steidl. However, as noted previously, nonlinearity in the response of Mesozoic materials is not statistically significant because of the weak trend in the data relative to the large data scatter.

In Figure 3.7, we compare the results of this study for NEHRP C and D sites to those of Borcherdt (2002), which were derived using a reference site approach with data from the 1994 Northridge earthquake. To facilitate the comparison, the results are presented for this figure in terms of averaged response spectral amplification levels across the period range of T = 0.1–0.5 s (denoted "F_a") and T = 0.5–2.0 s (denoted "F_v"). The results of this study show lower amplification levels and less variation with PHA_r than was found by Borcherdt. One possible reason for the difference between the amplification levels of this study and those of Borcherdt is different reference site conditions used in the derivation of amplification factors. We used a rock-average reference site condition for active regions (corresponding approximately to soft rock with $V_{s-30} \approx$ 520–620 m/s), as compared to a relatively competent reference rock condition used by Borcherdt ($V_{s-30} \approx$ 850 m/s). The bias introduced by the different reference site conditions can be investigated with the V_{s-30}-based amplification factors of Borcherdt and

Glassmoyer (1994) and Field (2000), which are linear (no dependence on PHA_r). Therefore, the relative amplification between $V_{s\text{-}30}$ = 850 m/s and about 570 m/s represents the bias that would be expected between the results of this study and those of Borcherdt. Using the aforementioned references, these relative amplification values are approximately 1.15 for F_a and 1.3 for F_v. The average bias observed in Figure 3.7 (i.e., bias at $PHA_r \approx 0.1g$) for F_a is about 1.4 and for F_v is about 1.6. Accordingly, we attribute much of the difference between the amplification factors of this study and those of Borcherdt to the difference in reference site condition.

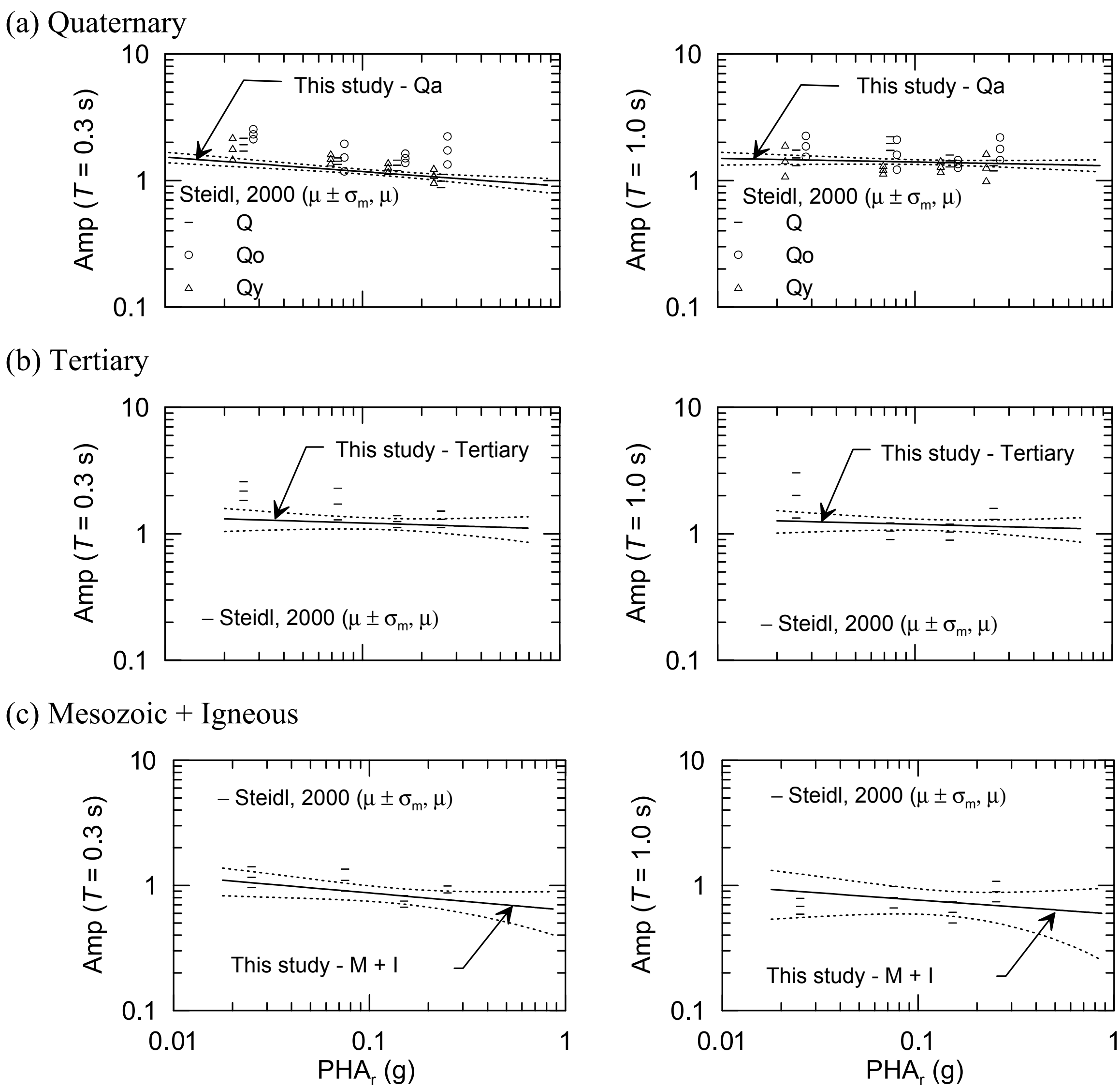

Fig. 3.6 Comparison of results from this study and Steidl (2000) for (a) Quaternary alluvium, (b) Tertiary sediments, and (c) Mesozoic and Igneous geology. For Steidl's results, symbol μ denotes median, symbol σ_m denotes standard error of the median.

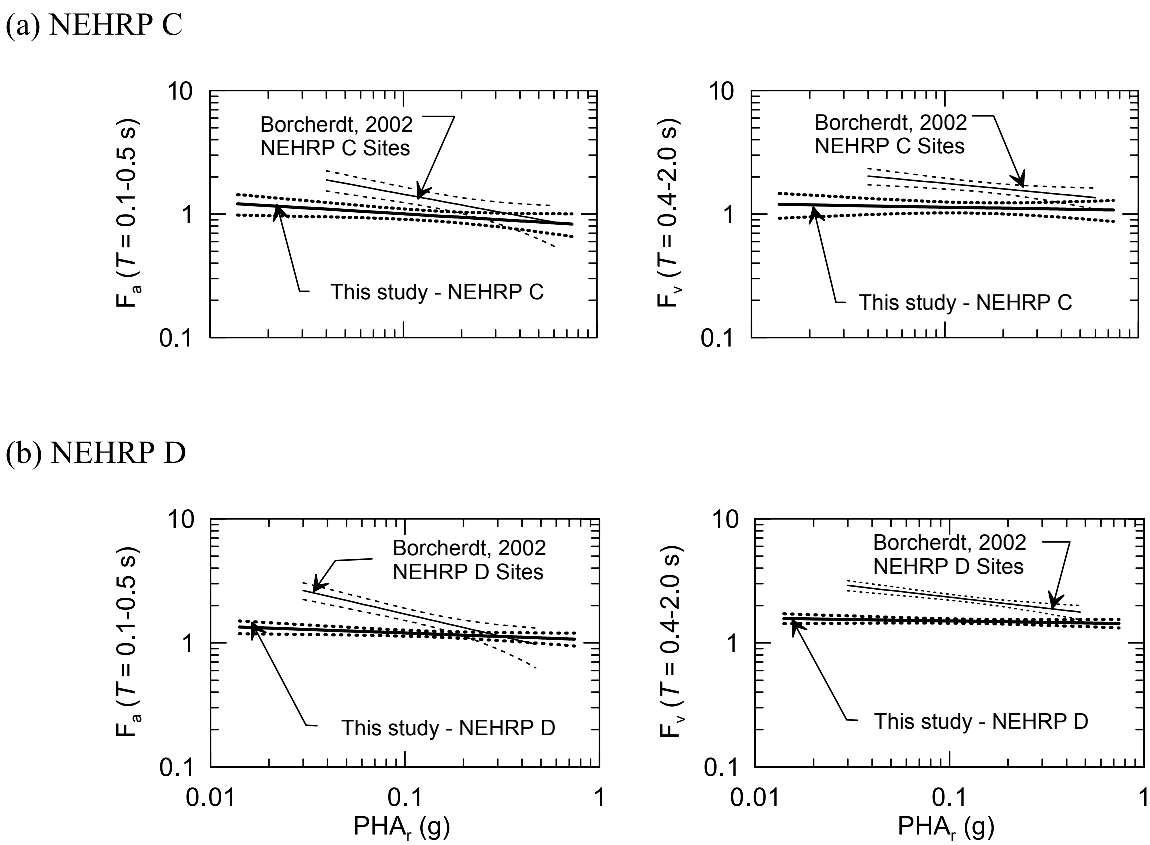

Fig. 3.7 Comparison of results from this study to those of Borcherdt (2002)

A third comparison is made between the surface geology-based (age + depositional environment) median amplification factors for T = 0.3 and 1.0 s and the site terms in the Abrahamson and Silva (1997) attenuation relationship. These comparisons are shown in Figure 3.8(a) for soil categories and Figure 3.8(b) for rock categories. Note that the Abrahamson and Silva site term is unity for rock. The median amplification factors of this study depart significantly from the Abrahamson and Silva site terms for both rock categories (T and M + I) and for the Hlm soil category. Conversely, the amplification factors for Qa are very close to the Abrahamson and Silva site term. Accordingly, use of the amplification factors from this study would have the greatest impact for geologic rock or soft soil site categories (or related categories from alternative classification schemes).

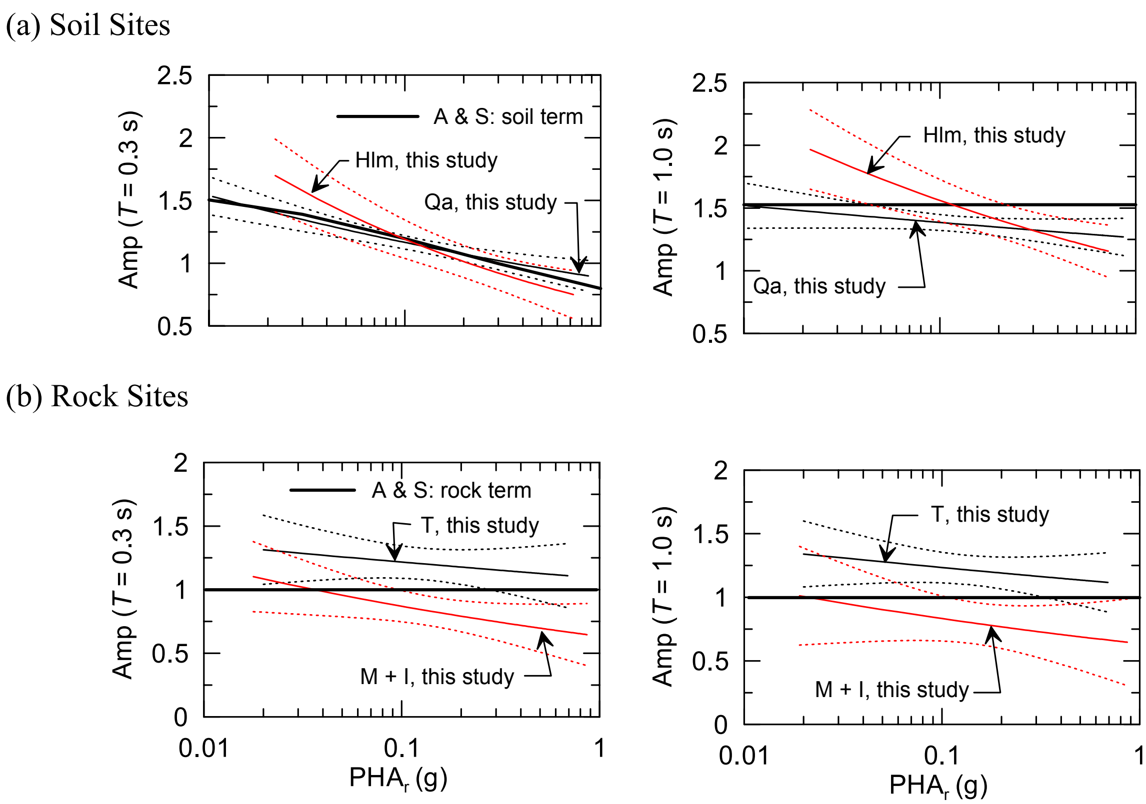

Fig. 3.8 Comparison of median results for surface geology categories (this study) with site terms in Abrahamson and Silva (1997) attenuation relationship

3.4.3 Magnitude- and Distance-Dependence of Results

In this section, we evaluate the magnitude- and distance-dependence of amplification factors and the magnitude dependence of intracategory error terms. The regression equation used in the above analyses (Eq. 3.3a) is based on the assumption that amplification for a given site category is a function of only reference motion amplitude. Due to the finite time required for soil profiles to reach their steady-state resonant response, some dependence of amplification on the magnitude/duration of strong shaking might be expected. In Figure 3.9(a) we present residuals between individual amplification factors at T = 0.3 and 1.0 s for Holocene sites and amplification-adjusted reference motions (using the regression results in Table 3.2a). Also shown are the results of regression analyses performed according to:

$$\ln(\varepsilon_{ij}) = e_i + f_i m + \tau_{ij} \tag{3.7}$$

where e_i and f_i are regression coefficients for category i, m = moment magnitude, and τ_{ij} is an error term. The regression results indicate a magnitude dependence in amplification factors at intermediate and long periods (e.g., $T \geq 1.0$ s) but not at short periods (e.g., $T \leq 0.3$ s). The standard error terms calculated from τ_{ij} at long periods are not reduced significantly from the values indicated in Table 3.2(a).

Plotted in Figure 3.9(b) are amplification-adjusted residuals for Holocene sites vs. site-source distance. Also shown are linear regression analyses performed according to

$$\ln(\varepsilon_{ij}) = g_i + h_i \ln r + \gamma_{ij} \tag{3.8}$$

where g_i and h_i are regression coefficients for category i, r = site-source distance (in km), and γ_{ij} is an error term No significant trend in the residuals with r is observed.

The variation of standard error term (σ) with magnitude and site category is shown in Figure 3.9(c) for age-only geologic categories, with the magnitude-dependent error terms from Abrahamson and Silva (1997) also shown for comparison. We find no significant magnitude dependence in the error terms, but do find an increase of σ with period. The Abrahamson and Silva (1997) error terms decrease uniformly with magnitude for m = 5–7, and also increase with period. Typically, error terms from this study are smaller than the Abrahamson and Silva terms for m < 5.75 and larger for m > 5.75.

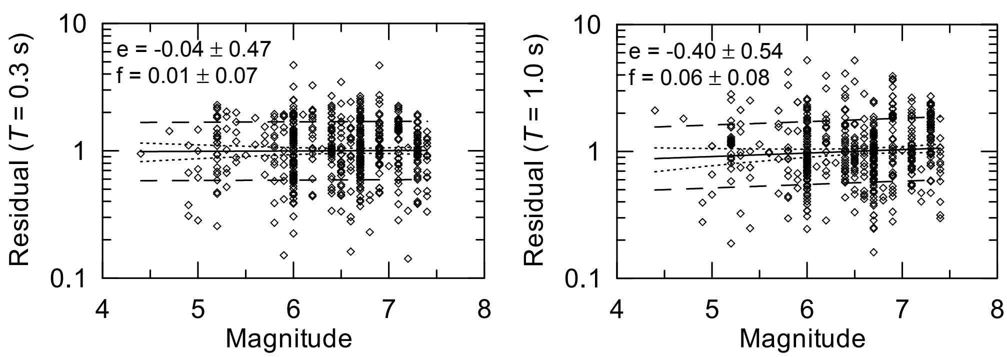

Fig. 3.9(a) Variation with magnitude of spectral acceleration residuals calculated using amplification-adjusted reference motions. Data are for Holocene soil sites.

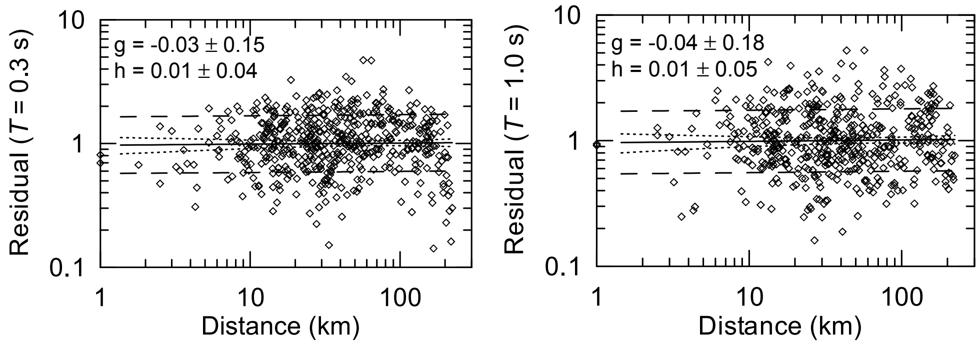

Fig. 3.9(b) Variation with site-source distance of spectral acceleration residuals calculated using amplification-adjusted reference motions. Data are for Holocene soil sites.

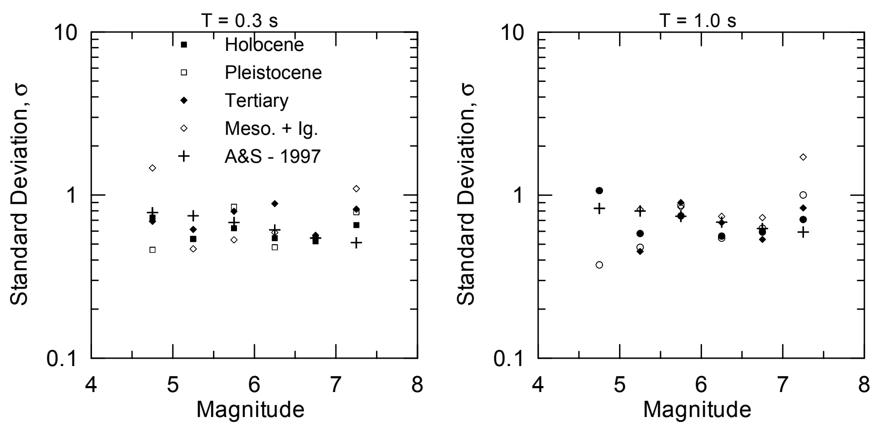

Fig. 3.9(c) Variation of standard error term σ with magnitude and geologic age. Compare to magnitude-dependent error term by Abrahamson and Silva (1997).

3.4.4 Intercategory Error Terms

One of the objectives of this research was to quantify the ability of different classification schemes to capture site-to-site variations of spectral acceleration. This is evaluated for a classification scheme using the intercategory standard error (σ_R), which is calculated as follows:

$$\sigma_R = \sqrt{\frac{\sum_{i=1}^{M} \sum_{j=1}^{N_i} \left(\varepsilon_{ij} - \varepsilon_i\right)^2}{\left(\sum_{i=1}^{M} N_i\right) - df}} \tag{3.9}$$

where M = the number of categories in the scheme and df = total number of degrees of freedom in regression equations for the scheme ($df = 2 \times M$). Intercategory standard error σ_R represents the average dispersion of data within all categories belonging to a given scheme. This is calculated for five classification schemes, three of which are based on surface geology, one on near-surface shear wave velocity ($V_{s\text{-}30}$), and one on geotechnical data.

Intercategory standard error terms for the soil and rock categories in each scheme are plotted as a function of period in Figures 3.10(a) and 3.10(b), respectively. For soil categories (Fig. 3.10a), the largest error terms at all periods are obtained from the $V_{s\text{-}30}$-based and geotechnical classification schemes. The smallest error terms are generally from detailed geology schemes such as age + depositional environment or age + material texture. Maximum differences in the category dispersion values are as large as 0.1 in natural logarithmic units. These variations in dispersion are large enough to have an important effect on seismic hazard calculations (Field and Petersen, 2000). Also shown in Figures 3.10 for reference are the error terms from the Abrahamson and Silva (1997) attenuation relationship. Note that these error terms are strongly magnitude dependent, an effect that was not observed in this study (e.g., Fig. 3.9c).

For rock sites (Fig. 3.10b), the error terms are generally minimized at intermediate to long period ($T \geq 0.3$ s) for the geology scheme (which is age-only for rock) and at short period (PHA) for the $V_{s\text{-}30}$-based scheme. The rock error terms for all schemes are larger than those for soil.

The data used to compile the intercategory error terms in Figures 3.10a–b include motions from all classified sites. These data sets are inconsistent to the extent that the various schemes have different numbers of classified sites. Accordingly, we compiled a list of 109 sites (with 187 recordings) for which classifications are available by all five of the categorization schemes considered herein. The intercategory error terms for this consistent data set are of a similar magnitude and show similar trends to those for the full data set (Stewart et al., 2001).

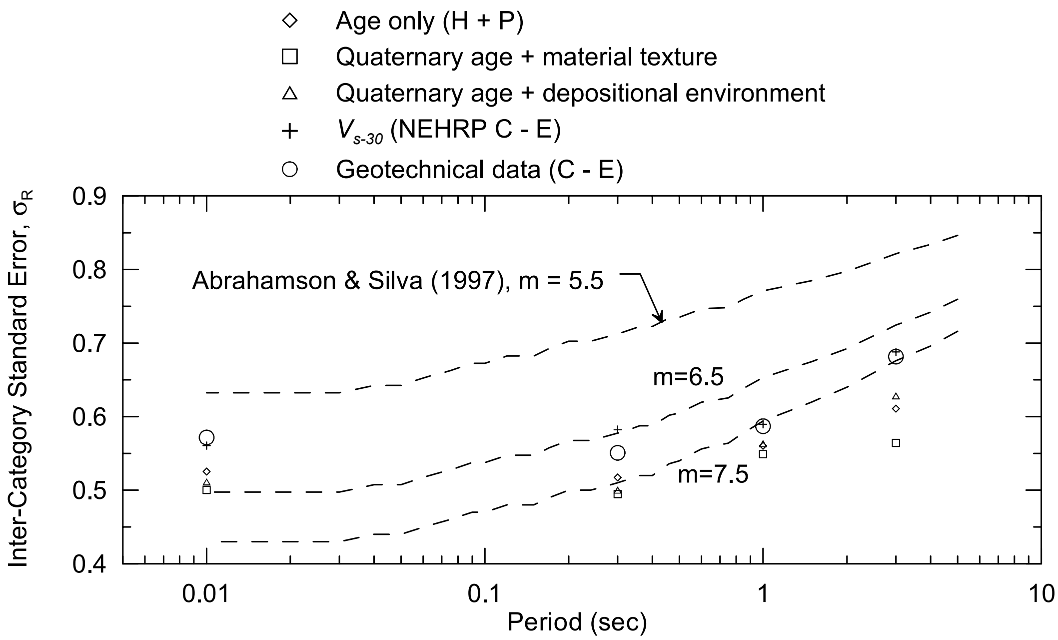

Fig. 3.10(a) Intercategory standard error terms for spectral acceleration (this study) and error terms derived by Abrahamson and Silva (1997). Results apply for categories within respective schemes associated with young sediments (soil).

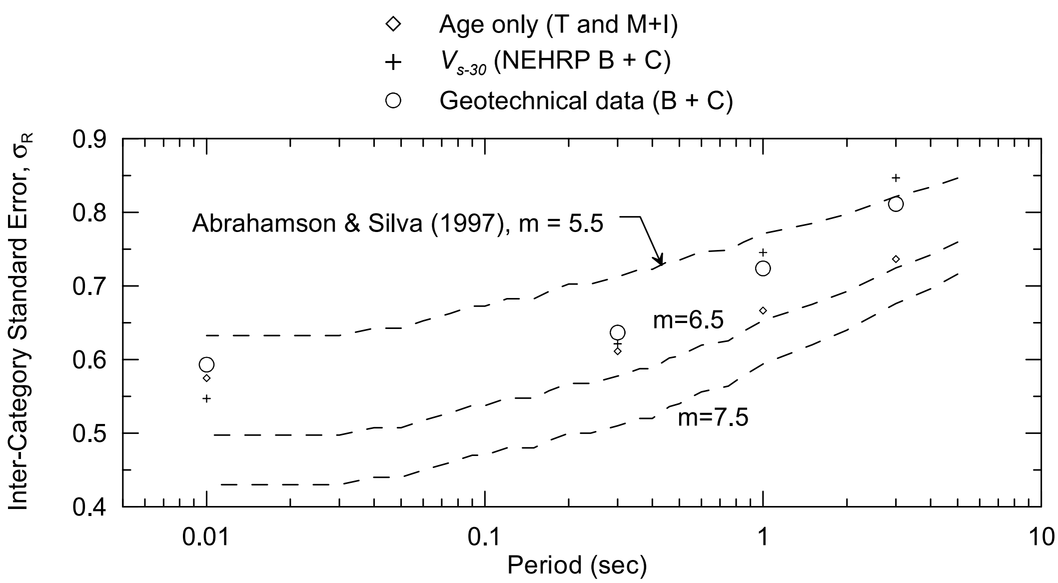

Fig. 3.10(b) Intercategory standard error terms for spectral acceleration (this study) and error terms derived by Abrahamson and Silva (1997). Results apply for categories within respective schemes associated with soft rock and rock conditions.

3.5 CONCLUSIONS AND RECOMMENDATIONS

The identification of an "optimized" classification scheme for strong motion studies should consider two factors: (1) the degree to which amplification factors defined for categories within the scheme are capable of capturing site-to-site variations in ground motion, as measured by the dispersion of prediction residuals and (2) the degree to which amplification levels between categories within the various schemes are distinct from each other. With respect to the first criterion, the results of this study suggest that for soil sites amplification factors defined for detailed surface geology classification schemes minimize the average dispersion of prediction residuals. Variations in dispersion between schemes are as large as 0.1 in natural logarithmic units, a difference that is sufficiently large to have an important effect on the results of hazard calculations (Field and Petersen, 2000). For rock sites, dispersion is minimized at short periods (PHA) with the use of the NEHRP scheme and at long periods ($T \geq 0.3$ s) with the use of age-only surface geology. With respect to the second criterion, the NEHRP classification scheme (site categories distinguished on the basis of V_{s-30}) is the only one for which amplification levels between categories are generally distinct across a wide period range. At small periods, detailed surface geology categories also have distinct amplification levels.

Based on the results for soil sites, classification schemes based on detailed surface geology appear to provide an effective means by which to delineate site conditions for the evaluation of site amplification factors for short–period response spectral acceleration (e.g., PHA). The NEHRP scheme is also effective, particularly for evaluating amplification factors across a broad range of spectral periods. With regard to surface geology schemes, recommended categories for materials of Quaternary age are delineated on the basis of depositional environment or material texture as follows:

<u>Depositional Environment</u>	<u>Material Texture</u>
Quaternary alluvium	Holocene coarse-grained
Holocene lacustrine/marine	Holocene fine/mixed texture
	Pleistocene

For rock sites (i.e., pre-Quaternary materials), geologic classifications are based principally on age (i.e., the categories are T and M+I), and the dispersion of prediction residuals is relatively large. Future studies may be able to identify rock site categories defined on the basis of age +

fracture spacing/degree-of-weathering that reduce the large dispersion at small periods. Lacking such data, however, the NEHRP classification scheme appears to provide an effective means of defining short-period amplification factors for rock sites.

At moderate to long periods ($T \geq 1.0$ s), the results of this study do not point to one scheme as being optimized with respect to the two criteria listed above. We speculate that this finding results in part from the fact that all of the classification schemes considered herein are based on features of relatively shallow geologic materials, which more significantly influence short-period components of ground motions than long-period components. Consideration of basin geometric parameters can improve amplification models for soil sites (see Chapter 5).

The results of this study can be applied to hazard analyses through a probability density function (PDF) that describes spectral acceleration conditional on site category as well as magnitude, distance, and other seismological variables. This PDF is usually log-normally distributed. The median of this distribution can be taken as the product of the median from a rock attenuation model and the applicable amplification factor. Rock attenuation models utilizing a database and regression approach similar to that of Abrahamson and Silva (1997) are considered appropriate for use with the amplification factors of this study. Appropriate relations therefore include Abrahamson and Silva (1997) and Sadigh et al. (1997). The recommended amplification functions from this study are given by Equation 3.3(a) and the coefficients in Appendix A. The median amplification factors are significantly different from the Abrahamson and Silva site terms for rock categories (e.g., T, M+I) and soft soil categories (e.g., Hlm). The standard error term (σ_{haz}) for the PDF can be taken as

$$\sigma_{haz} = \sqrt{\sigma^2 + 0.23^2} \qquad (3.10)$$

where σ is the appropriate category error term from this study. The additional error term of 0.23 accounts for inter-event variability, which was removed by use of the event term during the derivation of reference motions in this study. The value of 0.23 was obtained during the data regressions of Abrahamson and Silva (1997).

4 Nonlinear Site Amplification as Function of Shallow Shear Wave Velocity (V_{s-30})

In this chapter, empirical relationships are developed to predict nonlinear (i.e., amplitude-dependent) amplification factors for 5% damped response spectral acceleration as a continuous function of average shear wave velocity in the upper 30 m, V_{s-30}. As was done in Chapter 3, amplification factors are evaluated as residuals between spectral accelerations from recordings and modified rock attenuation relationships for active regions. Amplification at low- and mid-periods is shown to increase with decreasing V_{s-30} and to exhibit nonlinearity that is dependent on V_{s-30}. The degree of nonlinearity is large for NEHRP category E (V_{s-30} < 180 m/s) but decreases rapidly with V_{s-30}, and is small for V_{s-30} > ~ 300 m/s. The results can be used as V_{s-30}-based site factors with attenuation relationships. The results also provide an independent check of site factors published in the NEHRP provisions, and apparent bias in some of the existing NEHRP factors is identified. Moreover, the results provide evidence that data dispersions are dependent on V_{s-30}. The work presented in this chapter has been accepted for publication in *Earthquake Spectra* (Choi and Stewart, 2005).

4.1 STATEMENT OF THE PROBLEM

Most modern U.S. seismic design codes for building structures represent seismic demand in terms of 5%-damped response spectral ordinates. These spectral ordinates are affected by seismic source, travel path, and site response effect. In the NEHRP provisions for the design of new buildings (BSSC, 2001), source and path effects are accounted for in maps showing the results of probabilistic seismic hazard analyses (PSHA) for the U.S. (Frankel et al., 2000) and so-called maximum considered earthquake (MCE) maps, which are modified from PSHA maps using deterministic seismic hazard analyses (DSHA) in areas of large hazard by consensus judgment (Leyendecker et al., 2000). These maps are prepared for a particular site condition referred to as the "reference site condition." In the NEHRP provisions, site condition is generally parameterized on the basis of the average shear wave velocity in the upper 30 m of the site (V_{s-30}), which is defined as the ratio of 30 m to the vertical shear wave travel time through the upper 30 m of the site. The V_{s-30}-based site categories in the NEHRP provisions are given in Table 2.6. An exception to the V_{s-30} criteria is made for soft clays (defined as having undrained shear strength < 24 kPa, plasticity index > 20, and water content > 40%), for which category E is assigned if the thickness of soft clay exceeds 3 m regardless of V_{s-30}. The reference site condition for which the PSHA maps are intended to apply is the B–C boundary, or V_{s-30} = 760 m/s.

The effects on spectral ordinates of site conditions that deviate from the reference velocity are accounted for with site factors that are a function of site category and the amplitude of shaking for the reference site condition (Dobry et al., 2000). The site factors given in the NEHRP provisions are plotted in Figure 4.1. By definition, site factors represent the ratio of spectral ordinates for a particular site condition to the value of the ordinates that would be expected for the reference condition. The specific factors given in the provisions are F_a, which is defined over a low-period range (T = 0.1–0.5 s), and F_v, which is defined over a midperiod range (T = 0.4–2.0 s). The ground motion parameters for the reference site condition that are used in conjunction with site factors are T = 0.2 s spectral acceleration (S_a) for F_a (denoted "S_s") and S_a at T = 1.0 s for F_v (denoted "S_1"). When the design ground motions are estimated as the product of the amplification factors given in Figure 4.1 and spectral ordinates S_s or S_1 derived from PSHA, two implicit assumptions are being made: (1) the amplification factor defines the ratio of the median ground motion amplitude on the subject site condition to the median amplitude on the reference site condition, and (2) the data dispersion within the two site categories are identical. The former assumption is correct as long as both distributions are log-normally distributed, while the accuracy of the second assumption is investigated subsequently in this chapter.

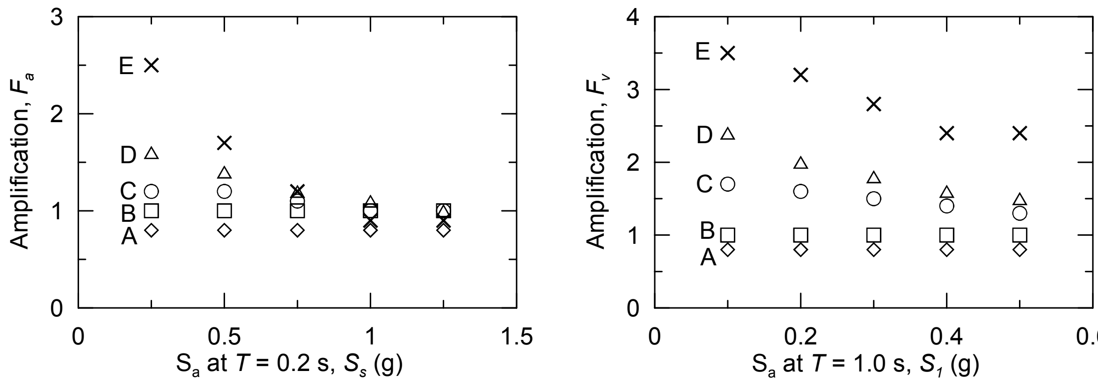

Fig. 4.1 Site factors F_a and F_v given in NEHRP provisions (BSSC, 2001)

One important element of PSHA or DSHA is the attenuation relationship used to evaluate the probabilistic distribution of a given spectral ordinate given that an earthquake with particular source characteristics (e.g., moment magnitude, focal mechanism) has occurred at a particular distance from the site. The output of an attenuation model applies only for a particular site condition (i.e., the average site condition at the strong motion accelerometers that produced the data used to derive the attenuation relation), and hence PSHA/DSHA results also apply only for the average site condition in the attenuation model. It follows from the above that since the B–C boundary is the reference condition for which the NEHRP PSHA and MCE maps are intended to apply, the attenuation relations used in the hazard analyses should also be appropriate for this site condition. Unfortunately, this is not the case. The attenuation relations used to develop the PSHA maps for $T > 0$ s spectral ordinates (i.e., not peak acceleration) in the 2000 version of the NEHRP provisions are Boore et al. (1997) and Sadigh et al. (1997). The Boore et al. relation can be implemented directly for the B–C boundary because site condition is parameterized by $V_{s\text{-}30}$. However, the ground motions used to define the rock attenuation model by Sadigh et al. were recorded primarily at rock and shallow (< 20 m) soil sites in California, most of which have $V_{s\text{-}30}$ values significantly less than 760 m/s. In fact, a borehole compilation by Silva et al. (1997) for this particular "rock" site condition found the median value of $V_{s\text{-}30}$ to be approximately 520 m/s. A similar compilation by Boore et al. (1997) found an average velocity for rock sites of about 620 m/s. Given the above, the fact that the NEHRP PSHA and MCE maps were derived with these relations (with equal weight given to each) suggests that the actual reference site condition is not the assumed value of 760 m/s, but actually corresponds to a softer condition. The hazard analyses underlying the 2003 maps were expanded to include the Abrahamson and Silva (1997) and Campbell and Bozorgnia (2003) attenuation relations, although these relations were also developed for site categories inconsistent with the NEHRP B–C boundary.

In this chapter, statistical models for site factors that are a function of $V_{s\text{-}30}$ and the amplitude of shaking on the reference site condition are developed. The models are based on statistical analyses of residuals between recorded ground motions in active regions and reference motion predictions developed using modified rock attenuation relationships. The models are useful:

1. to validate the existing NEHRP site factors (which were developed based on both observation and analysis, as discussed further below);
2. as site terms for use with attenuation relations;
3. to identify variations in data dispersion with magnitude, distance, and $V_{s\text{-}30}$; and
4. to develop correction factors that can be used to adjust the predictions of attenuation models (i.e., Abrahamson and Silva, 1997; Campbell and Bozorgnia, 2003; Sadigh et al., 1997) to the NEHRP-assumed reference condition ($V_{s\text{-}30}$ = 760 m/s).

The third item above is important because the NEHRP PSHA maps are based on the dispersion estimated from attenuation relations (which is generally independent of site condition). Values of dispersion for specific site conditions that depart significantly from those in the attenuation relations would imply that the mapped PSHA spectral ordinates are biased for those site conditions. The fourth item above is important for the development of PSHA maps applicable to the NEHRP B–C site condition. Application of correction factors has been discussed in past NEHRP committee deliberations, but has not yet been carried out for the Abrahamson and Silva and Sadigh et al. attenuation functions (the Campbell and Bozorgnia results were corrected using the linear site factor model of Boore et al., 1997; Campbell, 2003, *personal communication*).

4.2 EXISTING NEHRP AMPLIFICATION FACTORS

The NEHRP site factors shown in Figure 4.1 are based on both empirical data analysis and the results of ground response analyses (Dobry et al., 2000). The empirical studies were performed by Borcherdt and Glassmoyer (1994), Borcherdt (1994), and Joyner et al. (1994) using strong motion data recorded in the San Francisco Bay Area during the 1989 Loma Prieta earthquake, and provide amplification factors (F_a and F_v) that apply for relatively weak levels of shaking [peak horizontal acceleration for reference (rock) site condition, $PHA_r \approx 0.1$ g]. These amplification factors were derived using a reference site approach, in which the amplification is defined as the ratio of Fourier spectral ordinates of motions recorded on soil to those recorded on nearby reference rock sites, with appropriate corrections for variations in site-source distance between the two accelerometers. The analytical studies consisted of 1-D equivalent linear and nonlinear ground response analyses by Dobry et al. (1994) and Seed et al. (1994), and were used to extend the F_a and F_v values to $PHA_r \approx 0.4–0.5$g. For both the empirical and analytical studies, site factors were defined relative to a competent rock site condition, which in the San Francisco Bay Area corresponds specifically to Franciscan formation bedrock of Cretaceous and Jurassic age.

Since the adoption of the site factors in Figure 4.1, a number of studies have investigated the adequacy of the NEHRP factors by comparing them to alternative factors derived using non–Loma Prieta strong motion data sets [e.g., from Northridge recordings (Borcherdt, 2002a, 2002b), numerous southern California earthquakes (Harmsen, 1997; Field, 2000; Steidl, 2000), and strong motion databases for active regions (Joyner and Boore, 2000; amplification models developed in Chapter 3)].

Borcherdt (2002a, 2002b) investigated amplification levels within NEHRP categories using recordings from the 1994 Northridge earthquake, mostly from stiff soil and soft rock sites. A reference site approach was used to define amplification factors, with reference motions taken from local stations with metamorphic rock (e.g., weathered granite, gneiss) or sedimentary rock (in which case amplification factors were adjusted so that the effective reference site condition is relatively firm rock). Average Northridge amplification factors were found to match very well with the NEHRP amplification factors at both small periods (F_a) and at longer periods (F_v). The Northridge results also demonstrated decreasing amplification with increasing reference motion amplitude, an effect that had not been observed from the Loma Prieta recordings. This effect was not observed in Loma Prieta because most recordings sites are at large distances from the source, so that PHA_r values are small.

The work by Harmsen (1997) involved the evaluation of amplification factors within NEHRP categories using data from multiple southern California earthquakes normalized relative to a single reference rock site (Caltech Seismic Lab). A number of researchers affiliated with the Southern California Earthquake Center (SCEC) evaluated amplification factors using a consistent data set consisting only of southern California earthquakes (Field, 2000; Steidl, 2000). Field (2000) evaluated amplification factors as a direct function of $V_{s\text{-}30}$ using a non-reference site approach in which amplification factors were derived as a term within a southern California attenuation relationship. Steidl (2000) also used a non-reference site approach, evaluating site factors as a function of V_{s-30} using residuals from the Sadigh et al. (1993) attenuation relationship for rock sites (similar to the Sadigh et al., 1997 relation). The amplification factors from the Harmsen and Field studies are independent of PHA_r. In the Steidl study, amplification factors were developed for PHA_r < 0.1g and all PHA_r ranges. Joyner and Boore (2000) developed amplification factors within NEHRP categories using a procedure similar to that of Field (2000) described above, although the short period factors are expressed as a function of reference motion amplitude. In Chapter 3, nonlinear amplification factors within NEHRP categories relative to the Abrahamson and Silva (1997) attenuation relationship were developed.

Most of the above models provide discrete amplification factors within NEHRP categories; only the Field and Harmsen studies provide amplification factors as a continuous function of V_{s-30}. At present, there are no amplification models that are both PHA_r dependent and a continuous function of V_{s-30}. Amplification factors from the above studies are compared to each other and to the results of this study subsequently in this chapter (Fig. 4.12).

4.3 DATA RESOURCES

The modified phase I ground motion database described in Section 2.1 is utilized here, along with the V_{s-30}-based site classifications described in Section 2.2.2. Among these data, recordings at large distance (>100 km) are removed because the currently available data are too sparse to support the development of empirical ground motion models at that distance range. Therefore, 366 recordings from 34 events at 209 strong motion stations are used. Of these sites, 174 have borehole-accelerograph separation distances < 160 m, 13 from 160–450 m, and 22 from 450–1600 m. The distributions of V_{s-30} values for sites and motions are shown in Figure 4.2 along with the median V_{s-30} value in each category. The results in Figure 4.2 differ from those in Figure 2.3 in that the present figure (4.2) applies for the modified phase I database, whereas the previous figure (2.3) apples for the phase II database.

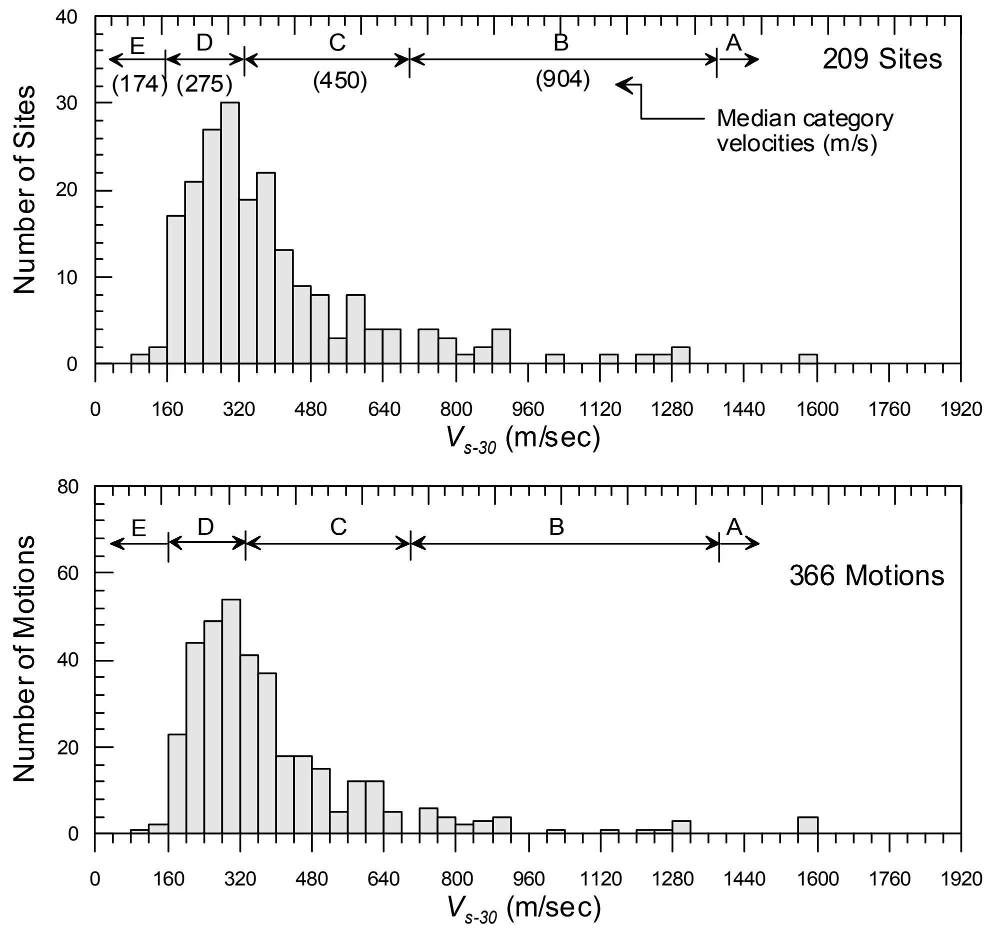

Fig. 4.2 Histogram of V_{s-30} values for strong motion sites and strong motion recordings used in this study

4.4 DEVELOPMENT OF AMPLIFICATION MODEL

Model development begins with two stages of preliminary analysis. In the first stage, amplification factors within bins defined on the basis of V_{s-30} are investigated to evaluate the variation of nonlinearity (i.e., dependence of amplification on PHA_r) with V_{s-30}. In the second stage, amplification levels near a baseline reference amplitude of PHA_r=0.1 g are studied to identify an appropriate model for the variation of amplification (at the baseline amplitude) with V_{s-30}. The baseline amplitude of 0.1 g was selected because it represents a midrange amplitude on a log-scale for motions in most site categories and because this amplitude is low enough that the effects of soil nonlinearity should be small. The results from these two stages of analysis are used to develop a functional form for a "unified" model (i.e., a model that combines the effects of V_{s-30} and nonlinearity). The regression parameters for this unified model are then evaluated using a mixed effects regression procedure (e.g., Abrahamson and Youngs, 1992). The following subsections describe the two stages of preliminary data analysis, the regression analyses used to develop the unified model, comparisons of model predictions to data, and the analysis of standard deviation terms. The results are then compared to those of previous studies.

4.4.1 Amplification within $V_{s\text{-}30}$ Categories

Amplification factors evaluated in Chapter 3 (Eq. 3.1) are compiled to evaluate the degree to which nonlinearity in amplification factors varies with $V_{s\text{-}30}$. For the preliminary analyses discussed in this section, reference motion parameter $(S_r)_{ij}$ is taken as the median spectral acceleration calculated from the Abrahamson and Silva (1997) attenuation relationship for rock sites, with modifications for rupture directivity effects and event terms. The Abrahamson and Silva rock attenuation relationship provides ground motion estimates that are appropriate for a soft rock site condition with $V_{s\text{-}30}$ values reported to be in the range of 520–620 m/s (Silva et al., 1997; Boore et al., 1997). The rupture directivity correction is made for sites near the seismic source using the empirical model by Somerville et al. (1997), later modified by Abrahamson (2000). For well-recorded events, the event term represents the period-dependent average residual between motions from a given event and the general attenuation model (the event terms used at this stage of the analyses were provided by Abrahamson). These terms are evaluated during the development of attenuation models with a mixed effects regression procedure (Abrahamson and Youngs, 1992). The use of an event term in the evaluation of $(S_r)_{ij}$ is intended to remove bias in the attenuation model that might be present for a particular event.

Amplification factors computed using Equation 3.1 were sorted into the following $V_{s\text{-}30}$ categories for intracategory regression analysis:

E: $V_{s\text{-}30} < 180$ m/s + soft clay

D_{lv}: $180 < V_{s\text{-}30} < 310$ m/s

CD: $310 < V_{s\text{-}30} < 520$ m/s

C_{hv}: $520 < V_{s\text{-}30} < 760$ m/s

B: $760 < V_{s\text{-}30} < 1500$ m/s

These ranges of $V_{s\text{-}30}$ essentially match the NEHRP categories, except that NEHRP C and D are subdivided into three bins (C_{hv}, CD, and D_{lv}) to better capture the variation of the sediment nonlinearity with $V_{s\text{-}30}$.

Using the data within the above velocity ranges, regression analyses are performed according to Equation 3.3(a) by means of the ordinary least-squares procedures in which equal weight is given to all data points. The least-squares procedure is used because of the inclusion of event terms in $(S_r)_{ij}$. For each $V_{s\text{-}30}$ category, spectral amplification levels for the periods of T = 0.01 s [$F(0.01)$], T = 0.3 s [$F(0.3)$], T = 1.0 s [$F(1.0)$] and T = 3.0 s [$F(3.0)$] are plotted in Figure 4.3. Also plotted are results of regression analyses performed according to Equation 3.3(a) (solid lines), ± 95% confidence intervals on the median amplification (dotted lines), and median regression ± log-normal standard deviation term (dashed lines). Note that the thick dotted lines in Figure 4.3 represent predictions of the unified model that are discussed subsequently. Presented in Table 4.1 are regression coefficients and standard deviation terms. As described in Chapter 3, the estimation error terms for parameters a_i and b_i in Table 4.1 are the half-widths of the ±95% confidence intervals on the parameters.

Table 4.1 Regression coefficients for S_a amplification factors

Category	Period	a	b	Std. Dev.	Rejection confidence for b=0 model (%)
B	0.01	0.06 ± 0.99	0.03 ± 0.42	0.50	12
	0.3	-0.23 ± 0.88	0.03 ± 0.37	0.44	14
	1.0	-0.84 ± 1.63	-0.21 ± 0.68	0.77	48
	3.0	-1.57 ± 1.02	-0.54 ± 0.40	0.37	99
C_{hr}	0.01	0.25 ± 0.48	0.10 ± 0.19	0.50	69
	0.3	-0.05 ± 0.64	0.01 ± 0.26	0.67	4
	1.0	-0.09 ± 0.85	-0.01 ± 0.35	0.84	5
	3.0	-0.59 ± 1.09	-0.13 ± 0.48	0.87	43
CD	0.01	-0.03 ± 0.29	-0.09 ± 0.12	0.59	86
	0.3	-0.09 ± 0.30	-0.09 ± 0.13	0.63	83
	1.0	0.43 ± 0.37	0.07 ± 0.16	0.67	58
	3.0	0.53 ± 0.65	0.16 ± 0.32	0.89	69
D_{lr}	0.01	-0.38 ± 0.23	-0.29 ± 0.10	0.49	100
	0.3	-0.26 ± 0.22	-0.23 ± 0.10	0.47	100
	1.0	0.19 ± 0.22	-0.11 ± 0.10	0.45	97
	3.0	0.47 ± 0.28	0.02 ± 0.14	0.51	19
E	0.01	-0.85 ± 0.63	-0.64 ± 0.25	0.40	100
	0.3	-0.76 ± 0.69	-0.57 ± 0.28	0.44	100
	1.0	-0.37 ± 0.73	-0.53 ± 0.29	0.46	100
	3.0	0.42 ± 0.79	-0.21 ± 0.34	0.47	80

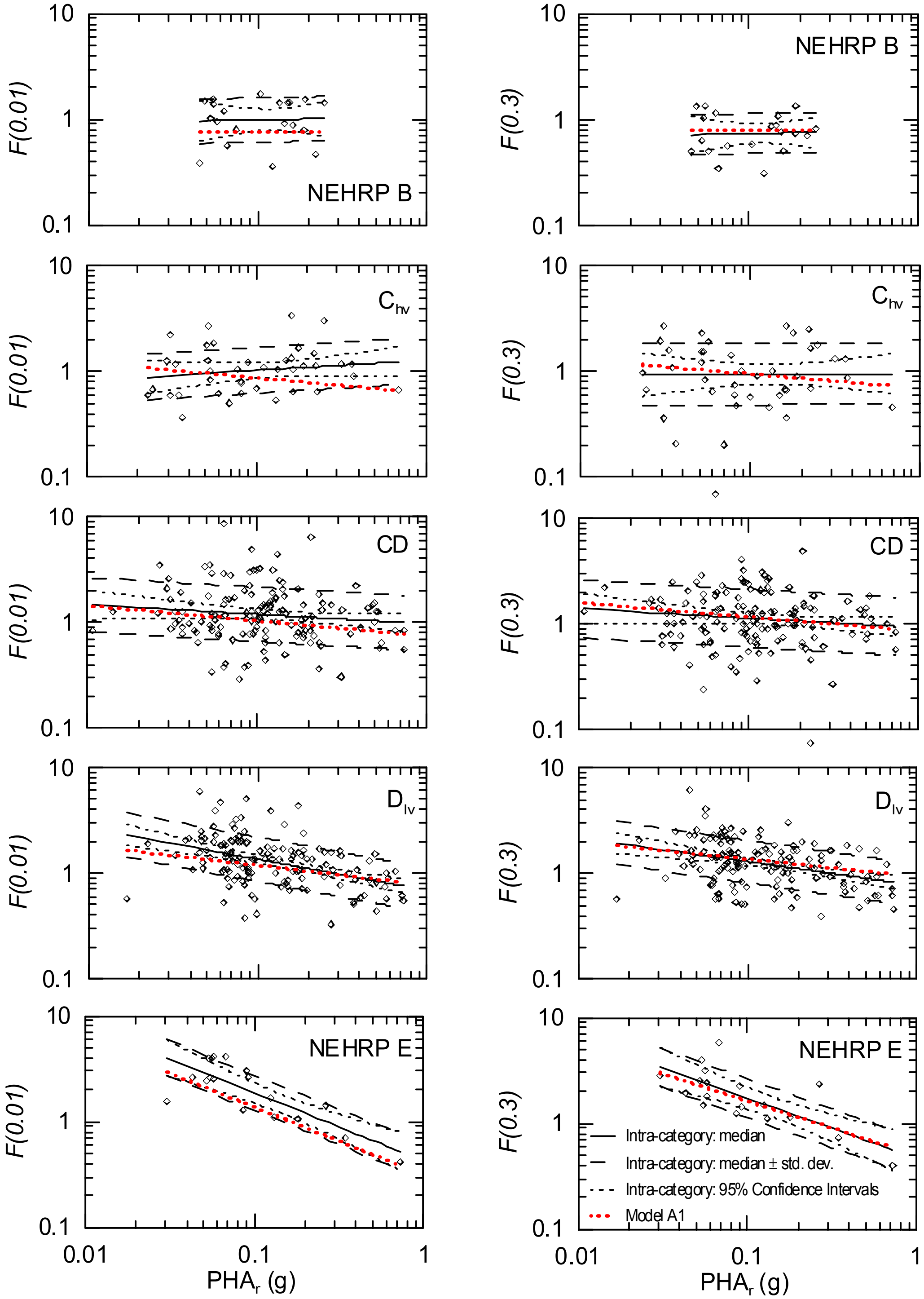

Fig. 4.3 Spectral acceleration amplification factors, intracategory regression results, and predictions of unified model for velocity categories plotted relative to PHA of reference motion (PHA$_r$)

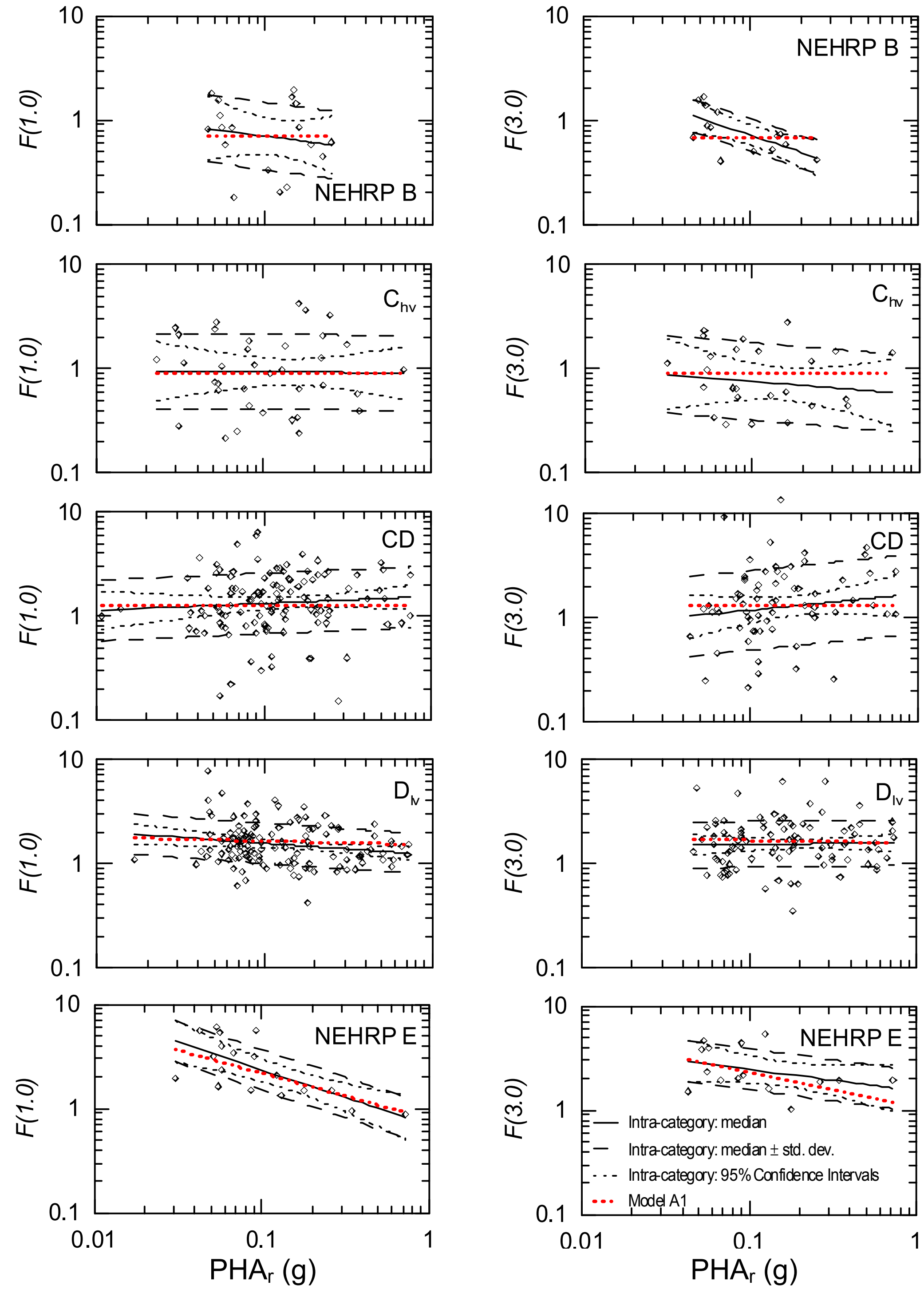

Fig. 4.3 ***continued***

The b parameters compiled from the above analyses are plotted as discrete data points with error bounds in Figure 4.4. The results show statistically significant nonlinearity (by the criteria described in Chapter 3) at small $V_{s\text{-}30}$, corresponding to the E category. Values of b decrease to a relatively consistent value slightly offset from zero for $V_{s\text{-}30}$ > ~300 m/s. The nonlinearity at these large $V_{s\text{-}30}$ values is not statistically significant. Based on the trend of the discrete points in Figure 4.4, the following model is postulated to simulate the variation of b with PHA_r:

$$b = b_1 \qquad \text{category E} \qquad (4.1a)$$

$$b = b_2 + \left(V_{s-30} - b_V\right)^2 \frac{b_1 - b_2}{\left(180 - b_V\right)^2} \qquad 180 < V_{s\text{-}30} < b_V \text{ (m/s)} \qquad (4.1b)$$

$$b = b_2 \qquad b_V < V_{s\text{-}30} < 520 \text{ (m/s)} \qquad (4.1c)$$

$$b = b_2 - \left(V_{s-30} - 520\right)\frac{b_2}{240} \qquad 520 < V_{s\text{-}30} < 760 \text{ (m/s)} \qquad (4.1d)$$

$$b = 0 \qquad V_{s\text{-}30} > 760 \text{ (m/s)} \qquad (4.1e)$$

where the units of $V_{s\text{-}30}$ are in m/s, and b_1, b_2, and b_V are model parameters estimated from the data. A parabolic fit was used in lieu of a linear fit because the parabola predicts lower levels of nonlinearity for 180 < $V_{s\text{-}30}$ < b_V, which is more consistent with the data. The decrease of b_2 to zero at high $V_{s\text{-}30}$ is motivated by the statistical insignificance of nonlinearity for high-velocity sites. Values of parameters b_1, b_2, and b_V were estimated from regression analyses described subsequently in this chapter, and the continuous lines in Figure 4.4 represent the outcome of those analyses.

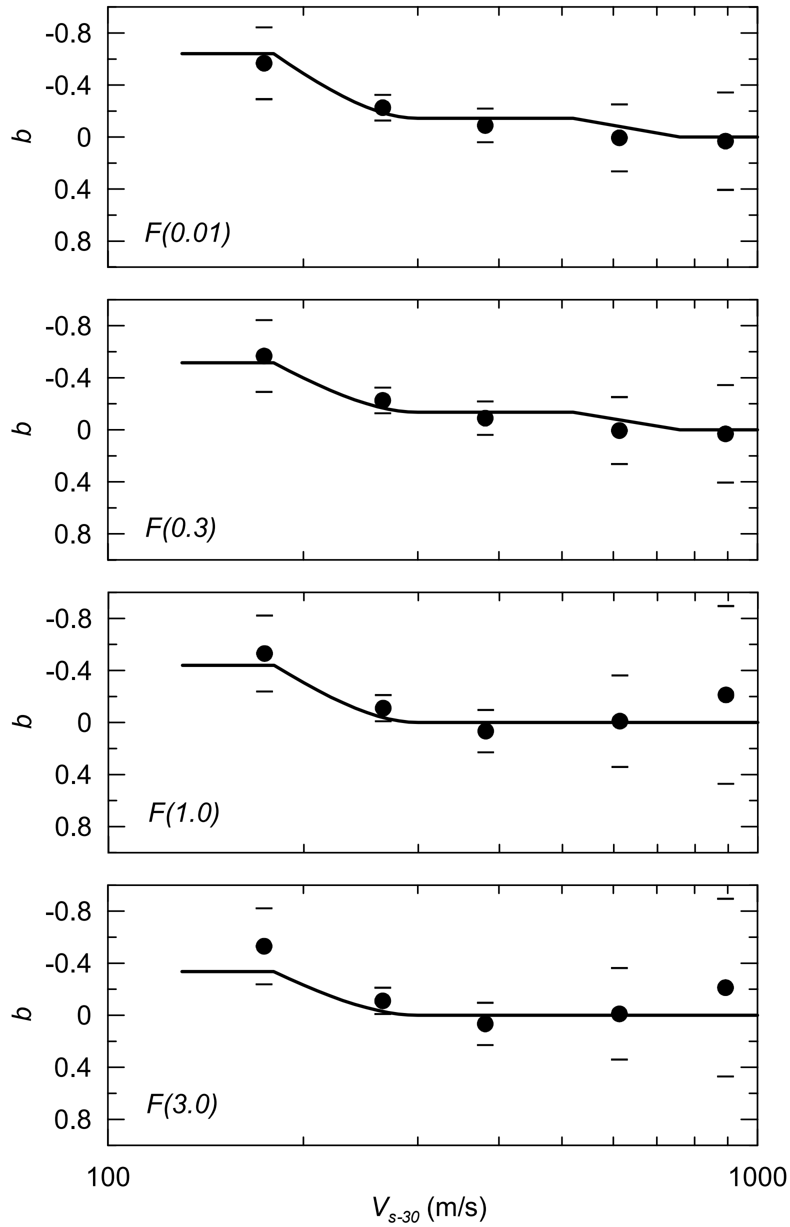

Fig. 4.4 Variation of slope parameter *b* (defined in Eq. 3.3(a)) with V_{s-30}. Plotted are discrete results for V_{s-30} data bins and continuous lines showing model defined by Equation 4.1(a)–(d), whose parameters are determined from mixed effects regression analyses.

4.4.2 Variation of Amplification with $V_{s\text{-}30}$

In this section, the variation of amplification factors with $V_{s\text{-}30}$ is investigated, which is accomplished by compiling data points from each category "near" a reference site baseline shaking level of PHA_r = 0.1 g. The use here of only data near this baseline shaking level is intended to isolate the $V_{s\text{-}30}$ dependence of the amplification factors from the dependence on PHA_r. These data points are identified as follows. Suppose for example that the median value of $F(0.3)$ from regression [i.e., Eq. 3.3(a)] at the baseline amplitude is $F^{ba}(0.3)$. Then the PHA_r values along the median regression fit for the category (i.e., the solid lines in Fig. 4.3) corresponding to an amplification departure (in natural logarithmic units) from $F^{ba}(0.3)$ of 0.05 [i.e., amplification levels in natural logarithmic units of $\ln(F^{ba}(0.3)) \pm 0.05$] are found. Data points between these two PHA_r levels are selected. When the regression fit shows no significant nonlinearity, most or all of the data is selected, whereas significant nonlinearity limits the data range selected (e.g., data were taken from PHA_r = 0.09–0.11 g for $F^{ba}(0.3)$ s in NEHRP category E). The value of ±0.05 used in the above process was selected by judgment; it was found to provide a collection of data points sufficiently large enough that statistically stable amplification values can be defined while simultaneously maintaining insignificant PHA_r dependence of amplification.

Data points selected by the above process are shown in Figure 4.5 along with a regression fit using the following power law equation,

$$F^{ba}(T) = \left(\frac{V_{s-30}}{V_{ref}^{ba}} \right)^{c^{ba}} \tag{4.2}$$

where V_{ref}^{ba} and c^{ba} are regression coefficients (given in Fig. 4.5) and superscript "*ba*" on $F(T)$ and the regression parameters denote the use of amplification factors selected by the above process (i.e., near the baseline amplitude). Note that parameter V_{ref}^{ba} is simply the value of $V_{s\text{-}30}$ at which $F^{ba}(T)$ is unity. Plotted adjacent to the power law fit are the ± 95% confidence intervals on the median amplification. Also shown for reference are within-category median $F(0.3)$ and $F(1.0)$ values at PHA_r = 0.1 g (i.e., the ordinates of the solid lines from Fig. 4.3 at PHA_r = 0.1 g), which are plotted with an × at the median $V_{s\text{-}30}$ value for within-category data. The vertical line drawn through the × represents the range of amplification values that would be expected for PHA_r = 0.01 to 1.0 g based on intracategory regression results. The results in Figure 4.5 show the expected significant increase of amplification with decreasing $V_{s\text{-}30}$, although the variation with reference motion amplitude is also important (especially for category E).

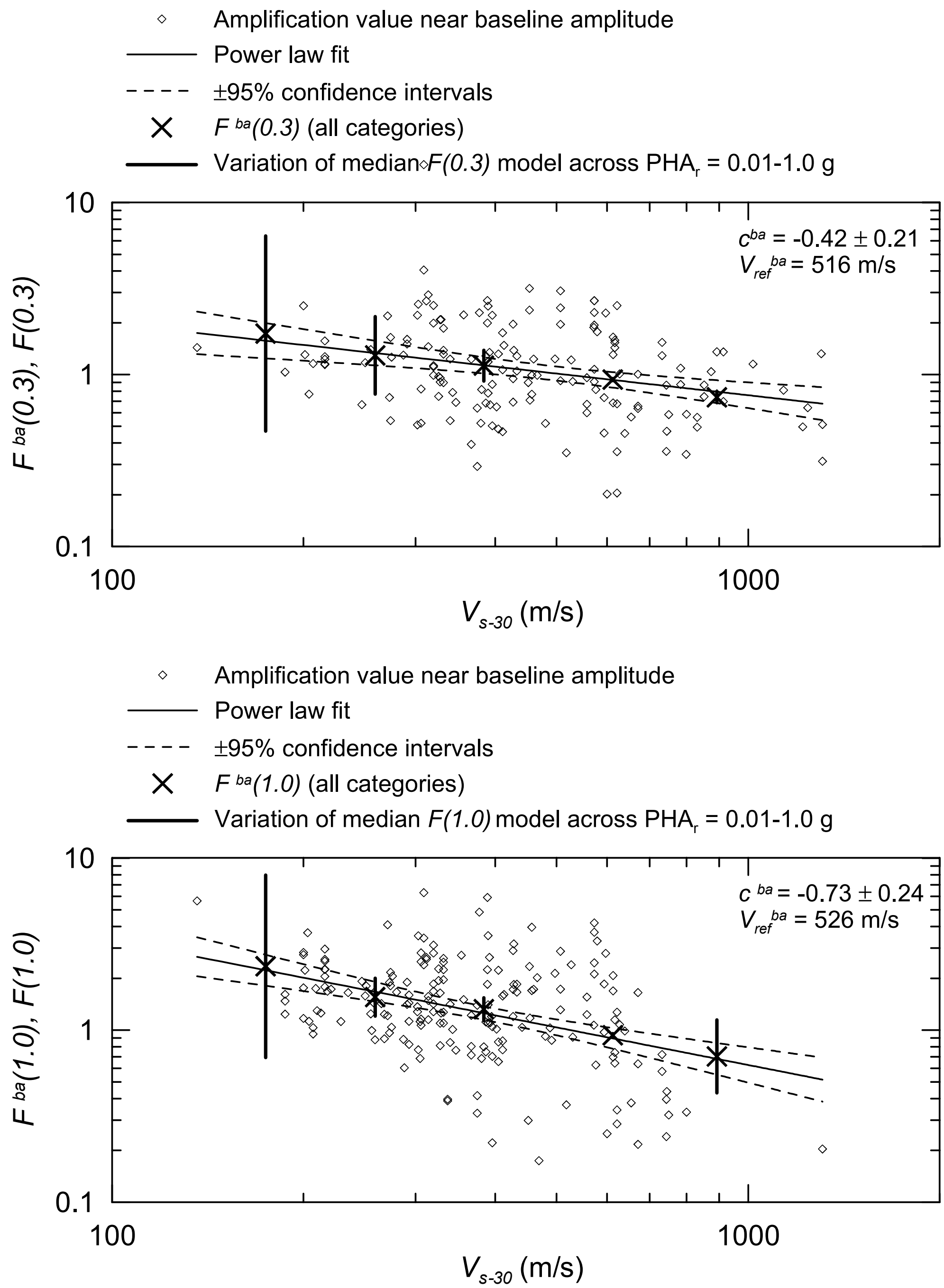

Fig. 4.5 Variation of amplification factors $F^{ba}(0.3)$ and $F^{ba}(1.0)$ with $V_{s\text{-}30}$ for consistent ground motion amplitude (data points and power law regression fit), along with intracategory variation of $F(0.3)$ and $F(1.0)$ with reference motion amplitude (vertical lines)

4.4.3 Mixed Effects Regression for Unified Model

The models for $V_{s\text{-}30}$- and PHA_r-dependence of amplification in Equations 4.1–4.2 can now be combined to form a unified model for amplification factors. This model is expressed as follows:

$$ln(F_{ij}) = c\,ln\left(\frac{V_{s-30\,ij}}{V_{ref}}\right) + b\,ln\left(\frac{PHA_{r\,ij}}{0.1}\right) + \eta_i + \varepsilon_{ij} \tag{4.3}$$

where PHA_r is expressed in units of g, b is a function of regression parameters as given in Equation 4.1, c and V_{ref} are regression parameters, η_i is a random effect term for earthquake event i (should have zero median across all events, standard deviation is denoted "τ") and ε_{ij} represents the intra-event model residual for motion j in event i (should have median near zero for well recorded events, standard deviation is denoted "σ"). In order to simplify the regression process to produce stable results, parameter b_2 in Equation 4.1 was estimated using all data with $V_{s\text{-}30} > b_V$. However, as a practical matter, the data controlling b_2 in the regression are sites with velocities between approximately 300 and 600 m/s. As noted previously, the decrease of b_2 to zero at high $V_{s\text{-}30}$ is a judgment-based adjustment to the model motivated by the statistical insignificance of nonlinearity for high velocity sites. The total standard deviation that is appropriate for use with the median amplification from Equation 4.3 is

$$\sigma_{total} = \sqrt{\sigma^2 + \tau^2} \tag{4.4}$$

Regression analyses are performed according to Equation 4.3 using a mixed effects model similar to that of Abrahamson and Youngs (1992) as implemented in the program R (Pinheiro and Bates, 2000). The amplification factors used in these regressions are modified from those presented in Chapter 3 (i.e., Eq. 3.1), in that event terms are not incorporated into the reference site ground motions, S_r. Event terms are omitted from the reference motion at this stage because event terms are estimated as part of the mixed effects regression procedure (i.e., term η_i). In addition, reference motions are now evaluated using multiple attenuation models. The models and corresponding site conditions used to evaluate S_r values are as follows:

A1. Abrahamson and Silva, (1997): rock

A2. Sadigh et al., (1997): rock

A3. Campbell and Bozorgnia, (2003): generic rock

The Boore et al. (1997) attenuation relationship was considered for use as well. It was decided not to develop site factors relative to this attenuation model in part because the site factor in that attenuation model is already cast in terms of $V_{s\text{-}30}$, with 760 m/s taken as the reference value. Moreover, because the strong motion database contains few sites with high $V_{s\text{-}30}$, the Boore et al. attenuation model for the reference site condition is based largely on data from softer sites, and hence the attenuation results are strongly influenced by the (linear) site factor. It was considered inappropriate to implement an attenuation model that is so dependent on one site factor with a new (different) site factor.

Several issues complicated the regression process. First, a stable estimate of b_V could not be obtained from the regression, so alternative values of b_V were used as fixed values during the regression of other parameters. Optimal b_V values varied somewhat from period to period, but generally a value of 300 m/s provides a reasonable fit to the data. A second complication is that parameter b_1,when estimated by regression, was found to be relatively small in an absolute sense (i.e., indicating small nonlinearity) and to be poorly constrained (i.e., large estimation uncertainty). The low values underpredict the nonlinearity for category E materials, for which the available data are not sufficiently abundant to strongly affect the regression results. Accordingly, b_1 was set at values from intracategory regressions.

Example values of model parameters (and their estimation errors) derived directly from the regression are presented in Table 4.2. The parameters are also listed in Appendix B for T = 0.01 – 5.0 s. The results in Appendix B have been smoothed with respect to period.

Table 4.2 Regression parameters (unsmoothed) for unified model for site amplification. Parameters without error terms are estimated deterministically (as described in text).

Atten. Model	Parameter	b_1	b_2	b_v	c	V_{ref} (m/s)	τ	σ	σ_{total}[1]
	F(0.01)	-0.52	-0.14 ± 0.04	300	-0.36 ± 0.06	418 ± 72	0.27	0.49	0.56
A1	*F(0.3)*	-0.52	-0.11 ± 0.05	300	-0.46 ± 0.07	532 ± 93	0.35	0.54	0.64
	F(1.0)	-0.44	0.00 ± 0.05	300	-0.69 ± 0.07	519 ± 69	0.41	0.55	0.69
	F(3.0)	-0.35	0.00 ± 0.07	300	-0.77 ± 0.09	445 ± 65	0.41	0.62	0.75
	F(0.01)	-0.61	-0.20 ± 0.04	300	-0.34 ± 0.06	567 ± 110	0.24	0.49	0.55
A2	*F(0.3)*	-0.49	-0.21 ± 0.04	300	-0.44 ± 0.07	601 ± 103	0.29	0.55	0.62
	F(1.0)	-0.48	-0.12 ± 0.05	300	-0.66 ± 0.08	646 ± 90	0.35	0.57	0.67
	F(3.0)	-0.43	-0.14 ± 0.07	300	-0.72 ± 0.10	545 ± 68	0.38	0.62	0.73
	F(0.01)	-0.55	-0.04 ± 0.05	300	-0.34 ± 0.06	501 ± 90	0.23	0.49	0.54
A3	*F(0.3)*	-0.51	-0.05 ± 0.05	300	-0.44 ± 0.07	610 ± 106	0.29	0.53	0.61
	F(1.0)	-0.49	-0.04 ± 0.06	300	-0.67 ± 0.07	709 ± 107	0.39	0.56	0.68
	F(3.0)	-0.42	-0.22 ± 0.08	300	-0.72 ± 0.09	710 ± 87	0.39	0.61	0.72

[1] $\sigma_{total}^2 = \tau^2 + \sigma^2$

The c and V_{ref} parameters for T = 0.3 s and T = 1 s identified in Table 4.2 for model A1 are similar to those evaluated previously in Figure 4.5. As shown by the lines in Figure 4.4, the parameters describing nonlinearity parameter b for model A1 define a curve consistent with the b-values from discrete velocity bins.

Median amplification factors for models A1–A3 are compared in Figure 4.6 for velocities at the median of the sites within each NEHRP category. At small periods (T = 0.01 s and 0.3 s), the models A1 and A2 results are generally similar both in terms of the amplification level and the dependence of amplification on PHA_r. At these small periods model A3 has less PHA_r dependence for categories C–D and thus has higher amplification levels for PHA_r > ~0.1 g than models A1–A2.

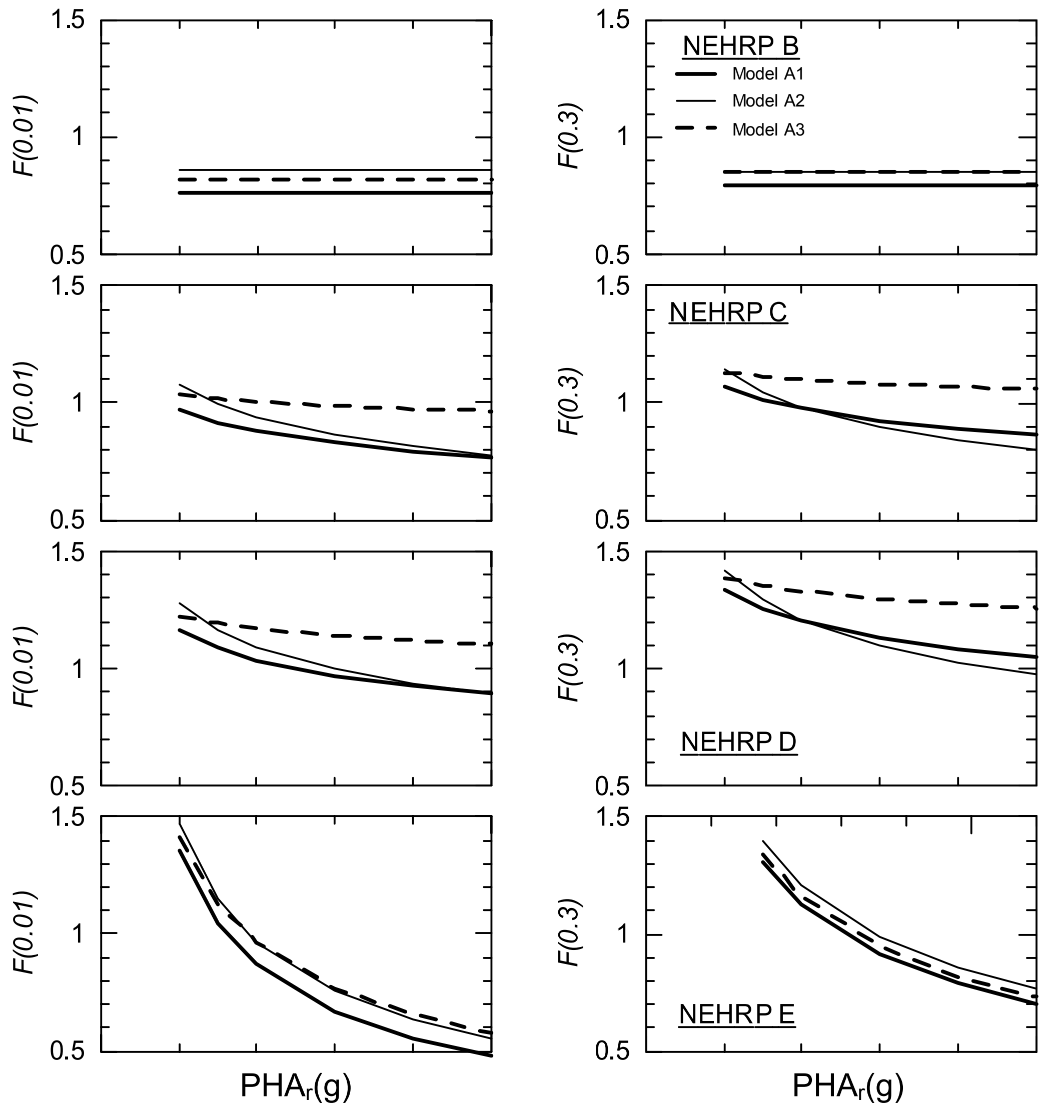

Fig. 4.6 Variation with PHA_r of median amplification factors from models A1–A3 at mid-$V_{s\text{-}30}$ value for each NEHRP bin

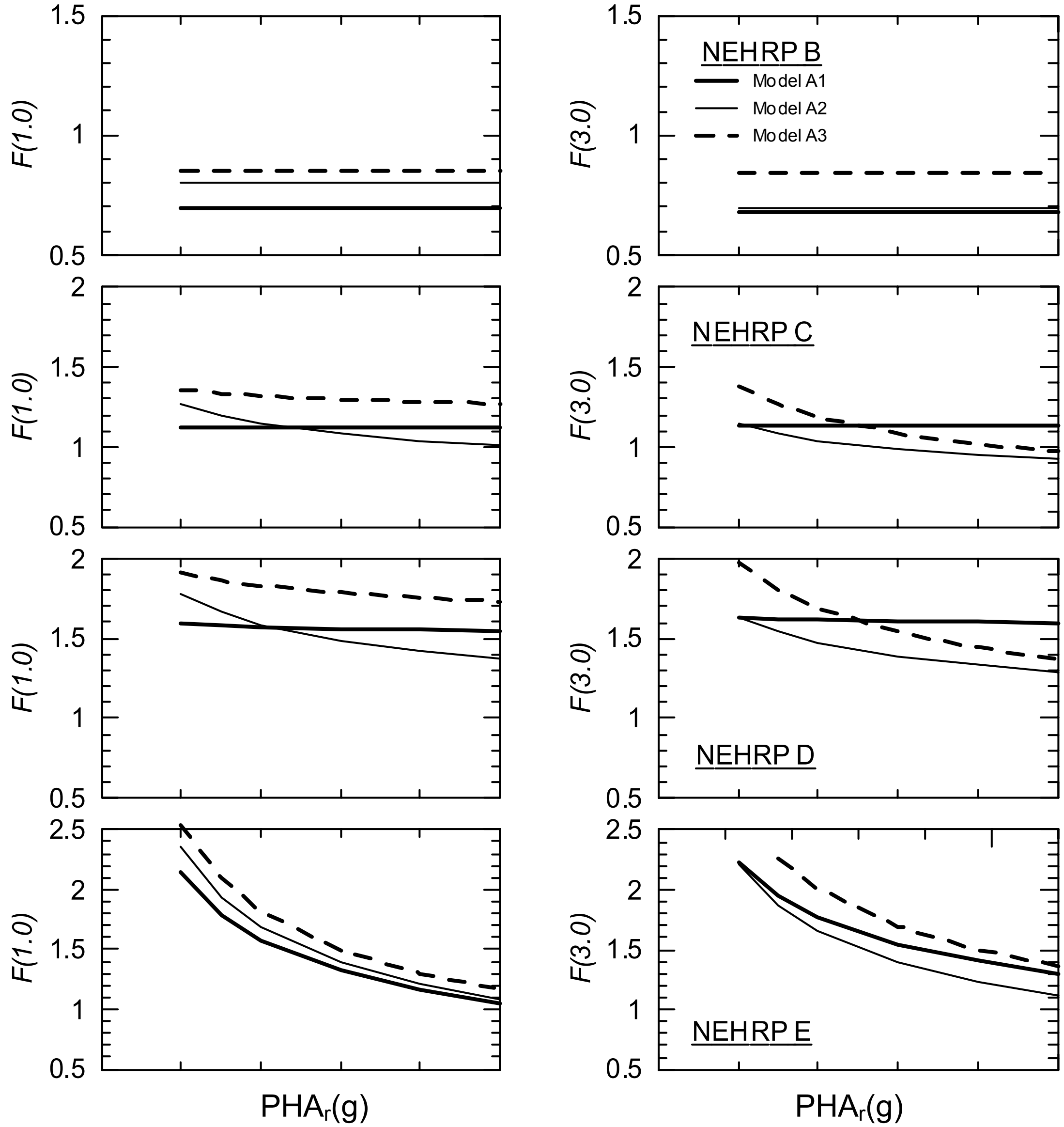

Fig. 4.6 ***continued***

From Figure 4.6 it is seen that at T = 1.0 s, A3 amplification levels exceed A1–A2, although the amount of PHA_r dependence is comparable. For T = 3.0 s, PHA_r dependence of models A2 and A3 are similar, whereas A1 is relatively linear. For all three models (A1–A3), the results at all periods are similar for category E.

As shown in Figure 4.7, the relatively linear short-period site terms associated with A3 are a result of different distance scaling formulations in the attenuation models, which produces relatively low reference rock motions at close distance for Campbell and Bozorgnia (2003) as compared to Abrahamson and Silva (1997) or Sadigh et al. (1997). These low reference motions in turn cause the model A3 amplification factors at close distance (thus high PHA_r) to be large (nearly as high as those at low PHA_r), which results in the minimal nonlinearity.

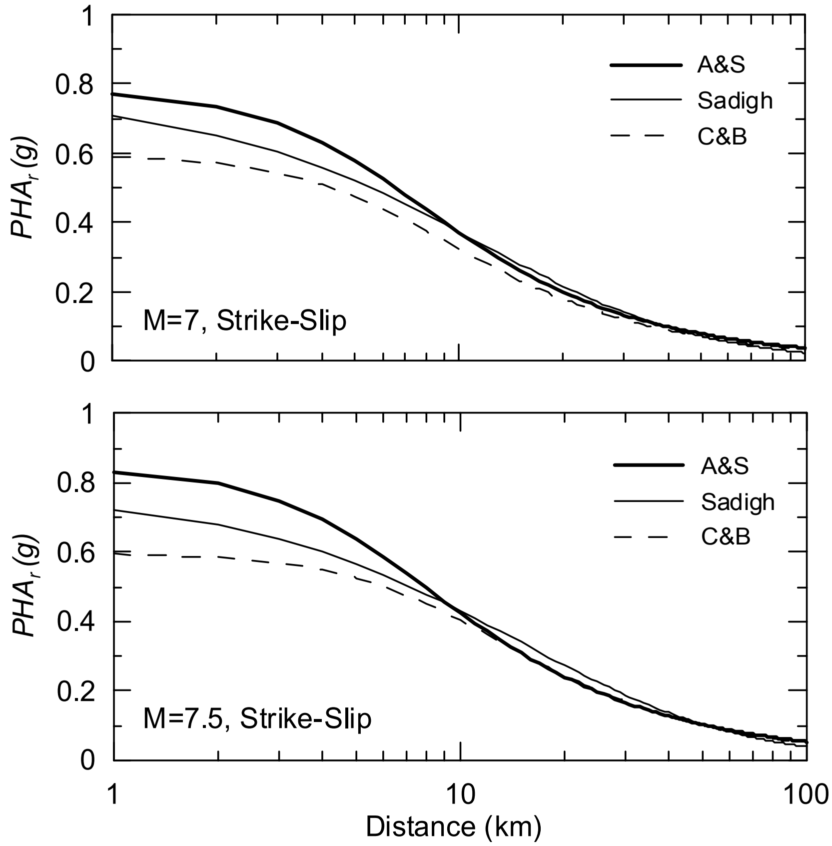

Fig. 4.7 Variation with distance of PHA_r for each attenuation model

4.4.4 Comparisons of Model Predictions to Data

The sufficiency of models A1–A3 is investigated by plotting intra-event prediction residuals (ε_{ij} in Eq. 4.3) against prediction variables $V_{s\text{-}30}$ and PHA_r in Figure 4.8. The results show no apparent trend in model residuals with $V_{s\text{-}30}$ or PHA_r [Figs. 4.8(a),(c),(e)], and no significant bias for data within the previously used $V_{s\text{-}30}$ bins, as demonstrated by median residuals near unity [Figs. 4.8(b),(d),(f)]. In Figure 4.3 we plot with thick, dotted lines the model predictions against data within $V_{s\text{-}30}$ bins. The unified model is seen to provide predicted median amplification levels for each category that are reasonably consistent with the intracategory regression results.

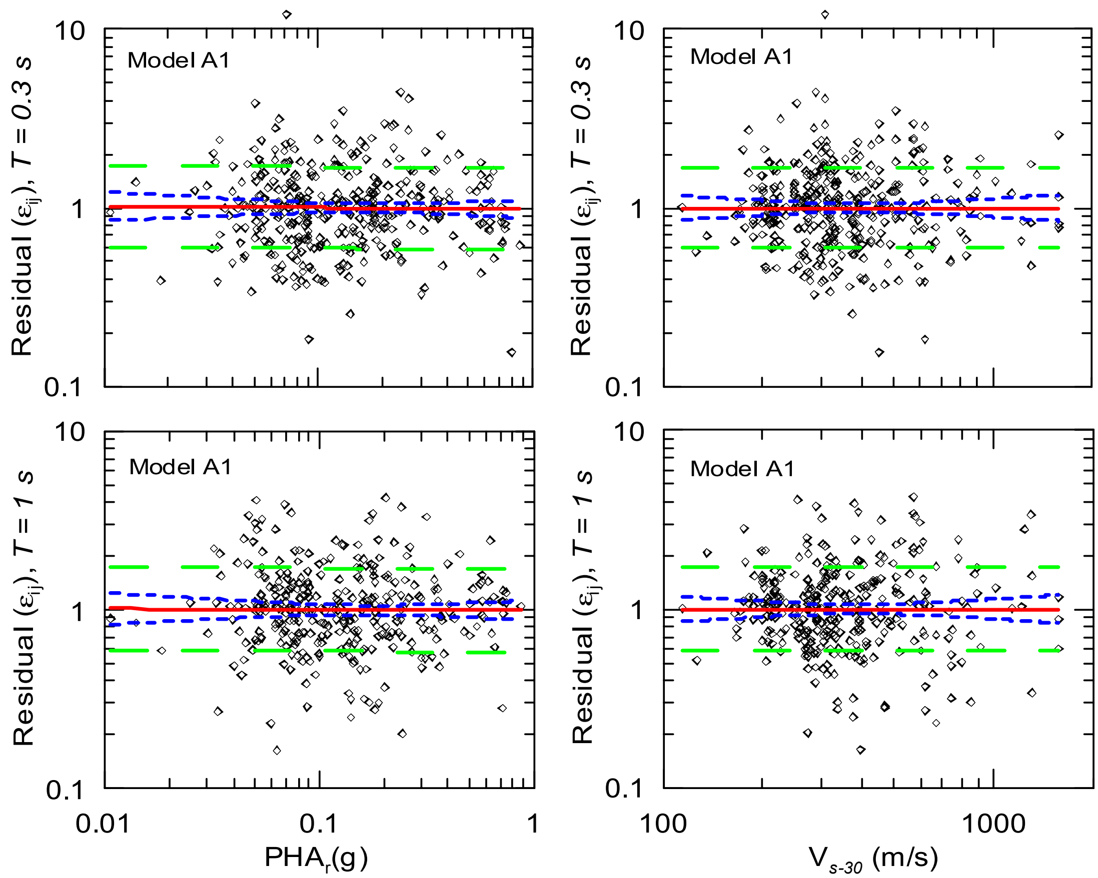

Fig. 4.8(a) Residuals of model A1 (in arithmetic units) plotted against $V_{s\text{-}30}$ and PHA$_r$

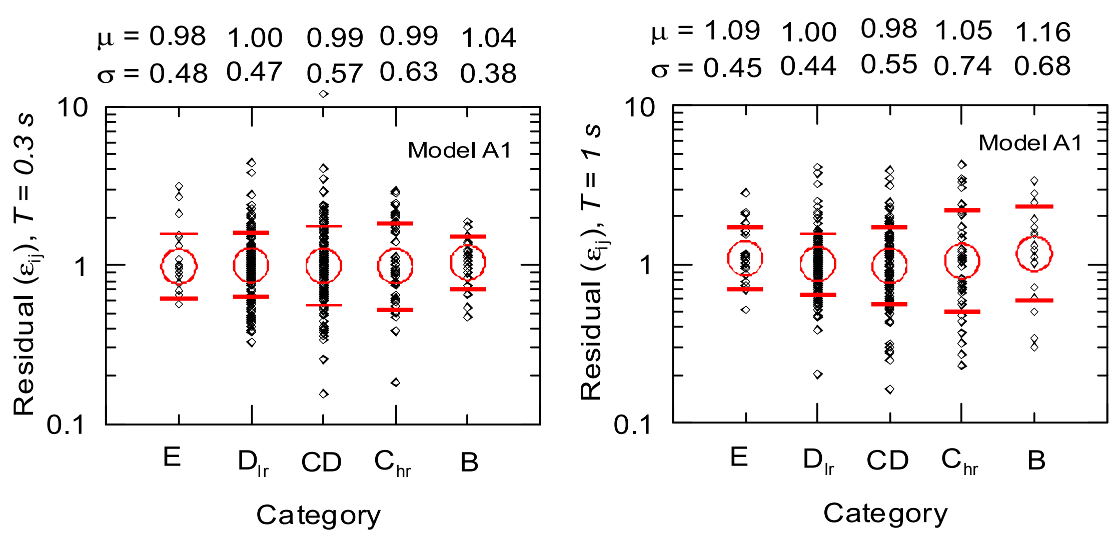

Fig. 4.8(b) Residuals of model A1 (in arithmetic units) within NEHRP site categories along with median (μ) and median ± one standard deviation (σ) of residuals

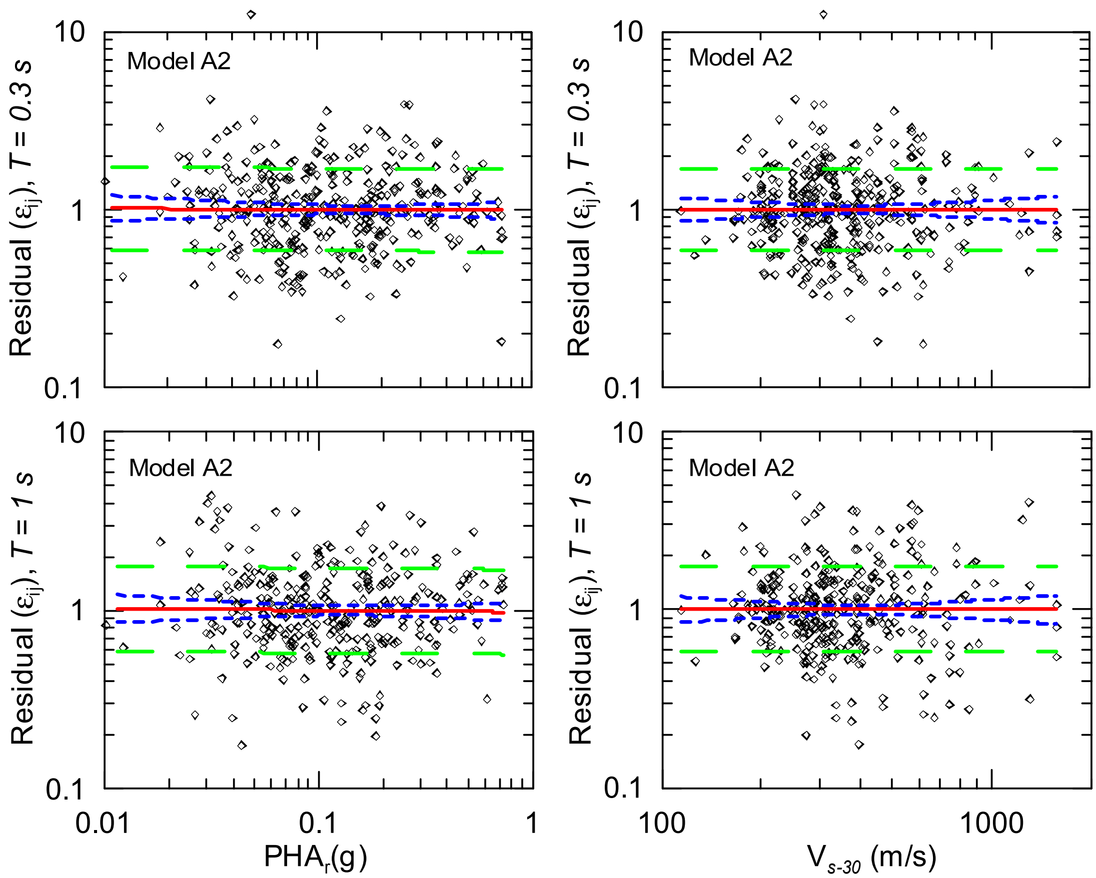

Fig. 4.8(c) Residuals of model A2 (in arithmetic units) plotted against $V_{s\text{-}30}$ and PHA$_r$

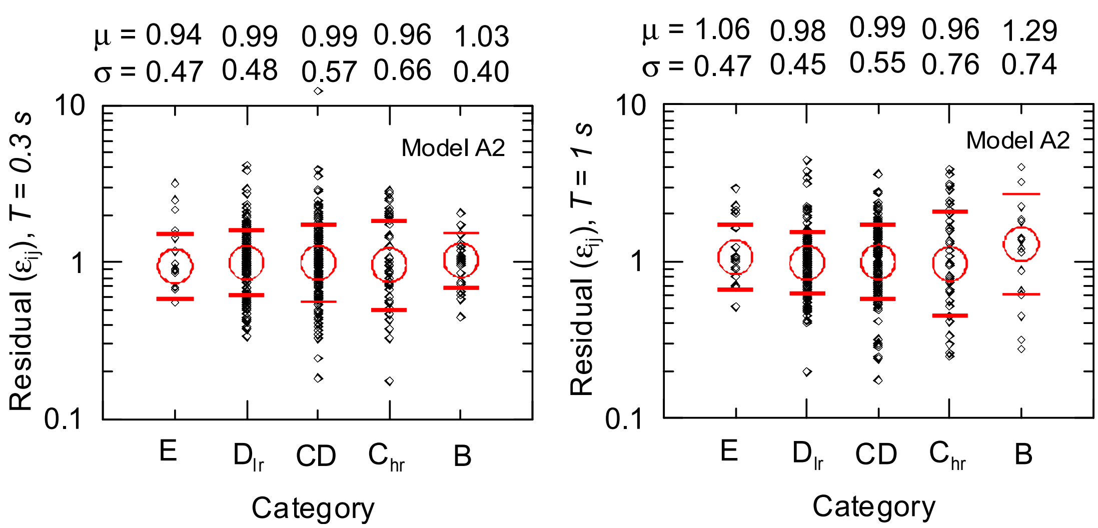

Fig. 4.8(d) Residuals of model A2 (in arithmetic units) within NEHRP site categories along with median (μ) and median ± one standard deviation (σ) of residuals

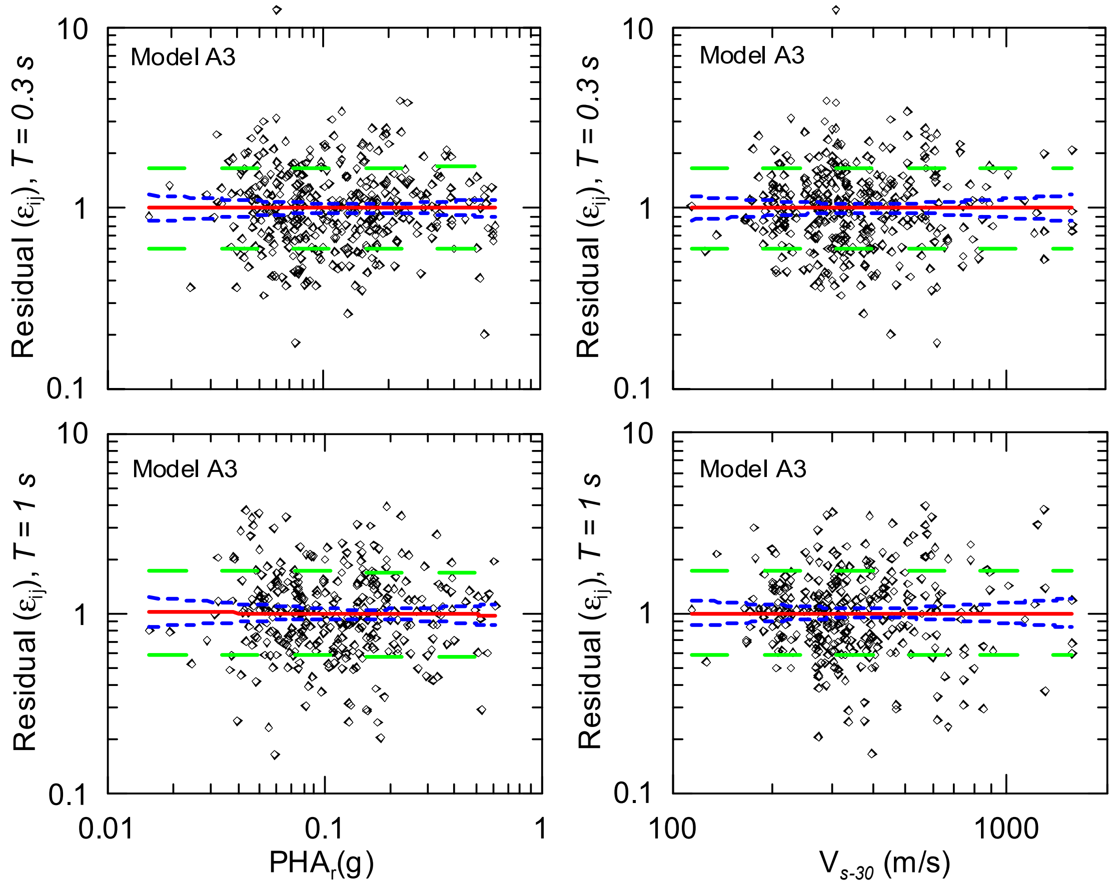

Fig. 4.8(e) Residuals of model A3 (in arithmetic units) plotted against V_{s-30} and PHA$_r$

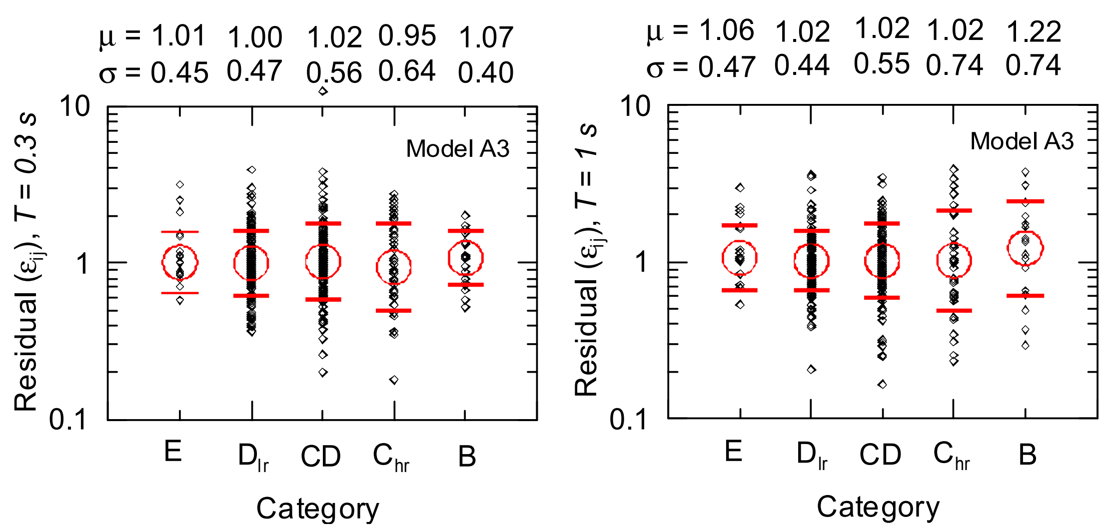

Fig. 4.8(f) Residuals of model A3 (in arithmetic units) within NEHRP site categories along with median (μ) and median ± one standard deviation (σ) of residuals

4.4.5 Analysis of Standard Deviation Terms

The dispersion of the amplification factors is investigated as a function of magnitude (*m*), site-source distance (*r*), and $V_{s\text{-}30}$. The magnitude dependence of dispersion is examined using a procedure similar to that of Youngs et al. (1995). The data are binned into groups of 0.5 magnitude width with an overlap of 0.25, and mixed-effects regression analyses are performed within each bin using regression Equation 4.3, but with the regression coefficients set to the values from the unsmoothed mixed-effect analysis results obtained previously. This analysis provides inter- and intra-event standard deviation terms (τ and σ, respectively) within each magnitude bin. Standard deviation terms τ and σ and their 95% confidence intervals are plotted in Figure 4.9(a) for models A1–A3 at periods 0.01 s, 0.3 s, 1.0 s, and 3.0 s. The confidence intervals on the dispersion reflect the estimation uncertainty, and in general are wide when the data bin is sparsely populated. Note that the confidence intervals around the standard deviation estimates are not symmetric. This is a common feature of variance estimated with a maximum likelihood procedure (Raudenbush and Bryk, 2002) because the distribution of the variance estimate is skewed.

The results in Figure 4.9(a) do not indicate a significant magnitude dependence of either τ or σ. Note that for $T = 3$ s, the first, the second, and the last magnitude bins have small number of data, so that τ and σ from those bins are less reliable, as reflected by the wide confidence intervals. These results differ from magnitude-dependent standard deviation terms identified by Youngs et al. (1995) and incorporated into most modern attenuation models (e.g., those underlying models A1–A3). Note also that the confidence intervals on τ are much larger than those on σ. This occurs because there are relatively few earthquakes within each magnitude bin to constrain the τ estimates.

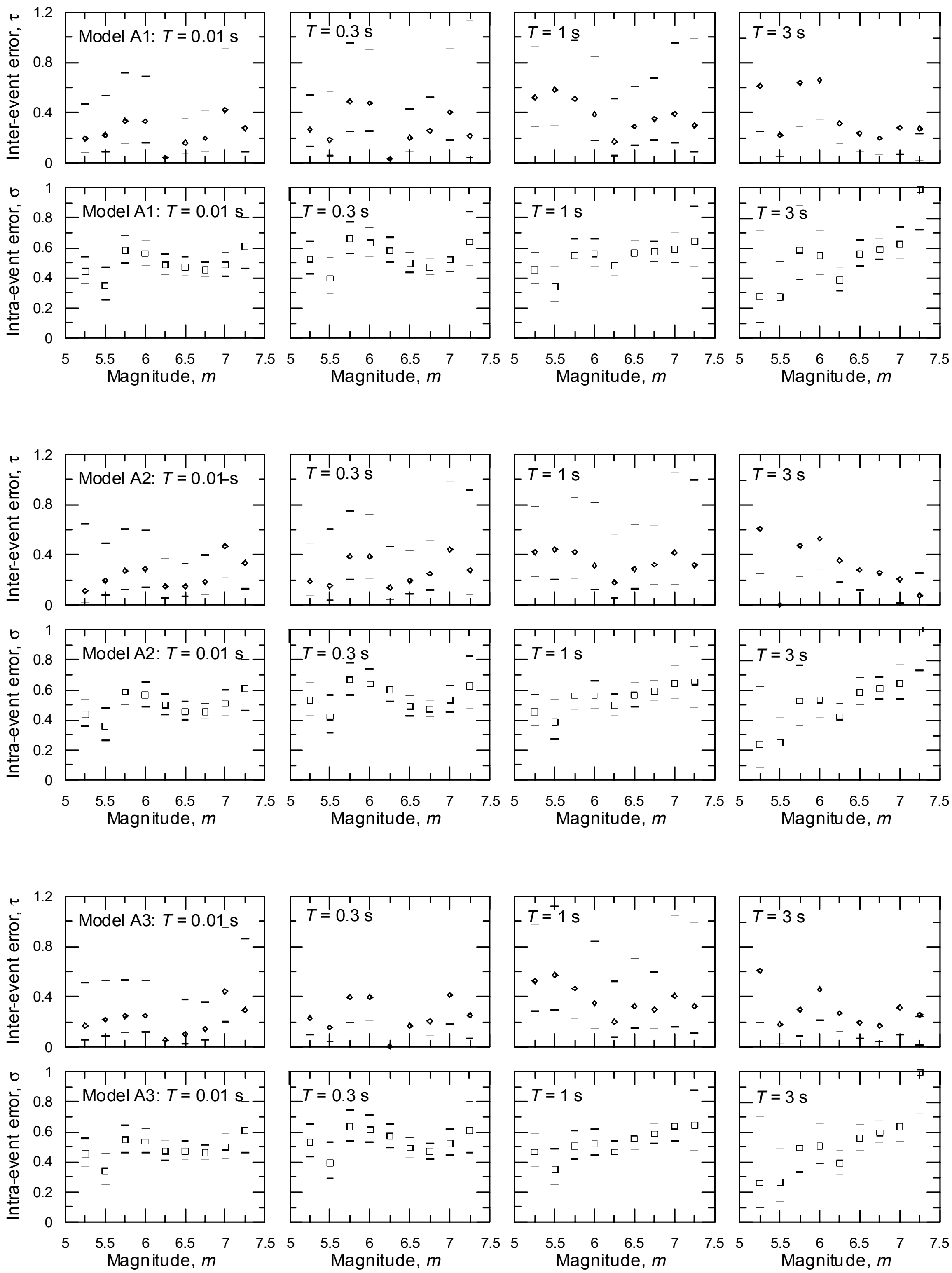

Fig. 4.9(a) Variation of inter- and intra-event standard deviation (and their estimation error) with magnitude, models A1–A3

The variation of the dispersion of ε_{ij} (denoted "σ") with distance and $V_{s\text{-}30}$ is investigated by partitioning the model residuals according to overlapping distance bins and non-overlapping $V_{s\text{-}30}$ bins, and then evaluating σ within each bin. The results of these analyses are shown in Figure 4.9b ($V_{s\text{-}30}$) and 4.9c (distance) for models A1–A3 at $T = 0.01$ s, 0.3 s, 1.0 s, and 3.0 s. As illustrated in Figure 4.9(b), standard deviation term σ generally increases with $V_{s\text{-}30}$, although the amount of increase is strongly period dependent. At small periods ($T \leq \sim 0.15$ s) the amount of increase of σ is small between well-populated $V_{s\text{-}30}$ bins for which the results are reliable (generally < 0.05). However, for $T \geq 1.0$ s, the amount of increase between these bins ranges from about 0.1–0.3, with larger increases occurring at longer periods. The results for the largest $V_{s\text{-}30}$ bin (760–1310 m/s) vary erratically from period to period due to a paucity of data, and are not considered reliable.

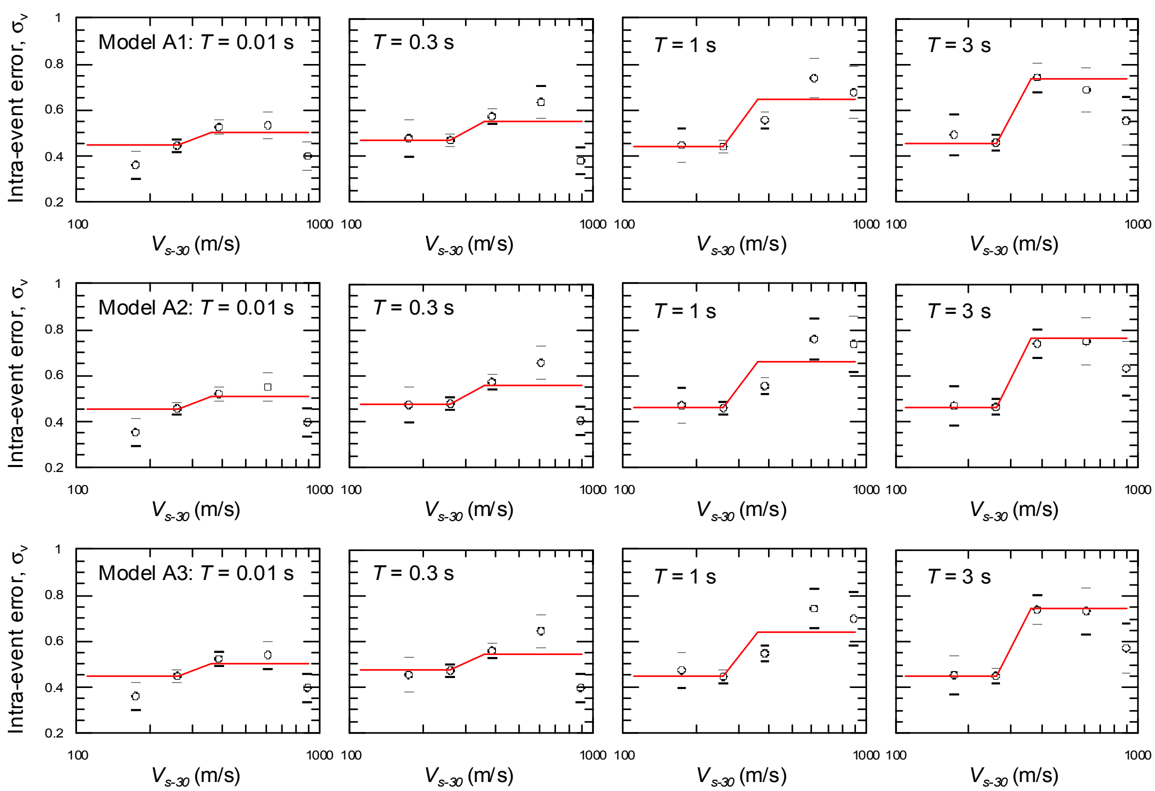

Fig. 4.9(b) Variation of intra-event standard deviation with $V_{s\text{-}30}$, models A1–A3

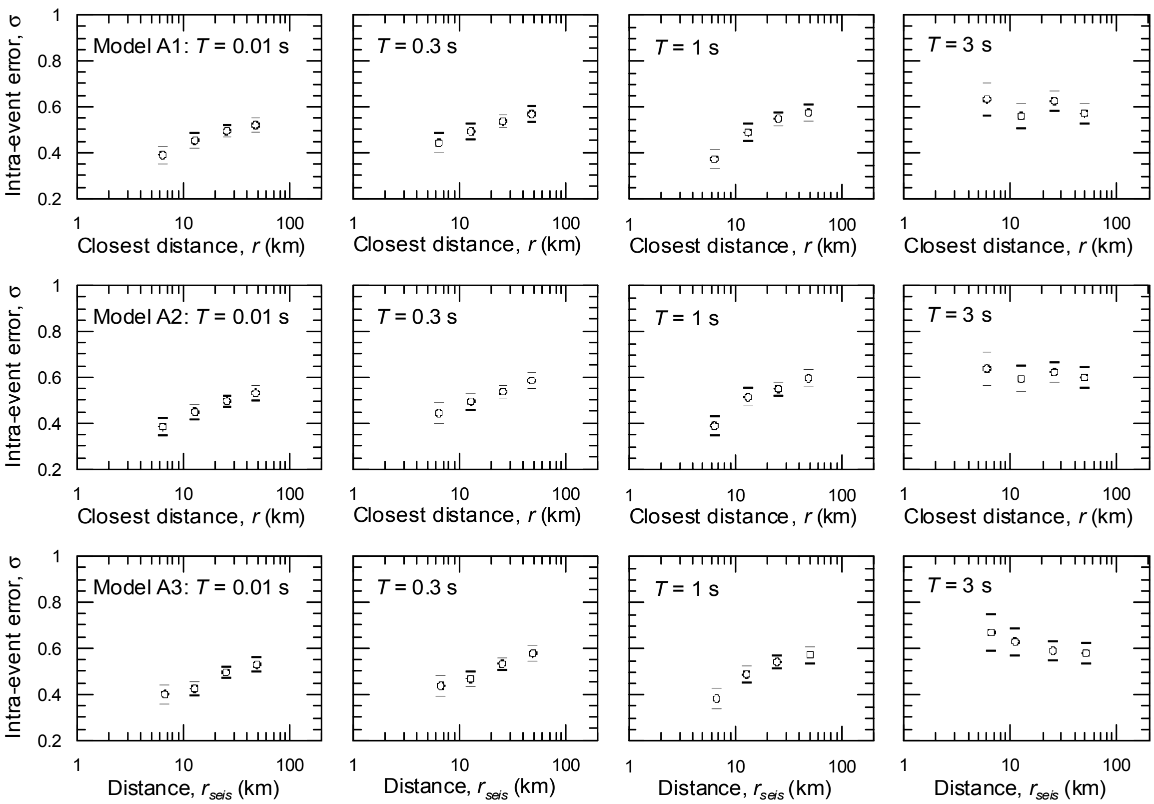

Fig. 4.9(c) Variation of intra-event standard deviation with distance, models A1–A3

As shown in Figure 4.9(c), preliminary data analyses indicate that standard deviation terms increase with distance (r) for periods $T \leq 1.0$ s. However, when the r dependence of σ is investigated within well populated $V_{s\text{-}30}$-bins, the trend of σ increasing with r is lost as illustrated in Figure 4.10(a). Moreover, when the $V_{s\text{-}30}$ dependence of σ is investigated within well populated r bins, the trend of σ increasing with $V_{s\text{-}30}$ is retained as shown in Figure 4.10(b). Thus, the $V_{s\text{-}30}$ dependence of σ appears to be more robust than the r dependence.

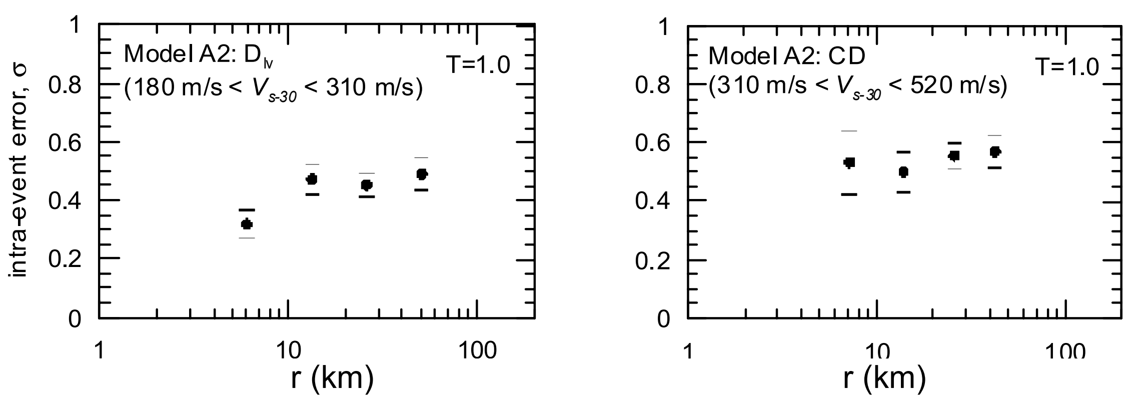

Fig. 4.10(a) Example variations of σ with distance within $V_{s\text{-}30}$ bins, model A2

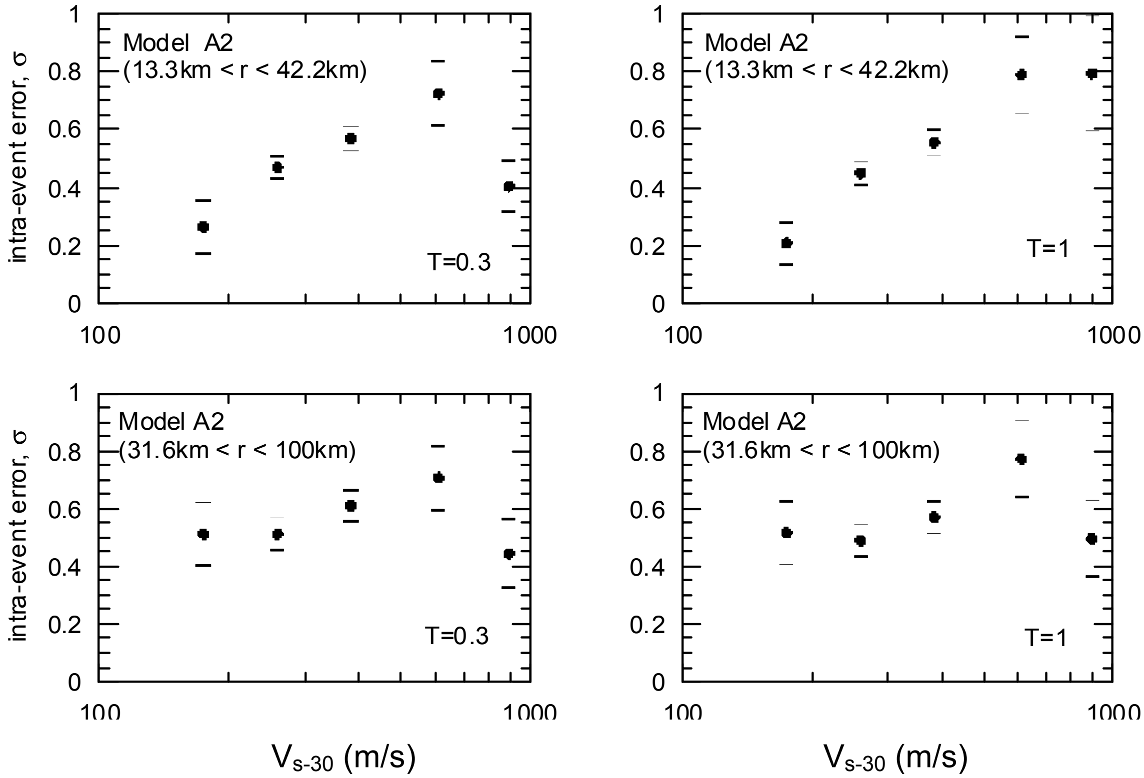

Fig. 4.10(b) Example variations of σ with $V_{s\text{-}30}$ within distance bins, model A2

Based on the above findings, a simple $V_{s\text{-}30}$-dependent model for the intra-event standard deviation is proposed. The standard deviation calculated by this model is denoted "σ_v"; the symbol σ is retained for the overall intra-event standard deviation without consideration of $V_{s\text{-}30}$. In this model, σ_v is taken as constant at low and high $V_{s\text{-}30}$, with log-linear interpolation for intermediate velocities. The threshold velocities were selected after analysis of many plots similar to those in Figure 4.9(b). The model is cast as follows:

$$V_{s\text{-}30} \leq 260 \text{ m/s: } \sigma_v = e_1 \tag{4.5}$$

$$260 < V_{s\text{-}30} \leq 360 \text{ m/s: } \sigma_v = e_1 + e_2 \cdot \ln(V_{s-30}/260) \text{ where, } e_2 = \frac{(e_3 - e_1)}{\ln(360/260)}$$

$$V_{s\text{-}30} > 360 \text{ m/s: } \sigma_v = e_3$$

An example fit based on Equation 4.5 is shown by the line in Figure 4.9(b). Coefficients e_1 and e_3 are evaluated at all periods and are listed in Appendix B. The coefficients are estimated using data from well-populated bins at low and high velocity. The model in Equation 4.5 necessarily smoothes true bin-to-bin variation of σ, but in general the model is not systematically biased high or low across the suite of periods considered for any particular velocity bin. An exception is soft soil sites (i.e., NEHRP E), for which the model tends to overpredict σ at most periods (although, coincidentally, the model provides a good fit for E at T = 0.3 s, 1.0 s, and 3.0 s as shown in Fig. 4.9b). For these soft soil sites, standard deviation is better estimated with site-specific ground response analysis (Baturay and Stewart, 2003), although use of the present model in PSHA will be conservative at the long return periods often used in engineering design.

Smoothed values of τ, σ, e_1, and e_3 are plotted in Figure 4.11. For models A1–A3, while both τ and σ are period dependent, the period dependence of σ_v is dependent on site condition. No significant period dependence is found for relatively soft soils (i.e., e_1 in Fig. 4.11, $V_{s\text{-}30}$ < 260 m/s), but strong dependence is found for stiffer materials (e_3, $V_{s\text{-}30}$ > 360 m/s).

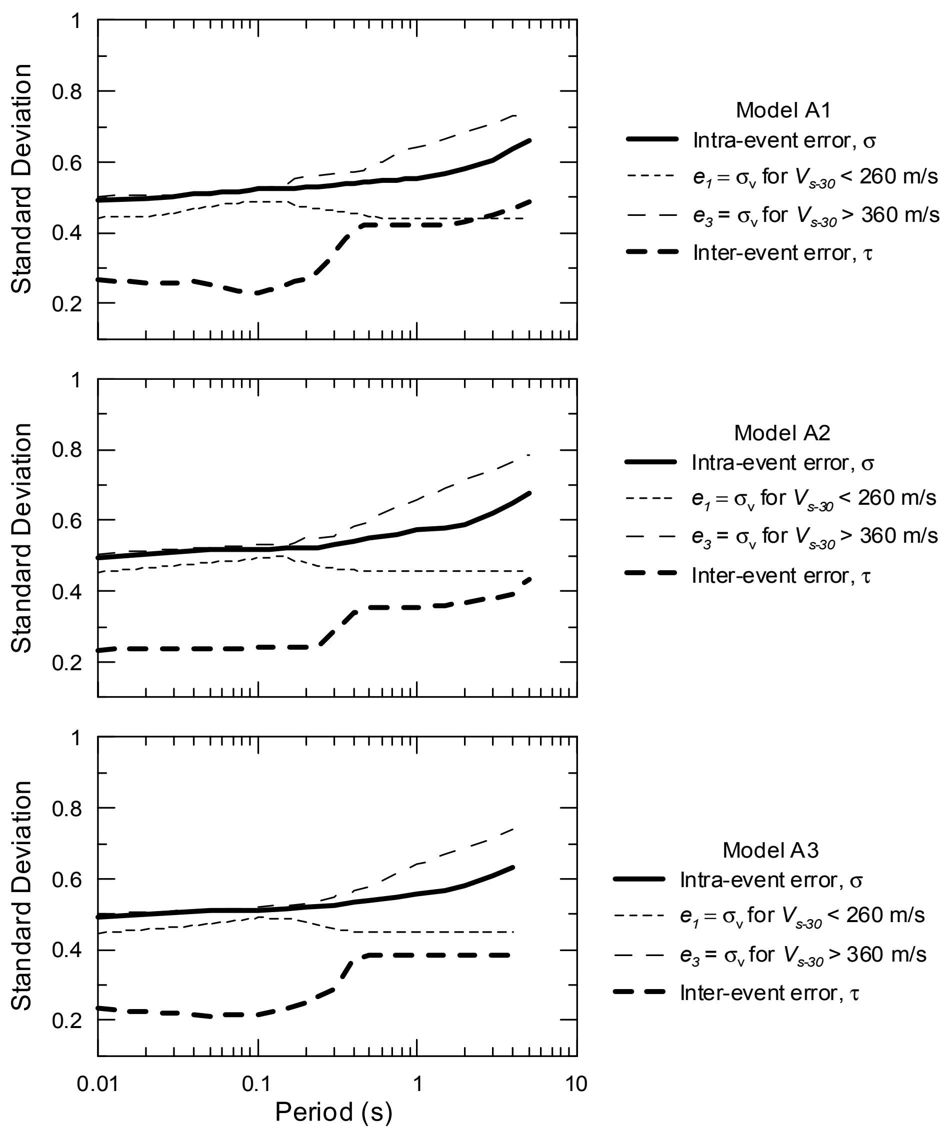

Fig. 4.11 Variation of standard deviation terms with period (models A1–A3) showing strong period dependence of σ for relatively stiff soils but weak dependence for softer soils

4.5 COMPARISONS TO AMPLIFICATION FACTORS BY OTHERS

4.5.1 Velocity Dependence of Amplification

Models A1–A3 regression results from Equation 4.3 are plotted for PHA_r = 0.1 g in Figure 4.12, and are compared to the results of previous studies discussed in Section 4.2. Parameters c and V_{ref} are also compared to those from previous studies in Table 4.3. The slope values c are seen to be comparable to those from previous studies (except Steidl). However, the V_{ref} values for models A1–A3 are significantly smaller than those from other studies, which reflects the relatively soft reference site condition associated with the attenuation relationships used here to develop reference motions. However, models A1–A3 V_{ref} values are generally similar to the $V_{s\text{-}30}$ values compiled by Silva et al. (1997) (median = 520 m/s) and Boore et al. (1997) (average = 620 m/s) from boreholes at rock sites in active regions.

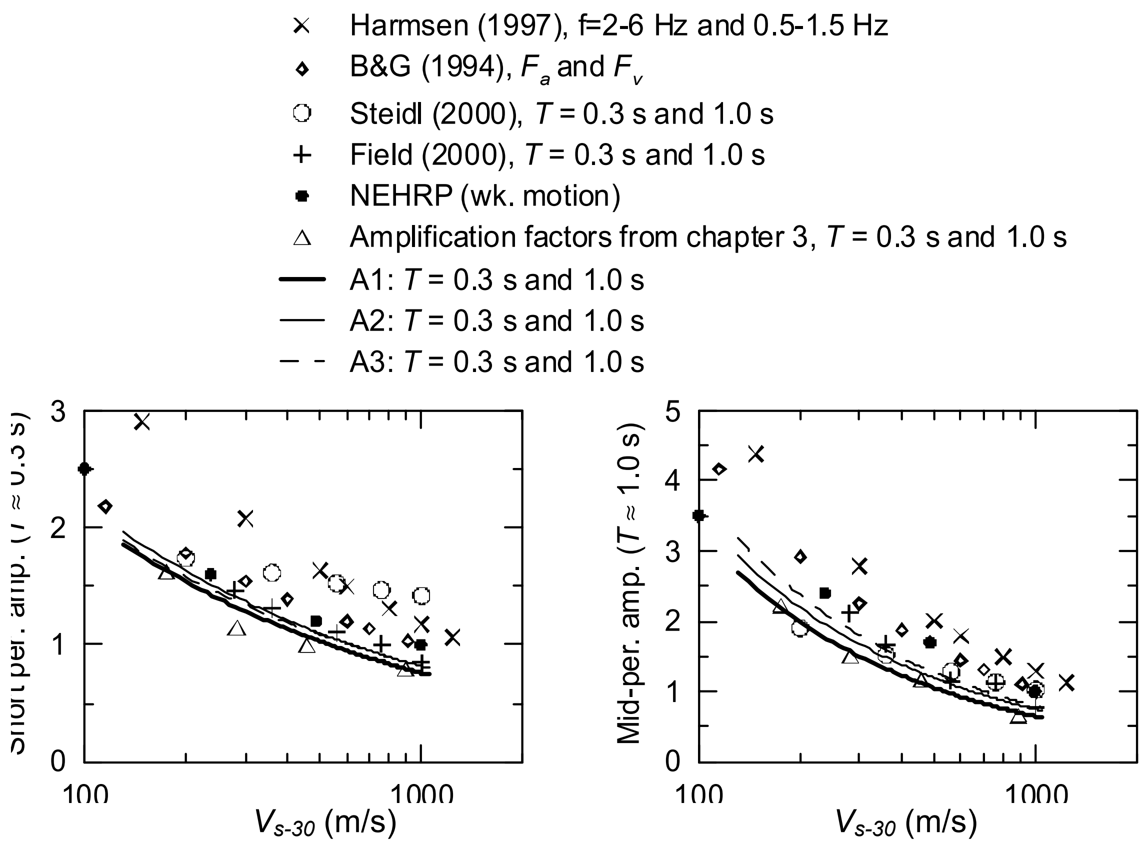

Fig. 4.12 Comparison of $V_{s\text{-}30}$ dependence of *F(0.3)* and *F(1.0)* parameters (evaluated at PHA_r = 0.1g) from this study to short- and mid-period amplification functions from previous studies

Table 4.3 Comparison of power law slope (*c*) and reference velocity (V_{ref}) parameters from this study (unsmoothed) to those from previous work

Parameter		This Study A1[1]	A2[1]	A3[1]	B & G (1994)[2]	Harmsen (1997)[3]	Field (2000)[4]	Steidl (2000)[5]
c	*F(0.3)*	-0.46 ± 0.07	-0.44 ± 0.07	-0.44 ± 0.07	-0.36	-0.56	-0.35	-0.13
	F(1.0)	-0.69 ± 0.07	-0.66 ± 0.08	-0.67 ± 0.07	-0.64	-0.66	-0.70	-0.39
V_{ref}	*F(0.3)*	532 ± 93	601 ± 103	610 ± 106	997	1370	760	--
(m/s)	*F(1.0)*	519 ± 69	646 ± 90	709 ± 107	1067	1140	760	1054

[1] results of present study - before smoothing

[2] results for period range T = 0.1-0.5 s in *F(0.3)* row, results for T=0.4-2.0 s shown in *F(1.0)* row

[3] results for period range T = 0.17-0.5 s in *F(0.3)* row, results for T=0.7-2.0 s shown in *F(1.0)* row

[4] value of V_{ref} preselected as 760 m/s and other regression parameters adjusted accordingly

[5] results for data with PHA < 0.1g, -- = not established

4.5.2 Amplification Levels within NEHRP Categories

In this section the amplification factors within NEHRP categories predicted by models A1–A3 are compared with those utilized within the NEHRP provisions (BSSC, 2001) and those identified by previous investigators. It is necessary to first remove the bias associated with inconsistent reference site conditions before such comparisons can be made.

The regression model in Equation 4.3 enables insight to be developed into the bias associated with the use of a rock-average site condition (in active regions) to represent the intended NEHRP reference condition of V_{s-30} = 760 m/s. This bias can be calculated as follows:

$$\ln B(T) = c \cdot \ln\left(\frac{V_{ref}}{760}\right) \tag{4.6}$$

where *B(T)* indicates bias at period *T*. Equation 4.6 strictly holds only when nonlinearity parameter *b* is the same for velocities of V_{ref} and 760 m/s. While that is generally not strictly true (due to the linear taper in *b* indicated by Eq. 4.1.d), Equation 4.6 nonetheless provides a very good approximation of bias because of the small nonlinearity at these high velocities. At T = 0.3 and 1.0 s, the resulting biases for models A1–A3 are approximately 1.09–1.17 and 1.05–1.28, respectively.

The *B(T)* values are combined with the A1–A3 amplification models to enable comparisons to the site factors in the NEHRP provisions for a consistent reference site condition of V_{s-30} = 760 m/s. Plotted in Figure 4.13 are the NEHRP factors along with the average of bias-adjusted predictions of amplification models A1–A3 over a range of V_{s-30} appropriate to the respective categories. In the averaging across models A1–A3, equal weight was given to each model. The variability between the models in this case is smaller than that shown in Figure 4.6 because of the bias removal, which adjusts all of the models to a common reference velocity of 760 m/s. Also shown in Figure 4.13 are (1) the Borcherdt (2002b) amplification factors, which apply for a slightly stiffer reference site condition of $V_{s\text{-}30}$ = 850 m/s, (2) the results of amplification factors for NEHRP categories in Chapter 3, which have been adjusted to a reference site condition of 760 m/s using the bias adjustment factor in Equation 4.6, and (3) the Joyner and Boore (2000) amplification factors for reference condition $V_{s\text{-}30}$ = 760 m/s.

The bias-adjusted average amplification factors from this study are generally smaller than those given in the NEHRP provisions. For categories B–D, the upper-bound bias-adjusted factors from this study are similar to the NEHRP factors. The nonlinearity represented by the NEHRP factors for categories B–E is generally similar to that for models A1–A3. In the case of category D, the NEHRP nonlinearity appears to coincide with the midrange nonlinearity from the present study. For category E, the bias-adjusted factors from this study are generally comparable to NEHRP at small periods, but are considerably smaller than NEHRP for midperiods.

The offset between these bias-adjusted factors and the NEHRP factors warrants further discussion. The issue is whether the NEHRP factors are conservatively biased. One possible explanation for the discrepancy is that the NEHRP factors, as presently formulated, apply for a site condition stiffer than the intended target of 760 m/s. Recall that the empirical basis for the NEHRP factors is observations from the 1989 Loma Prieta earthquake (corresponding to $PHA_r \approx$ 0.1g). As reported by Borcherdt and Glassmoyer (1994), the velocity at which the amplification function derived from those data is unity is approximately 1000 m/s. This velocity is contradicted somewhat by Borcherdt (2002b), who reports that the average velocity at those sites based on borehole measurements is 795 m/s. Nonetheless, the regressed site amplification model used in the development of the NEHRP factors is unity near 1000 m/s, so that is the effective reference velocity. Thus, the existing NEHRP factors are likely biased for their intended reference site condition of 760 m/s by amounts on the order of ~12% for F_a and ~20% for F_v (based on Eq. 4.6). Accordingly, it appears that a significant portion of the discrepancies observed in Figure 4.13 can be explained by apparent bias in the present NEHRP factors.

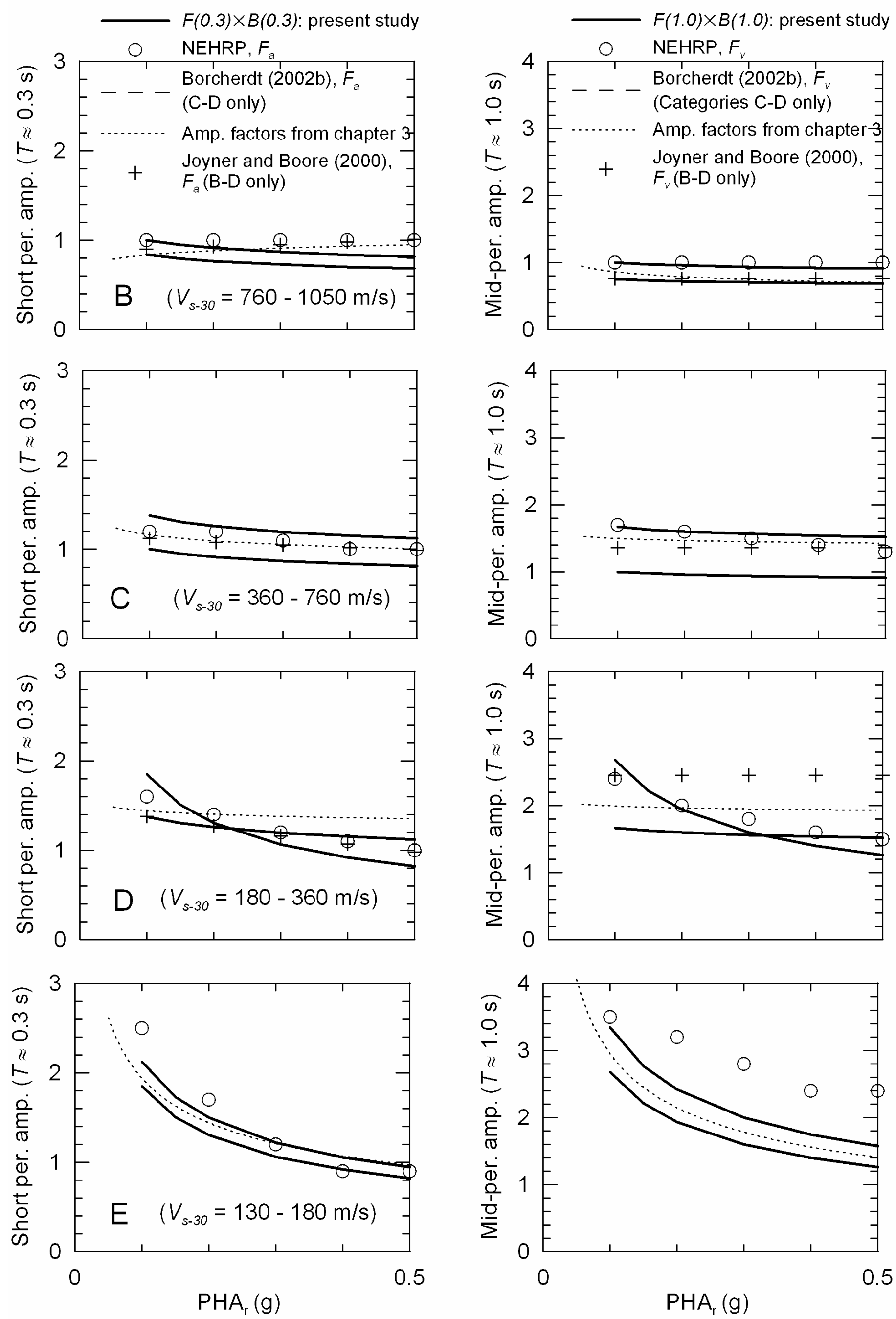

Fig. 4.13 **Comparison of bias-adjusted average amplification factors (reference site condition of $V_{s\text{-}30}$ = 760 m/s) from models A1–A3 for indicated velocity ranges to amplification factors by others, including (1) NEHRP (intended to apply for reference site condition of $V_{s\text{-}30}$ = 760 m/s), (2) Borcherdt, 2002b (reference condition of approximately 850 m/s), (3) amplification factors from Chapter 3, bias adjusted (using Eq. 4.6) to reference condition of $V_{s\text{-}30}$ = 760 m/s, and (4) Joyner and Boore (2000) for reference condition of $V_{s\text{-}30}$ = 760 m/s**

The amplification factors from Borcherdt (2002b) are generally larger than the NEHRP factors and the results of this study. This may be due in part to the stiffer reference site condition of $V_{s\text{-}30}$ = 850 m/s. The amplification factors from Chapter 3 either fall near the middle of the range of velocity-dependent factors from this study (e.g., C, E), or are near the middle of the range at low PHA_r but have different nonlinearity and hence different amplification at high PHA_r (e.g., D). In the case of category D, the category nonlinearity is compatible with the upper end of the velocity range, which, when coupled with a low PHA_r amplification near the middle of the range, provides amplification values that are large at high PHA_r. The amplification factors by Joyner and Boore are generally consistent with the results of the present study except for long-period amplification for category D.

4.5.3 Standard Deviation Terms

Figure 4.14 shows the standard deviation terms calculated in this study along with those proposed in the various attenuation relationships used here. The top frame compares model A1 standard deviation terms to those from the Abrahamson and Silva attenuation relationship. The inter- and intra-event standard deviation terms are plotted separately, and the intra-event terms are separated by site condition. Note that the Abrahamson and Silva terms are magnitude dependent. The standard deviation terms from this study are generally consistent with Abrahamson and Silva, except that model A1 τ is period dependent, and exceeds the Abrahamson and Silva τ for $T > 0.3$ s. The middle frame is based on model A2 and Sadigh et al. (1997) soil attenuation, and shows only the total standard deviation (σ_{total}). The standard deviation from model A2 is generally similar to the Sadigh results for soil. The bottom frame is based on model A3 and the Campbell and Bozorgnia (2003) attenuation, and again shows total standard deviation (σ_{total}). The model A3 standard deviation terms for stiff soils/rock are larger than the Campbell and Bozorgnia terms, whereas the model A3 results for relatively soft soils is consistent with the Campbell and Bozorgnia results.

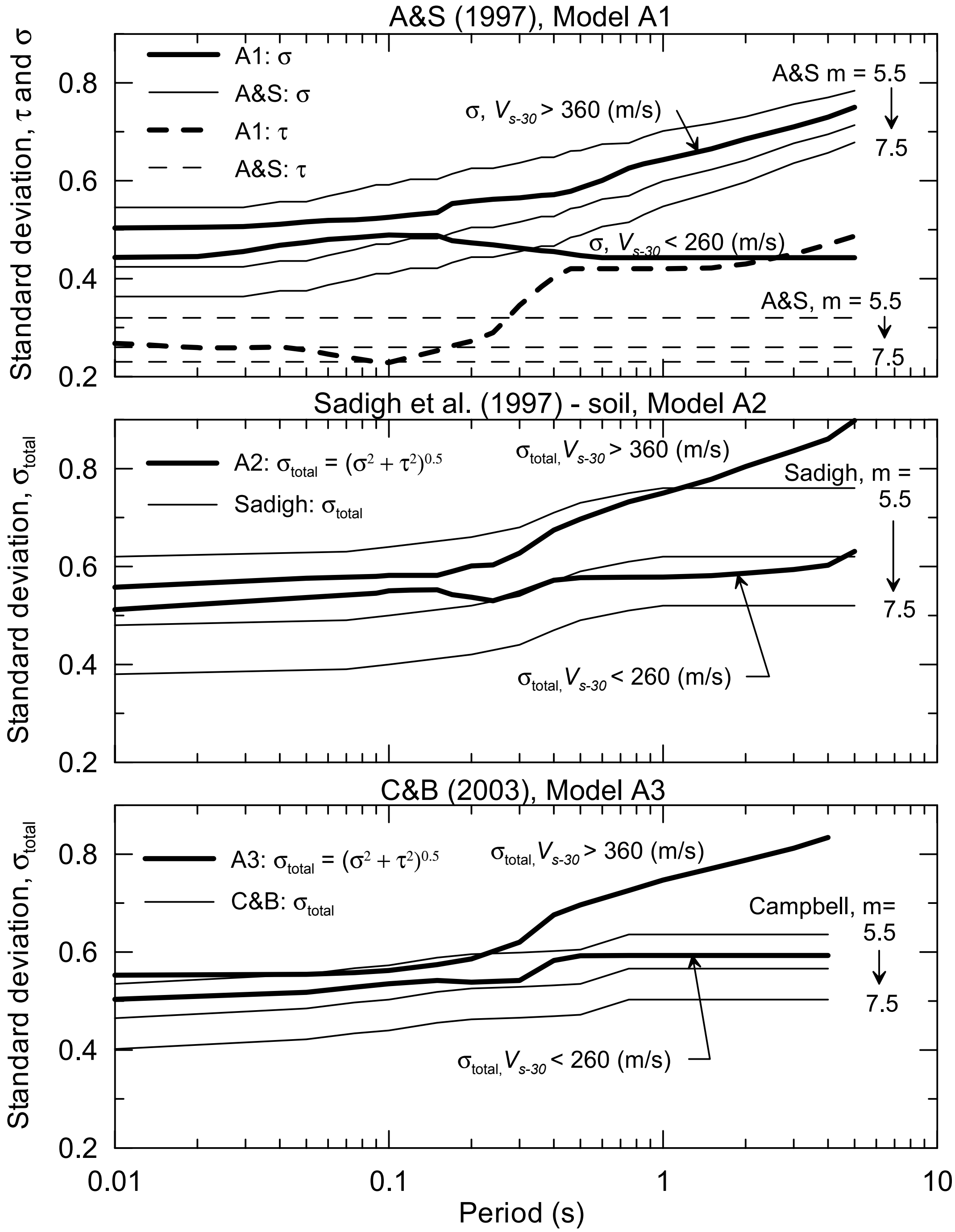

Fig. 4.14 Comparison of error terms from this study to those from attenuation models

4.5.4 Effectiveness of V_{s-30} as Site Condition Metric

In Section 3.4.4, the relative effectiveness of several classification schemes for use in strong motion prediction was assessed by evaluating an intra-event standard deviation term that represents the average prediction dispersion across all categories in each scheme. Since the standard deviation terms were calculated across all categories, they were denoted "intercategory standard deviation (σ_R)."

A scheme is considered to be relatively effective at capturing site-to-site variations in ground motion when σ_R is small, and is less effective when σ_R is large. As shown in Figure 4.15, it was found that detailed surface-geology-based classification schemes are more effective than NEHRP categories (i.e., Table 2.6) or a geotechnical scheme (Rodriguez-Marek et al., 2001). In Figure 4.15, the intra-event standard deviation from this study is compared to those found in Chapter 3. The relatively low standard deviations from this study indicate that with the model proposed herein, the $V_{s\text{-}30}$ site metric is more effective than NEHRP or geotechnical classification schemes at most periods, and roughly equally effective as detailed surface geology.

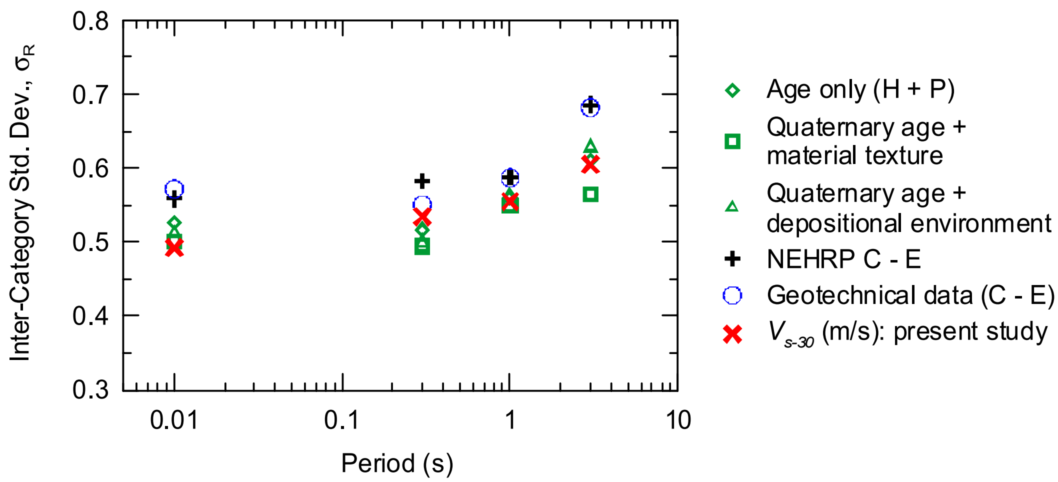

Fig. 4.15 Intercategory standard deviation terms for spectral acceleration, soil categories

4.6 CONCLUSIONS AND RECOMMENDATIONS

In this chapter, a model is developed for ground motion amplification that is a function of $V_{s\text{-}30}$ and PHA_r. The amplification factors are defined relative to "rock" reference motions from several attenuation relationships for active tectonic regions, including those of Abrahamson and Silva (1997), Sadigh et al. (1997), and Campbell and Bozorgnia (2003). Amplification at short- and mid-period ranges is shown to decrease with increasing velocity in a manner similar to trends identified in previous studies. The nonlinearity of amplification factors is found to vary with $V_{s\text{-}30}$, being significant for $V_{s\text{-}30} < 180$ m/s, and relatively small for $V_{s\text{-}30} > 300$ m/s. Standard deviation terms are found to have a significant dependence on $V_{s\text{-}30}$. The databases used in model development cover the parameter spaces $V_{s\text{-}30}$ = 130-1300 m/s and PHA_r = 0.02–0.8g, and the model is considered valid only across that range of parameters.

The model resulting from this work can be used as a site term in empirical attenuation relations, and could be utilized to parameterize site effects in the future development of attenuation relationships. The model is applied by using Equation 4.3 with $V_{s\text{-}30}$ defined from site characterization, PHA_r defined for reference rock conditions using one of the attenuation relationships used here, and b defined per Equation 4.1. Model parameters can be taken from Appendix B for the corresponding attenuation models (i.e., A1—Abrahamson and Silva; A2—Sadigh et al.; A3—Campbell and Bozorgnia). For modeling ground motions during a future earthquake, event term η in Equation 4.3 is generally taken as zero for calculation of the median. The corresponding error term can be taken as σ_{total} from the Appendix B, or for a more accurate assessment, can be evaluated using Equation 4.4 with τ taken from the appendix and σ calculated using the site-dependent model in Equation 4.5 (in which case, σ is denoted "σ_v").

The results of this work provide insight into the accuracy of the site coefficients in the existing NEHRP provisions and commentary (BSSC, 2001). Several important implications of this work are as follows:

1. An entirely different procedure is utilized for evaluating amplification factors than that employed in the development of the current NEHRP recommendations (described in Dobry et al., 2000). In many cases, there are significant discrepancies between amplification factors in this study and those in the NEHRP provisions, with site factors in this study generally being lower. These new results warrant consideration for future versions of the NEHRP provisions and commentary.
2. The standard deviation analysis results provide evidence for $V_{s\text{-}30}$ dependence of intra-event dispersion (σ). For relatively soft materials, σ has no significant period dependency and is relatively low. For stiffer materials, σ is strongly period dependent such that the offset from the soft soil values is small at low periods but reaches values up to 0.3 at long periods. This result suggests a potential for bias in the procedure by which spectral ordinates are evaluated in the NEHRP provisions. In that procedure, design spectral ordinates are calculated as the product of PSHA results and amplification factors. The bias would arise when the dispersion values used in the attenuation relationship for PSHA are different from what is appropriate for the site category.

3. The development of national hazard maps appropriate for the reference site condition of $V_{s\text{-}30}$ = 760 m/s requires the correction of existing attenuation models because the databases used in the development of these models do not share the NEHRP reference site condition. The correction factors for the various attenuation models can be evaluated using Equation 4.6 and the coefficients tabulated in the appendix.

5 Ground Motion Amplification as Function of Basin Geometry

5.1 INTRODUCTION

Many urban regions are situated on deep sediment-filled basins. A basin consists of alluvial deposits and sedimentary rocks that are geologically younger and have lower seismic wave velocities than the underlying rocks upon which they have been deposited (Somerville et al., 2004). Basins have thickness ranging from 100 m to over 10 km. Waves that become trapped in deep sedimentary basins can produce amplitudes up to 50% stronger at intermediate and low frequencies ($f < \sim 1$ Hz) than those recorded on comparable surface materials outside basins, and their significant durations (measured using the Husid plot) can be twice as long (e.g., Graves et al., 1998).

The nonlinear amplification factor models developed in previous chapters are based on characteristics of near-surface sediments. In this chapter, the degree to which additional information on relatively deep basin structures can improve model predictions is investigated. We begin by describing the physical mechanisms for basin response, namely basin edge effects and focusing effects. Results of several large simulation exercises for the southern California region are then presented. The simulated data from a large, recent, multi-investigator simulation exercise are then used to identify several basin geometric parameters that would be expected to correlate to ground motion amplification. Turning next to empirical studies, we first review the outcome of previous research, which has generally found a correlation between amplification and basin depth. Finally, the database described in Chapter 2 is used to evaluate amplification effects with respect to the basin geometric parameters identified from the simulations.

5.2 MECHANISMS OF BASIN RESPONSE

Geotechnical site response analyses are typically based on the distribution of near-surface shear wave velocities (i.e., maximum depths of exploration usually in the range of 20–100 m). The response of this soil layer is usually modeled assuming horizontal soil layering. At frequencies around 1 Hz and less, seismic wavelengths are much longer than typical depths of geotechnical exploration, and their amplitudes are therefore influenced by geological structures having depths of hundreds or thousands of meters that, in many cases, such as in sedimentary basins, are not horizontally layered. The lack of horizontal layering can lead to amplification or de-amplification of seismic waves. Two phenomena that tend to amplify seismic waves are *basin edge* effects and *focusing* effects.

5.2.1 Basin Edge Effects

As illustrated on the left side of Figure 5.1, a wave that enters a horizontal layer may resonate in the layer but cannot become trapped. However, if the wave enters a basin in the direction in which the basin is thickening, and enters the basin through its edge, it can become trapped within the basin if post-critical incidence angles develop. The resulting total internal reflection at the base of the layer is illustrated at the top right of Figure 5.1.

In the lower part of Figure 5.1, simple calculations of the basin response are compared with those for the horizontal layered model. In each case, incident waves are inclined from vertical. The left side of the figure shows the amplification due to impedance contrast effects that occurs on a flat soil layer overlying rock (bottom) relative to the rock response (top). A similar amplification effect is shown for the basin case on the right side of the figure. However, in addition to this amplification, the body wave entering the edge of the basin becomes trapped, generating a surface wave that propagates across the basin. This basin edge effect can amplify long-period components of ground motion and significantly increase the duration of strong shaking.

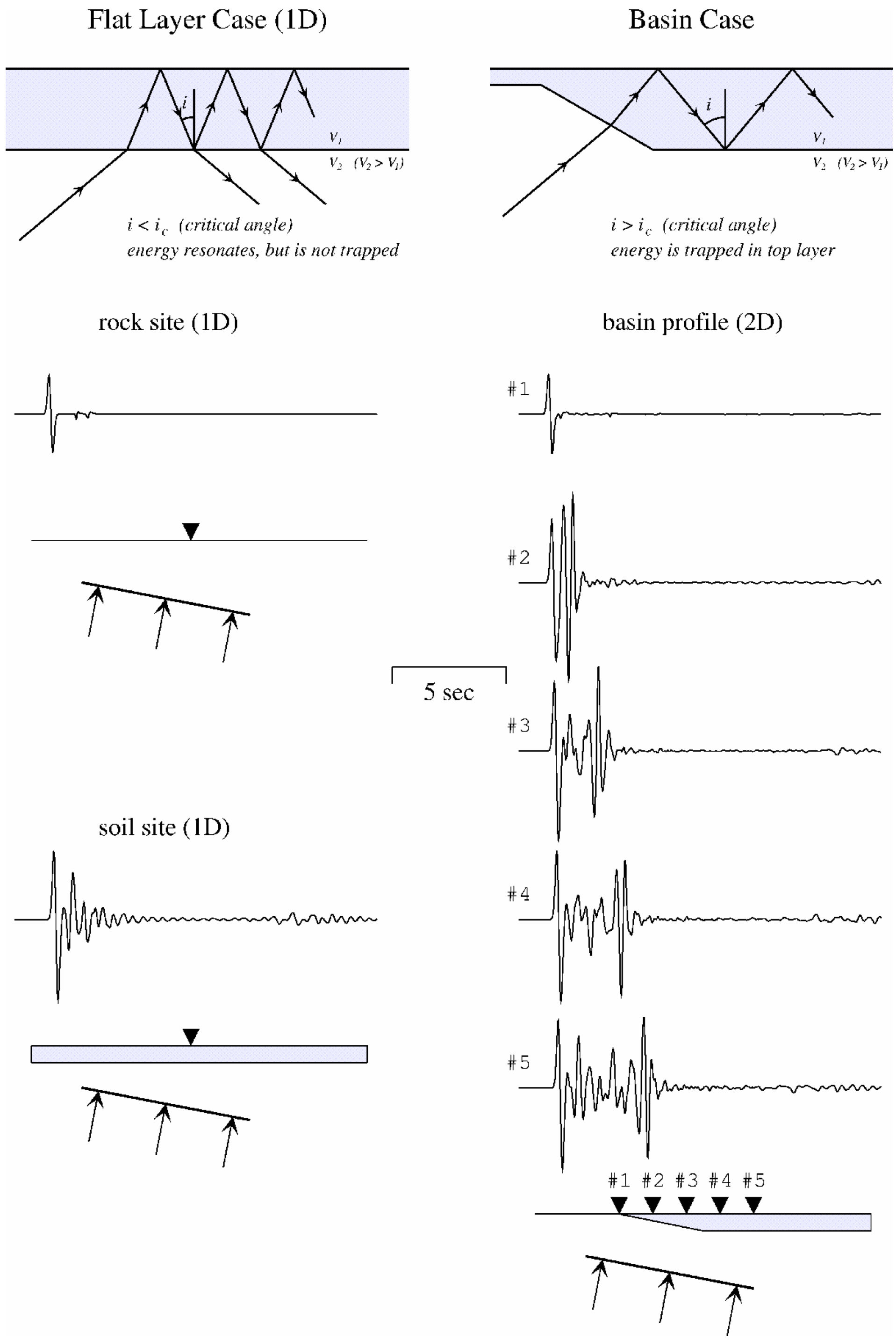

Fig. 5.1 Schematic diagram showing that seismic waves entering a sedimentary layer from below will resonate within layer and escape if layer is flat (left) but become trapped in layer if it has varying thickness and the wave enters layer through its edge (right). (Graves 1993).

A good example of basin edge effects is the ground motions along the south flank of the Santa Monica Mountains and into the Los Angeles basin near Santa Monica during the 1994 Northridge earthquake (Fig. 5.2). The earthquake occurred to the north, beneath the San Fernando Valley, and hence the waves entered the Los Angeles basin through the basin edge in Santa Monica. Figure 5.2 shows strong motion velocity time histories recorded on a profile of stations that begin in the San Fernando Valley, cross the Santa Monica Mountains, and extend into the Los Angeles basin (Graves et al., 1998). The two dashed lines indicate the arrival of shear waves from the two predominant subevents of the earthquake. The time histories recorded on rock sites in the Santa Monica Mountains are brief and are dominated by the direct waves. In contrast, the time histories recorded in the Los Angeles basin have long durations, and the peak velocities are associated not with the direct waves but from later arriving waves generated at the basin edge. Basin edge effects have also been observed in several other earthquakes, including the 1971 San Fernando, California (Hanks, 1975; Liu and Heaton, 1984) and the 1995 Kobe, Japan (Kawase, 1996; Pitarka et al., 1998).

5.2.2 Focusing Effects

Deep geologic structure can sometimes focus seismic waves (like a lens) in spatially restricted areas on the surface, in some cases becoming the dominant factor in the modification of local ground motion amplitudes. Such deep structure may be associated with folds and buried basins within the upper few kilometers of sedimentary basins, or the topography of the underlying sediment/basement interface. Because of the three-dimensional nature of the geologic structure, the amplification patterns are complex and depend on the azimuth of the incident waves.

The damage pattern caused by the Northridge earthquake included pockets of localized damage such as those in Sherman Oaks and Santa Monica that were not clearly correlated with surficial soil conditions (Hartzell et al., 1997). Subsequent tomographic surveys have identified sedimentary structures that appear to correlate with local zones of high ground motion and concentrated damage (Stephenson et al., 2000; Baher and Davis, 2003).

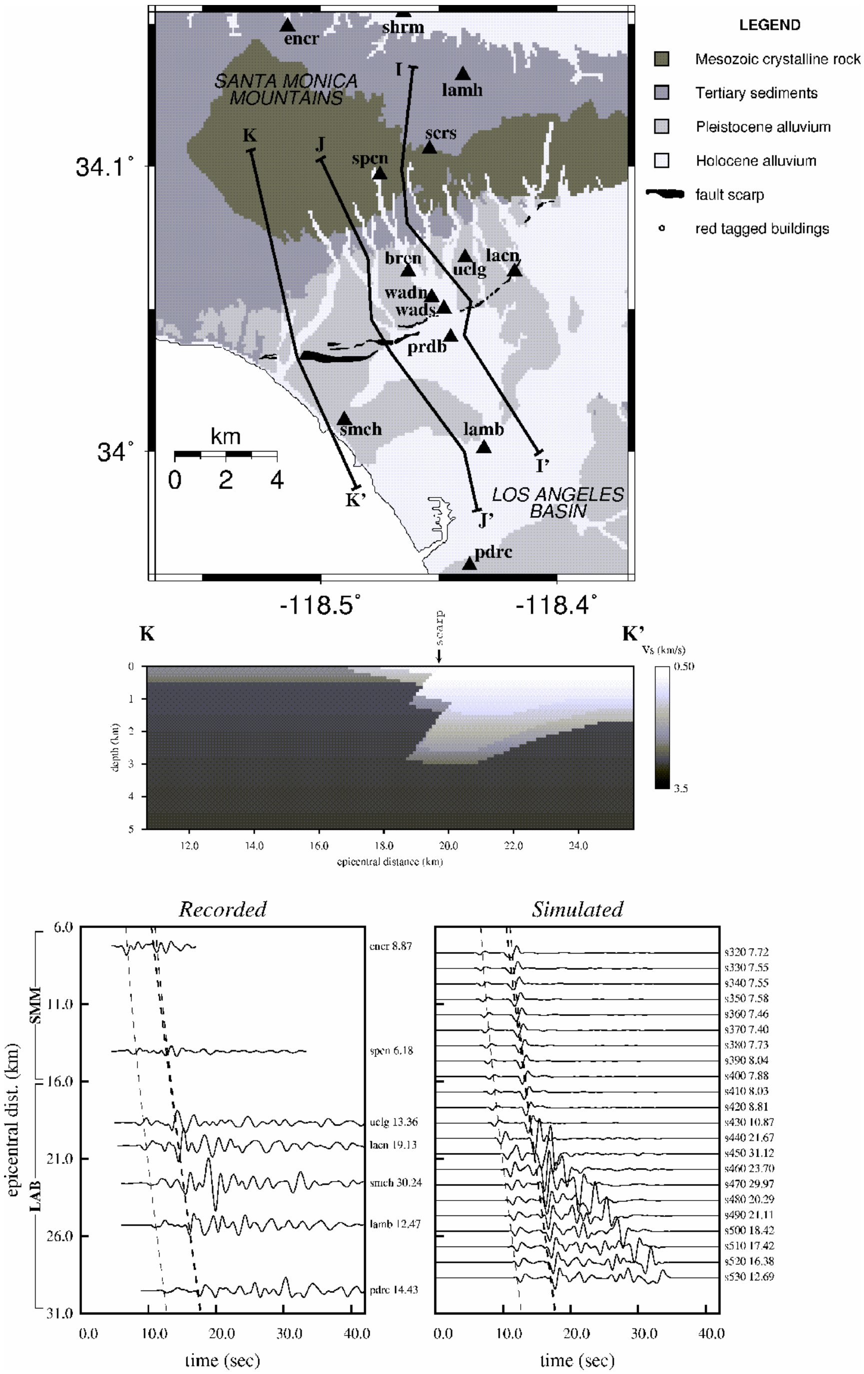

Fig. 5.2 Basin effects in Santa Monica from 1994 Northridge earthquake (Graves et al. 1998)

5.3 SIMULATION OF BASIN RESPONSE

5.3.1 Application of Simulation Procedures to Estimate Basin Response

Numerical simulation analyses for earthquake ground motions can be combined with 3D models for seismic velocity structure in sedimentary basins to predict waveforms. In general, ground motion simulation procedures include models for the seismic source, the wave propagation path from the source to very near the site, and the site response in the near-surface sediments. When basin effects are included in simulations, it is typically incorporated into the second of those models, i.e., the path effect. Path effects are typically simulated with Green's functions, which can be analytical or empirical.

Empirical Green's functions are derived from weak motion recordings at the site of interest, but also require that the seismic source be located in the region of interest (Hartzell, 1978, 1985; Irikura, 1983; Hutchings, 1994). These Green's functions are expected to be fairly realistic because they represent the velocity structure of the real earth. However, the requisite data are rarely available, and hence analytical Green's functions are more widely used.

Analytical Green's functions can be developed for varying degrees of geologic complexity in the region between the source and site. Several stochastic procedures (e.g., Boore 1983; Silva and Lee 1987) use a $1/r_{hypo}$ (r_{hypo} = hypocentral distance) geometrical spreading term that is appropriate for the attenuation of shear waves in a homogeneous medium. Green's functions for more realistic models of layered crust (Helmberger et al., 1992; Olson et al., 1984; Luco and Apsel 1983) are also used. Finite difference or finite element methods can be used to model wave propagation in a complex 2D or 3D earth structure, such as a sedimentary basin. These methods remain computationally intensive and are often limited to long-period (T > ~1 s) calculations.

In the present study, the purpose of examining basin simulation data is to help guide the selection of basin geometric parameters for analysis of the empirical data. The use of empirical data in lieu of simulated data to establish basin amplification factors is desirable because of the simulations' inability to predict high-frequency ground motions (f > 1 Hz) and potential bias in simulated amplification factors resulting from imperfections in the basin models (e.g., Section 2.3.4).

Numerical simulation exercises that have included basin response have been performed for a number of basins including those of Los Angeles, California (e.g.: Hartzell et al., 1999; Olsen, 2000; Komatitsch et al., 2004), Kobe, Japan (Pitarka et al., 1998), San Francisco Marina District, California (Zhang and Papageorgiou, 1996), Salt Lake City, Utah (Olsen and Schuster, 1994; Olsen et al.,1995), and Santa Clara, California (Frankel and Vidale, 1992). Day et al. (2004) have found significant variability in basin simulation results, typically because of numerical errors that had not been found during de-bugging of the computer code. Those errors were later corrected. However, the extent to which the previously published results are affected by such errors is unknown. Accordingly, in the following we focus on a relatively small subset of simulation results for the Los Angeles basin that were derived using codes that have been vetted through a relatively rigorous de-bugging process (Olsen, 2000; Day et al., 2004). The focus on the Los Angeles basin is also motivated by it being the geographic region of principal interest in the present study.

5.3.2 Simulation Results for Southern California Basins

Olsen (2000) performed ground motion simulations to estimate 3D site response effects in the Los Angeles basin for nine earthquake scenarios. The basin model used is essentially the same as that described in Section 2.3.2(a) except that an earlier version was applied (Magistrale et al., 1998). The ground motion simulations were performed for periods $T \geq 2$ s. The simulated ground motions were sampled at regular grid intervals, and were normalized by ground motions predicted by a regional 1D layered rock model (Hadley and Kanamori, 1977) modified for the linear site effect associated with 1D vertical shear wave propagation from rock to the surface. Hence, the estimated amplification levels are associated with the difference between the 3D basin effect and the 1D site effect.

Olsen's nine earthquake scenarios involve the following faults, as shown by the frames in Figure 5.3: Palos Verdes fault (PV), Elysian Park fault (EP), Santa Monica fault (SM), Newport-Inglewood fault (NI), south-east (SAFN) propagating San Andreas fault, north-west (SAFS) propagating San Andreas fault, 1994 Northridge (NR), 1933 Long Beach (LB), and 1987 Whittier-Narrows (WN).

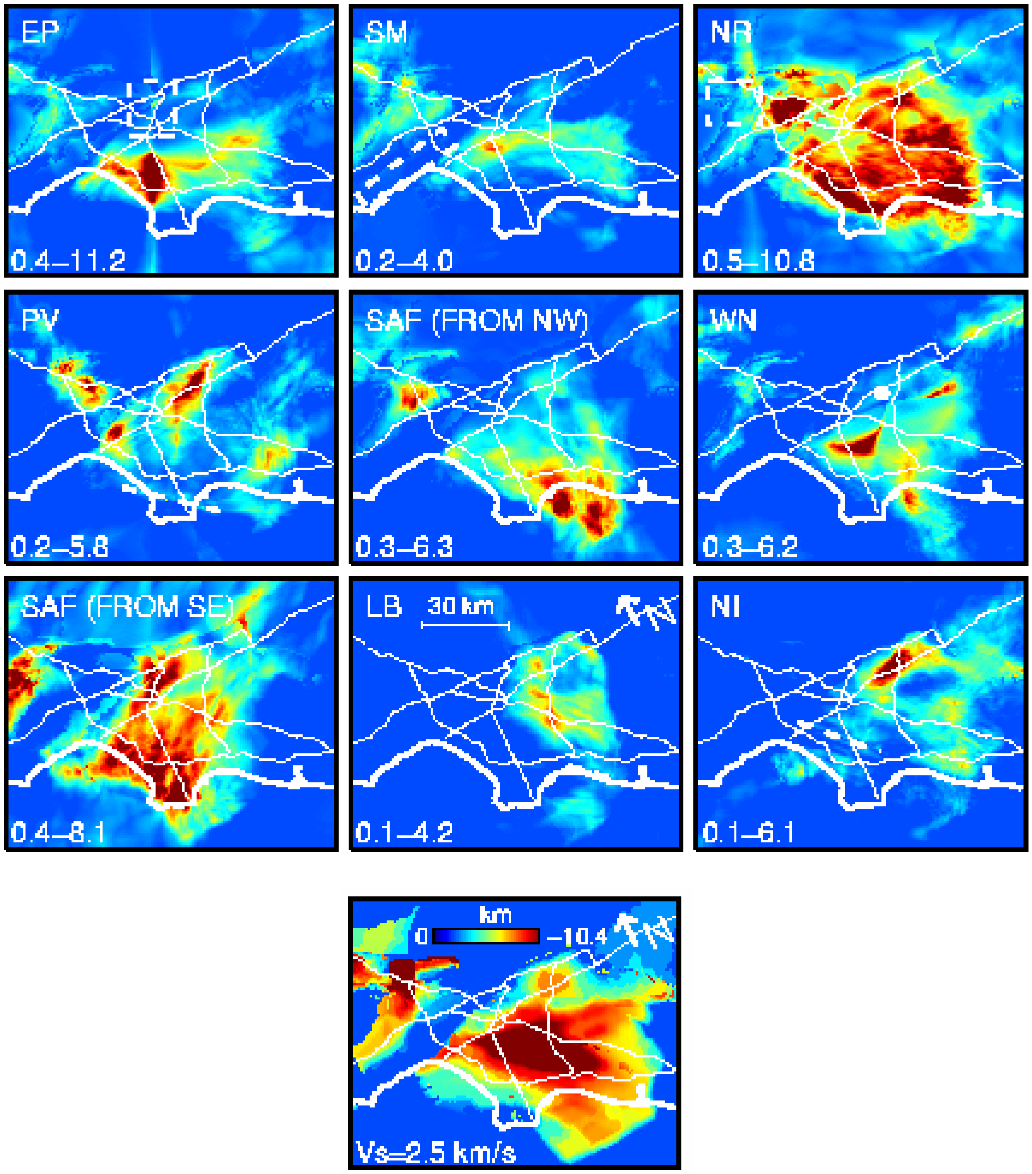

Fig. 5.3 Peak velocity amplification corrected for 1D vertical S wave amplification for nine earthquake scenarios and isosurface for depth to $V_s = 2.5$ km/s (Olsen, 2000). (Thin white lines show major freeways in the Los Angeles area, and thick white lines show coastlines. Dashed lines show surface projections of faults used in this study.)

Olsen's interpretation of the simulation results in Figure 5.3 yielded the following observations:

(a) In general, amplification increases with basin depth, as parameterized by the depth to the 2.5 km/s shear wave isosurface. The trend of amplification with depth from Olsen's simulation results is shown in Figure 5.4.

(b) The pattern and amplitude of the amplification distributions for the nine scenarios vary significantly within the basin area.

(c) Amplification factors tend to be greater for events located outside of basin margins than for events within or along the edge of basins. For example, the NR, SAFS, and SAFN scenarios generally generate larger amplification within the Los Angeles basin than PV, EP, LB, NI, SM, and WN.

(d) Some of the largest amplification occurs above the most steeply dipping basin edges, which results from critical body wave reflections and surface wave generation at basin edges.

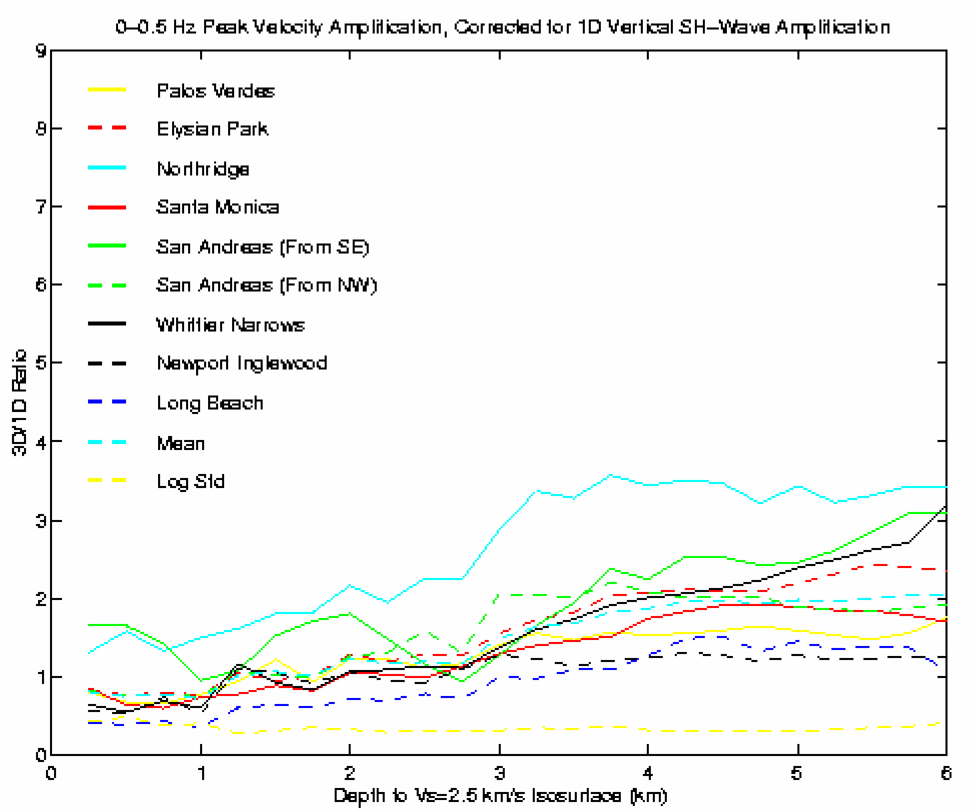

Fig. 5.4 Average peak velocity amplification corrected for 1D vertical S wave amplification and depth to V_s = 2.5 km/s isosurface (Olsen, 2000)

More recent 3D simulations of the Los Angeles and neighboring basins have been performed by a PEER basin simulation working group comprising Steven Day, Robert Graves, Jacobo Bielak, Kim Olsen, Douglas Dreger, Shawn Larsen, and Arben Pitarka. This group performed ground motion simulations using the Magistrale et al. (2000) basin model for the 10 source scenarios shown in Figure 5.5. As shown in Figure 5.6, the output grid consists of 1600 points (2 km spacing) over an 80km × 80 km area. The simulation results are considered valid for T = 2–10 sec. The interpretation of these results to date has focused principally on the basin depth effect, as represented by the 1.5 km/s shear wave isosurface depth. Average depth effects across multiple basins and multiple sources are shown in Figure 5.7. Day et al. (2004) have contrasted the 3D effect in Figure 5.7 with the site effects that would be predicted with 1D wave propagation, which are shown in Figure 5.8. The strong depth-dependent resonances observed in the 1D results are not present in the 3D results.

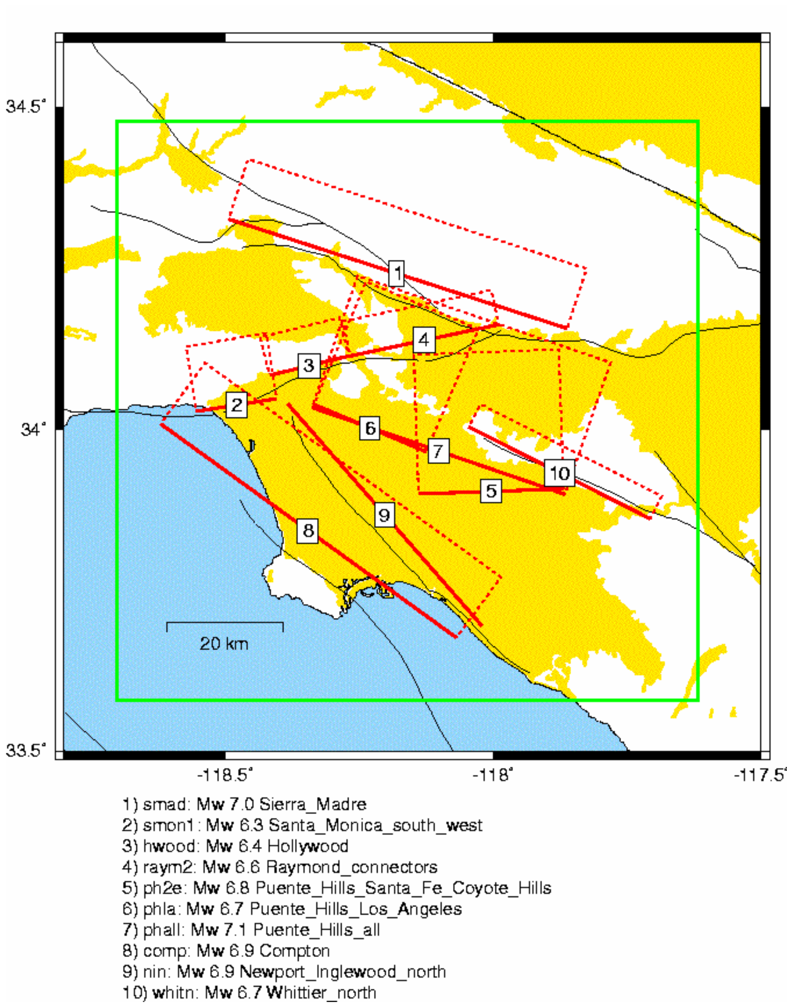

Fig. 5.5 Seismic sources for simulations by working group (Day et al., 2004)

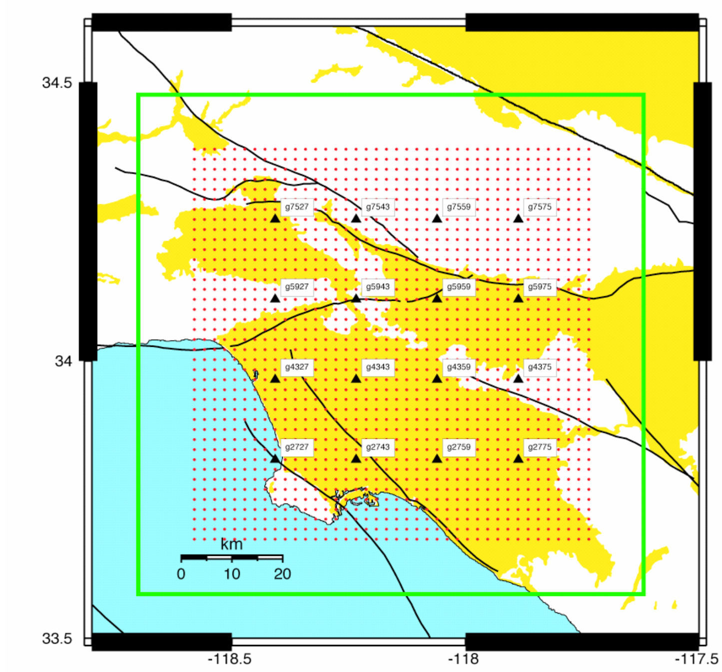

Fig. 5.6 Output grid for simulation by working group (Day et al., 2004)

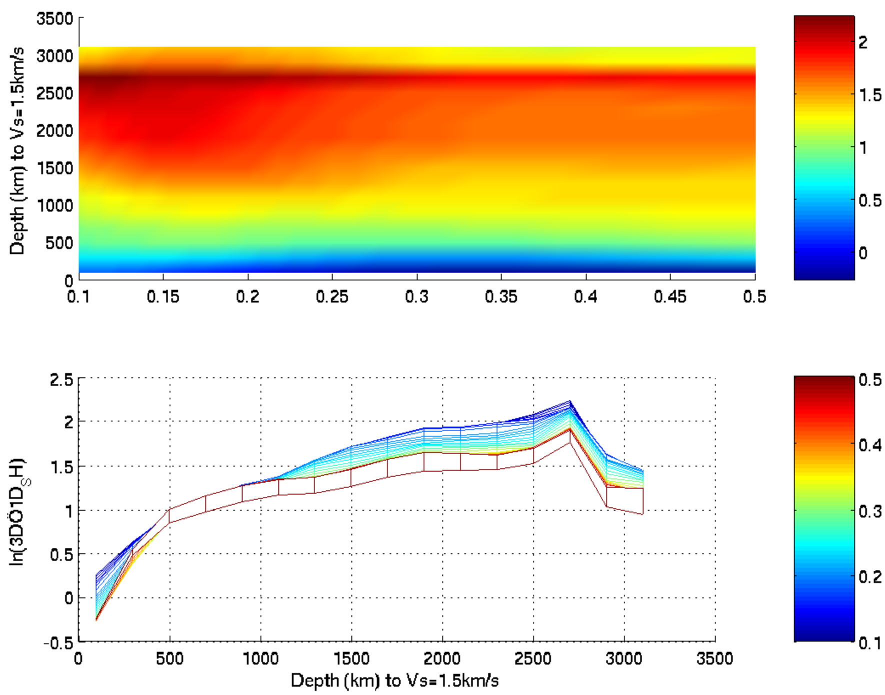

Fig. 5.7 Average depth effect across multiple basins and multiple sources ($3D_{sim}$ $/1D_{Rock\_sim}$) (Day et al., 2004)

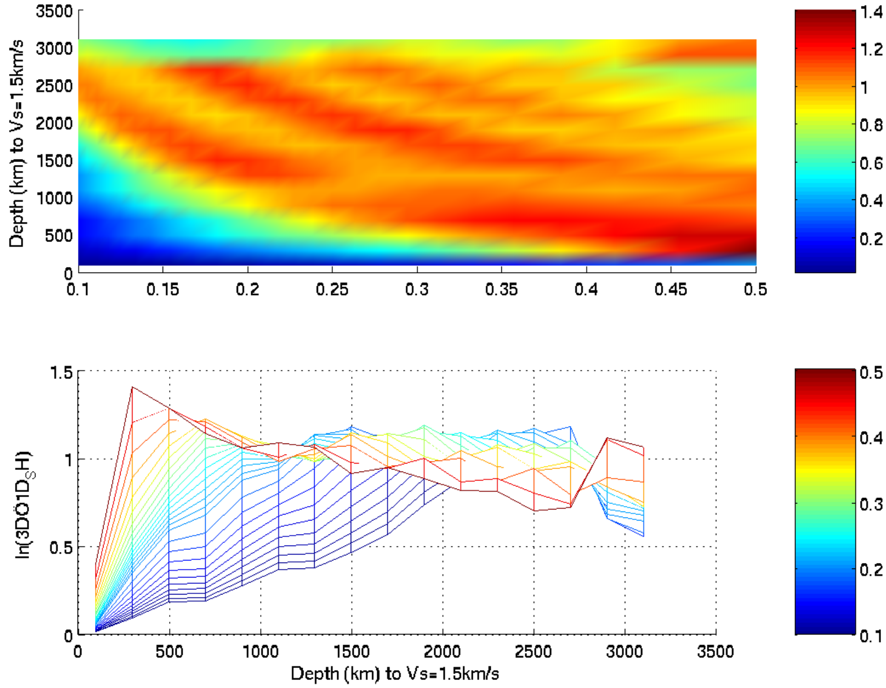

Fig. 5.8 Vertically incident SH-wave response relative to very hard rock (Day et al. 2004)

5.4 ANALYSIS OF SIMULATED GROUND MOTIONS

In this section, the basin analysis results developed by Day et al. (2004) are evaluated. The objective is to examine whether several candidate basin geometric parameters are capable of delineating trends in basin amplification from the simulated data. We first describe the candidate basin geometric parameters and then present statistical analyses of amplification factors relative to those parameters.

5.4.1 Candidate Basin Parameters

Based on the simulation results presented above, the parameters that are considered are listed below along with the rationale for their use:

- *Basin depth (as parameterized to depth to shear wave isosurface)*: Depth parameters have been successfully used in previous empirical studies (see Section 5.5), and have been found to be correlated with average basin effects evaluated from simulations (Figs. 5.4

and 5.7). The specific parameter considered is the depth to the 1.5 km/s shear wave isosurface, which is denoted "$z_{1.5}$." Other depth parameters have been used in previous studies, in particular $z_{2.5}$. However, as shown in Figure 5.9, $z_{1.5}$ and $z_{2.5}$ are strongly correlated and hence effectively contain the same information.

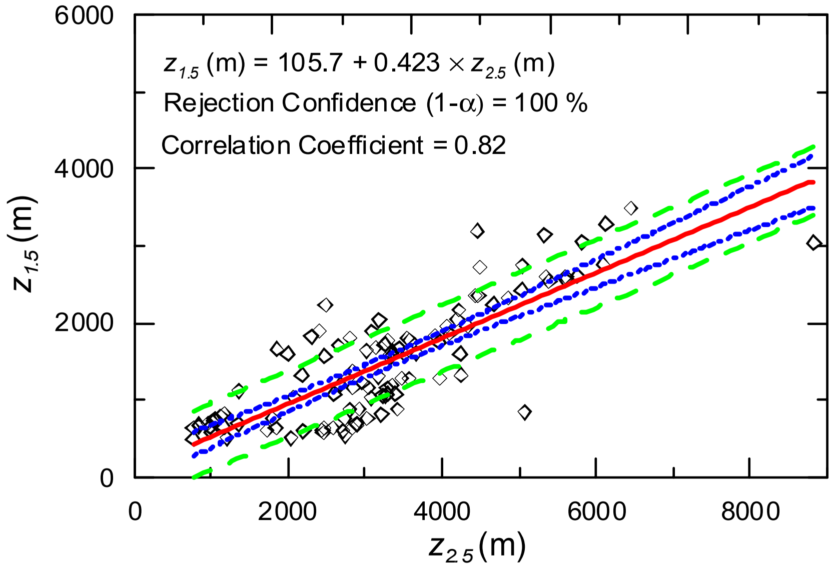

Fig. 5.9 Correlation between depths to 1500 m/s and 2500 m/s shear wave isosurface in southern California basin model of Magistrale et al. (2000)

- *Source and Site Basin Locations*: Events occurring beneath basins will not tend to produce basin edge-generated surface waves. Hence, 3D basin effects would be expected to be less pronounced than for events located outside the basin margin. This is consistent with Olsen's findings (b)–(c) listed in Section 5.3.2. To investigate this potential effect, we distinguish data with coincident source and site basin locations (CBL) from data with distinct source and site basin locations (DBL). Examples of CBL and DBL source-site pairs are given in Figure 5.10. As shown in the figure, establishment of the CBL or DBL designation requires protocols for defining the basin edge and establishing whether a particular source is inside or outside of the basin. The basin boundary is defined as the $z_{1.5}$ = 500 m contour ($z_{1.5}$ < 500 m is outside basin; $z_{1.5}$ > 500 m is inside basin). A source is considered to be inside of the basin margin if the surface projection of any portion of the fault plane lies within or along the edge of the basin boundary.

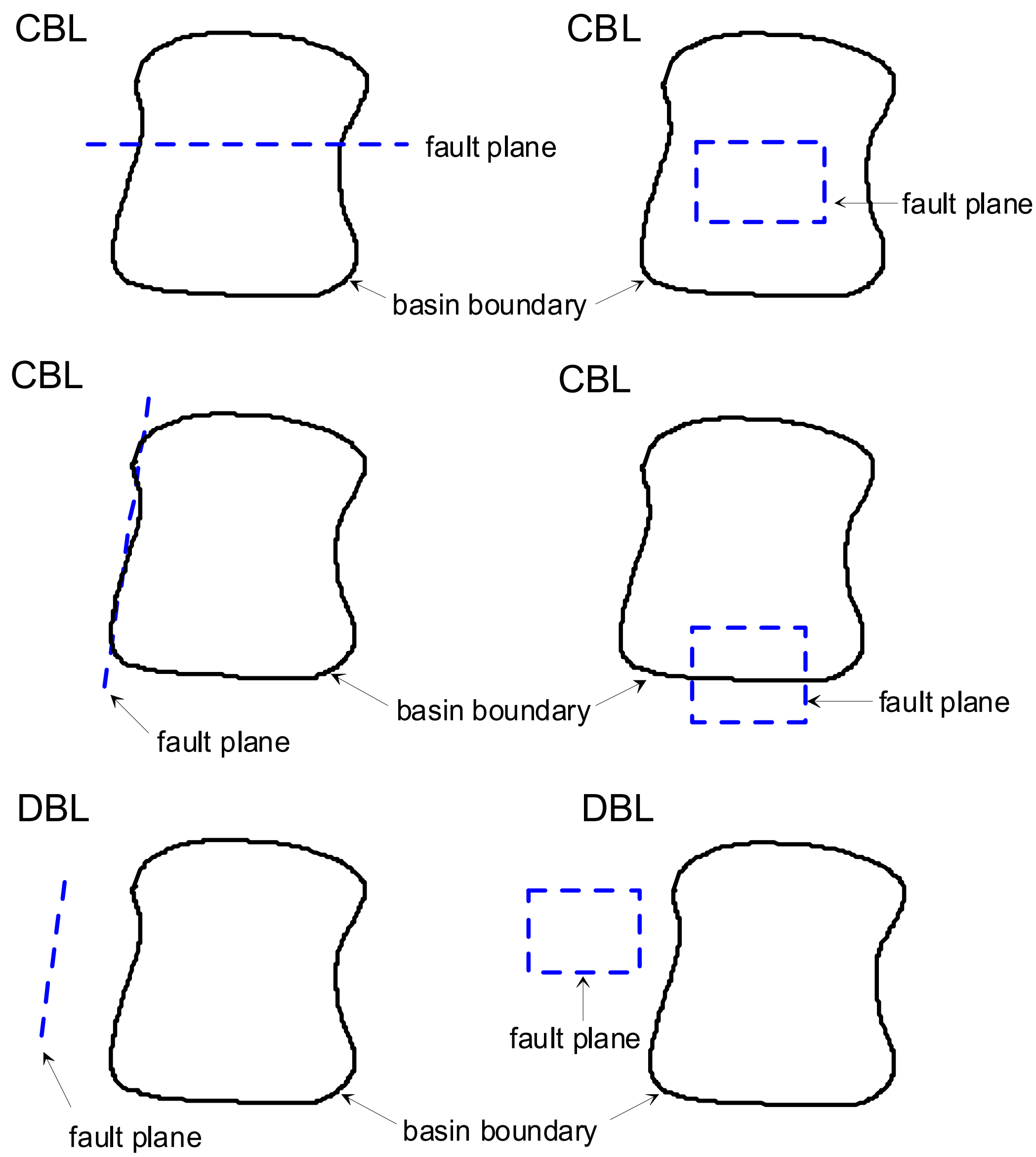

Fig. 5.10 Schematic illustration of coincident and distinct site-source basin locations (CBL and DBL, respectively)

5.4.2 Significance of Basin Parameters Based on Simulation Results

In this section, we evaluate site amplification within basins as a function of the basin geometric parameters introduced in Section 5.4.1. The analyses are performed using the simulated data described in Section 5.3. As noted previously, the simulated ground motions are computed at 1600 locations shown in Figure 5.6 for the earthquake sources depicted in Figure 5.5. Each simulated ground motion consists of three waveforms in two horizontal directions and the vertical direction. We utilize two separate suites of calculated waveforms—one being simulations that include the 3D basin geometry in the analysis of Green's functions (denoted "3D_sim"), the second being simulations that utilize a 1D layered rock model (denoted "1D_rock_sim").

Response spectral accelerations (at 5% damping) are calculated for the two horizontal waveforms at each "site" (Day et al., 2004). The geometric means of the horizontal spectral accelerations are denoted as "$(S_a)_{3D\_sim}$" and "$(S_a)_{1D\_rock\_sim}$" to distinguish the simulation results corresponding to the respective sets of Green's functions. Amplification factors associated with basin effects are then calculated as

$$AF = \frac{(S_a)_{3D\_sim}}{(S_a)_{1D\_rock\_sim}} \tag{5.1}$$

where AF = amplification factor, which is evaluated at periods of 2, 3, 4, and 5 sec. With 1600 sample locations and 10 sources, there are a total of 16,000 amplification factors in the simulated data set.

As shown in Figure 5.11, the variation of amplification factors with basin geometry is investigated by plotting the amplification factors as a function of basin depth for bins of data with coincident source and site basin locations (CBL) and distinct source and site basin locations (DBL). The trends in Figure 5.11 suggest different slopes in the $z_{1.5}$-AF data across different depth ranges. Accordingly, for each of the CBL and DBL data groups, bilinear regression analyses are performed according to

$$\ln(AF_i) = a_1 + a_2 \cdot (z_{1.5i} - d) + a_3 \cdot (z_{1.5i} - d) + \varepsilon_i \tag{5.2 a}$$

$$z_{1.5} < d: \qquad a_2 \neq 0 \qquad a_3 = 0 \tag{5.2 b}$$

$$z_{1.5} > d: \qquad a_2 = 0 \qquad a_3 \neq 0 \tag{5.2 c}$$

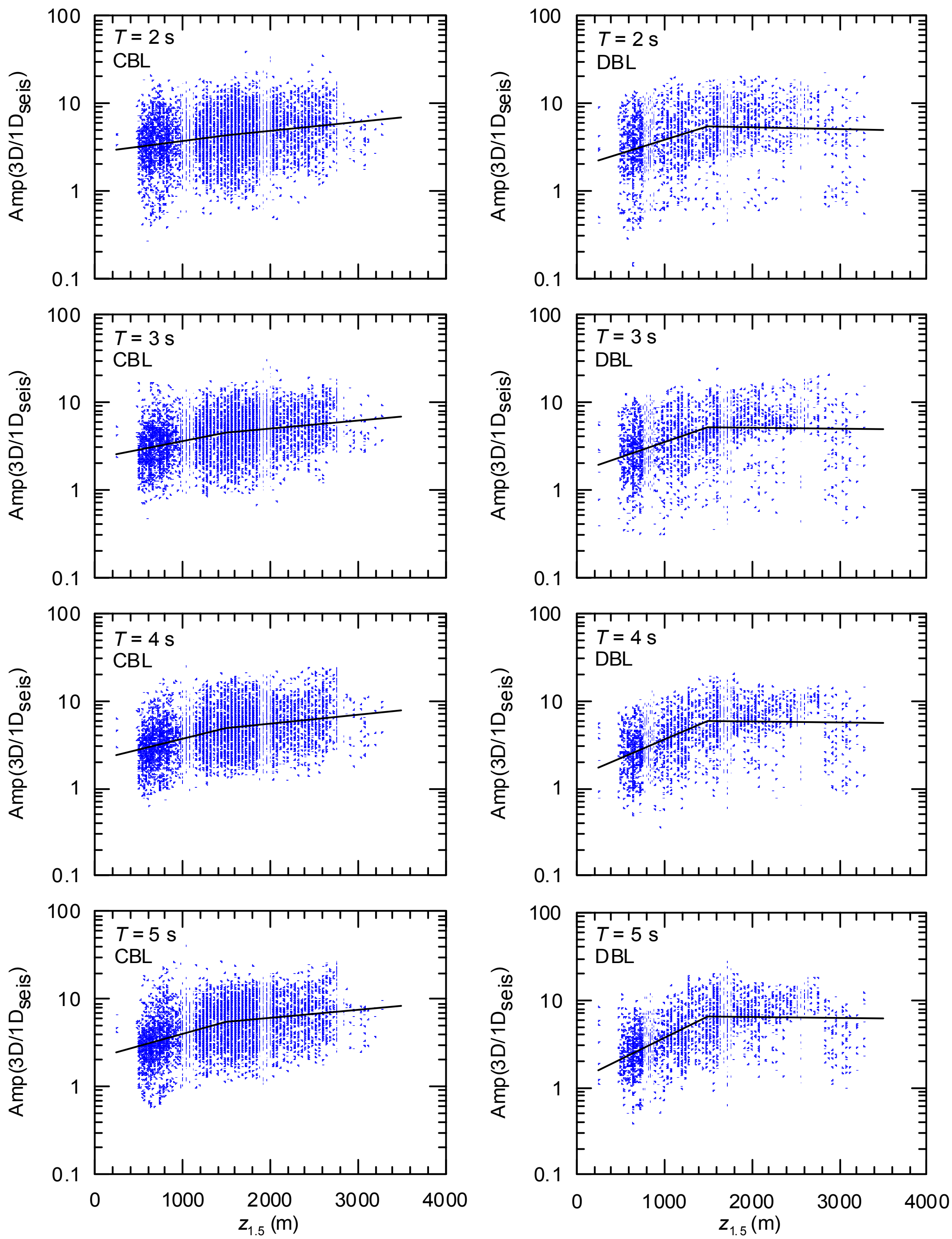

Fig. 5.11 Bilinear regression results along with data (i.e., amplification factors calculated using Eq. 5.1)

where, a_1, a_2, and a_3 are regression coefficients specific to the CBL and DBL data groups, $z_{1.5i}$ is depth in meters to the 1500 m/s shear wave isosurface for data point i, d = depth of intersection point in meters (i.e., depth at which slope-change occurs), and ε_i = residual between data point i and fit line.

Parameter d is relatively poorly constrained when established directly from regression analyses (i.e., the standard deviation of regression results is not sensitive to d in the range of 1100–2000 m). Hence, d was selected by judgment to be 1500 m, which provides a good visual fit to the data and avoids the occurrence of significant negative slopes for $z_{1.5} > d$ (i.e., maintains $a_3 \geq 0$).

Regression coefficients calculated using Equation 5.2 are presented in Table 5.1, and the resulting bilinear fit is superimposed on the data in Figure 5.11. Also shown in Table 5.1 are the results of hypothesis tests, which consist of compiling sample "t" statistics to test the null hypothesis of zero slope. This statistical testing provides a significance level = α that the null hypothesis cannot be rejected. For clarity of expression, we tabulate in Table 5.1 values of 1-α, which we refer to as a "rejection confidence" for a zero slope model. Large rejection confidence levels (i.e., > 95%) suggest significant depth dependence of amplification factors.

Table 5.1 Bilinear regression results

Category	Period (sec)	a_1	a_2	a_3	σ	Rejection confidence for a_2=0 (%)	Rejection confidence for a_3=0 (%)
CBL	2.0	1.5	3.1E-04	2.4E-04	0.63	100	100
	3.0	1.5	4.3E-04	2.3E-04	0.53	100	100
	4.0	1.6	5.6E-04	2.4E-04	0.54	100	100
	5.0	1.7	6.4E-04	2.3E-04	0.56	100	100
DBL	2.0	1.7	7.1E-04	-4.7E-05	0.74	100	71
	3.0	1.6	7.7E-04	-1.2E-05	0.68	100	24
	4.0	1.8	9.8E-04	-2.6E-05	0.59	100	54
	5.0	1.8	1.1E-03	-6.4E-06	0.56	100	15

Note: d is fixed as 1500 m

A direct comparison of the regression results for the CBL and DBL cases is presented in Figure 5.12. The results in Figure 5.12 and Table 5.1 indicate statistically significant depth dependence of amplification factors for the CBL data group across the full range of depths considered, but no significant depth dependence for $z_{1.5} > d$ in the DBL group. This is reflected by the hypothesis test results, which show high rejection confidence for zero slope models for all cases except DBL parameter a_3.

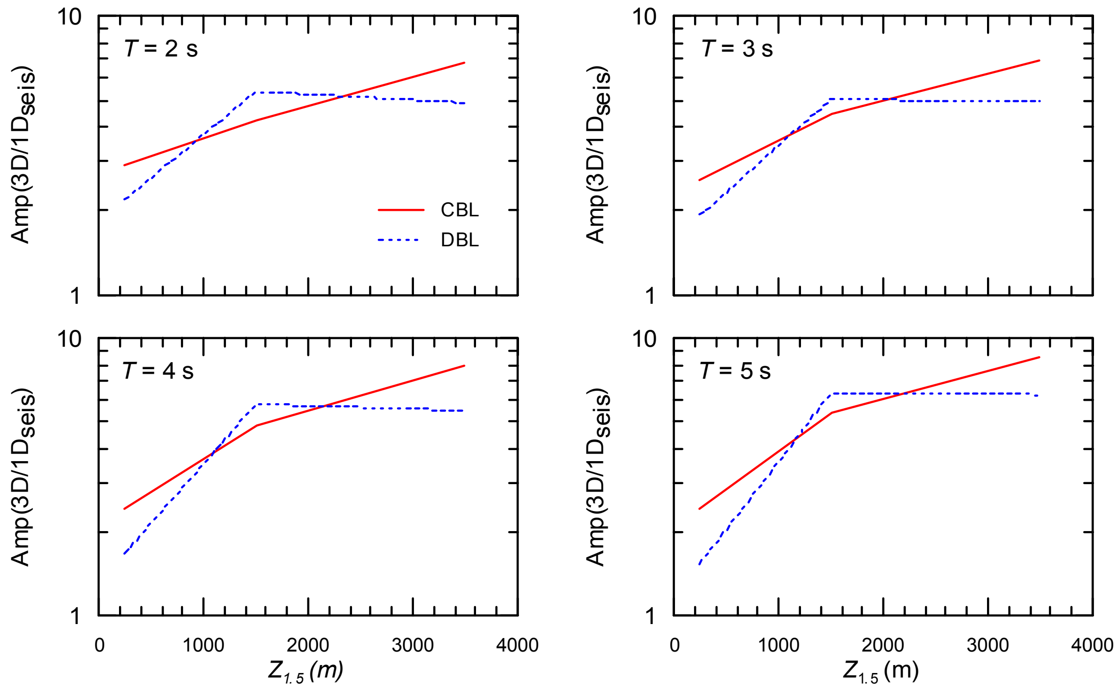

Fig. 5.12 Bilinear regression results

We speculate that the reason for the stronger depth dependence for the CBL data relative to the DBL data is the different mechanisms of basin response. In the CBL case, waves enter the basin from beneath as illustrated in Figure 5.13, and critical body wave reflections would not be expected to occur. This wave propagation problem is similar to classical 1D wave propagation, which has long been recognized as producing depth-dependent ground motion amplification (Seed et al., 1974; Ni et al., 1997; Chang and Bray, 1998; Silva et al., 1999; Hashash and Park, 2001, Luke et al., 2001; Salvati et al., 2001). On the other hand, in the DBL case seismic body waves enter the basin in the manner depicted on the right side of Figure 5.1, and as described in Section 5.2.1, this can lead to critical body wave reflections and surface wave propagation across the basin. The simulation results suggest that these basin edge-generated surface waves have amplitudes that are not particularly sensitive to basin depth (especially for $z_{1.5} > 1500$ m).

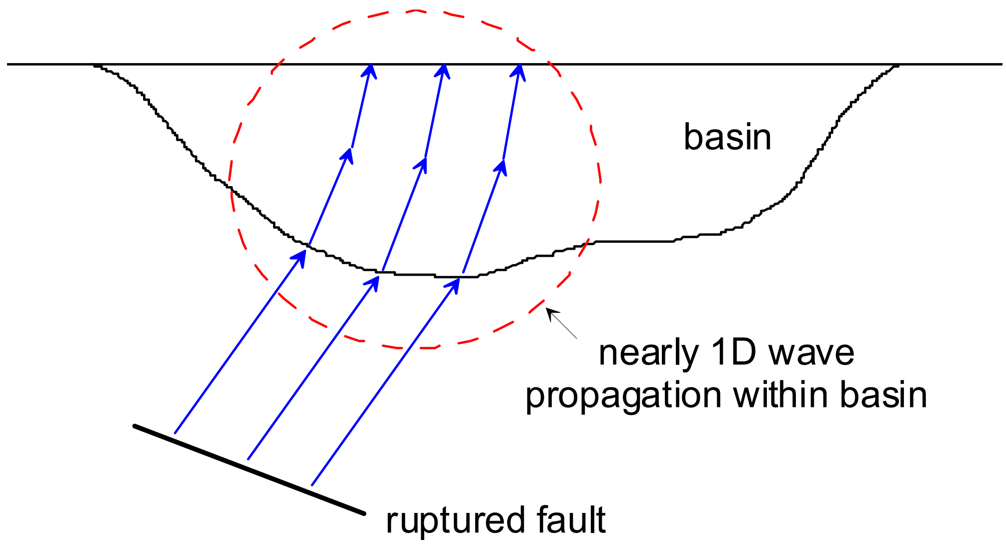

Fig. 5.13 Schematic illustration of seismic body waves entering basin from underlying seismic source

To evaluate the significance of the distinction between the CBL and DBL data groups, statistical F-tests were performed (Cook and Weiberg, 1999). The F test operates on submodels (in this case, the regression results for the CBL and DBL data sets) and produces an F statistic that can be compared to the F distribution to evaluate a significance level (p) for the test. Large values of p (e.g., $p > 0.05$) are taken to imply that the submodels are not distinct. The results are shown in Table 5.2 for the four periods considered—the p values are seen to be small, indicating distinct CBL and DBL submodels.

Table 5.2 F-statistics indicating distinction between depth-amplification regression models for CBL and DBL data groups

	T = 2 s		*T* = 3 s		*T* = 4 s		*T* = 5 s	
	F	p	F	p	F	p	F	p
CBL & DBL	21.75	0.00	21.12	0.00	33.29	0.00	45.43	0.00

5.5 PREVIOUS EMPIRICAL STUDIES

Major previous efforts to quantify basin effects through analysis of strong ground motion data include early studies by Trifunac and co-workers and Campbell and co-workers, a series of studies by researchers affiliated with the Southern California Earthquake Center (SCEC), and recent studies by Somerville et al. (2004) and Hruby and Beresnev (2003).

5.5.1 Early Studies

The first investigators to develop empirical models of site effects that include a sediment depth term were Trifunac and Lee (1978) and Westermo and Trifunac (1978). Depth terms were evaluated as "differences in elevation between the ground surface and the contact of alluvium and sedimentary layers with crystalline basement rock" (Westermo and Trifunac, 1978). Because of the limited quality of available data on sediment profiles, it was acknowledged that "considerable judgment and oversimplification were required before each station could be assigned a depth parameter." Nonetheless, attenuation models for Fourier spectral amplitude were developed in which spectral shape was significantly sensitive to sediment depth for periods ≥ 1.0 s (Trifunac and Lee, 1978).

Campbell (1997) developed attenuation relations for response spectral acceleration that included a depth term. Depth was defined to the top of Cretaceous or older deposits. For deep sediments, depth was determined from crustal velocity profiles where basement was defined as crystalline basement rock or sedimentary deposits with p-wave velocities ≥ 5 km/s or s-wave velocities ≥ 3 km/s. The empirical model is significantly sensitive to depths between about 1.0–5.0 km for periods ≥ 0.3 s. Long-period spectral accelerations were found to increase with depth.

5.5.2 SCEC Studies

The SCEC studies used a southern California strong motion database (Steidl and Lee, 2000) and the 3D seismic velocity model of southern California by Magistrale et al. (2000) (described in Section 2.3.2a). Using those databases, independent empirical analyses of basin effects were performed by Field (2000), Lee and Anderson (2000), Steidl (2000), and Joyner (2000).

Field (2000) used a random-effects regression procedure to customize the attenuation relationship of Boore et al. (1997) based on the southern California database of Steidl and Lee (2000). The Field attenuation model includes a site term that is a linear function of $V_{s\text{-}30}$. Using this attenuation model, Field examined the dependence of inter-event corrected residuals on basin depth, defined as depth to the 2500 m/s shear wave isosurface. As noted by Field, the use of inter-event corrected residuals in lieu of the residuals themselves is important so that event-specific bias in the data (usually associated with anomalous source effects) are not mapped into site terms. As shown in Figure 5.14, residuals were found to be significantly correlated to basin depth for peak horizontal acceleration (PHA) and spectral accelerations at 0.3, 1.0, and 3.0 s. The dependence of residuals on basin depth was considered to be statistically significant for each period. Field noted that sites near the center of the Los Angeles basin (about 6000 m depth) exhibited 1.0 s spectral accelerations that were up to a factor of two greater than sites near the edge.

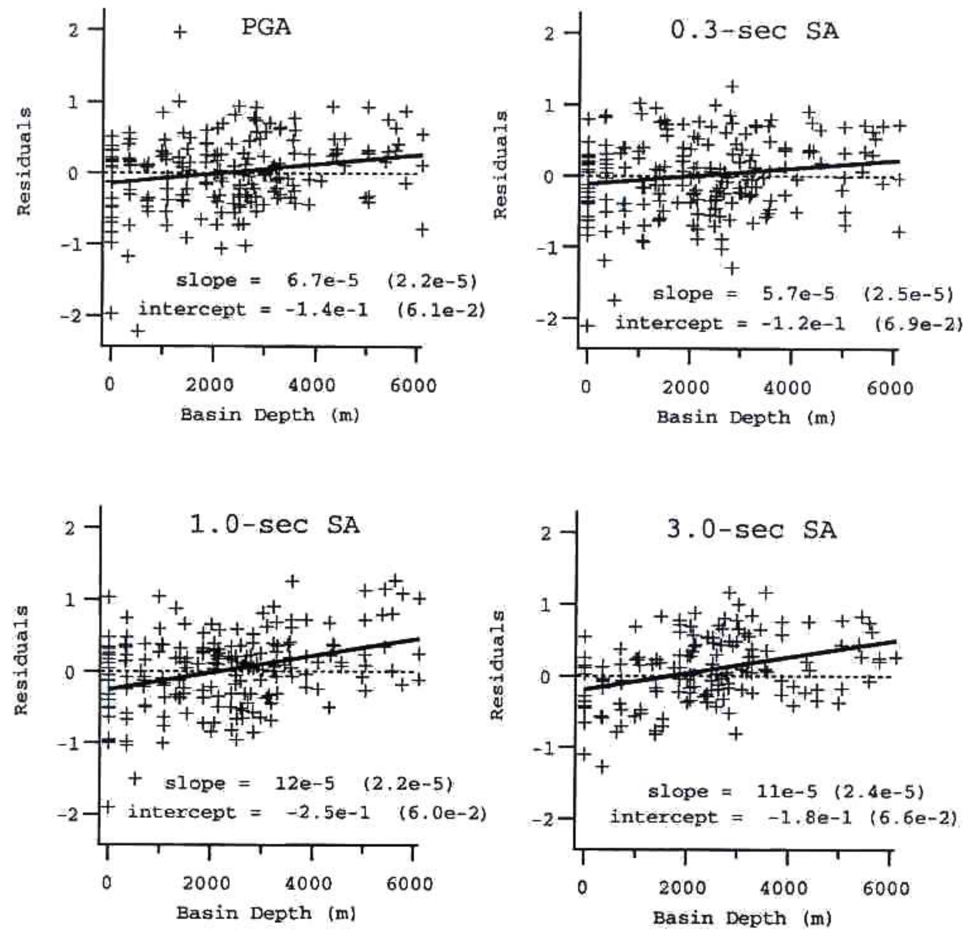

Fig. 5.14 Residuals versus basin depth (depth to V_s = 2.5 km/s isosurface). The values listed in parentheses are one-sigma uncertainties (Field, 2000).

The approach by Steidl (2000) was similar to that of Field (2000) except that the rock attenuation relationship of Sadigh et al. (1993), modified with surface-geology-based amplification factors, was used to calculate the residuals without inter-event corrections. The basin amplification factors were derived as a function of the depth to 2500 m/s shear wave isosurface. As shown in Figure 5.15, Steidl found the residuals to increase with basin depth across the period range of PHA (written as PGA in figure to 3.0 s), although the slope of the fit lines are generally less than half of the values by Field (2000).

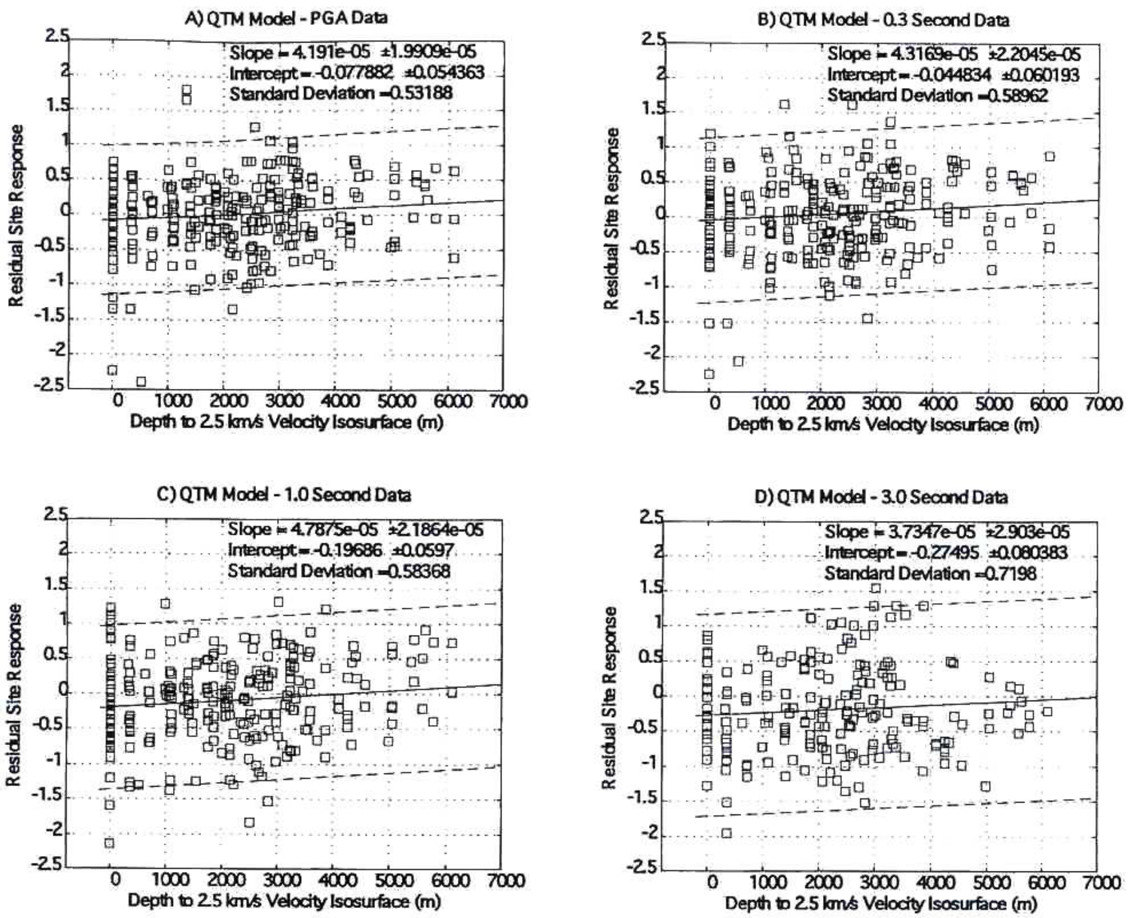

Fig. 5.15 Residual site response with respect to average QTM (Quaternary-Tertiary-Mesozoic) amplification factors plotted versus basin depth. Least-squares fit to residuals plotted as solid line with slope and intercept shown. (a) PGA, (b) 0.3 sec period, (c) 1.0 sec period, (d) 3.0 sec period (Steidl, 2000).

Lee and Anderson (2000) examined inter-event corrected residuals between data and predictions from the Abrahamson and Silva (1997) soil attenuation relationship, and correlated these residuals to various site parameters. Among the parameters considered were basin depth (i.e., depth to 2500 m/s shear wave isosurface), 3D/1D amplification predicted through simulations with generalized source locations, and site amplification from microtremors. As shown in Figure 5.16, residuals were found to be significantly correlated to basin depth. The slope of the fit lines is generally intermediate between those of Field and Steidl. When the depth dependency of residuals was removed, it was not possible to identify additional trends in the data with the model-based 3D/1D amplification. Accordingly, basin depth was considered a first-order basin response parameter that could not readily be improved upon with additional information.

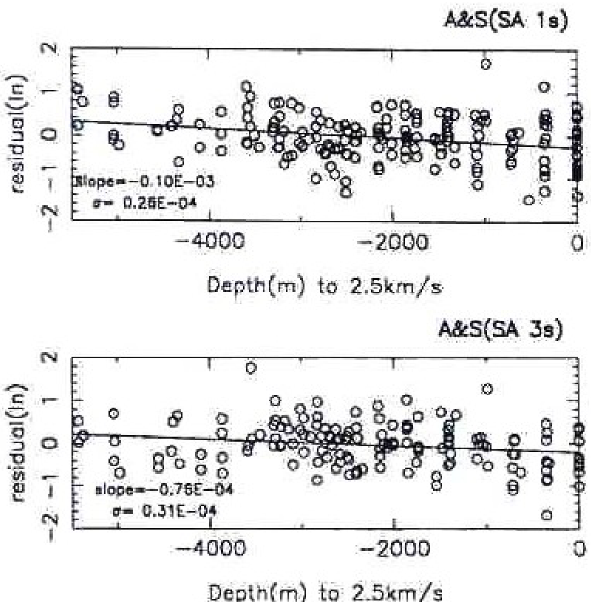

Fig. 5.16 Correlation of residuals from Abrahamson and Silva (1997) attenuation relationship with depth (in m) to 2.5 km/s V_s isosurface. Slope of least-squares fit to residuals and uncertainty on slope is given in plot (Lee and Anderson, 2000)

Joyner (2000) utilized a different parameterization of basin geometry, different ground motion intensity measures, and a different database than those discussed previously. In particular, the 5% damped pseudo-velocity response spectra was considered instead of acceleration response spectra, and the basin edge distance (R_B = distance from basin edge to site measured in direction of the site-source azimuth) was used for the basin geometric parameter instead of depth. The database consists of recordings from five large earthquakes that occurred outside of the Los Angeles basin, and recording stations within the basin. Amplification factors were derived relative to the soil attenuation relationships of Abrahamson and Silva (1997) and Joyner and Boore (1982). Linear regression analyses were performed to relate residuals to R_B (it is not clear whether those residuals were inter-event corrected). For the calculation of residuals, the distance term in the attenuation function was taken as the distance from the source to the edge of the basin. The resulting model predictions are shown in Figure 5.17 for spectral ordinates at 3 s, 4 s, and 5 s (based on Abrahamson and Silva residuals). The figure shows that within-basin pseudovelocity spectral ordinates are larger by as much as a factor of three than those predicted by the general attenuation model.

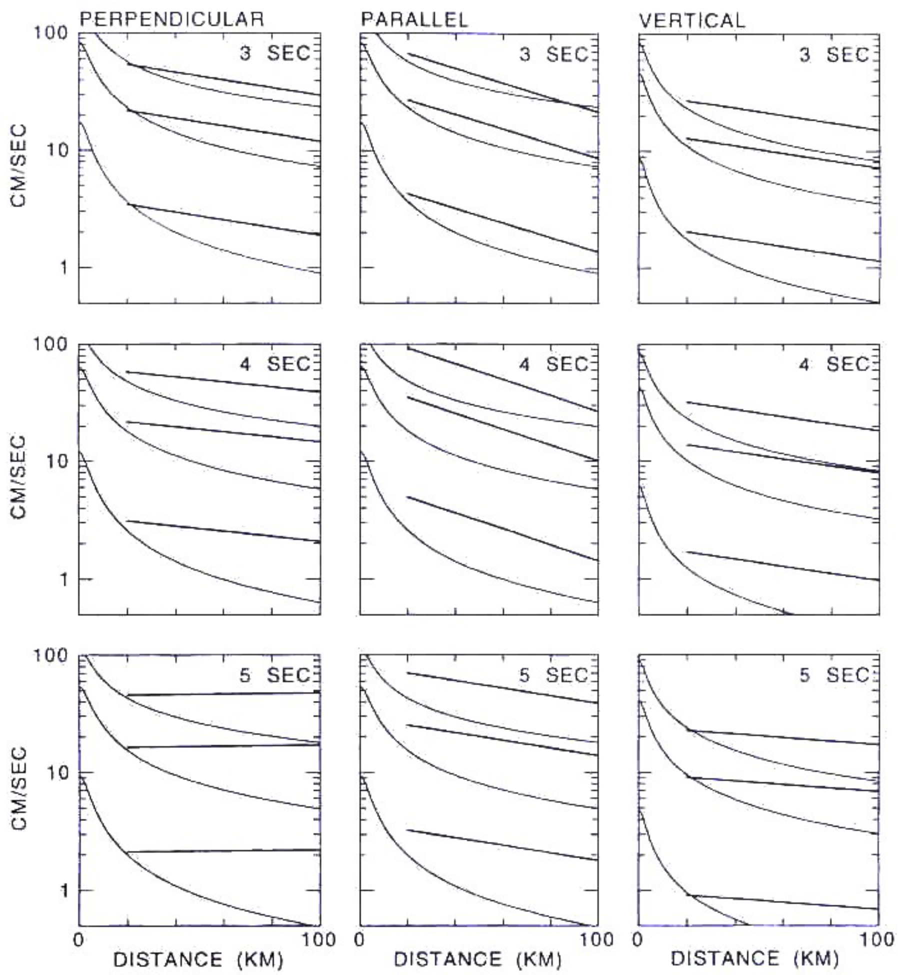

Fig. 5.17 Heavy line shows pseudovelocity response values (5% damping) given by Eq. 5.3 for moment magnitudes 5.5, 6.5, and 7.5 and a distance of 20 km from source to basin edge. Light line shows Abrahamson-Silva relationship (Joyner, 2000).

5.5.3 Recent Studies

Since the landmark series of SCEC studies, additional studies of basin effects have been conduced by Somerville et al. (2004) and Hruby and Beresnev (2003).

The study by Somerville et al. (2004) utilized a southern California database of 116 recordings from five events and five basins. Both coincident source and site-basin locations (CBL) and distinct source and site-basin locations (DBL) were included in the database, although a significant majority of the data are DBL. The basins considered are not limited to southern California (considered basins are Los Angeles, San Bernardino, San Fernando, Santa Clara, and Eel River). Similar to the study of Lee and Anderson (2000), residuals were evaluated with respect to the Abrahamson and Silva (1997) soil attenuation relationship. Residuals were considered on an event-by-event basis, and were also averaged across events without consideration of inter-event variability.

Correlations between the residuals and the basin geometric parameters of depth to 2500 m/s shear wave isosurface, basin edge distance R_B (similar to Joyner, 2000), and the ratio of depth to R_B were investigated. As shown in Figure 5.18, no significant trends were identified based on visual analysis of the residuals. However, it was reported that the Abrahamson and Silva soil attenuation relationship has positive residuals (corresponding to scale factors of about 1.65) at periods of 4 and 5 s for $z_{2.5}$ = 0–4 km and negative residuals for periods of 1.0, 1.5, and 2.0 s.

Hruby and Beresnev (2003) evaluated residuals for ground motions recorded in the Los Angeles basin during the 1987 Whittier Narrows and 1994 Northridge earthquakes relative to predictions from a stochastic finite fault simulation procedure (Beresnev and Atkinson, 1998, 2002). Since the simulation procedure had been calibrated to remove prediction bias and is based on 1D site modeling, the residuals would be expected to be related to average site amplification effects within the Los Angeles basin. Residuals of both Fourier amplitudes and durations were considered.

Residuals of Fourier spectral amplitude were investigated as a function of basin depth, defined as depth to the 2500 m/s shear wave isosurface. As shown in Figure 5.19, the results show a significant depth dependence across a wide frequency range. The slopes shown in the figure are about four to six times steeper than those evaluated by Field (2000).

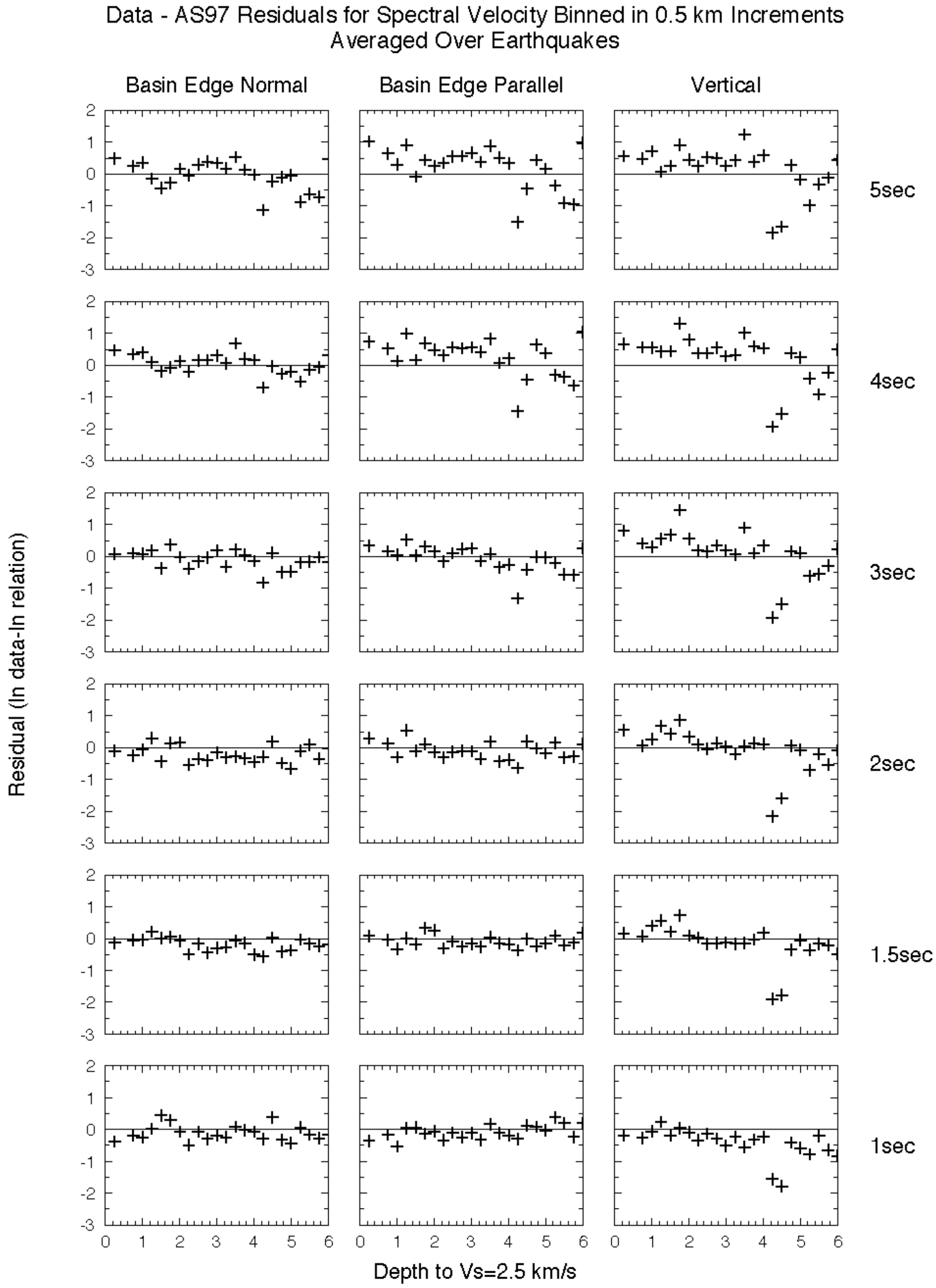

Fig. 5.18 Residuals of response spectral velocity of three components of motion recorded on basin sites for a series of periods, as function of depth to V_s=2500 m/s isosurface. Residuals for individual earthquake-basin pairs, binned at 0.5 km depth intervals have been aggregated (Somerville et al., 2004).

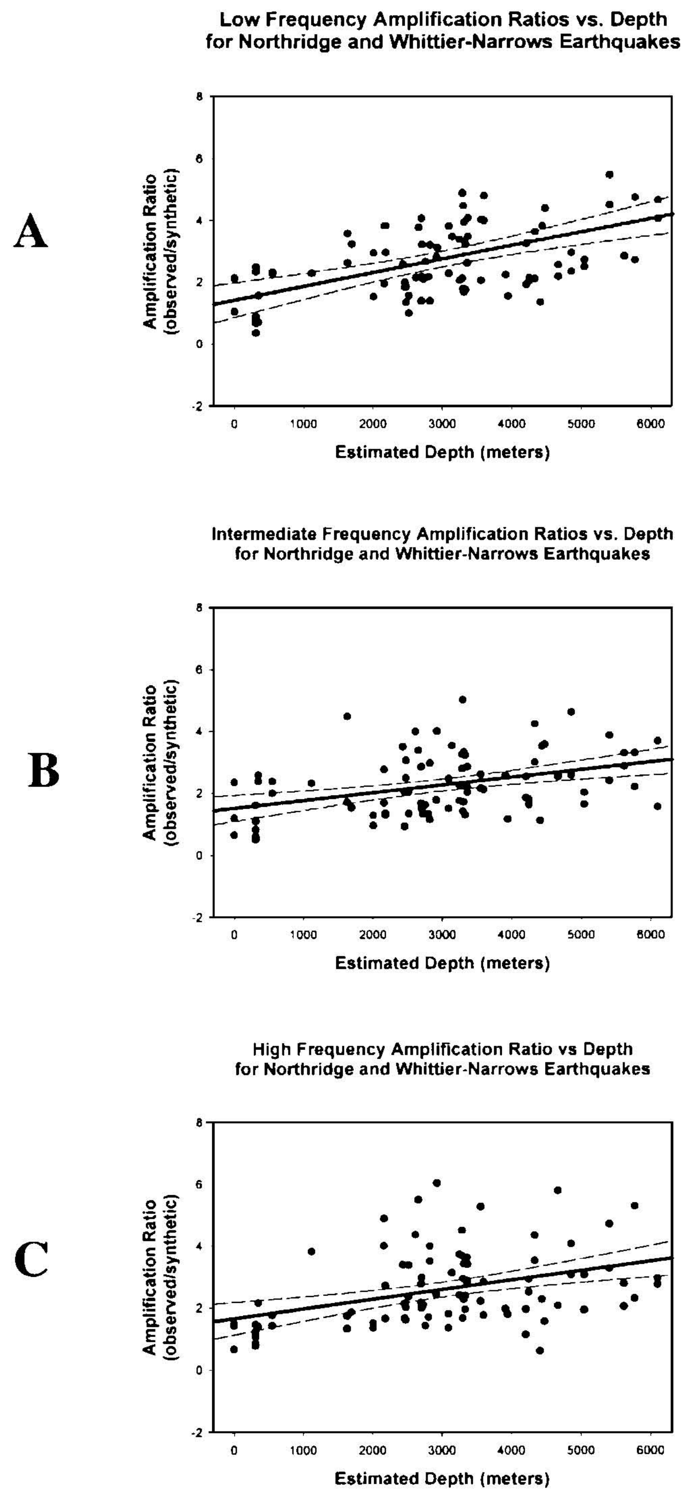

Fig. 5.19 Amplification ratio versus basin depth for (A) low frequencies (0.2–2.0 Hz), (B) intermediate frequencies (2.0–8.0 Hz), and (C) high frequencies (8.0–12.5 Hz). Dashed lines represent 95% confidence intervals (Hruby and Beresnev, 2003).

5.6 ANALYSIS OF BASIN AMPLIFICATION EFFECTS FROM STRONG MOTION RECORDINGS

In this section, empirical strong motion data are studied to evaluate potential effects of basin geometry on response spectral accelerations. The scope of this section is similar to the simulation data analyses reported in Section 5.4—the difference being the present use of recorded ground motion data in lieu of simulated data. Residuals are calculated with respect to ground motion predictions derived using rock attenuation relations coupled with various amplification factors that account for the average effects of shallow sediments on ground motions. The present analyses investigate whether additional information on sediment depth and the source location relative to the basin can improve ground motion predictions through reductions of bias and standard deviation. The parameters considered are identical to those identified in Section 5.4.1: $z_{1.5}$ and CBL/DBL designation for the source/site location.

The basin response analyses are discussed separately for the southern California and San Francisco Bay regions. This is followed in the next section with recommendations on how the results of the analyses should be applied in practice.

5.6.1 Analyses of Basin Response Using Southern California Data

In this section, site amplification within southern California basins is evaluated as a function of the basin geometric parameters. The analyses are performed using the strong motion database described in Chapter 2 and reference ground motions that combine a rock attenuation relationship with previously described amplification factors defined on the basis of various metrics of shallow site condition. The intent is to identify the dependence of the resulting residuals on basin geometric parameters and to evaluate whether data scatter can be reduced with the use of those parameters. We utilize only those metrics of shallow site condition that were the most promising in terms of minimizing standard deviation, namely $V_{s\text{-}30}$ (models developed in Section 4.4) and detailed surface geology (models developed in Sections 3.3–3.4). The following subsections describe the database used and the process by which residuals were calculated, the development of the basin amplification functions, and interpretation of the results (including comparisons to the results derived from simulated data and to the results of previous empirical studies).

(a) *Database and Calculation of Residuals*

Following the nomenclature of previous chapters (see Eqs. 3.3 and 4.3), intra-event residuals ε_{ij} for motion *j* from earthquake event *i* are calculated as the difference between data and model in natural log units,

$$\varepsilon_{ij} = \ln(S_{ij}) - [\ln(S_{r,ij}) + \ln(F_{m,ij}) + \eta_i] \tag{5.3}$$

where S_{ij} is the geometric mean of the 5% damped acceleration response spectral ordinates for the two horizontal components of the ground motion, $S_{r,ij}$ is the reference spectrum from an appropriate rock attenuation model coupled with near-fault corrections for rupture directivity (as needed, see details in Section 3.3.1), $F_{m,ij}$ is the amplification factor evaluated using either Equations 3.3 or 4.3 with error terms set to zero and the appropriate regression coefficients presented in Chapters 3–4 (the subscript "*m*" is used to distinguish model predictions for site *j* from the individual amplification values evaluated from data, which were denoted "F_{ij}"), and η_ι is the event term for earthquake *i* (evaluated as part of the regression analyses described in Section 3.3.1 and 4.4).

The strong motion data used to evaluate S_{ij} consist of recordings from basin and nonbasin sites in southern California. The development of the database is described in Chapter 2; the events contributing data are listed in Table 5.3. The subset of data with closest distance r < 100 km consists of 219 recordings from 12 events. For each recording site, depth parameter $z_{1.5}$ is evaluated from the Magistrale et al. (2000) basin model and an assessment is made regarding the location of the recording site's basin with respect to the source. A CBL classification is assigned if the source lies beneath the basin, whereas a DBL classification is used if the source location is distinct from that of the site basin (see Section 5.4.1 for details). The fault locations used to evaluate CBL/DBL were compiled as part of the Next-Generation Attenuation (NGA) project and were provided by Brian Chiou (2004, *personal communication*). For r < 100 km, the CBL subset consists of 84 recordings from five events, whereas DBL consists of 135 recordings from 11 events.

As noted previously, amplification factor $F_{m,ij}$ is evaluated only for metrics of shallow site condition that were found to minimize standard deviation, which are $V_{s\text{-}30}$ and detailed surface geology (based on geologic age and type of depositional environment). The specific amplification factor models that were used are listed below along with the accompanying rock attenuation relationship (for analysis of $S_{r,ij}$):

(1) Model B1: Attenuation relationship for rock by Abrahamson and Silva (1997) and $V_{s\text{-}30}$-based amplification model A1 (see Section 4.4 for details).

(2) Model B2: Attenuation relationship for rock by Sadigh et al., (1997) and $V_{s\text{-}30}$-based amplification model A2 (Section 4.4).

(3) Model B3: Attenuation relationship for soft rock by Campbell and Bozorgnia (2003) and $V_{s\text{-}30}$-based amplification model A3 (Section 4.4).

(4) Model B4: Attenuation relationship for rock by Abrahamson and Silva (1997) and detailed surface geology amplification model (age + depositional environment) developed in Sections 3.3–3.4

Table 5.3 Database used for analysis of basin effects in southern California

Event	Year	Mo-Day	Time	Mag	Number of Recordings			
					Model B1 - B3		Model B4	
					CBL	DBL	CBL	DBL
Kern County	1952	721	1153	7.4	-	-	-	2
Borrego Mtn	1968	409	230	6.8	-	-	-	1
Lytle Creek	1970	912	1430	5.4	-	2	-	2
San Fernando	1971	209	1400	6.6	-	6	-	6
Point Mugu	1973	221	1445	5.8	-	1	-	1
N. Palm Springs	1986	708	920	6.0	-	2	-	2
Whittier Narrows	1987	1001	1442	6.0	56	16	50	16
Whittier Narrows	1987	1004	1059	5.3	8	-	8	-
Landers	1992	628	1158	7.3	-	2	-	37
Big Bear	1992	628	1506	6.4	-	5	-	8
Northridge	1994	117	1231	6.7	16	70	16	65
Northridge Aftershock	1994	117	431	5.9	2	15	2	14
Northridge Aftershock	1994	320	1320	5.2	2	14	2	13
Hector Mine	1999	1016	946	7.1	-	2	-	19

Models B1–B3 are applied only for sites with r < 100 km, whereas B4 is applied without distance restrictions. Note that the analysis of residuals by the above models, used in conjunction with Equation 5.3, differs from most previous studies (i.e., Lee and Anderson, 2000; Steidl, 2000; Hruby and Beresnev, 2003; Somerville et al., 2004) in that amplification factors derived from detailed site data (in lieu of relatively generic rock/soil designations) are used in the analysis of residuals. Only the Field (2000) work calculated residuals from models that include a site-specific site term, although the Field site term is linear (see Section 5.5.2).

The database for models B1–B3 is consistent. Both sites with $V_{s\text{-}30}$ measured on-site and estimates of $V_{s\text{-}30}$ were utilized. Details on the measured and estimated $V_{s\text{-}30}$ values are presented in Section 2.2.2. The database for model B4 is slightly different because some sites lack $V_{s\text{-}30}$

information but have surface geology classifications, or are in surface geologic categories that are sparsely populated and for which empirical amplification factors are unavailable (e.g., Holocene fill and Pleistocene marine). Nonetheless, the database for model B4 is generally populated by a similar set of recordings to that for models B1–B3.

(b) Statistical Analysis of Basin Amplification Functions

The variation of amplification factors with basin geometry is investigated by plotting in Figure 5.20 the amplification factors as a function of basin depth for bins of data with coincident source and site basin locations (CBL) and distinct source and site basin locations (DBL). Unlike the simulated data in Figure 5.11, the data from recordings do not provide strong visual evidence of a bilinear relationship between residuals and $z_{1.5}$. Accordingly, for each of the CBL and DBL categories, linear regression analyses are performed as follows:

$$\ln(\varepsilon_{ij}) = a_1 + a_2 \cdot z_{1.5ij} + \kappa_{ij} \tag{5.4}$$

where a_1 and a_2 are regression coefficients, and κ_{ij} = residual term for ground motion j from event i, which has zero mean and standard deviation σ. Coefficients a_1 and a_2 and standard deviation term σ are evaluated for a range of periods for each of the four models B1–B4. The regression analyses are performed using ordinary least-squares procedures in lieu of mixed-effects procedures because the event term was included in the analysis of residuals (Eq. 5.3).

Example plots of regression model fits to the data are presented in Figure 5.20. The median values of residuals for the sites located outside basins are also presented with their standard deviation in Figure 5.20. Values of model parameters (and their estimation errors) derived directly from the regression are presented in Table 5.4. Also shown in Table 5.4 are the results of hypothesis tests, which consist of compiling sample 't' statistics to test the null hypothesis of zero slope. This statistical testing provides a significance level = α that the null hypothesis cannot be rejected. For clarity of expression, we tabulate in Table 5.4 values of 1-α, which we refer to as a "rejection confidence" for a zero slope model. Large rejection confidence levels (i.e., > 95%) suggest significant depth dependence of amplification factors. Regression parameters are listed in Appendix C. It should be noted that the regression parameters in Appendix C have been smoothed with respect to period. The results for T = 4 and 5 s are less reliable due to data sparseness.

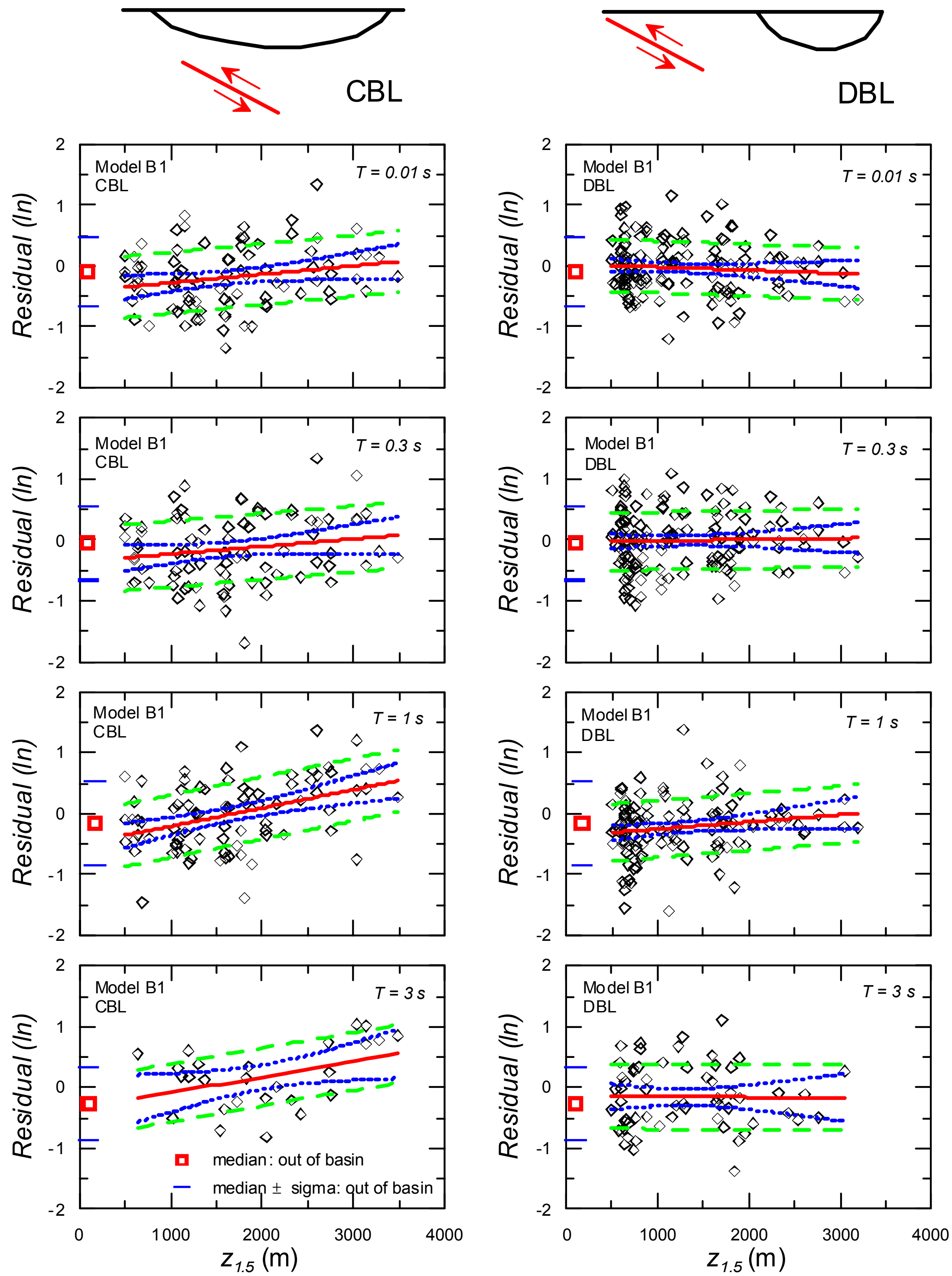

Fig. 5.20(a) Regression results for model B1—southern California basins

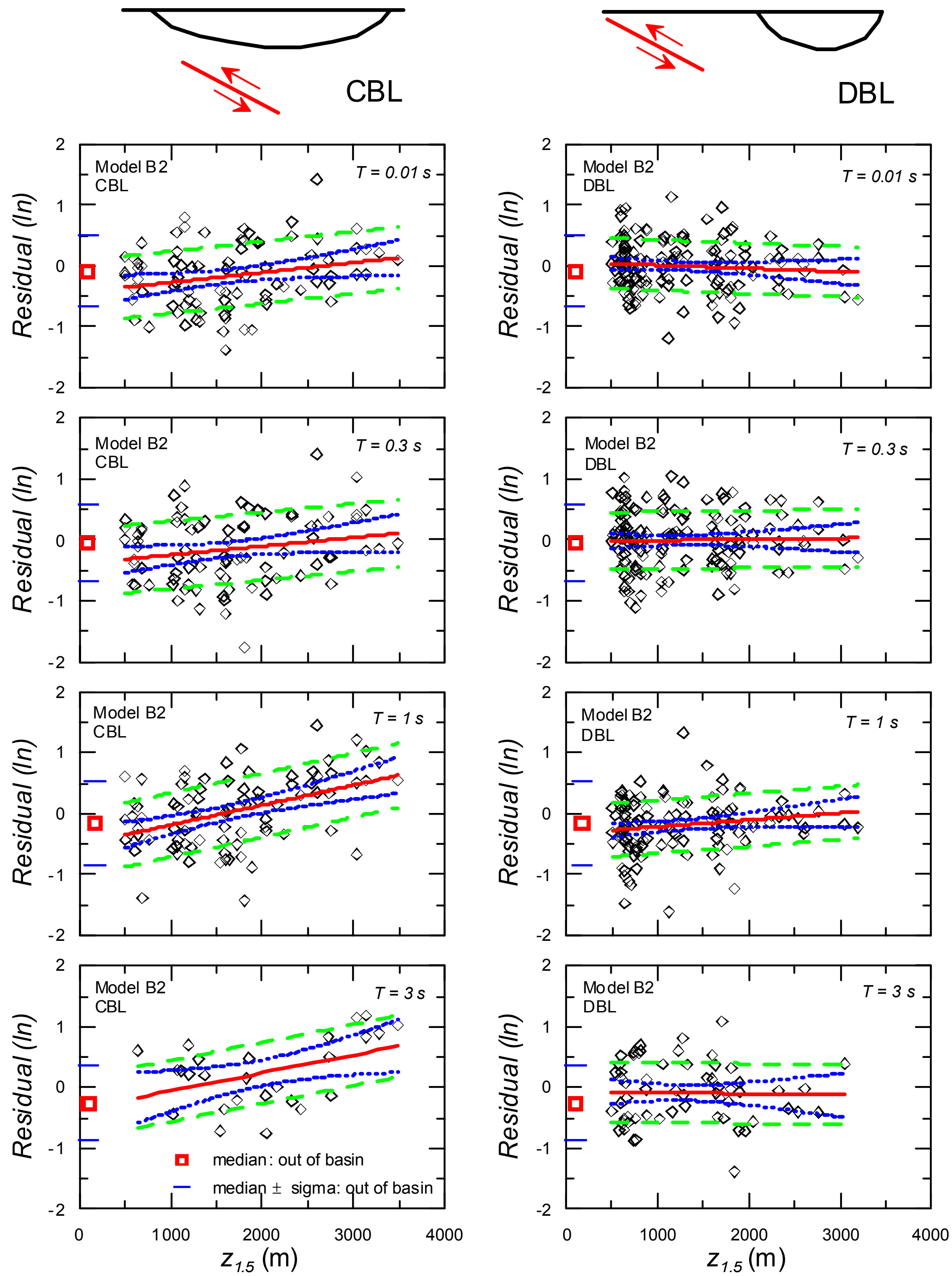

Fig. 5.20(b) Regression results for model B2—southern California basins

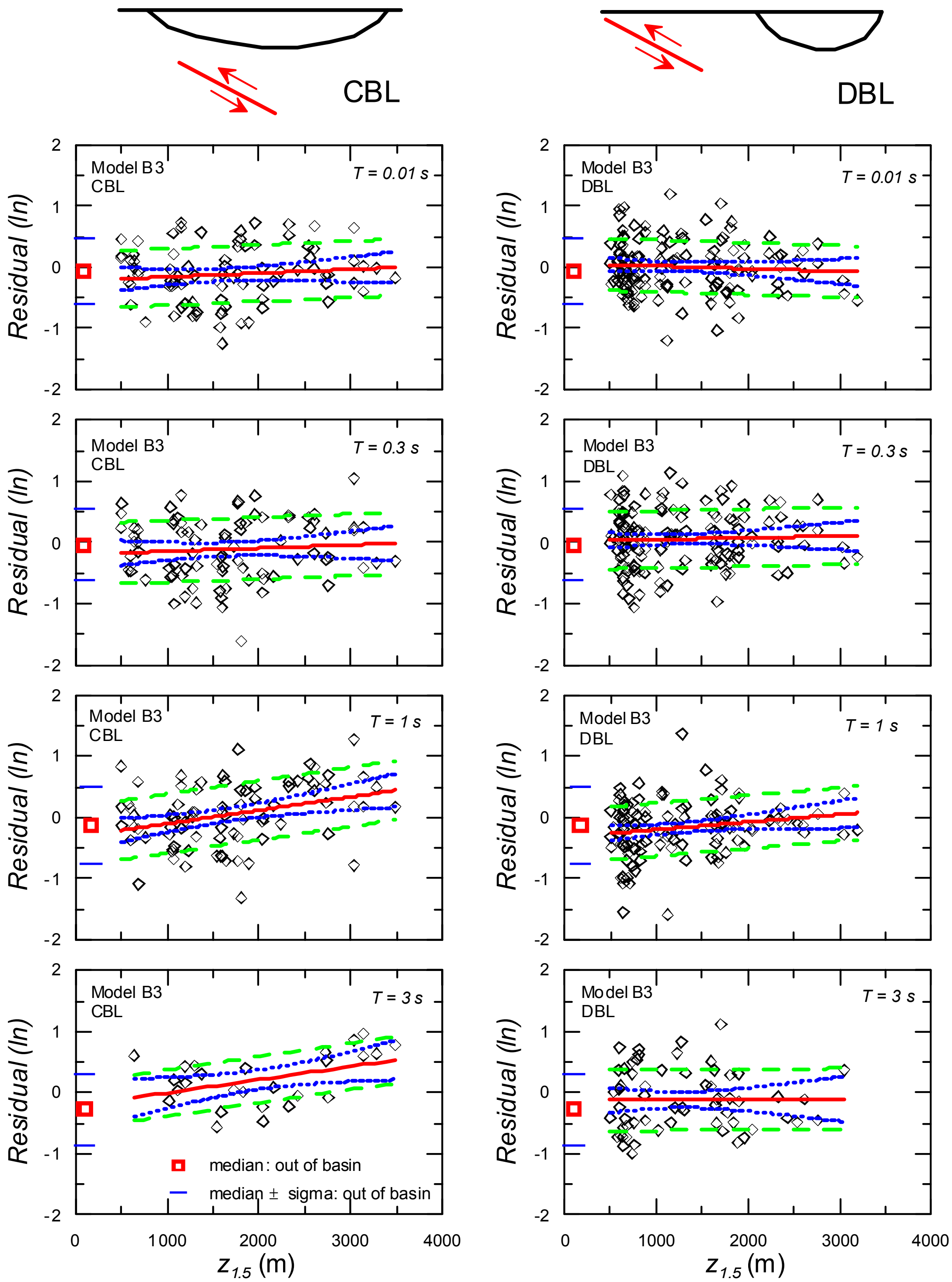

Fig. 5.20(c) Regression results for model B3—southern California basins

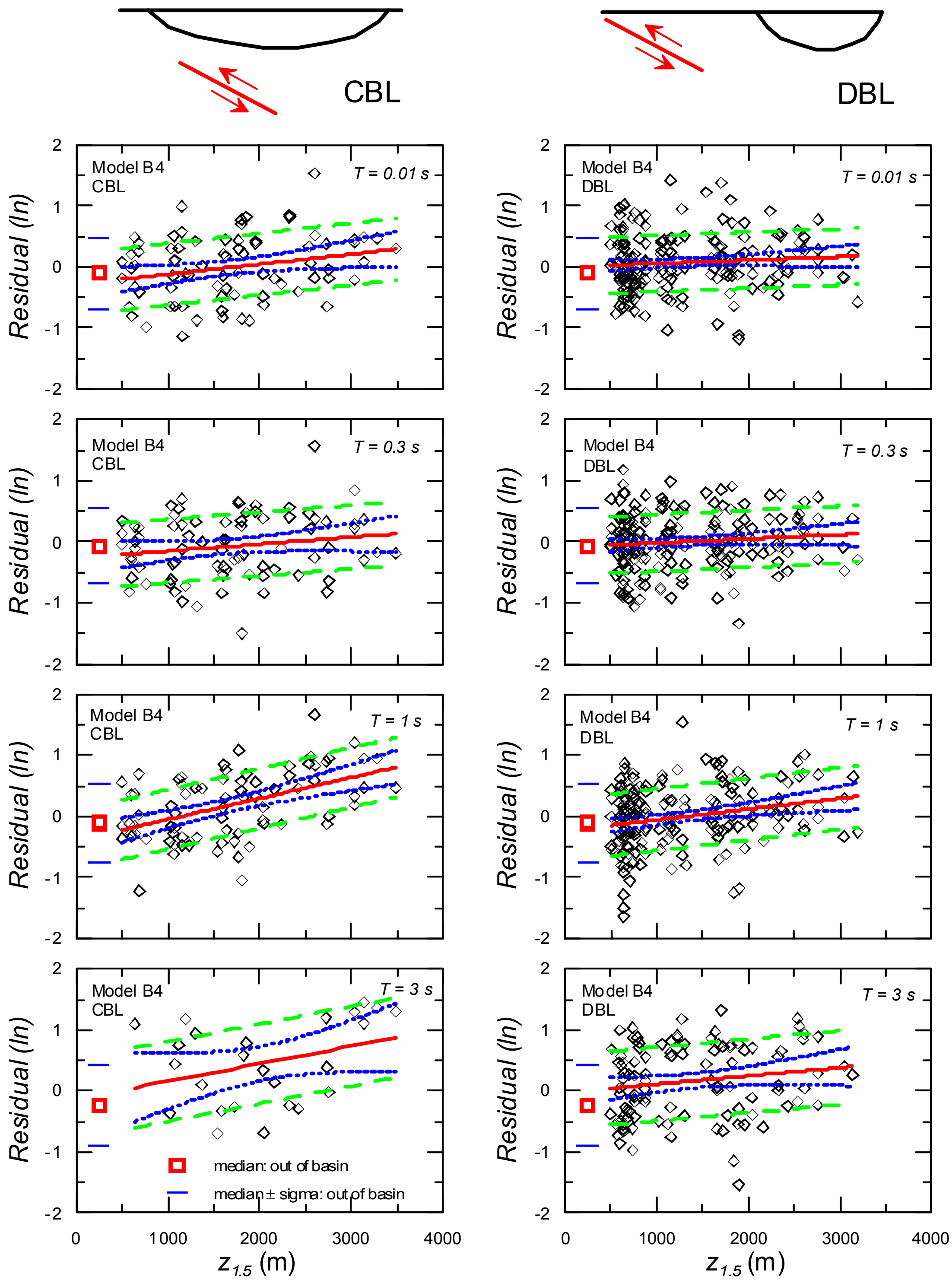

Fig. 5.20(d) Regression results for model B4—southern California basins

Table 5.4 Example regression results for basin response in southern California

Model	T (sec)	CBL a_1	CBL a_2	CBL σ	CBL 1-α (%)	DBL a_1	DBL a_2	DBL σ	DBL 1-α (%)
B1	0.01	-0.41 $\pm$ 0.26	1.4E-04 $\pm$ 1.4E-04	0.50	94	0.04 $\pm$ 0.16	-5.2E-05 $\pm$ 1.1E-04	0.43	65
	0.3	-0.35 $\pm$ 0.28	1.2E-04 $\pm$ 1.6E-04	0.55	88	-0.04 $\pm$ 0.17	2.2E-05 $\pm$ 1.2E-04	0.48	27
	1.0	-0.51 $\pm$ 0.27	3.0E-04 $\pm$ 1.5E-04	0.52	100	-0.37 $\pm$ 0.18	1.2E-04 $\pm$ 1.3E-04	0.47	93
	3.0	-0.34 $\pm$ 0.54	2.6E-04 $\pm$ 2.5E-04	0.48	96	-0.15 $\pm$ 0.30	-4.1E-06 $\pm$ 2.1E-04	0.53	3
B2	0.01	-0.43 $\pm$ 0.27	1.6E-04 $\pm$ 1.5E-04	0.51	97	0.06 $\pm$ 0.15	-5.3E-05 $\pm$ 1.1E-04	0.42	67
	0.3	-0.39 $\pm$ 0.29	1.4E-04 $\pm$ 1.6E-04	0.56	92	-0.03 $\pm$ 0.17	1.8E-05 $\pm$ 1.2E-04	0.47	23
	1.0	-0.51 $\pm$ 0.27	3.3E-04 $\pm$ 1.5E-04	0.53	100	-0.33 $\pm$ 0.17	1.1E-04 $\pm$ 1.2E-04	0.44	93
	3.0	-0.35 $\pm$ 0.57	3.0E-04 $\pm$ 2.6E-04	0.51	97	-0.06 $\pm$ 0.28	-2.2E-05 $\pm$ 2.0E-04	0.50	18
B3	0.01	-0.22 $\pm$ 0.24	6.2E-05 $\pm$ 1.3E-04	0.47	65	0.07 $\pm$ 0.16	-4.5E-05 $\pm$ 1.1E-04	0.43	58
	0.3	-0.20 $\pm$ 0.26	5.2E-05 $\pm$ 1.4E-04	0.51	52	0.02 $\pm$ 0.17	2.8E-05 $\pm$ 1.2E-04	0.47	36
	1.0	-0.32 $\pm$ 0.25	2.2E-04 $\pm$ 1.4E-04	0.49	100	-0.32 $\pm$ 0.17	1.2E-04 $\pm$ 1.2E-04	0.44	96
	3.0	-0.22 $\pm$ 0.43	2.2E-04 $\pm$ 2.0E-04	0.39	97	-0.13 $\pm$ 0.29	7.2E-06 $\pm$ 2.0E-04	0.50	6
B4	0.01	-0.28 $\pm$ 0.27	1.6E-04 $\pm$ 1.5E-04	0.51	97	0.00 $\pm$ 0.14	5.5E-05 $\pm$ 9.6E-05	0.46	74
	0.3	-0.27 $\pm$ 0.28	1.1E-04 $\pm$ 1.5E-04	0.52	86	-0.09 $\pm$ 0.14	6.9E-05 $\pm$ 9.7E-05	0.47	84
	1.0	-0.39 $\pm$ 0.26	3.4E-04 $\pm$ 1.4E-04	0.49	100	-0.23 $\pm$ 0.16	1.8E-04 $\pm$ 1.1E-04	0.51	100
	3.0	-0.13 $\pm$ 0.77	2.9E-04 $\pm$ 3.5E-04	0.67	90	-0.02 $\pm$ 0.26	1.3E-04 $\pm$ 1.7E-04	0.61	89

The results of the regression analyses and hypothesis tests generally indicate a statistically significant depth dependence of residuals in the CBL category for $T > 0.3$ s. The depth dependence of residuals is generally not significant at shorter periods. Accordingly, the regression results for the CBL category reported in Appendix C are the coefficients for $T > 0.3$ s. On the other hand, the DBL category generally lacks significant depth dependence of residuals for models B1–B3. For model B4, the DBL depth dependence is statistically significant, but still smaller than for CBL, and the a_2 parameters are generally larger than those for models B1–B3 (an explanation for this is given below). Note that these trends are generally consistent with those found for the simulated data, namely, more significant depth dependence for CBL than for DBL. Because the DBL residuals lack depth dependence, the a_1 coefficients reported in Appendix C are averages of residuals across all depths, whereas a_2 is set to zero.

For models B1–B3, median residuals for sites outside the basins are generally comparable to the median of DBL residuals. For the CBL case at $T > 0.3$ s, the median residual for sites outside of basins is generally consistent with the minimum level of the regression fit lines for the CBL sites. This result further supports the need to account for basin depth in the analysis of site effects for CBL sites. For model B4, the median residual for sites outside of basins is generally consistent with the minimum level of the regression fit lines for both the CBL and DBL sites.

To evaluate the statistical significance of the distinction between the CBL and DBL data groups, statistical F-tests were performed (Cook and Weiberg, 1999). The F test operates on submodels (in this case, the regression results for the CBL and DBL data sets) and produces an F statistic, which can be compared to the F distribution to evaluate a significance level (p) for the test. Large values of p (e.g., $p > 0.05$) are taken to imply that the submodels are not distinct, although the models may be considered moderately distinct for $0.05 < p < 0.15$. The results are shown in Table 5.5 for the 13 periods considered.

The results of F-tests on the $V_{s\text{-}30}$ based amplification models (B1–B3) generally indicate that the CBL and DBL data groups are significantly distinct. The periods of 1.5 and 2.0 s are consistent exceptions. The level of distinction between CBL and DBL is much less for model B4. These results generally suggest that use of the separate CBL and DBL categories is justified for $V_{s\text{-}30}$-based amplification models (B1–B3) but not for the more generic model B4. The lack of distinction for model B4 suggests that a single model that does not separate the CBL and DBL cases should be used. Accordingly, the B4 regression parameters reported in Appendix C do not separate DBL and CBL.

Table 5.5 F-statistics indicating distinction between CBL and DBL data groups for selected periods

T (sec)	Model B1 CBL & DBL		Model B2 CBL & DBL		Model B3 CBL & DBL		Model B4 CBL & DBL	
	F	p	F	p	F	p	F	p
0.01	5.49	0.00	6.59	0.00	2.84	0.06	2.39	0.09
0.05	7.98	0.00	9.08	0.00	4.34	0.01	5.03	0.01
0.1	3.20	0.04	4.11	0.02	2.75	0.07	2.28	0.10
0.15	3.76	0.02	4.74	0.01	4.23	0.02	2.82	0.06
0.2	5.96	0.00	7.45	0.00	5.96	0.00	2.44	0.09
0.3	3.17	0.04	3.83	0.02	3.37	0.04	1.39	0.25
0.4	5.81	0.00	6.59	0.00	4.15	0.02	2.42	0.09
0.5	5.29	0.01	5.79	0.00	3.42	0.03	2.05	0.13
0.75	2.95	0.05	3.85	0.02	1.58	0.21	3.89	0.02
1	3.30	0.04	4.06	0.02	2.66	0.07	2.64	0.07
1.5	1.51	0.22	2.00	0.14	0.76	0.47	2.00	0.14
2	1.45	0.24	2.08	0.13	0.66	0.52	1.16	0.31
3	3.17	0.05	3.97	0.02	3.37	0.04	1.15	0.32

The reason model B4 behaves differently from B1–B3 can be understood by considering the correlation between basin depth and V_{s-30} shown in Figure 5.21, which shows that deeper basin sediments generally have lower velocities. Since most sedimentary basin sites fall into a single geologic category (Quaternary alluvium), a consistent shallow site correction would be made in Equation 5.3 for all such sites for the B4 model. Conversely, different shallow site corrections would be made with the V_{s-30}-based models (B1–B3), which remove amplification effects that in model B4 would be attributed to depth. This is why the depth dependence for model B4 is stronger than for models B1–B3, especially for the DBL data. This is important because the depth dependence for the DBL group is sufficiently large for model B4 that the data are not distinct from CBL, according to the F-test.

Standard deviation terms from the B1–B4 models are compared to those from the corresponding nonbasin models in Figure 5.22. Separate frames are shown for each of the three models B1–B3. In each frame, the corresponding standard deviation for the V_{s-30}-based amplification models A1–A3 are shown. Also shown are standard deviation terms for model B4 without distinguishing the CBL and DBL data (due to the lack of distinction observed in the F tests, as noted above).

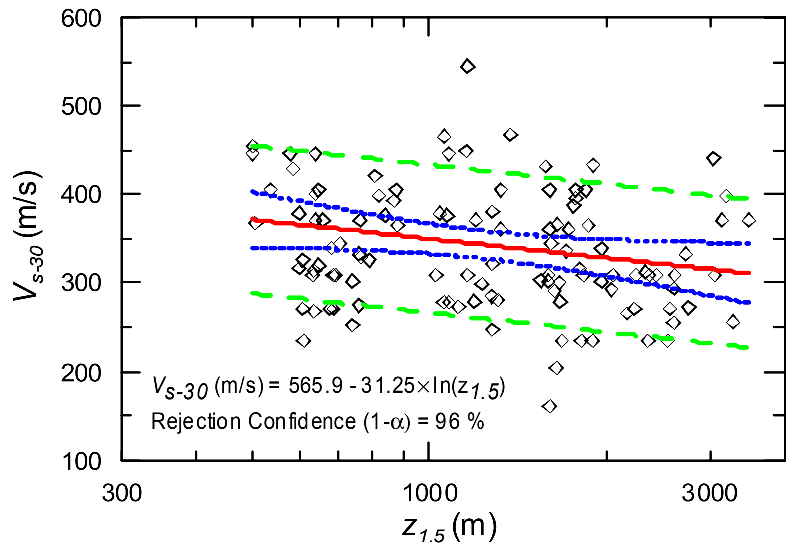

Fig. 5.21 Relationship between $z_{1.5}$ and V_{s-30} for southern California basin sites

There are two important features illustrated in Figure 5.22. The first relates to the benefit of using the basin models as a supplement to the V_{s-30}-based site factors. At short periods, the average of the DBL and CBL standard deviation terms is similar to the standard deviation of the underlying A1–A3 models, indicating that use of the basin models is not significantly reducing overall data dispersion. This should not be surprising, as the residuals were not found to be significantly depth dependent across most of this period range. However, for $T > 1$ s, both the DBL and CBL error terms are significantly less than those for the A1–A3 models, indicating a significant improvement in predictive capability. The reduction of standard deviation is generally greatest for the DBL category, and is as large as 0.15 in natural log units.

The second important feature relates to the use of the relatively simple B4 model (with combined CBL and DBL data) versus the more complex B1–B3 models. The standard deviation terms for model B4 are generally comparable to those for models B1–B3 at short periods, but for longer periods ($T > 1$ s), standard deviations for models B1–B3 are significantly reduced. This shows that the CBL/DBL basin models coupled with the V_{s-30}-based amplification factors provide the optimal treatment of site effects from the standpoint of minimizing standard deviation across a broad range of periods.

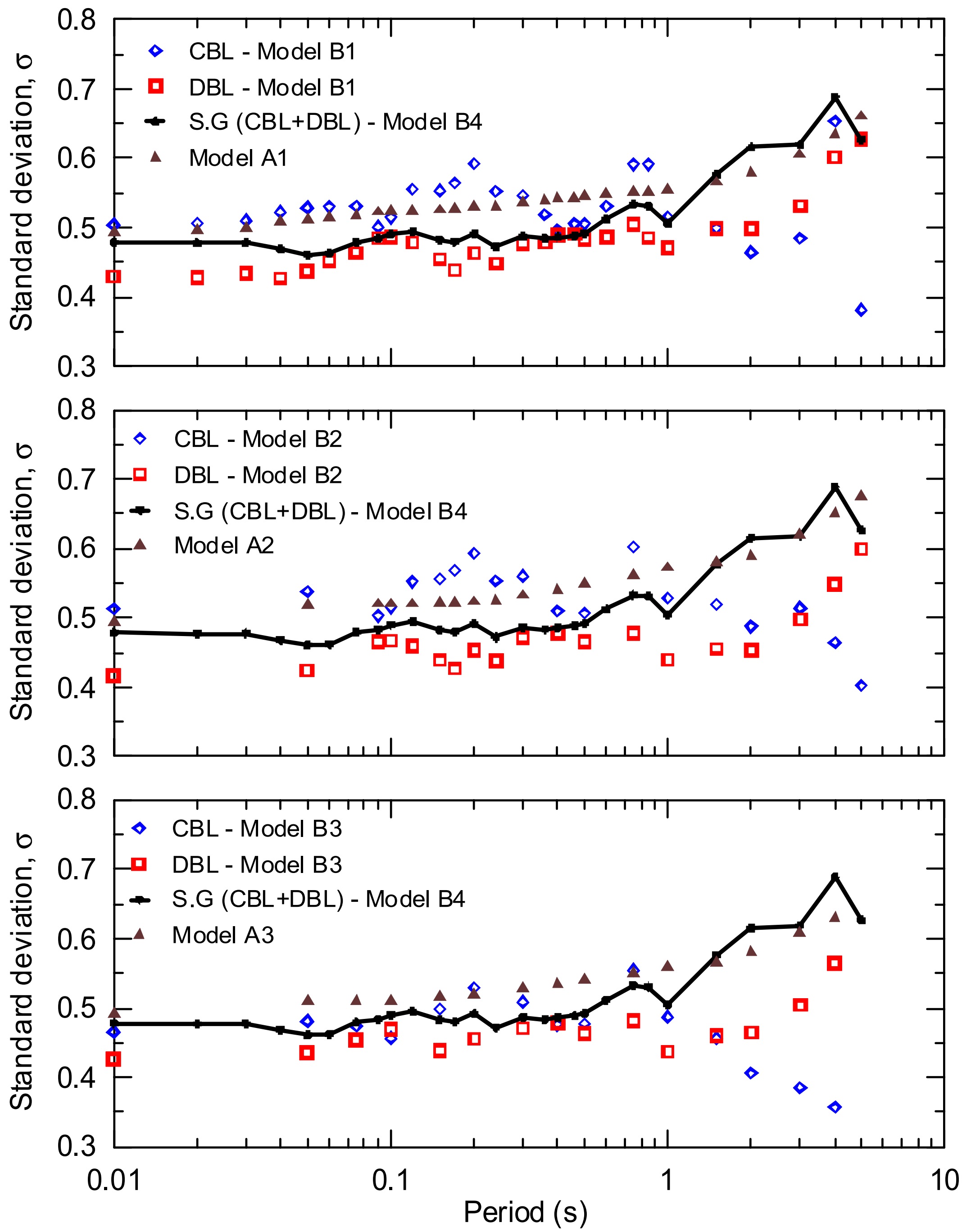

Fig. 5.22 Comparison of standard deviation terms for basin and nonbasin models, southern California data

(c) Comparison to Other Results

As noted previously, the significant dependence of residuals on $z_{1.5}$ for the CBL category and the general lack of this dependence for DBL are consistent with the regressions that utilized basin simulation data in Section 5.4. Both sets of results indicate a clear benefit of distinguishing CBL and DBL conditions for analyses of basin response. Physical explanations for the different trends were provided previously in Section 5.4.2.

Previous empirical studies of basin response summarized in Section 5.5 did not distinguish between the CBL and DBL conditions, although since most of the data are derived from the Northridge and Whittier Narrows earthquakes, both conditions are well represented in the southern California database used by SCEC researchers. Accordingly, many of those previous studies presented averaged basin effects across both conditions, which generally indicated depth-dependent residuals (Field, 2000; Lee and Anderson, 2000; Steidl, 2000; Hruby and Beresnev, 2003). As we found similar results for B4, the results of the present study are generally consistent with the previous results at long periods. At short periods (T < 0.3 s), the results of the present study B1–B4 generally show a lack of depth-dependent residuals, which is different from the previous work.[1]

We speculate that the differences in the depth dependence of short-period residuals in this study versus the previous SCEC work arises because we removed site effects associated with shallow site conditions before calculating basin effects, whereas the previous studies generally did not. In the cases of models B1–B3, the fact that $V_{s\text{-}30}$ is correlated with depth (Fig. 5.21) implies that the corrections for $V_{s\text{-}30}$-based site effects remove amplification that in previous studies was attributed only to depth. In other words, the dependence of short-period amplification on depth that was found in previous studies may be in large part a $V_{s\text{-}30}$ effect. This is an attractive concept because the physics of site response are such that short-period amplification should be most significantly dependent on $V_{s\text{-}30}$, and long-period amplification should be most significantly dependent on depth. The reason for the lack of depth dependence of B4 at short periods is less clear.

To compare the depth dependences of the SCEC models to those of the models B1–B4 directly, regression analyses are performed according to Equation 5.5 in which $z_{2.5}$ is used as a depth parameter (similar to the SCEC work).

---

[1] However, it should be noted that the rejection confidences for T = 0.01 s and 0.02 s are very close to 95% (94.7% and 94.1% respectively), and then are reduced for periods beyond those associated with *PHA*.

$$\ln(\varepsilon_{ij}) = a_1 + a_2 \cdot z_{2.5ij} + \kappa_{ij} \tag{5.5}$$

where a_1 and a_2 are regression coefficients, and κ_{ij} = residual term for ground motion j from event i, which has zero mean and standard deviation σ. The slopes (i.e., the depth dependence of residuals) of the regression analyses results are shown in Figure 5.23. It is found that the slopes of the SCEC models are generally smaller than those of the CBL data for models B1–B3, and larger than those of the DBL data for the models B1–B3. On the other hand, the slopes of model B4 are generally within the range of the SCEC slopes.

Interestingly, the one previous study that did not identify residuals with significant depth dependence was Somerville et al. (2004), whose database is constituted principally of DBL data. In that sense, their results are consistent with those of the present study.

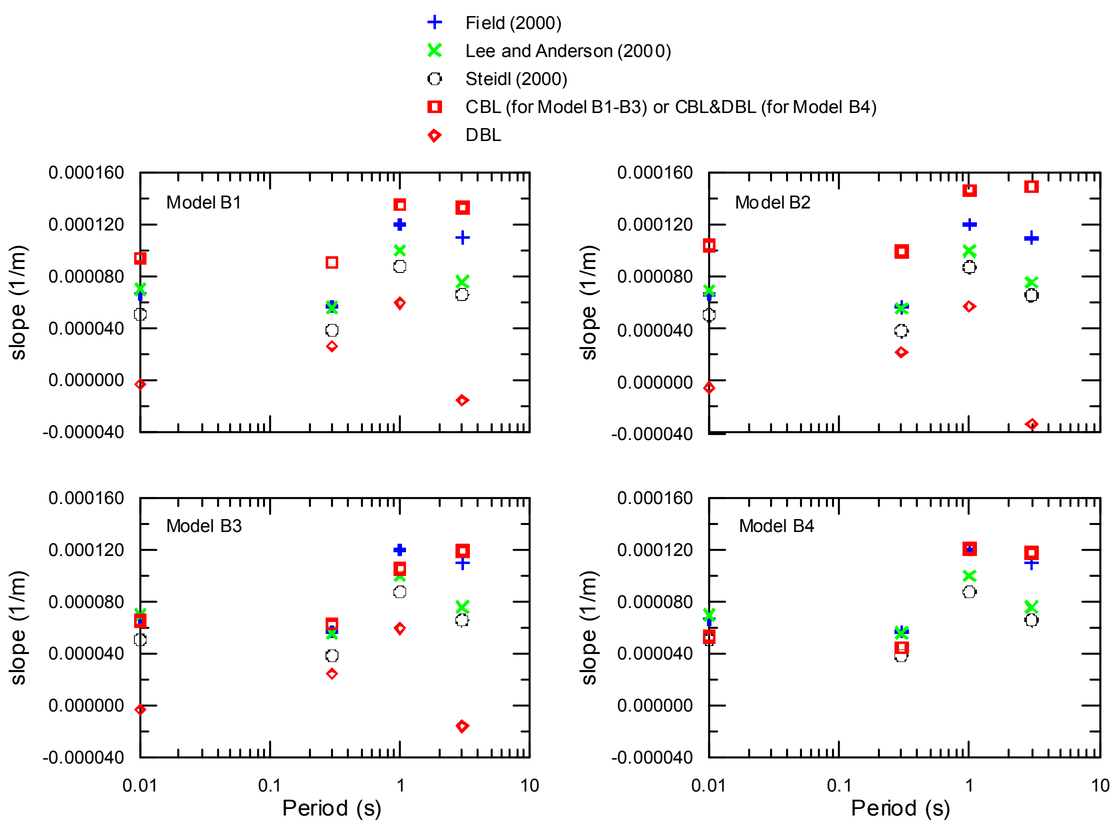

Fig. 5.23 Comparison of slope parameters representing depth dependence of residuals for SCEC models and models B1–B4, southern California data. Note that slopes at T = 0.01 s are not representative of slopes between 0.01 and 0.3 s, for which the slopes are generally near zero (see footnote 1, p. 153).

5.6.2 Analyses of Basin Response Using San Francisco Bay Area Data

The strong motion data set for the San Francisco Bay Area (SFBA) is considerably more limited than that for southern California. Most of the data come from two events, the 1984 Morgan Hill and 1989 Loma Prieta earthquakes. As described in Section 2.3.2(b), the model of basin geometry is somewhat less robust than the southern California models, and defining the basin margin is relatively difficult. For both of these reasons, the analysis of basin effects on strong motions for the SFBA is simplified from the procedures given in Section 5.6.1 in that CBL and DBL conditions are not distinguished. However, since the Morgan Hill and Loma Prieta earthquakes occurred outside of the basins with most of the recording sites, it should be borne in mind that the SFBA area results principally apply to the DBL condition.

The analysis of residuals ε_{ij} for each recording was performed using Equation 5.3 and the same procedures that were outlined in Section 5.6.1(a). The events contributing data for SFBA are listed in Table 5.6. There are a total of 138 recordings from eight events for models B1–B3 and a total 137 recordings from seven events for model B4.

Table 5.6 Database used for analysis of basin effects in San Francisco Bay Area

Event	Year	Mo-Day	Time	Mag	Number of Recordings Model B1 - B3	Number of Recordings Model B4
San Francisco	1957	322	1944	5.3	1	-
Hollister	1974	1128	2301	5.2	3	3
Coyote Lake	1979	806	1705	5.7	10	10
Livermore	1980	124	1900	5.8	7	7
Livermore	1980	127	233	5.4	8	8
Morgan Hill	1984	424	2115	6.2	29	29
Hollister	1986	126	1920	5.4	4	4
Loma Prieta	1989	1018	5	6.9	76	76

Regression analyses were performed according to Equation 5.4 to relate residuals ε_{ij} to basin depth $z_{1.5}$. Plots of the data and regression model fits are presented in Figure 5.24 for selected periods. Unsmoothed regression parameters and their estimation error are listed in Table 5.7. Also shown in Table 5.7 are the results of hypothesis tests to evaluate the rejection confidence (1-α) for zero slope models. The results indicate zero or even slightly negative slopes at short periods. Positive slopes are found for periods $T \geq 2$ s. The magnitude of slope parameter a_2 is comparable to that for the CBL data in southern California at $T = 3$ s, but at midperiods a_2 values for SFBA are much smaller. Even at the longer periods, the hypothesis tests indicate moderate rejection confidence levels for the zero slope models at a number of periods. Overall, the SFBA data do not show a clear depth dependence of residuals, which given the DBL condition of most of the data, is generally consistent with the results from southern California.

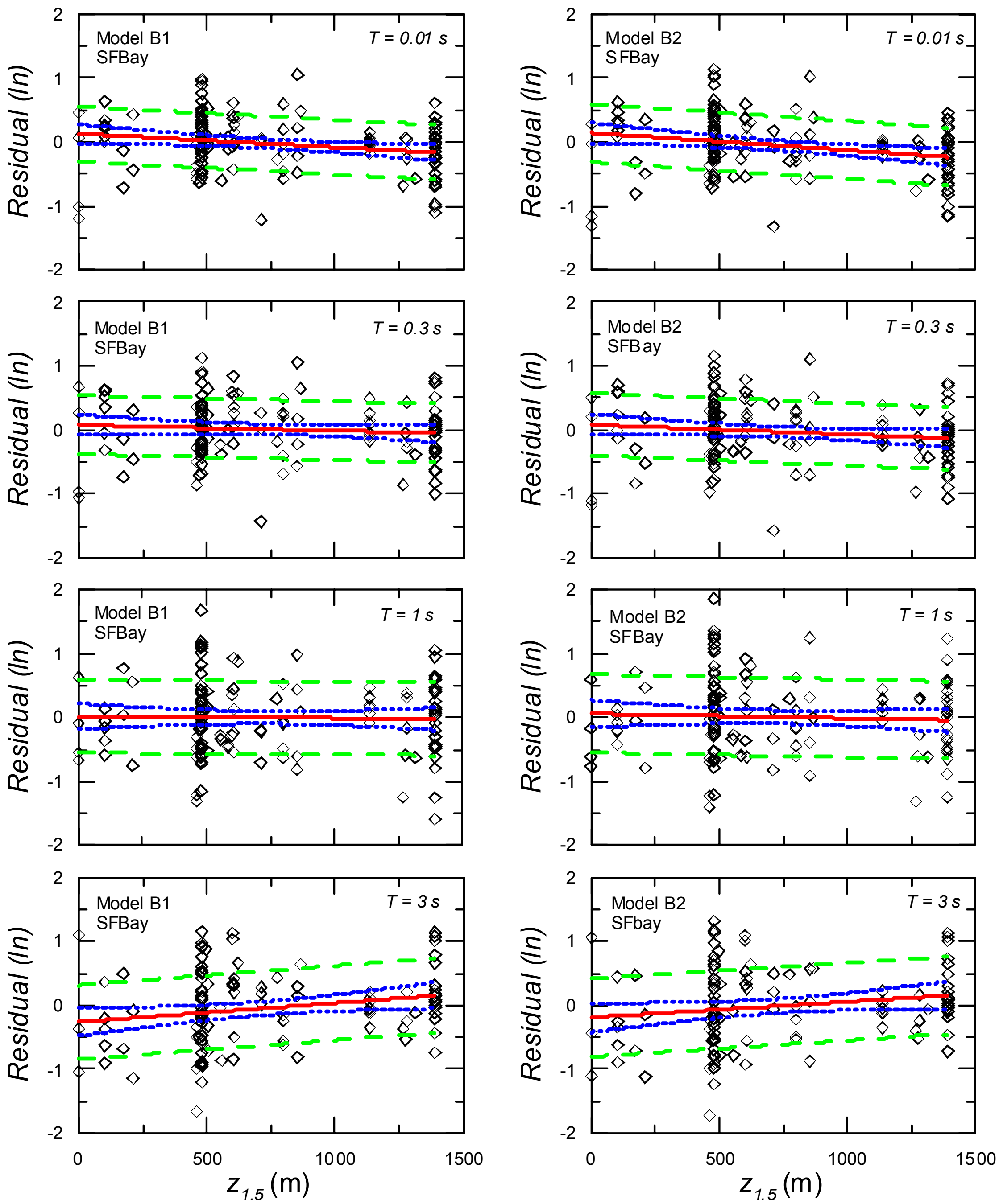

Fig. 5.24(a) Regression results for models B1 and B2—San Francisco Bay Area basins

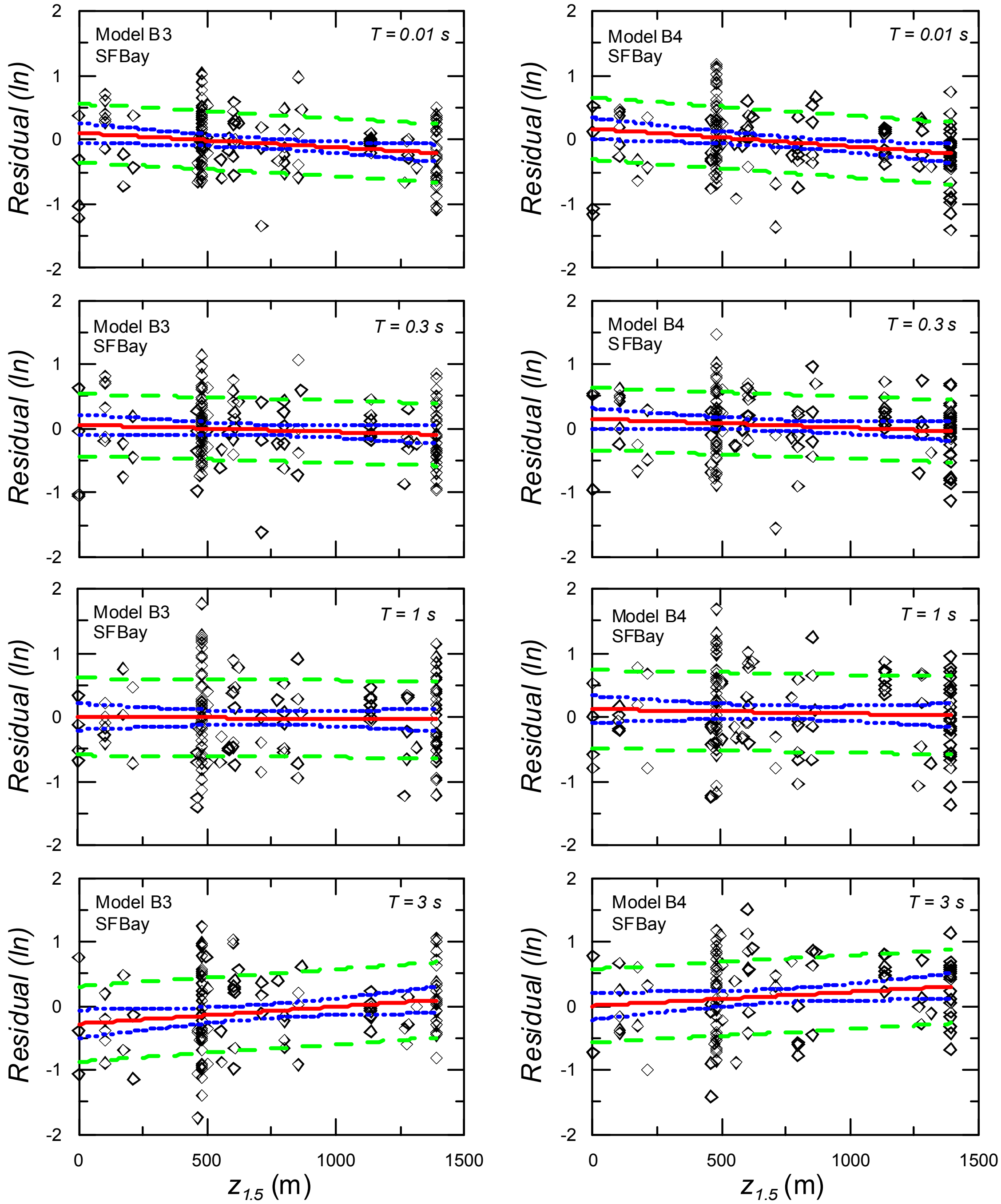

Fig. 5.24(b) Regression results for models B3 and B4—San Francisco Bay Area basins

Table 5.7 Example regression results for basin response in San Francisco Bay Area

Model	T (sec)	a_1	a_2	σ	$1\text{-}\alpha$ (%)
B1	0.01	0.13 ± 0.15	$-2.1\text{E-}04 \pm 1.7\text{E-}04$	0.43	98
	0.3	0.08 ± 0.16	$-9.4\text{E-}05 \pm 1.8\text{E-}04$	0.46	69
	1.0	0.02 ± 0.20	$-2.8\text{E-}05 \pm 2.3\text{E-}04$	0.58	19
	3.0	-0.26 ± 0.22	$3.0\text{E-}04 \pm 2.6\text{E-}04$	0.58	98
B2	0.01	0.14 ± 0.16	$-2.7\text{E-}04 \pm 1.8\text{E-}04$	0.46	100
	0.3	0.08 ± 0.17	$-1.5\text{E-}04 \pm 1.9\text{E-}04$	0.49	89
	1.0	0.06 ± 0.21	$-7.2\text{E-}05 \pm 2.4\text{E-}04$	0.61	45
	3.0	-0.19 ± 0.23	$2.5\text{E-}04 \pm 2.7\text{E-}04$	0.61	93
B3	0.01	0.10 ± 0.16	$-2.2\text{E-}04 \pm 1.8\text{E-}04$	0.45	99
	0.3	0.05 ± 0.17	$-1.1\text{E-}04 \pm 1.9\text{E-}04$	0.49	72
	1.0	0.01 ± 0.21	$-3.3\text{E-}05 \pm 2.4\text{E-}04$	0.60	22
	3.0	-0.28 ± 0.22	$2.7\text{E-}04 \pm 2.6\text{E-}04$	0.59	95
B4	0.01	0.17 ± 0.17	$-2.7\text{E-}04 \pm 1.9\text{E-}04$	0.48	99
	0.3	0.15 ± 0.17	$-1.4\text{E-}04 \pm 1.9\text{E-}04$	0.49	84
	1.0	0.12 ± 0.21	$-6.7\text{E-}05 \pm 2.4\text{E-}04$	0.61	42
	3.0	0.00 ± 0.22	$2.1\text{E-}04 \pm 2.6\text{E-}04$	0.58	90

5.7 RECOMMENDATIONS FOR BASIN RESPONSE ANALYSIS

Previous chapters of this report have presented relatively simple site amplification functions that account for the effects of shallow geologic conditions on response spectral acceleration. A basic issue associated with basin models is to identify the conditions for which it is worthwhile to apply them as a further correction to the shallow site models. The statistical analyses reported in Section 5.6 indicates that the use of basin models is generally worthwhile for periods $T > \sim 0.75$ s. The basin models are worthwhile because they reduce the intra-event standard deviation, σ. This was shown in Figure 5.22.

The second basic issue is how the basin corrections should be applied. Two general formulations for basin effects have been presented. The first is intended for application with $V_{s\text{-}30}$-based site factors. Three models were developed, denoted “B1–B3,” which are complementary to the A1–A3 models developed in Chapter 4. The second formulation is intended for application with the surface-geology-based site factors developed in Chapter 3, and is denoted “B4.” All basin models involve adjusting the median of the log-normal distribution of spectral acceleration according to Equation 5.4. Smoothed regression coefficients and intra-event standard deviation terms for use in conjunction with Equation 5.4 are presented in Appendix C.

The application of models B1–B3 is somewhat more complicated than the application of B4. This is because the former (B1–B3) requires identification of basin depth at the site ($z_{1.5}$) as well as identifying whether the seismic source location is coincident with the site basin location (CBL) or distinct from the site basin location (DBL), while the latter (B4) requires only $z_{1.5}$. At the long periods of interest to basin effect analyses, the use of B1–B3 is preferred because intra-event standard deviations are lower than for B4, which is shown in Figure 5.22. The standard deviations for the B1–B3 models are relatively low because of distinctly different trends of amplification with $z_{1.5}$ in the CBL and DBL categories.

6 Summary and Conclusions

6.1 SCOPE OF RESEARCH

Seismic hazard analyses (i.e., deterministic seismic hazard analysis and probabilistic seismic hazard analysis) require attenuation relationships to estimate ground motion intensity measures (*IMs*) such as spectral acceleration. In particular, attenuation relationships provide statistical moments of a probabilistic distribution of *IM* conditioned on parameters such as magnitude, site-source distance, site condition, and style-of-faulting parameters. Ground motion data are usually log-normally distributed, in which case the distribution can be represented by a median and standard deviation, σ (in natural logarithmic units). Since site conditions are generally parameterized broadly in attenuation relations (i.e., rock or soil), estimates from attenuation relationships necessarily represent values averaged across the broad range of possible site conditions within the “rock” or “soil” categories. Accordingly, ground motion estimates for site conditions that are different from the category average could be inaccurate.

An objective of this study was to evaluate the degree to which more detailed information on shallow site conditions can improve ground motion predictions relative to what is obtained with attenuation relationships. A related objective was to investigate the degree to which additional information on relatively deep basin structure can improve model predictions. This “improvement” in ground motion prediction generally involves (1) removing potential bias in median ground motion estimates that might be present for a particular site condition and (2) reducing the uncertainty in ground motion estimates, as measured by standard deviation term, σ.

An extensive effort was undertaken to characterize site conditions at strong motion stations to enable the empirical ground motion studies undertaken in this research. Information was compiled on shallow site condition to enable classification of the sites according to (1) surface geologic categories, (2) categories based on a so-called NEHRP classification scheme, which are based on average shear wave velocity in the upper 30 m ($V_{s\text{-}30}$), (3) geotechnical site categories that consider soil stiffness and depth (although the range of depths differentiated by the method are shallow and do not enable parameterization of deep basin structure), and (4) direct use of $V_{s\text{-}30}$ as a site parameter. Also compiled were parameters that reflect the relatively deep sedimentary structure at many of the strong motion sites. Through evaluation of seismological simulation results by others, it was decided to consider sediment thickness as parameterized by depth to the 1.5 km/s shear wave isosurface ($z_{1.5}$) as well as the location of the source inside or outside of the basin in which the site is located. The site/source location consideration is an original feature of this research; sites located in a basin overlying the source are denoted as having coincident source and site basin locations (CBL) and are differentiated from distinct source and site basin locations (DBL).

To investigate the effect of shallow site conditions on ground motions, empirical amplification models were developed. To facilitate the development of those models, site conditions were described according to categories associated with site classification schemes (Chapter 3) or by the average shear wave velocity in the upper 30 m, $V_{s\text{-}30}$ (Chapter 4). Amplification factors were derived for individual ground motion recordings using a non-reference site method in which 5% damped response spectral accelerations from recorded ground motions were normalized by reference motions derived from modified rock attenuation relationships for active regions. The amplification models were developed through statistical regression analyses to relate amplification to site parameters and the amplitude of shaking on the reference site condition. The amplification models provide estimates of the median *IM* for the site condition. Standard deviation (σ) is also estimated from the data residuals.

The evaluation of basin amplification effects utilized residuals between data and ground motion predictions for shallow site conditions. Statistical analyses were performed to relate those residuals to $z_{1.5}$ for CBL and DBL sites. The qualitative nature of those relationships was compared to similar relationships derived using data from ground motion simulations for southern California basins (by others). The results are interpreted to identify the conditions for which use of the basin models is beneficial from the standpoint of bias and dispersion reduction.

6.2 RESEARCH FINDINGS AND RECOMMENDATIONS

The results of this research can be broadly categorized as follows: (a) results providing insight into the optimal site categorization scheme for deriving amplification factors, (b) results showing the variation of amplification factors and standard deviation with shallow site descriptors, and (c) results related to the use of basin parameters for defining additional contributions to site amplification beyond that associated with shallow site condition. The major conclusions from the study are grouped according to those subjects in the sections that follow. A comprehensive set of recommendations for using amplification factors are then provided.

6.2.1 Major Technical Findings

(a) Optimal Classification Scheme Based on Shallow Site Descriptors

The identification of an "optimized" classification scheme should consider two factors: (1) the degree to which amplification factors defined for categories within the scheme are capable of capturing site-to-site variations in ground motion, as measured by the dispersion of prediction residuals and (2) the degree to which amplification levels between categories within the various schemes are distinct from each other. For the $V_{s\text{-}30}$-based site descriptor, there are no site categories, so the efficacy of the scheme is evaluated solely on the basis of the dispersion of prediction residuals.

Dispersion criteria: Site descriptors found to be effective at minimizing standard deviation are $V_{s\text{-}30}$ or, for soil sites, a detailed description of surface geology that takes into consideration sediment age + depositional environment or age + sediment texture. For rock sites, NEHRP- and age only surface-geology-based site categories are roughly equally effective. The results supporting this conclusion were presented in Figures 4.15 and 3.10(b).

Criteria for distinct site categories: The NEHRP classification scheme is the only one for which amplification levels between categories are generally distinct across a wide period range. At small periods, detailed surface geology categories also have distinct amplification levels.

In consideration of these results, the optimal descriptors of shallow site condition for strong motion studies appear to be $V_{s\text{-}30}$ or detailed surface geology.

(b) Trends in Amplification Factors and Standard Deviation Terms

The unified model of site amplification as a function of V_{s-30} shows a number of important trends. Similar trends can generally be identified from careful examination of category-based amplification models.

Amplification for a broad range of periods was found to decrease with increasing velocity. The nonlinearity of amplification factors varies with V_{s-30}, being significant across a broad period range for V_{s-30} < 180 m/s, and relatively small for V_{s-30} > 300 m/s. Representative results are shown in Figure 4.6.

Standard deviation (σ) generally increases with V_{s-30}, although the amount of increase is strongly period dependent. At small periods ($T \leq \sim 0.15$ s) the amount of increase of σ is small, but for $T \geq 1.0$ s, increases from low to high V_{s-30} are 0.1-0.3 in natural logarithmic units, with larger increases occurring at longer periods. Representative results are shown in Figure 4.9(b).

The V_{s-30}-based amplification models developed in this research provide insight into the accuracy of the site coefficients in the existing NEHRP provisions and commentary (BSSC, 2001). As shown in Figure 4.13, there are significant discrepancies between amplification factors in this study and those in the NEHRP provisions, with site factors in this study generally being lower. There will be additional bias for soft soil sites due to the lower standard deviation for those sites. This bias in standard deviation causes ground motion levels estimated by the current NEHRP provisions to be too large. Finally, it was found that the rock attenuation relationships used in the development of national seismic hazard maps contain a bias because they are formulated for softer rock conditions than the reference site condition of V_{s-30} = 760 m/s. The correction factors for the various attenuation models can be evaluated using Equation 4.6 and coefficients tabulated in Appendix B.

(c) Amplification as a Function of Basin Parameters

Effect on ground motions: For sites located in basins overlying the seismic source, ground motions at periods $T > \sim 0.3$ s increase with sediment thickness, as parameterized by depth to the 1.5 km/s shear wave isosurface ($z_{1.5}$). No significant dependence on $z_{1.5}$ is observed at short periods. When the seismic source is located outside of the basin margin, ground motions are not observed to vary with $z_{1.5}$ at short or long periods.

Benefit of using basin amplification models: The statistical analyses reported in Section 5.6 indicates that the use of basin models is generally worthwhile for periods $T > \sim 0.75$ s. The basin models are worthwhile because they reduce the intra-event standard deviation, σ relative to the use of $V_{s\text{-}30}$-based amplification factors alone. This was shown in Figure 5.22. The basin models are most effective at minimizing standard deviation when they are coupled with $V_{s\text{-}30}$-based models for shallow site amplification (in lieu of amplification factors defined from more generic surface-geology-based amplification factors).

6.2.2 Recommendations for Application of Amplification Factors

Amplification factor models are applied by modifying the median ground motion from a rock attenuation relationship and by replacing the standard deviation term. It is generally recommended that amplification factors be derived using $V_{s\text{-}30}$-based shallow site factors coupled with basin amplification factors that account for sediment depth and the location of the source inside or outside of the basin boundary. The $V_{s\text{-}30}$-based model is applied by using Equations 4.1 and 4.3 with model parameters from Appendix B for the corresponding attenuation models (i.e., A1—Abrahamson and Silva; A2—Sadigh et al.; A3—Campbell and Bozorgnia). The corresponding error term can be taken as σ_{total} from Appendix B or for a more accurate assessment, can be evaluated using Equation 4.4 with τ taken from Appendix B and σ calculated using the site-dependent model in Equation 4.5 (in which case, σ is denoted "σ_v"). The basin models involve further adjusting the median of the log-normal distribution of spectral acceleration according to Equation 5.4 (using basin model B1 in conjunction with A1, B2 with A2, etc.). Smoothed regression coefficients and intra-event standard deviation terms for use in conjunction with Equation 5.4 are presented in Appendix C.

An alternative procedure that might be simpler to apply involves using surface-geology-based amplification functions from this study in conjunction with basin model B4. The surface geology-based factors are given by Equation 3.3(a) and the coefficients in Appendix A. The median amplification factors are significantly different from the Abrahamson and Silva site terms for rock categories (e.g., T, M+I) and soft soil categories (e.g., Hlm). The standard deviation term is given by Equation 3.10. The corresponding basin model is B4 (used with Equation 5.4 and the coefficients in Appendix C), which does not distinguish CBL and DBL source/site locations. Application of the simpler procedure is accompanied by the "penalty" of increased standard deviation.

6.3 RECOMMENDATIONS FOR FUTURE RESEARCH

Some issues that should be considered in future research include:

- Data from a series of Taiwan earthquakes and the recent Alaska earthquakes are not included in this research. It will be of interest to evaluate whether the amplification trends with $V_{s\text{-}30}$ and basin parameters identified from the present research (based principally on California data) are also observed in data from other regions.
- The basin geometry for the San Francisco Bay Area is not as well constrained as that for southern California. Due in part to the relatively low quality of the model, source and site basin location parameters (i.e., CBL or DBL) were not applied to the analysis of ground motion data. Research is ongoing to better define the basin geometry, and once this work is complete, the ground motion analyses should be repeated to evaluate whether the trends from southern California are replicated.
- The amplification factor models from this study may need to be re-evaluated as new attenuation models are developed (e.g., models from the Next Generation Attenuation project).

REFERENCES

Abrahamson, N.A. (2000). "Effects of rupture directivity on probabilistic seismic hazard analysis," *Proc. 6th Int. Conf. on Seismic Zonation*, Palm Springs.

Abrahamson, N.A. and Shedlock, K.M. (1997). "Overview (of modern attenuation relationships)," *Seism. Res. Letters*, 68(1), 9-23.

Abrahamson, N.A. and Silva, W.J. (1997). "Empirical response spectral attenuation relations for shallow crustal earthquakes," *Seism. Res. Letters*, 68(1), 94-127.

Abrahamson, N.A. and Youngs, R.R. (1992). "A stable algorithm for regression analyses using the random effects model," *Bull. Seism. Soc. Am.*, 82, 505-510.

Anderson, J.G., Trifunac, M.D., Teng, T.-L., Amini, A., and Moslem, K. (1981). "Los Angeles vicinity strong motion accelerograph network," *Report No. CE 81-04*, Univ. of Southern California.

Ang, A.H.-S. and Tang, W.H. (1975). *Probability Concepts in Engineering Planning and Design, Volume I – Basic Principles*, John Wiley & Sons, New York, NY.

Baher, S.A., and Davis, P.M. (2003). "An application of seismic tomography to basin focusing of seismic waves and Northridge earthquake damage" *Journal of Geophysical Research-Solid Earth*, 108(B2), Art. No.2122.

Baturay, M.B. and Stewart, J.P. (2003). "Uncertainty and bias in ground motion estimates from ground response analyses," *Bull. Seism. Soc. Am.*, 93, 2025-2042.

Bazzuro, P. (1998). "Probabilistic seismic demand analysis," *Ph.D. Dissertation*, Civil Engineering Dept., Stanford University.

Beresnev, I.A. and Atkinson, G.M. (2002). "Source parameters of earthquakes in Eastern and Western North America based on finite-fault modeling," *Bull. Seism. Soc. Am.*, 92 (2), 695-710.

Beresnev, I.A. and Atkinson, G.M. (1998). "FINSIM: a FORTRAN program for simulating stochastic acceleration time histories from finite faults," *Seism. Res. Letters*, 69 (1), 27-32.

Boatwright, J., Seekins, L.C., and Mueller, C.S. (1991). "Ground motion amplification in the Marina," *Bull. Seism. Soc. Am.*, 81, 1980-1997.

Boore, D.M. (2003). "A compendium of P- and S-wave velocities from surface- to-borehole logging: Summary and reanalysis of previously published data and analysis of unpublished data," *Open-File Rept.*, 03-191., U.S. Geol. Surv.

Boore, D.M. (1983). “Stochastic simulation of high-frequency ground motions based on seismological models of the radiated spectra,” *Bull. Seism. Soc. Am.* 73, 1865-1894.

Boore, D.M., Joyner, W.B., and Fumal, T.E. (1997). “Equations for estimating horizontal response spectra and peak acceleration from western North American earthquakes: A summary of recent work,” *Seism. Res. Letters*, 68(1), 128-153.

Borcherdt, R.D. (2002a). “Empirical evidence for acceleration-dependent amplification factors,” *Bull. Seism. Soc. Am.*, 92, 761-782.

Borcherdt, R.D. (2002b). “Empirical evidence for site coefficients in building code provisions,” *Earthquake Spectra*, 18 (2), 189-217.

Borcherdt, R.D. (1994). “Estimates of site-dependent response spectra for design (methodology and justification),” *Earthquake Spectra*, 10(4), 617-653.

Borcherdt, R. D. and Glassmoyer, G. (1994). "Influences of local geology on strong and weak ground motions recorded in the San Francisco Bay region and their implications for site-specific building-code provisions" The Loma Prieta, California Earthquake of October 17, 1989--Strong Ground Motion, *Profess. Paper 1551-A,* U.S. Geol. Surv. A77-A108.

Brocher, T.M. and Pope, D.C. (1994). “Onshore-offshore wide-angle seismic recordings of the San Francisco Bay area seismic imaging experiment (BASIX): Data from the Northern California seismic network,” *Open-File Rept., 94-0156*., U.S. Geol. Surv.

Building Seismic Safety Council, BSSC (2001). *NEHRP Recommended Provisions for Seismic Regulations for New Buildings and Other Structures, Part 1 – Provisions and Part 2 – Commentary*, Federal Emergency Management Agency, Washington D.C., February.

Campbell, K.W. (2001). Erratum to Campbell, 2000, *Seism. Res. Letters*, 72(4), p 474.

Campbell, K.W. (2000). Erratum to Campbell, 1997, *Seism. Res. Letters*, 71(3), 352-354.

Campbell, K.W. (1997). “Empirical near-source attenuation relations for horizontal and vertical components of peak ground acceleration, peak ground velocity, and pseudo-absolute acceleration response spectra,” *Seism. Res. Letters*, 68(1), 154-179.

Campbell, K. W. and Bozorgnia, Y. (2003). “Updated near-source ground-motion (attenuation) relations for the horizontal and vertical components of peak ground acceleration and acceleration response spectra,” *Bull. Seism. Soc. Am.,* 93, 314-331.

Chang, S.W., and Bray, J.D. (1998). “Implications of recent strong motion data for seismic building code design at deep, stiff soil sites,” *Proc., NEHRP Conference and Workshop on*

Research on the Northridge, California Earthquake of January 17, 1994, California Universities for Research in Earthquake Engineering, Richmond, California, 90-99.

Choi, Y. and Stewart, J.P. (2005). "Nonlinear site amplification as function of 30m shear wave velocity," *Earthquake Spectra*, 21(1), in press.

Cook, R.D. and Weisberg, S. (1999). *Applied regression including computing and graphics*, John Wiley & Sons, Inc., New York, NY.

Carver, D. and Hartzell, S. H. (1996). "Earthquake site response in Santa Cruz, California," *Bull. Seism. Soc. Am.*, 86, 55-65.

Chang, S.W. (1996). "Seismic response of deep stiff soil deposits," *Ph.D. Dissertation*, Univ. of California, Berkeley.

Dickenson, S.E. (1994). "The dynamic response of soft and deep cohesive soils during the Loma Prieta earthquake of October 17, 1989," *Ph.D. Dissertation*, Univ. of California, Berkeley.

Dobry, R., Borcherdt, R.D., Crouse, C.B., Idriss, I.M., Joyner, W.B., Martin, G.R., Power, M.S., Rinne, E.E., and Seed, R.B. (2000). "New site coefficients and site classification system used in recent building seismic code provisions," *Earthquake Spectra*, 16 (1), 41-67.

Dobry, R., Martin, G.R., Parra, E. and Bhattacharyya, A. (1994). "Development of site-dependent ratios of elastic response spectra (RRS) and site categories for buildings seismic codes," *Proceedings of the 1992 NCEER/SEAOC/BSSC Workshop on Site Response During Earthquakes and Seismic Code Provisions*, G.R. Martin, ed., University of Southern California, National Center for Earthquake Engineering Research Special Publication NCEER-94-SP01, Buffalo, NY.

Earthquake Engineering Research Center (1995). "Geotechnical reconnaissance of the effects of the January 17, 1995 Hyogoken-Nanbu earthquake, Japan," *Report No. UCB/EERC-95/01*, University of California, Berkeley, N. Sitar, editor.

Faust, L.Y. (1951). "Seismic velocity as a function of depth and geologic time," *Geophysics*, 16, 192-206.

Field, E.H. (2000). "A modified ground motion attenuation relationship for southern California that accounts for detailed site classification and a basin depth effect," *Bull. Seism. Soc. Am.*, 90, S209-S221.

Field, E.H., and Jacob, K.H. (1995). "A comparison and test of various site-response estimation techniques, including three that are not reference-site dependent," *Bull. Seism. Soc. Am.*, 85, 1127-1143.

Field, E.H. and Petersen, M.D. (2000). "A test of various site-effect parameterizations in probabilistic seismic hazard analyses of Southern California," *Bull. Seism. Soc. Am*., 90, S222-S244.

Frankel, A., Mueller, C., Barnhard, T., Leyendecker, E., Wesson, R., Harmsen, A., Klein, F, Perkins, D., Dickman, N., Hanson, S., and Hopper, M. (2000). "USGS national seismic hazard maps," *Earthquake Spectra*, 16 (1), 1-20.

Frankel, A. and Vidale, J. (1992). "A three-dimensional simulation of seismic waves in the Santa Clara Valley, California, from a Loma Prieta aftershock," *Bull. Seism. Soc. Am*., 82, 2045-2074.

Fukushima, Y., Irikura, K., Uetake, T., and Matsumoto, H. (2000). "Characteristics of observed peak amplitude for strong ground motion from the 1995 Hyokoken Nanbu (Kobe) earthquake," *Bull. Seism. Soc. Am*., 90, 545-565.

Fumal, T. E. (1978). "Correlation between seismic wave velocities and physical properties of near surface geologic materials in the southern San Francisco bay region, California," *Open-File Rept*., *78-1067*, U.S. Geol. Surv., 114pp.

Geomatrix Consultants (1993). "Compilation of geotechnical data for strong motion stations in the Western United States," *Report to Lawrence Livermore National Lab*., Project No. 2256.

Graves, R. W. (1993). "Modeling three-dimensional site response effects in the Marina District, San Francisco, California," *Bull. Seism. Soc. Am.*, 83, 1042-1063.

Graves, R. W., A. Pitarka, and P. G. Somerville (1998). "Ground motion amplification in the Santa Monica area: effects of shallow basin edge structure," *Bull. Seism. Soc. Am.*, 88, 1224-1242.

Hadley, D. and Kanamori, H. (1977). "Seismic structure of the Transverse Ranges, California," *Geol. Soc. Am. Bull*. 88, 1469-1478.

Hanks, T. C. (1975). "Strong ground motion of the San Fernando, California earthquake: Ground displacements," *Bull. Seism. Soc. Am.*, 65, 193-225.

Harmsen, S.C. (1997). "Determination of site amplification in the Los Angeles urban area from inversion of strong motion records," *Bull. Seism. Soc. Am.*, 87, 866-887.

Hartzell, S. (1985). "The use of small earthquake as Green's functions," in *Strong Motion Simulation and Earthquake Engineering Application*s, Publication 85-02, R. E. Scholl and J. L. King, ed., Earthquake Engineering Research Institut*e,* El Centro, CA.

Hartzell, S. (1978). “Earthquake aftershocks as Green’s functions,” *Geophysical Research Letter,* 5, 1-4.

Hartzell, S.A., Cranswick, E., Frankel, A., Carver, D., and Meremonte, M. (1997). “Variability of site response in the Los Angeles urban area,” *Bull. Seism. Soc. Am.*, 87, 1377-1400.

Hartzell, S.A., Carver, D., Cranswick, E., and Frankel, A. (2000). “Variability of site response in Seattle, Washington,” *Bull. Seism. Soc. Am.*, 90, 1237-1250.

Hartzell, S., Harmsen, S., Frankel, A., and Larsen, S., (1999). “Calculation of broadband time histories of ground motion; Comparison of methods and validation using strong-ground motion from the 1994 Northridge earthquake,” *Bull. Seism. Soc. Am.,* 89, 1484-1504.

Hashash, Y.M.A. and Park, D. (2001). “Nonlinear one-dimensional seismic ground motion propagation in the Mississippi embayment,” *Engineering Geology*, 62 (1-3), 185-206.

Helmberger, D, Stead, R, Ho-Liu, P., and Dreger, D. (1992). “Broadband modeling of regional seismograms; Imperial Valley to Pasadena,” *Geophysical Journal International*, 110 (1), 42-54.

Hole, J.A. (1992). “Nonlinear high-resolution three-dimensional seismic travel time tomography,” *J. Geophys. Res.*, 97, 6553-6562.

Hole, J.A., Brocher, T.M., Klemperer, S.L., Parsons, T., Benz, H.M., and Furlong, K.P. (2000). “Three-dimensional seismic velocity structure of the San Francisco Bay area,” *J. Geophys. Res.*, *105*, B6, 13859-13874.

Hruby, C.E. and Beresnev, I.A. (2003). “Empirical corrections for basin effects in stochastic ground motion prediction, based on Los Angeles basin analysis,” *Bull. Seism. Soc. Am.,* 93 (4), 1679-1690.

Hutchings, L., (1994). “Kinematic earthquake models and synthesized ground motion using empirical Green’s functions,” *Bull. Seism. Soc. Am*., 84, 1028-1050.

Irikura, K. (1983). “Semi-empirical estimation of strong ground motions during large earthquakes,” *Bulletin, Disaster Prevention Research Institute,* Kyoto University, Kyoto, Japan, Vol 33, pp 63-104.

Joyner, W.B. (2000). “Strong motion from surface waves in deep sedimentary basins,” *Bull. Seism. Soc. Am.*, 90, S95-S112.

Joyner, W.B. and Boore, D.M. (2000). “Recent developments in earthquake ground motion estimation,” *Proc. 6th Int. Conf. on Seismic Zonation*, Earthquake Engineering Research Institute, Oakland, CA.

Joyner, W.B. and Boore, D.M. (1994). “Errata: Method for regression analysis of strong motion data,” *Bull. Seism. Soc. Am.*, 84, 955-956.

Joyner, W.B. and Boore, D.M. (1993). “Prediction of earthquake response spectra,” *Open-File Rept. 82-977*. U.S. Geol. Surv., 16pp.

Kawase, H. (1996). “The cause of the damage belt in Kobe: The‘basin edge effect,’ constructive interference of the direct S-wave with the basin induced diffracted/Rayleigh waves,” *Seism. Res. Letters*, 67(5), 25-34.

Komatitsch, D., Liu, Q., Tromp, J., Süss, P., Stidham, C., and Shaw, J.H. (2004). “ Simulations of ground motion in the Los Angeles basin based upon the spectral-element method,” *Bull. Seism. Soc. Am.*, 94, 187-206.

Lee, Y. and Anderson, J.G. (2000). “A custom southern California ground motion relationship based on analysis of residuals,” *Bull. Seism. Soc. Am.*, 90, S170-S187.

Lee, C.-T., Cheng, C.-T., Liao, C.-W., and Tsai, Y.-B. (2001). “Site classification of Taiwan free-field strong motion stations,” *Bull. Seism. Soc. Am*., 91, 1283-1297.

Leyendecker, E.V., Hunt, R.J., Frankel, A.D., and Rukstales, K.S. (2000). “Development of maximum considered earthquake ground motion maps,” *Earthquake Spectra*, 16 (1), 21-40.

Liu, H. L., and Heaton, T. H. (1984). “Array analysis of the ground velocities and accelerations from the 1971 San Fernando California earthquake,” *Bull. Seism. Soc. Am.*, 74, 1951-1968.

Luco, J. E., and Apsel, R. J. (1983). “On the Green’s functions for a layered half-space, I,” *Bull. Seism. Soc. Am.,* 73, 909-929.

Ludwig, W.J., Nafe, J.E., and Drake, C.L. (1970). “Seismic refraction,” in *The Sea*, Maxwell, A.E. (editor) Vol. 4, Wiley-Interscience, New York, 53-84.

Luke, B.A., Matasovic, N., and Kemnitz, M. (2001). “Evaluating the seismic response of deep sandy soil deposits,” *Bull. Seism. Soc. Am.*, 91 (6), 1516-1525.

Magistrale, H., Day, S., Clayton, R., and Graves, R. (2000). “The SCEC southern California reference three-dimensional seismic velocity model version 2,” *Bull. Seism. Soc. Am.*, 90, S65-S76.

Magistrale, H., Graves, R., and Clayton, R. (2000). “A standard three-dimensional seismic velocity model for southern California: Version 1,” *EOS Trans. AGU* 79, F605.

Martin, G.M. editor (1994). *Proceedings of the NCEER/SEAOC/BSSC Workshop on Site Response during Earthquakes and Seismic Code Revisions*, Univ. of Southern Calif.

McCulloh, T.H. (1960). “Gravity variation and the geology of the Los Angeles basin of California,” *Profess. Paper 400-B*, U.S. Geol. Surv., 320-325.

Morton, D.M., Hauser, R.M., and Ruppert, K.R. (1999). “Preliminary Digital Geologic Map of the Santa Ana 30' x 60' Quadrangle, Southern California,” *Open-File Rept. 99-172*, U.S. Geol. Surv., Menlo Park, CA.

Nafe, J.E. and Drake, C.L. (1960). “Physical properties of marine sediments,” in *The SEA*, Hill, M.N. (Editor) Vol. 3. Interscience, New York, 794-815

Ni, S.D., Siddharthan, R.V., and Anderson, J.G. (1997). “Characteristics of nonlinear response of deep saturated soil deposits,” *Bull. Seism. Soc. Am.,* 87, 342-355.

Olson, A.H., Orcutt, J.A., and Frazier, G.A. (1984). “The discrete wavenumber/finite element method for synthetic seismograms,” *J.R. Astr. Soc*., 77, 421 – 460.

Olsen, K.B. (2000). “Site amplification in the Los Angeles basin from three-dimensional modeling of ground motion,” *Bull. Seism. Soc. Am.,* 90, S77-S94.

Olsen, K.B. and Schuster, G.T. (1994). “Three-dimensional modeling of site amplification in East Great Salt Lake Basin,” *Tech. Rept., 1434-93-G-2345*, U.S. Geol. Surv., 102 pp.

Olsen, K.B., Pechmann, J.C., and Schuster, G.T. (1995). “Simulation of 3-D elastic wave propagation in the Salt Lake Basin,” *Bull. Seism. Soc. Am.,* 85, 1688-1710.

Pinheiro, J. C. and Bates, D. M. (2000). *Mixed-Effects Models in S and S-PLUS,* Springer.

Pitarka, A., K. Irikura, T. Iwata and H. Sekiguchi (1998). “Three-dimensional simulation of the near-fault ground motion for the 1995 Hyogo-ken Nanbu (Kobe), Japan, earthquake,” *Bull. Seism. Soc. Am*. 88, 428-440.

Rathje, E., Idriss, I. M. and Somerville, P. (2000). Chapter 4: Strong ground motions and site effects. Kocaeli, Turkey Earthquake of August 17, 1999 Reconnaissance Report, T.L. Youd, J.P. Bardet, and J.D. Bray, eds., *Earthquake Spectra*, Supplement A to Vol. 16, 65-96.

Rathje, E.M., Stokoe II, K.H., and Rosenblad, B. (2003). “Strong motion station characterization and site effects during the 1999 earthquakes in Turkey,” *Earthquake Spectra*, 19(3), 653-675.

Raudenbush, S.W. and Bryk, A.S. (2002). *Hierarchical linear models: applications and data analysis methods*, 2^{nd} Edition, Sage Publications, Thousand Oaks, CA.

Rodriguez-Marek, A., Bray, J.D., and Abrahamson, N.A. (2001). “An empirical geotechnical seismic site response procedure,” *Earthquake Spectra*, 17(1), 65-87.

Sadigh, K. (1993). "A review of attenuation relationships for rock site conditions from shallow crustal earthquakes in an interplate environment," *Proc. Int. Workshop on Strong Motion Data*, 2, 179-236, Menlo Park, CA.

Sadigh, K., Chang, C.-Y., Abrahamson, N.A., Chiou, S.J., and Power, M.S. (1993). "Specification of long-period ground motions: updated attenuation relationships for rock site conditions and adjustment factors for near-fault effects," *Proc. Seminar on Seismic Isolation, Passive Energy Dissipation, and Active Control*, Applied Technology Council Publication No. 17-1, Vol. 1, 59-70.

Sadigh, K., Chang, C.-Y., Egan, J.A., Makdisi, F., and Youngs, R.R. (1997). "Attenuation relations for shallow crustal earthquakes based on California strong motion data," *Seism. Res. Letters*, 68(1), 180-189.

Salvati, L.A., Lok, T.M.H., and Pestana, J.M. (2001). "Seismic response of deep stiff granular soil deposits," *Proc. Fourth International Conference on Recent Advances in Geotechnical Earthquake Engineering and Soil Dynamics* [computer file]; 6 pages

Sato, T., Graves, R.W. and Somerville, P.G. (1999). "3D finite difference simulations of long period strong motions in the Tokyo metropolitan are during the 1990 Odawara earthquake (Mj 5.1) and the Great 1923 Kanto earthquake (Ms 8.2) in Japan," *Bull. Seism. Soc. Am.*, 89, 579-598.

Seed, R.B., Dickenson, S.E., Rau, G.A., White, R.K., and Mok, C.M. (1994). "Observations regarding seismic response analyses for soft and deep clay sites," *Proceedings of the 1992 NCEER/SEAOC/BSSC Workshop on Site Response During Earthquakes and Seismic Code Provisions*, G.R. Martin, ed., University of Southern California, National Center for Earthquake Engineering Research Special Publication *NCEER-94-SP01*, Buffalo, NY.

Seed, H. B. and Idriss, I. M. (1982) "Ground motions and soil liquefaction during earthquakes" *Monograph Series, Vol. 5*, Earthquake Engineering Research Institute.

Seed, H.B., Ugas, C. and Lysmer, J. (1974). "Site-dependent spectra for earthquake-resistant design," *Report No. UCB/EERC-74/12*, Earthquake Engineering Research Center, University of California.

Silva, W.J., Abrahamson, N., Toro, G., and Costantino, C. (1997). "Description and validation of the stochastic ground motion model," *Report to Brookhaven National Laboratory*, Associated Universities, Inc., Upton, NY, available at: http://www.pacificengineering.org.

Silva, W.J. and Lee, K. (1987). “WES RASCAL code for synthesizing earthquake ground motions,” *in State of the Art for Assessing Earthquake Hazards in the United States, Report 24*, U.S. Army Engineers Waterway Experiment Station, *Misc. Paper S-73-1*.

Silva, W.J., Li, S., Darragh, R., and Gregor, N. (1999). “Surface geology based strong motion amplification factors for the San Francisco Bay and Los Angeles areas,” Report to Pacific Earthquake Engineering Research Center.

Silva, W.J., Darragh, R., Gregor, N., Martin, G., Abrahamson, N., and Kircher, C. (2000). “Reassessment of site coefficients and near-fault factors for building code provisions,” *Report to U.S. Geol. Surv.*, National Earthquake Hazards Reduction Program.

Shoja-Taheri, J. and Anderson, J. G. (1988). “The 1978 Tabas, Iran, earthquake: an interpretation of the strong motion records,” *Bull. Seism. Soc. Am*., 78, 142-171.

Sokolov, V.Y. (1997). “Empirical models for estimating Fourier-amplitude spectra of ground acceleration in the northern Caucasus (Racha seismogenic zone),” *Bull. Seism. Soc. Am.*, 87, 1401-1412.

Sokolov, V.Y., Loh, C.-H., and Wen, K.-L. (2000). “Empirical study of sediment-filled basin response: The case of Taipei City,” *Earthquake Spectra*, 16(3), 681-707.

Somerville, P.G., Collins, N.F., Graves, R.W. and Pitarka, A. (2004). “An engineering ground motion model for basin generated surface waves,” *Proc. 13th World Conference on Earthquake Engineering*, Vancouver, Canada, Paper 515.

Somerville, P.G., Smith, N.F., Graves, R.W. and Abrahamson, N.A. (1997). “Modification of empirical strong ground motion attenuation relations to include the amplitude and duration effects of rupture directivity,” *Seism. Res. Letters,* 68, 199-222.

Spudich, P., Joyner, W.B., Lindh, A.G., Boore, D.M., Margaris, B.M., and Fletcher, J.B. (1999). “SEA99: A revised ground motion prediction relation for use in extensional tectonic regimes,” *Bull. Seism. Soc. Am.*, 89, 1156-1170.

Steidl, J.H. (2000). “Site response in southern California for probabilistic seismic hazard analysis,” *Bull. Seism. Soc. Am.*, 90, S149-S169.

Steidl, J.H. and Lee, Y. (2000). “The SCEC phase III strong-motion database,” *Bull. Seism. Soc. Am.*, 90, S113-S135.

Stephenson, W. J., Williams, R. A., Odum, J. K., and Worley, D. M. (2000). “High-resolution seismic reflection surveys and modeling across an area of high damage from the 1994 Northridge earthquake, Sherman Oaks, California,” *Bull. Seism. Soc. Am.*, 90, 643-654.

Stewart, J.P. and Liu, A.H. (2000). "Ground motion amplification as a function of surface geology," *Proc. SMIP2000 Seminar on Utilization of Strong Motion Data*, California Strong Motion Instrumentation Program, Sacramento, CA, 1-22.

Stewart, J.P., Liu, A.H., Choi, Y., and Baturay, M.B. (2001). "Amplification factors for spectral acceleration in active regions," *Report No. PEER-2001/10*, Pacific Earthquake Engineering Research Center, UC Berkeley, California.

Stewart, J.P., Liu, A.H., and Choi, Y. (2003). "Amplification factors for spectral acceleration in tectonically active regions," *Bull. Seism. Soc. Am.*, 93 (1), 332-352.

Süss, M. P. and Shaw, J. H. (2003). "P wave seismic velocity structure derived from sonic logs and industry reflection data in the Los Angeles basin, California," *Journal of Geophysical Research-Solid Earth*, 108 (B3): Art. No. 2170.

Toomey, C.H and Foulger, G.R. (1989). "Tomographic inversion of local earthquake data from the Hengill-Grensdalur central volcano complex, Iceland," *J. Geophys. Res.,* 94, 17497-17510.

Trifunac, M.D. and Lee, V.W. (1978). "Dependence of the Fourier amplitude spectra of strong motion acceleration on the depth of sedimentary deposits," *Report No. CE 78-14*, University of Southern California, Civil Engineering Department.

Vidale, J.E. (1990). "Finite-difference calculation of travel times in three dimensions," *Geophysics, 55*, 521-526.

Wen, K-L. and Peng, H-Y. (1998). "Strong motion observations in the Taipei basin," The Effects of Surface Geology on Seismic Motion, Recent Progress and New Horizon on ESG Study, *Proceedings of the Second International Symposium*, A.A. Balkema, Rotterdam, Vol. 1, p. 263-270.

Westermo, B.D., and Trifunac, M.D. (1978). "Correlations of the frequency dependent duration of strong earthquake ground motion with the magnitude, epicentral distance, and depth of sediments at the recording site," *Report No. CE 78-12*, University of Southern California, Civil Engineering Department.

Wills, C.J. and Silva, W. (1998). "Shear wave velocity characteristics of geologic units in California," *Earthquake Spectra*, 14(3), 533-556.

Wills, C.J. Petersen, M., Bryant, W.A., Reichle, M., Saucedo, G.J., Tan, S., Taylor, G., and Treiman, J. (2000). "A site conditions map for California based on geology and shear wave velocity," *Bull. Seism. Soc. Am.*, 90, S187-S208.

Wright, T.L. (1991). “Structural geology and tectonic evolution of the Los Angeles basin, California,” *AAPG Memoir 52*, 35-134.

Yerkes, R.F., McCulloh, T.H., Schoellhamer, J.E., and Vedder, J.G. (1965). “Geology of the Los Angeles basin of California: an introduction,” *Profess. Paper 420-A*, U.S. Geol. Surv., 1-57.

Youngs, R.R. (1993). “Soil amplification and vertical to horizontal ratios for analysis of strong motion data from active tectonic regions,” Appendix 2C in Guidelines for Determining Design Basis Ground Motions, Vol. 2, Electrical Power Research Institute, *Report No. TR-102293*.

Youngs, R.R., Abrahamson, N.A., Makdisi, F.I., and Sadigh, K. (1995). “Magnitude-dependent variance of peak ground acceleration,” *Bull. Seism. Soc. Am.*, 85, 1161-1176.

Zhang, B., and Papageorgiou, A.S. (1996). “Simulation of the response of the Marina district basin, San Francisco, California, to the 1989 Loma Prieta earthquake,” *Bull. Seism. Soc. Am.*, 86, 1382-1400.

Appendix A

App. A.1 Surface geology categories (smoothed)

Period	M+I			T			P			Hlm			Qa			Hc			Hm		
(s)	a	b	σ	a	b	σ	a	b	σ	a	b	σ	a	b	σ	a	b	σ	a	b	σ
0.01	-0.13	-0.08	0.52	0.23	-0.02	0.62	0.14	0.02	0.47	-0.59	-0.39	0.47	-0.15	-0.13	0.52	-0.11	-0.10	0.52	-0.50	-0.33	0.51
0.02	-0.13	-0.08	0.52	0.17	-0.03	0.62	0.08	0.00	0.47	-0.55	-0.39	0.48	-0.14	-0.13	0.52	-0.10	-0.10	0.52	-0.48	-0.31	0.52
0.03	-0.11	-0.05	0.54	0.14	-0.03	0.63	0.03	0.00	0.48	-0.57	-0.36	0.49	-0.24	-0.14	0.52	-0.17	-0.10	0.52	-0.51	-0.29	0.52
0.04	-0.17	-0.03	0.56	-0.05	-0.03	0.64	-0.19	-0.02	0.48	-0.63	-0.33	0.50	-0.49	-0.14	0.51	-0.39	-0.10	0.53	-0.60	-0.29	0.52
0.05	-0.17	-0.02	0.55	-0.05	-0.04	0.66	-0.19	-0.01	0.47	-0.72	-0.34	0.47	-0.47	-0.13	0.51	-0.38	-0.09	0.53	-0.67	-0.27	0.50
0.06	-0.13	0.00	0.55	-0.05	-0.03	0.65	-0.19	-0.03	0.46	-0.70	-0.31	0.45	-0.46	-0.14	0.50	-0.36	-0.08	0.54	-0.66	-0.27	0.50
0.08	-0.11	-0.01	0.54	-0.05	-0.04	0.63	-0.20	-0.03	0.45	-0.70	-0.32	0.48	-0.43	-0.12	0.50	-0.29	-0.05	0.54	-0.66	-0.26	0.49
0.09	-0.10	-0.01	0.52	-0.05	-0.02	0.62	-0.09	0.01	0.45	-0.67	-0.31	0.52	-0.36	-0.11	0.51	-0.20	-0.01	0.55	-0.64	-0.25	0.49
0.10	-0.13	-0.02	0.51	-0.05	-0.03	0.61	-0.07	0.00	0.45	-0.67	-0.29	0.53	-0.35	-0.11	0.52	-0.18	-0.01	0.55	-0.62	-0.23	0.51
0.12	-0.16	-0.05	0.52	-0.05	-0.03	0.62	-0.05	0.01	0.45	-0.66	-0.30	0.54	-0.29	-0.10	0.53	-0.14	-0.03	0.55	-0.60	-0.23	0.52
0.15	-0.28	-0.11	0.54	-0.04	-0.03	0.62	-0.07	-0.01	0.46	-0.67	-0.33	0.54	-0.29	-0.12	0.53	-0.12	-0.04	0.54	-0.61	-0.27	0.52
0.17	-0.33	-0.12	0.55	-0.02	-0.05	0.63	-0.08	-0.03	0.46	-0.66	-0.33	0.54	-0.31	-0.14	0.52	-0.12	-0.05	0.54	-0.61	-0.29	0.52
0.20	-0.36	-0.12	0.56	-0.02	-0.06	0.64	-0.02	-0.01	0.47	-0.66	-0.32	0.52	-0.32	-0.15	0.52	-0.12	-0.08	0.54	-0.59	-0.28	0.51
0.24	-0.39	-0.14	0.56	0.00	-0.06	0.65	0.14	0.03	0.48	-0.49	-0.27	0.50	-0.20	-0.12	0.50	-0.11	-0.06	0.53	-0.47	-0.25	0.49
0.30	-0.40	-0.14	0.57	0.03	-0.05	0.65	0.22	0.07	0.48	-0.39	-0.25	0.48	-0.10	-0.11	0.51	-0.08	-0.08	0.53	-0.36	-0.24	0.47
0.36	-0.41	-0.12	0.65	0.04	-0.07	0.66	0.24	0.06	0.50	-0.26	-0.21	0.46	-0.02	-0.10	0.50	-0.01	-0.06	0.51	-0.27	-0.23	0.46
0.40	-0.44	-0.12	0.67	0.04	-0.06	0.66	0.25	0.06	0.50	-0.25	-0.22	0.46	0.00	-0.09	0.51	-0.01	-0.08	0.51	-0.23	-0.25	0.46
0.46	-0.46	-0.13	0.70	0.07	-0.05	0.64	0.25	0.02	0.52	-0.23	-0.21	0.46	0.04	-0.09	0.52	0.02	-0.08	0.51	-0.17	-0.23	0.48
0.50	-0.48	-0.14	0.71	0.07	-0.07	0.64	0.24	0.03	0.53	-0.17	-0.21	0.46	0.09	-0.08	0.53	0.04	-0.07	0.51	-0.10	-0.19	0.49
0.60	-0.55	-0.16	0.72	0.10	-0.07	0.63	0.27	0.03	0.53	-0.13	-0.23	0.49	0.12	-0.09	0.54	0.06	-0.08	0.53	0.00	-0.18	0.53
0.75	-0.53	-0.16	0.73	0.18	-0.03	0.64	0.27	0.03	0.53	-0.02	-0.21	0.49	0.09	-0.11	0.56	0.07	-0.09	0.55	0.05	-0.18	0.56
0.85	-0.44	-0.12	0.75	0.18	-0.02	0.65	0.25	-0.01	0.53	0.01	-0.21	0.48	0.10	-0.10	0.57	0.09	-0.07	0.56	0.07	-0.16	0.56
1.00	-0.45	-0.12	0.75	0.09	-0.05	0.58	0.21	-0.02	0.53	0.03	-0.22	0.45	0.20	-0.06	0.58	0.13	-0.06	0.57	0.10	-0.14	0.56
1.50	-0.47	-0.11	0.76	0.01	-0.04	0.63	-0.12	-0.18	0.52	0.08	-0.21	0.43	0.02	-0.14	0.61	-0.16	-0.18	0.61	0.14	-0.14	0.56
2.00	-0.72	-0.19	0.77	-0.07	-0.07	0.67	-0.21	-0.22	0.51	0.09	-0.22	0.49	-0.05	-0.18	0.63	-0.19	-0.20	0.63	0.18	-0.13	0.56
3.00	-0.74	-0.22	0.77	-0.08	-0.09	0.69	-0.30	-0.28	0.51	0.10	-0.23	0.48	-0.05	-0.19	0.66	-0.20	-0.21	0.67	0.23	-0.09	0.55
4.00	-0.75	-0.24	0.78	-0.09	-0.11	0.70	-0.40	-0.31	0.55	0.10	-0.24	0.48	-0.05	-0.20	0.68	-0.21	-0.23	0.72	0.25	-0.13	0.54
5.00	-0.75	-0.26	0.78	-0.10	-0.13	0.85	-0.40	-0.34	0.59	0.10	-0.25	0.48	-0.05	-0.21	0.69	-0.22	-0.25	0.78	0.28	-0.17	0.62

App. A.2 NEHRP and geotechnical categories (smoothed)

Period	NEHRP B			NEHRP C			NEHRP D			NEHRP E			Geot. B			Geot. C			Geot. D			Geot. E		
(s)	a	b	σ	a	b	σ	a	b	σ	a	b	σ	a	b	σ	a	b	σ	a	b	σ	a	b	σ
0.01	0.09	0.05	0.49	-0.06	-0.05	0.55	0.08	-0.07	0.57	-0.62	-0.52	0.48	0.07	0.07	0.56	0.11	-0.04	0.60	-0.02	-0.08	0.56	-0.82	-0.63	0.40
0.02	0.10	0.01	0.50	-0.07	-0.06	0.55	0.06	-0.07	0.57	-0.70	-0.51	0.48	0.09	0.07	0.56	0.10	-0.05	0.60	-0.03	-0.09	0.55	-0.75	-0.61	0.40
0.03	0.10	0.11	0.50	-0.12	-0.04	0.55	0.03	-0.06	0.56	-0.75	-0.51	0.49	0.05	0.09	0.56	0.07	-0.03	0.60	-0.07	-0.08	0.55	-0.74	-0.57	0.42
0.04	0.10	0.12	0.48	-0.31	-0.08	0.55	-0.17	-0.09	0.55	-0.81	-0.51	0.47	-0.05	0.08	0.56	-0.13	-0.07	0.60	-0.23	-0.09	0.53	-0.89	-0.56	0.40
0.05	0.16	0.18	0.45	-0.41	-0.09	0.55	-0.19	-0.07	0.54	-1.04	-0.54	0.44	-0.13	0.07	0.55	-0.18	-0.07	0.60	-0.28	-0.09	0.52	-0.99	-0.55	0.38
0.06	0.21	0.20	0.46	-0.40	-0.09	0.54	-0.20	-0.07	0.54	-1.05	-0.54	0.43	-0.13	0.06	0.55	-0.19	-0.08	0.60	-0.30	-0.08	0.51	-0.98	-0.55	0.38
0.08	0.19	0.17	0.45	-0.40	-0.11	0.54	-0.19	-0.07	0.55	-1.11	-0.54	0.43	-0.18	0.03	0.52	-0.18	-0.07	0.60	-0.30	-0.09	0.53	-1.14	-0.58	0.36
0.09	-0.07	0.06	0.42	-0.39	-0.08	0.55	-0.13	-0.05	0.56	-1.11	-0.54	0.44	-0.23	0.02	0.52	-0.15	-0.06	0.59	-0.23	-0.07	0.55	-1.12	-0.57	0.40
0.10	0.09	0.15	0.43	-0.38	-0.09	0.56	-0.12	-0.05	0.58	-1.05	-0.51	0.45	-0.22	0.02	0.53	-0.15	-0.06	0.60	-0.22	-0.07	0.56	-1.12	-0.54	0.40
0.12	0.16	0.17	0.44	-0.38	-0.10	0.55	-0.11	-0.04	0.58	-0.95	-0.46	0.46	-0.28	0.00	0.54	-0.16	-0.06	0.58	-0.17	-0.05	0.56	-1.12	-0.55	0.35
0.15	0.40	0.22	0.44	-0.38	-0.14	0.57	-0.10	-0.06	0.58	-0.74	-0.43	0.49	-0.19	0.01	0.57	-0.18	-0.11	0.58	-0.15	-0.06	0.55	-1.12	-0.57	0.36
0.17	0.30	0.22	0.46	-0.36	-0.13	0.58	-0.12	-0.10	0.56	-0.70	-0.43	0.50	-0.17	0.03	0.60	-0.24	-0.14	0.57	-0.12	-0.07	0.54	-1.14	-0.61	0.36
0.20	0.36	0.25	0.48	-0.35	-0.13	0.60	-0.12	-0.09	0.55	-0.63	-0.42	0.50	-0.14	0.04	0.62	-0.28	-0.15	0.57	-0.09	-0.05	0.54	-1.08	-0.59	0.36
0.24	0.05	0.16	0.47	-0.30	-0.12	0.61	-0.02	-0.07	0.54	-0.55	-0.41	0.52	-0.10	0.08	0.65	-0.23	-0.15	0.58	-0.02	-0.05	0.52	-0.89	-0.56	0.32
0.30	-0.06	0.08	0.45	-0.22	-0.09	0.64	0.11	-0.04	0.54	-0.45	-0.41	0.54	-0.04	0.15	0.70	-0.10	-0.12	0.62	0.08	-0.04	0.51	-0.83	-0.55	0.36
0.36	-0.12	0.15	0.58	-0.19	-0.09	0.67	0.15	-0.03	0.53	-0.41	-0.40	0.53	-0.02	0.17	0.76	-0.02	-0.11	0.64	0.12	-0.04	0.50	-0.79	-0.54	0.37
0.40	-0.16	0.11	0.61	-0.14	-0.07	0.70	0.16	-0.04	0.51	-0.40	-0.40	0.54	0.00	0.19	0.75	0.01	-0.09	0.65	0.13	-0.04	0.49	-0.78	-0.53	0.39
0.46	-0.30	0.03	0.63	-0.11	-0.07	0.70	0.20	-0.07	0.49	-0.36	-0.40	0.54	0.01	0.18	0.75	0.04	-0.09	0.66	0.18	-0.06	0.48	-0.70	-0.52	0.44
0.50	-0.37	0.00	0.65	-0.07	-0.06	0.70	0.26	-0.04	0.49	-0.31	-0.40	0.54	0.02	0.19	0.76	0.09	-0.07	0.66	0.20	-0.05	0.49	-0.57	-0.52	0.47
0.60	-0.46	-0.02	0.67	-0.06	-0.07	0.72	0.30	-0.03	0.51	-0.25	-0.40	0.50	0.02	0.16	0.75	0.12	-0.06	0.68	0.24	-0.06	0.49	-0.30	-0.48	0.48
0.75	-0.65	-0.14	0.70	0.02	-0.06	0.72	0.40	-0.01	0.49	-0.18	-0.40	0.46	0.06	0.15	0.74	0.15	-0.05	0.70	0.36	-0.03	0.49	-0.20	-0.46	0.45
0.85	-0.70	-0.13	0.77	0.04	-0.05	0.73	0.39	-0.01	0.49	-0.12	-0.39	0.44	0.15	0.20	0.74	0.11	-0.06	0.71	0.38	-0.02	0.49	-0.18	-0.45	0.40
1.00	-0.72	-0.13	0.78	0.07	-0.03	0.74	0.38	-0.02	0.48	-0.09	-0.39	0.47	0.24	0.25	0.73	0.04	-0.08	0.72	0.41	-0.01	0.49	-0.12	-0.42	0.45
1.50	-0.88	-0.27	0.57	0.04	-0.03	0.77	0.34	-0.04	0.50	-0.02	-0.38	0.48	0.19	0.21	0.70	-0.06	-0.09	0.75	0.42	-0.03	0.51	0.07	-0.33	0.45
2.00	-1.33	-0.43	0.47	-0.01	-0.04	0.80	0.27	-0.07	0.51	0.03	-0.37	0.48	-0.41	-0.01	0.68	-0.12	-0.09	0.76	0.33	-0.05	0.55	0.14	-0.29	0.45
3.00	-1.47	-0.50	0.36	-0.08	-0.07	0.87	0.27	-0.09	0.55	0.09	-0.35	0.49	-0.44	-0.08	0.77	-0.12	-0.10	0.79	0.22	-0.10	0.59	0.25	-0.18	0.45
4.00	-1.55	-0.52	0.33	-0.20	-0.09	0.92	0.27	-0.09	0.57	0.10	-0.32	0.50	-0.47	-0.11	0.82	-0.12	-0.10	0.83	0.15	-0.14	0.65	0.30	-0.15	0.45
5.00	-1.60	-0.54	0.37	-0.25	-0.10	1.04	0.27	-0.10	0.66	0.12	-0.31	0.50	-0.50	-0.15	0.94	-0.12	-0.10	0.99	0.10	-0.16	0.71	0.33	-0.10	0.45

Appendix B

Models A1–A3 (smoothed)

Model A1 - Smoothed								
Period (sec)	b_1	V_{ref} (m/sec)	c	b_2	τ	σ	e_1	e_3
0.01	-0.64	418 ± 72	-0.36 ± 0.06	-0.14 ± 0.04	0.27	0.49	0.44	0.50
0.02	-0.63	490 ± 101	-0.34 ± 0.06	-0.12 ± 0.04	0.26	0.50	0.45	0.51
0.03	-0.62	324 ± 58	-0.33 ± 0.06	-0.11 ± 0.04	0.26	0.50	0.46	0.51
0.04	-0.61	233 ± 49	-0.31 ± 0.06	-0.11 ± 0.04	0.26	0.51	0.47	0.51
0.05	-0.64	192 ± 48	-0.29 ± 0.06	-0.11 ± 0.04	0.25	0.51	0.47	0.52
0.06	-0.64	181 ± 53	-0.25 ± 0.06	-0.11 ± 0.04	0.25	0.52	0.48	0.52
0.075	-0.64	196 ± 57	-0.23 ± 0.06	-0.11 ± 0.04	0.24	0.52	0.48	0.52
0.09	-0.64	239 ± 64	-0.23 ± 0.07	-0.12 ± 0.04	0.23	0.52	0.49	0.52
0.10	-0.60	257 ± 61	-0.25 ± 0.07	-0.13 ± 0.04	0.23	0.52	0.49	0.53
0.12	-0.56	299 ± 66	-0.26 ± 0.07	-0.14 ± 0.04	0.24	0.52	0.49	0.53
0.15	-0.53	357 ± 83	-0.28 ± 0.07	-0.18 ± 0.04	0.25	0.53	0.49	0.54
0.17	-0.53	406 ± 86	-0.29 ± 0.07	-0.19 ± 0.04	0.26	0.53	0.48	0.55
0.20	-0.52	453 ± 97	-0.31 ± 0.07	-0.19 ± 0.04	0.27	0.53	0.47	0.56
0.24	-0.52	493 ± 91	-0.38 ± 0.07	-0.16 ± 0.04	0.29	0.53	0.47	0.56
0.30	-0.52	532 ± 93	-0.44 ± 0.07	-0.14 ± 0.05	0.35	0.54	0.46	0.57
0.36	-0.51	535 ± 97	-0.48 ± 0.07	-0.11 ± 0.05	0.38	0.54	0.46	0.57
0.40	-0.51	535 ± 104	-0.50 ± 0.07	-0.10 ± 0.05	0.40	0.54	0.46	0.57
0.46	-0.50	535 ± 87	-0.55 ± 0.07	-0.08 ± 0.05	0.42	0.54	0.45	0.58
0.50	-0.50	535 ± 82	-0.60 ± 0.07	-0.06 ± 0.05	0.42	0.54	0.45	0.59
0.60	-0.49	535 ± 73	-0.66 ± 0.07	-0.03 ± 0.05	0.42	0.55	0.44	0.60
0.75	-0.47	535 ± 75	-0.69 ± 0.07	0.00 ± 0.05	0.42	0.55	0.44	0.63
0.85	-0.46	535 ± 73	-0.69 ± 0.07	0.00 ± 0.05	0.42	0.55	0.44	0.63
1.00	-0.44	535 ± 69	-0.70 ± 0.07	0.00 ± 0.05	0.42	0.56	0.44	0.64
1.50	-0.40	535 ± 63	-0.72 ± 0.08	0.00 ± 0.06	0.42	0.57	0.44	0.67
2.00	-0.38	535 ± 61	-0.73 ± 0.08	0.00 ± 0.06	0.43	0.58	0.44	0.69
3.00	-0.34	535 ± 65	-0.74 ± 0.09	0.00 ± 0.07	0.45	0.61	0.44	0.71
4.00	-0.31	535 ± 110	-0.75 ± 0.09	0.00 ± 0.07	0.47	0.64	0.44	0.73
5.00	-0.30	535 ± 166	-0.75 ± 0.14	0.00 ± 0.11	0.49	0.66	0.44	0.75

Model A2 - Smoothed								
Period (sec)	b_1	V_{ref} (m/sec)	c	b_2	τ	σ	e_1	e_3
0.01	-0.61	567 $\pm$ 110	-0.34 $\pm$ 0.06	-0.20 $\pm$ 0.04	0.24	0.49	0.45	0.51
0.05	-0.66	521 $\pm$ 128	-0.26 $\pm$ 0.06	-0.25 $\pm$ 0.04	0.24	0.52	0.48	0.52
0.09	-0.62	497 $\pm$ 147	-0.21 $\pm$ 0.07	-0.24 $\pm$ 0.04	0.24	0.52	0.49	0.53
0.10	-0.58	464 $\pm$ 122	-0.22 $\pm$ 0.07	-0.24 $\pm$ 0.04	0.24	0.52	0.50	0.53
0.12	-0.53	444 $\pm$ 109	-0.24 $\pm$ 0.06	-0.24 $\pm$ 0.04	0.24	0.52	0.50	0.53
0.15	-0.51	508 $\pm$ 134	-0.25 $\pm$ 0.06	-0.24 $\pm$ 0.04	0.24	0.52	0.50	0.53
0.17	-0.50	545 $\pm$ 128	-0.26 $\pm$ 0.06	-0.24 $\pm$ 0.04	0.24	0.52	0.49	0.54
0.20	-0.50	580 $\pm$ 142	-0.29 $\pm$ 0.06	-0.23 $\pm$ 0.04	0.24	0.52	0.48	0.55
0.24	-0.50	600 $\pm$ 119	-0.36 $\pm$ 0.07	-0.23 $\pm$ 0.04	0.25	0.52	0.47	0.55
0.30	-0.49	620 $\pm$ 103	-0.43 $\pm$ 0.07	-0.22 $\pm$ 0.04	0.29	0.53	0.47	0.56
0.40	-0.49	640 $\pm$ 119	-0.50 $\pm$ 0.07	-0.21 $\pm$ 0.04	0.34	0.54	0.46	0.58
0.50	-0.49	640 $\pm$ 99	-0.55 $\pm$ 0.07	-0.19 $\pm$ 0.04	0.35	0.55	0.46	0.60
0.75	-0.48	645 $\pm$ 99	-0.63 $\pm$ 0.08	-0.15 $\pm$ 0.05	0.36	0.56	0.46	0.64
1.00	-0.48	646 $\pm$ 90	-0.67 $\pm$ 0.08	-0.15 $\pm$ 0.05	0.36	0.57	0.46	0.66
1.50	-0.47	640 $\pm$ 85	-0.70 $\pm$ 0.08	-0.14 $\pm$ 0.05	0.36	0.58	0.46	0.69
2.00	-0.46	580 $\pm$ 75	-0.72 $\pm$ 0.08	-0.14 $\pm$ 0.05	0.37	0.59	0.46	0.72
3.00	-0.43	545 $\pm$ 68	-0.72 $\pm$ 0.10	-0.14 $\pm$ 0.07	0.38	0.62	0.46	0.75
4.00	-0.40	540 $\pm$ 121	-0.72 $\pm$ 0.10	-0.13 $\pm$ 0.07	0.39	0.65	0.46	0.77
5.00	-0.39	535 $\pm$ 130	-0.72 $\pm$ 0.14	-0.13 $\pm$ 0.11	0.44	0.68	0.46	0.79

Model A3 - Smoothed								
Period (sec)	b_1	V_{ref} (m/sec)	c	b_2	τ	σ	e_1	e_3
0.01	-0.55	501 $\pm$ 90	-0.34 $\pm$ 0.06	-0.04 $\pm$ 0.05	0.23	0.49	0.45	0.50
0.05	-0.57	676 $\pm$ 179	-0.26 $\pm$ 0.06	-0.05 $\pm$ 0.05	0.21	0.51	0.47	0.51
0.075	-0.61	780 $\pm$ 280	-0.21 $\pm$ 0.06	-0.11 $\pm$ 0.05	0.22	0.51	0.48	0.52
0.10	-0.57	643 $\pm$ 198	-0.22 $\pm$ 0.07	-0.12 $\pm$ 0.05	0.22	0.51	0.49	0.52
0.15	-0.52	541 $\pm$ 142	-0.24 $\pm$ 0.06	-0.13 $\pm$ 0.05	0.23	0.52	0.49	0.53
0.20	-0.51	565 $\pm$ 129	-0.28 $\pm$ 0.06	-0.07 $\pm$ 0.05	0.25	0.52	0.48	0.53
0.30	-0.51	610 $\pm$ 106	-0.41 $\pm$ 0.07	-0.04 $\pm$ 0.05	0.29	0.53	0.46	0.55
0.40	-0.50	640 $\pm$ 134	-0.50 $\pm$ 0.07	-0.02 $\pm$ 0.05	0.37	0.54	0.45	0.57
0.50	-0.50	660 $\pm$ 102	-0.59 $\pm$ 0.07	-0.02 $\pm$ 0.05	0.39	0.54	0.45	0.58
0.75	-0.49	703 $\pm$ 101	-0.65 $\pm$ 0.07	-0.02 $\pm$ 0.06	0.39	0.55	0.45	0.62
1.00	-0.49	709 $\pm$ 107	-0.68 $\pm$ 0.07	-0.04 $\pm$ 0.06	0.39	0.56	0.45	0.64
1.50	-0.48	710 $\pm$ 117	-0.71 $\pm$ 0.08	-0.12 $\pm$ 0.06	0.39	0.57	0.45	0.67
2.00	-0.46	710 $\pm$ 113	-0.72 $\pm$ 0.08	-0.17 $\pm$ 0.06	0.39	0.58	0.45	0.69
3.00	-0.42	710 $\pm$ 87	-0.72 $\pm$ 0.09	-0.22 $\pm$ 0.08	0.39	0.61	0.45	0.72
4.00	-0.40	710 $\pm$ 161	-0.72 $\pm$ 0.10	-0.25 $\pm$ 0.08	0.39	0.63	0.45	0.74

Appendix C

App. C.1 Regression coefficients for models B1–B3 in CBL category for southern California (smoothed). Coefficients without error bounds taper model to zero correction at small period, and were not directly estimated by regression. Plots shows coefficients before smoothing and smoothed fits.

Model B1			
Period (sec)	a_1	a_2	σ
<= 0.1	0	0	
0.12	0.09	1.0E-05	
0.15	-0.23 ± 0.29	2.5E-05 ± 1.6E-04	0.56
0.17	-0.26 ± 0.29	5.5E-05 ± 1.6E-04	0.57
0.2	-0.30 ± 0.31	8.0E-05 ± 1.7E-04	0.58
0.24	-0.34 ± 0.29	1.0E-04 ± 1.6E-04	0.56
0.3	-0.40 ± 0.28	1.4E-04 ± 1.6E-04	0.55
0.36	-0.48 ± 0.27	1.7E-04 ± 1.5E-04	0.53
0.40	-0.50 ± 0.26	1.8E-04 ± 1.4E-04	0.53
0.46	-0.53 ± 0.26	2.1E-04 ± 1.4E-04	0.53
0.50	-0.54 ± 0.26	2.2E-04 ± 1.4E-04	0.53
0.60	-0.58 ± 0.28	2.6E-04 ± 1.5E-04	0.53
0.75	-0.60 ± 0.31	3.0E-04 ± 1.7E-04	0.52
0.85	-0.59 ± 0.31	3.1E-04 ± 1.7E-04	0.52
1.00	-0.58 ± 0.27	3.1E-04 ± 1.5E-04	0.51
1.50	-0.54 ± 0.28	3.0E-04 ± 1.5E-04	0.50
2.00	-0.49 ± 0.28	2.9E-04 ± 1.5E-04	0.49
3.00	-0.34 ± 0.54	2.6E-04 ± 2.5E-04	0.48
4.00	0.10 ± 0.84	1.7E-04 ± 3.7E-04	0.48
5.00	0.04 ± 0.53	8.5E-05 ± 2.4E-04	0.48

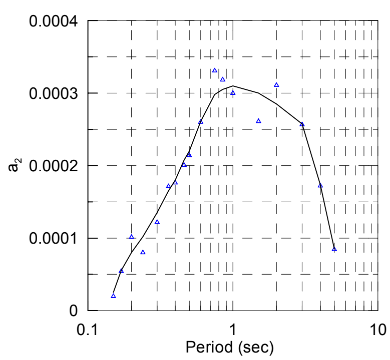

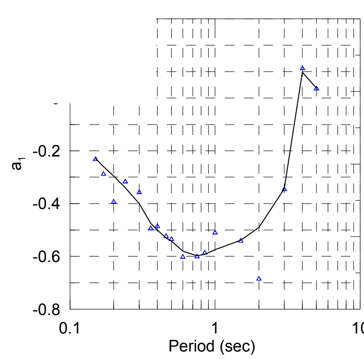

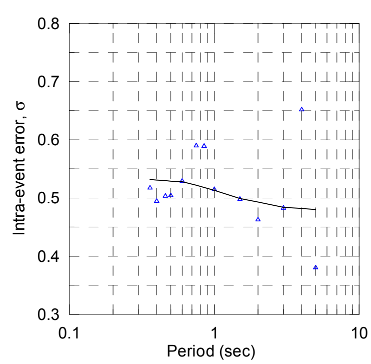

Appendix C.1 *(continued)*

Model B2			
Period (sec)	a_1	a_2	σ
<= 0.1	0	0	
0.12	-0.10	2.0E-05	
0.15	-0.25 ± 0.29	5.0E-05 ± 1.6E-04	0.56
0.17	-0.30 ± 0.30	7.7E-05 ± 1.6E-04	0.57
0.2	-0.34 ± 0.31	1.0E-04 ± 1.7E-04	0.57
0.24	-0.38 ± 0.29	1.2E-04 ± 1.6E-04	0.56
0.3	-0.43 ± 0.29	1.6E-04 ± 1.6E-04	0.55
0.4	-0.51 ± 0.26	2.0E-04 ± 1.4E-04	0.53
0.5	-0.57 ± 0.26	2.4E-04 ± 1.4E-04	0.53
0.75	-0.58 ± 0.31	3.1E-04 ± 1.7E-04	0.53
1	-0.58 ± 0.27	3.3E-04 ± 1.5E-04	0.53
1.5	-0.57 ± 0.29	3.3E-04 ± 1.6E-04	0.52
2	-0.56 ± 0.30	3.3E-04 ± 1.6E-04	0.51
3	-0.35 ± 0.57	3.0E-04 ± 2.6E-04	0.49
4	-0.16 ± 0.60	1.8E-04 ± 2.6E-04	0.46
5	-0.09 ± 0.56	1.5E-04 ± 2.5E-04	0.40

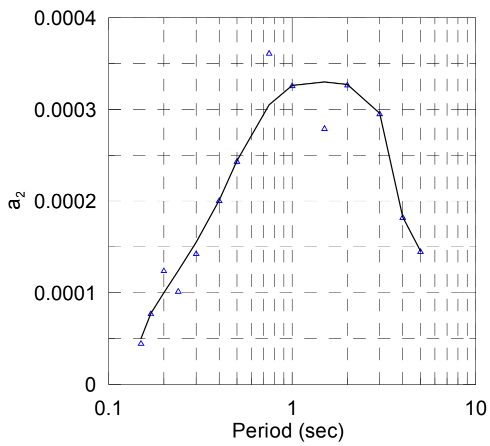

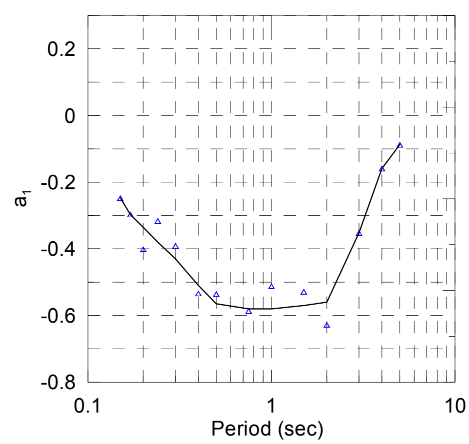

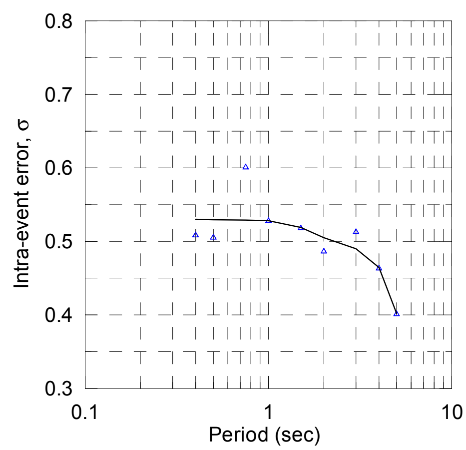

App. C.1 *(continued)*

Model B3			
Period (sec)	**a_1**	**a_2**	**σ**
<= 0.15	0	0	
0.2	-0.18 $\pm$ 0.27	2.8E-05 $\pm$ 1.5E-04	0.53
0.3	-0.27 $\pm$ 0.26	7.5E-05 $\pm$ 1.4E-04	0.51
0.40	-0.33 $\pm$ 0.25	1.1E-04 $\pm$ 1.4E-04	0.52
0.50	-0.39 $\pm$ 0.25	1.4E-04 $\pm$ 1.4E-04	0.52
0.75	-0.41 $\pm$ 0.29	2.0E-04 $\pm$ 1.6E-04	0.50
1.00	-0.41 $\pm$ 0.25	2.2E-04 $\pm$ 1.4E-04	0.49
1.50	-0.33 $\pm$ 0.25	2.3E-04 $\pm$ 1.4E-04	0.46
2.00	-0.28 $\pm$ 0.25	2.3E-04 $\pm$ 1.3E-04	0.42
3.00	-0.22 $\pm$ 0.43	2.2E-04 $\pm$ 2.0E-04	0.38
4.00	-0.09 $\pm$ 0.46	1.1E-04 $\pm$ 2.0E-04	0.36

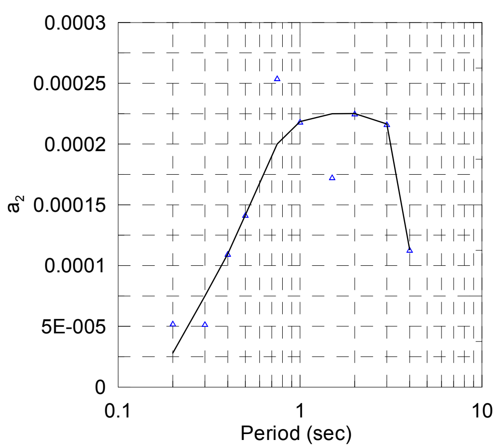

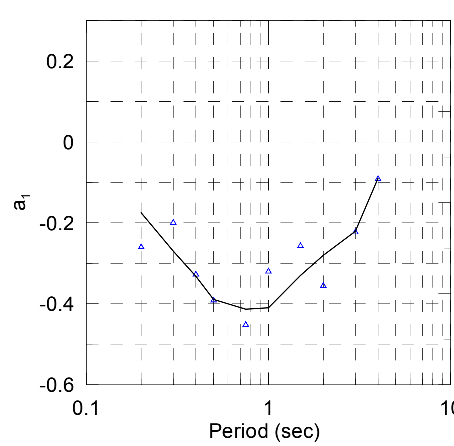

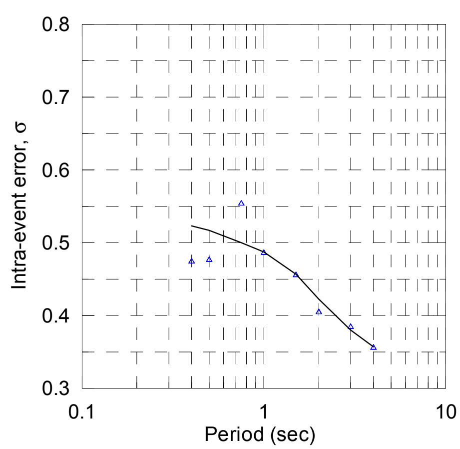

App. C.2 Regression coefficients for model B4 for southern California (smoothed). Coefficients are applicable to both CBL and DBL categories. Coefficients without error bounds taper model to zero correction at small period, and were not directly estimated by regression. Plots shows coefficients before smoothing and smoothed fits.

Model B4			
Period (sec)	a_1	a_2	σ
<= 0.20	0	0	
0.24	-0.04 ± 0.12	8.1E-06 ± 7.7E-05	0.48
0.30	-0.09 ± 0.13	4.5E-05 ± 7.9E-05	0.49
0.36	-0.12 ± 0.13	8.0E-05 ± 7.9E-05	0.48
0.40	-0.14 ± 0.13	1.0E-04 ± 7.9E-05	0.49
0.46	-0.17 ± 0.13	1.3E-04 ± 7.9E-05	0.49
0.50	-0.19 ± 0.13	1.4E-04 ± 8.0E-05	0.49
0.60	-0.23 ± 0.13	1.9E-04 ± 8.3E-05	0.50
0.75	-0.30 ± 0.14	2.3E-04 ± 8.9E-05	0.51
0.85	-0.30 ± 0.14	2.3E-04 ± 8.8E-05	0.52
1.00	-0.30 ± 0.13	2.4E-04 ± 8.4E-05	0.53
1.50	-0.23 ± 0.16	2.3E-04 ± 1.0E-04	0.58
2.00	-0.18 ± 0.18	2.3E-04 ± 1.1E-04	0.61
3.00	-0.08 ± 0.24	2.0E-04 ± 1.4E-04	0.64
4.00	0.00 ± 0.27	7.7E-05 ± 1.6E-04	0.64
5.00	0.25 ± 0.30	7.8E-05 ± 1.7E-04	0.65

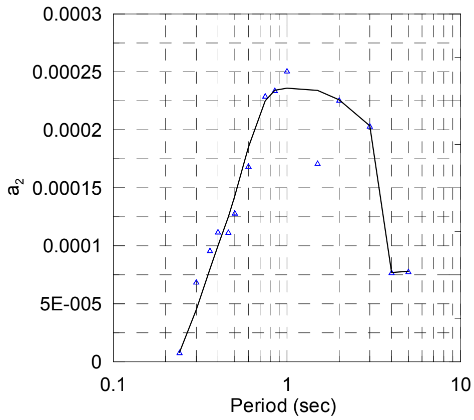

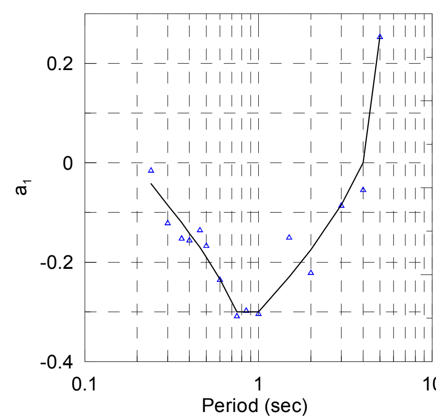

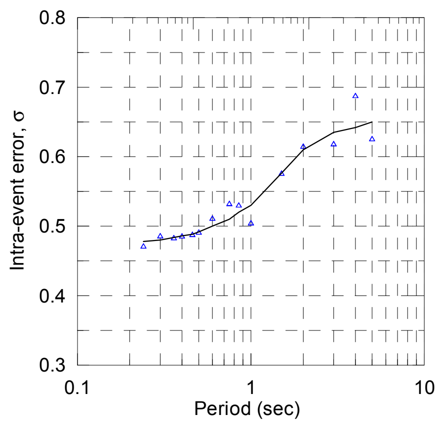

App. C.3 Regression coefficients for models B1–B3 in DBL category for southern California (smoothed). Coefficients a_1 and a_2 are not given because residuals are not significantly depth dependent.

MODEL B1		
Period (sec)	median of ε_{ij}	σ
0.01	1.00	0.43
0.02	1.00	0.43
0.03	1.00	0.43
0.04	1.00	0.44
0.05	1.00	0.45
0.06	1.00	0.45
0.075	1.00	0.46
0.09	1.00	0.46
0.1	1.00	0.46
0.12	1.00	0.46
0.15	1.00	0.47
0.17	1.00	0.47
0.2	1.00	0.47
0.24	1.00	0.48
0.3	1.00	0.48
0.36	1.00	0.48
0.4	1.00	0.48
0.46	0.99	0.48
0.5	0.97	0.49
0.6	0.92	0.49
0.75	0.88	0.49
0.85	0.85	0.49
1	0.83	0.50
1.5	0.80	0.50
2	0.80	0.50
3	0.91	0.53
4	1.28	0.60
5	1.30	0.62

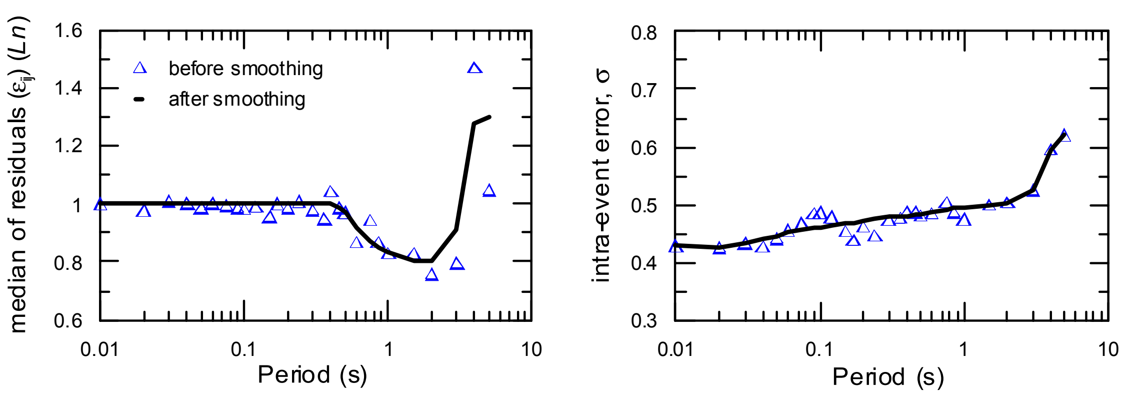

App. C.3 *(continued)*

MODEL B2		
Period (sec)	median of ε_{ij}	σ
0.01	1.00	0.42
0.05	1.00	0.44
0.09	1.00	0.44
0.1	1.00	0.44
0.12	1.00	0.44
0.15	1.00	0.44
0.17	1.00	0.45
0.2	1.00	0.45
0.24	1.00	0.45
0.3	1.00	0.45
0.4	1.01	0.45
0.5	1.00	0.45
0.75	0.98	0.45
1	0.90	0.45
1.5	0.88	0.46
2	0.89	0.46
3	0.94	0.49
4	1.02	0.55
5	1.03	0.59

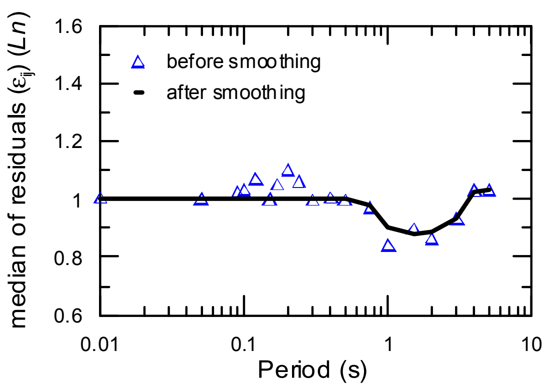

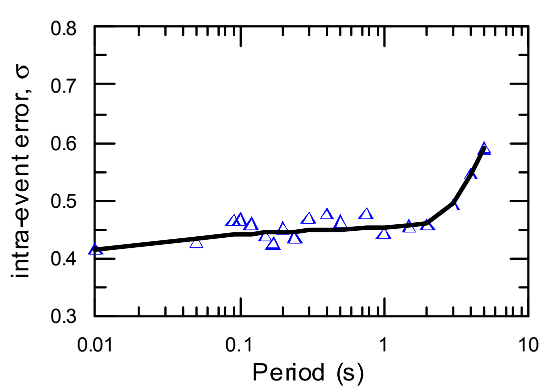

App. C.3 *(continued)*

MODEL B3		
Period (sec)	median of ε_{ij}	σ
0.01	1.00	0.43
0.05	1.00	0.45
0.075	1.00	0.45
0.1	1.00	0.45
0.15	1.00	0.45
0.2	1.00	0.46
0.3	1.00	0.46
0.4	1.00	0.46
0.5	1.00	0.46
0.75	0.94	0.46
1	0.92	0.47
1.5	0.90	0.47
2	0.90	0.47
3	0.90	0.50
4	0.91	0.56

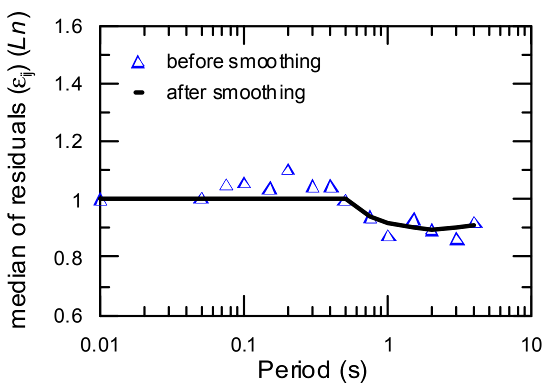

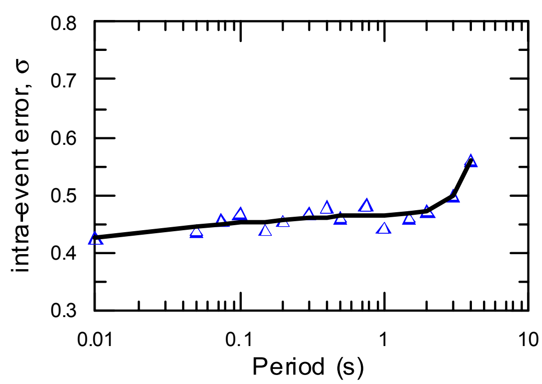

App. C.4 **Regression coefficients for models B1–B4 in San Francisco Bay Area (smoothed). Coefficients a_1 and a_2 are not given because residuals are not significantly depth dependent.**

MODEL B1		
Period (sec)	median of ε_{ij}	σ
0.01	1.00	0.44
0.02	1.00	0.44
0.03	1.00	0.45
0.04	1.00	0.46
0.05	1.00	0.47
0.06	1.00	0.48
0.075	1.00	0.48
0.09	1.00	0.49
0.1	1.00	0.48
0.12	1.00	0.48
0.15	1.00	0.48
0.17	1.00	0.47
0.2	1.00	0.47
0.24	1.00	0.46
0.3	1.00	0.46
0.36	1.00	0.46
0.4	1.00	0.46
0.46	1.00	0.47
0.5	1.00	0.47
0.6	1.00	0.48
0.75	1.00	0.54
0.85	1.00	0.55
1	1.00	0.57
1.5	1.00	0.58
2	1.00	0.58
3	1.00	0.56
4	1.00	0.52
5	1.00	0.45

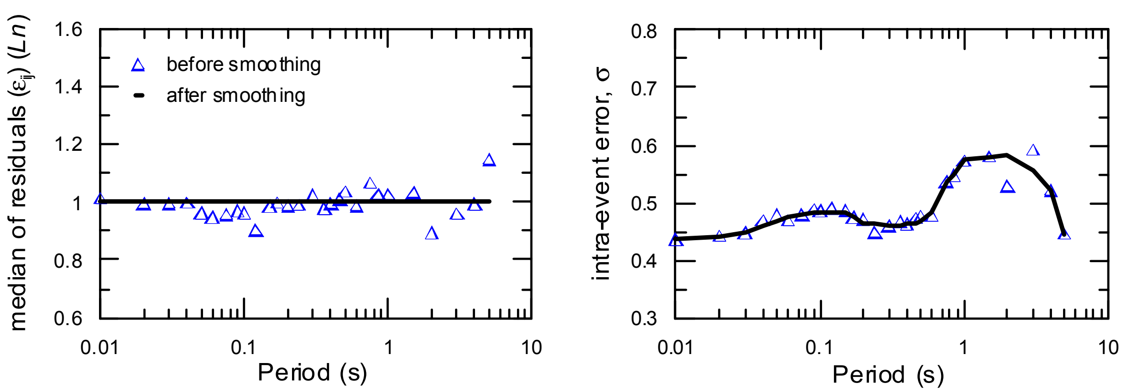

App. C.4 *(continued)*

MODEL B2		
Period (sec)	median of ε_{ij}	σ
0.01	1.00	0.47
0.05	1.00	0.51
0.09	1.00	0.51
0.1	1.00	0.51
0.12	1.00	0.51
0.15	1.00	0.51
0.17	1.00	0.50
0.2	1.00	0.48
0.24	1.00	0.48
0.3	1.00	0.49
0.4	1.00	0.49
0.5	1.00	0.51
0.75	1.00	0.57
1	1.00	0.61
1.5	1.00	0.61
2	1.00	0.61
3	1.00	0.58
4	1.00	0.55
5	1.00	0.46

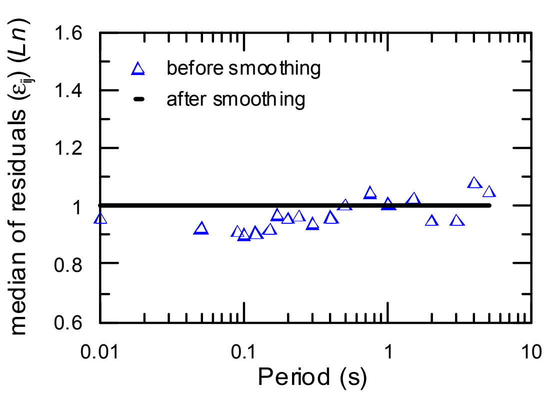

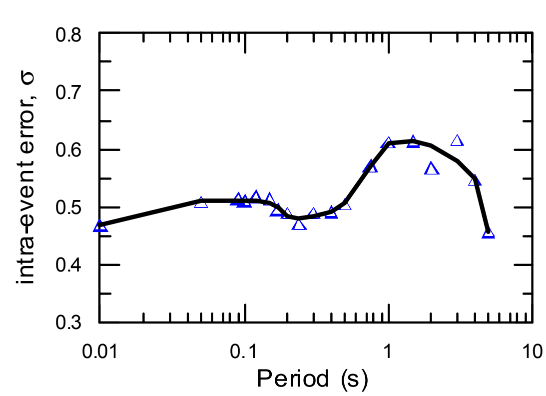

App. C.4 *(continued)*

MODEL B3		
Period (sec)	**median of ε_{ij}**	**σ**
0.01	1.00	0.46
0.05	1.00	0.51
0.075	1.00	0.52
0.1	1.00	0.52
0.15	1.00	0.52
0.2	1.00	0.49
0.3	1.00	0.48
0.4	1.00	0.48
0.5	1.00	0.49
0.75	1.00	0.55
1	1.00	0.58
1.5	1.00	0.59
2	1.00	0.58
3	1.00	0.57
4	1.00	0.57

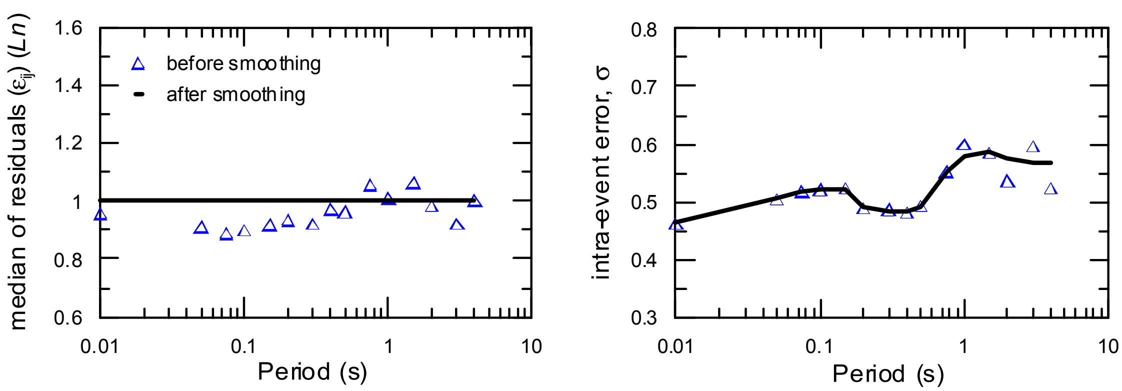

App. C.4 *(continued)*

MODEL B4		
Period (sec)	median of ε_{ij}	σ
0.01	1.00	0.50
0.02	1.00	0.50
0.03	1.00	0.50
0.04	1.00	0.51
0.05	1.01	0.49
0.06	1.01	0.48
0.075	1.01	0.48
0.09	1.02	0.48
0.1	1.03	0.48
0.12	1.03	0.48
0.15	1.04	0.48
0.17	1.05	0.48
0.2	1.05	0.49
0.24	1.06	0.49
0.3	1.06	0.49
0.36	1.06	0.49
0.4	1.06	0.50
0.46	1.06	0.50
0.5	1.06	0.51
0.6	1.06	0.53
0.75	1.07	0.58
0.85	1.07	0.59
1	1.07	0.61
1.5	1.07	0.61
2	1.10	0.60
3	1.24	0.54
4	1.25	0.49
5	1.25	0.45

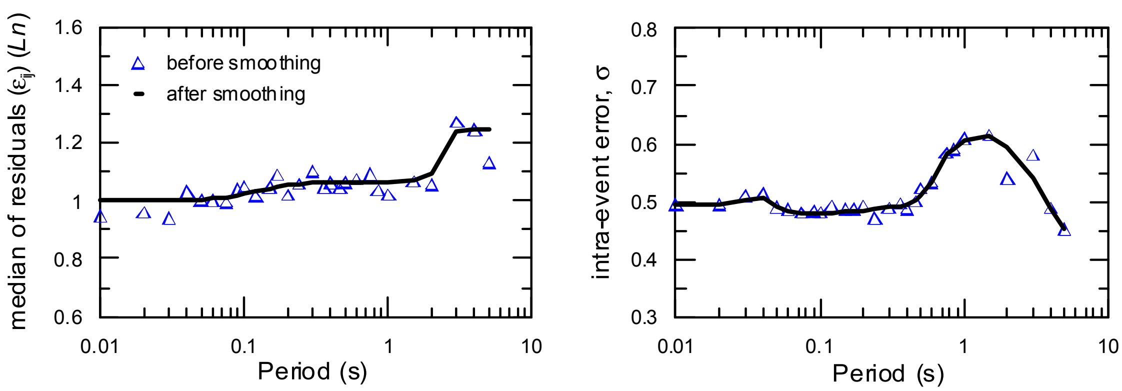

PEER REPORTS

PEER reports are available from the National Information Service for Earthquake Engineering (NISEE). To order PEER reports, please contact the Pacific Earthquake Engineering Research Center, 1301 South 46th Street, Richmond, California 94804-4698. Tel.: (510) 231-9468; Fax: (510) 231-9 461.

PEER 2005/01 *Empirical Characterization of Site Conditions on Strong Ground Motion.* Jonathan P. Stewart, Yoojoong Choi, and Robert W. Graves. June 2005.

PEER 2004/09 *Electrical Substation Equipment Interaction: Experimental Rigid Conductor Studies.* Christopher Stearns and André Filiatrault. February 2005.

PEER 2004/08 *Seismic Qualification and Fragility Testing of Line Break 550-kV Disconnect Switches.* Shakhzod M. Takhirov, Gregory L. Fenves, and Eric Fujisaki. January 2005.

PEER 2004/07 *Ground Motions for Earthquake Simulator Qualification of Electrical Substation Equipment.* Shakhzod M. Takhirov, Gregory L. Fenves, Eric Fujisaki, and Don Clyde. January 2005.

PEER 2004/06 *Performance-Based Regulation and Regulatory Regimes.* Peter J. May and Chris Koski. September 2004.

PEER 2004/05 *Performance-Based Seismic Design Concepts and Implementation: Proceedings of an International Workshop.* Peter Fajfar and Helmut Krawinkler, editors. September 2004.

PEER 2004/04 *Seismic Performance of an Instrumented Tilt-up Wall Building.* James C. Anderson and Vitelmo V. Bertero. July 2004.

PEER 2004/03 *Evaluation and Application of Concrete Tilt-up Assessment Methodologies.* Timothy Graf and James O. Malley. October 2004.

PEER 2004/02 *Analytical Investigations of New Methods for Reducing Residual Displacements of Reinforced Concrete Bridge Columns.* Junichi Sakai and Stephen A. Mahin. August 2004.

PEER 2004/01 *Seismic Performance of Masonry Buildings and Design Implications.* Kerri Anne Taeko Tokoro, James C. Anderson, and Vitelmo V. Bertero. February 2004.

PEER 2003/18 *Performance Models for Flexural Damage in Reinforced Concrete Columns.* Michael Berry and Marc Eberhard. August 2003.

PEER 2003/17 *Predicting Earthquake Damage in Older Reinforced Concrete Beam-Column Joints.* Catherine Pagni and Laura Lowes. October 2004.

PEER 2003/16 *Seismic Demands for Performance-Based Design of Bridges.* Kevin Mackie and Božidar Stojadinovi . August 2003.

PEER 2003/15 *Seismic Demands for Nondeteriorating Frame Structures and Their Dependence on Ground Motions.* Ricardo Antonio Medina and Helmut Krawinkler. May 2004.

PEER 2003/14 *Finite Element Reliability and Sensitivity Methods for Performance-Based Earthquake Engineering.* Terje Haukaas and Armen Der Kiureghian. April 2004.

PEER 2003/13 *Effects of Connection Hysteretic Degradation on the Seismic Behavior of Steel Moment-Resisting Frames.* Janise E. Rodgers and Stephen A. Mahin. March 2004.

PEER 2003/12 *Implementation Manual for the Seismic Protection of Laboratory Contents: Format and Case Studies.* William T. Holmes and Mary C. Comerio. October 2003.

PEER 2003/11 *Fifth U.S.-Japan Workshop on Performance-Based Earthquake Engineering Methodology for Reinforced Concrete Building Structures.* February 2004.

PEER 2003/10 *A Beam-Column Joint Model for Simulating the Earthquake Response of Reinforced Concrete Frames.* Laura N. Lowes, Nilanjan Mitra, and Arash Altoontash. February 2004.

PEER 2003/09 *Sequencing Repairs after an Earthquake: An Economic Approach.* Marco Casari and Simon J. Wilkie. April 2004.

PEER 2003/08 *A Technical Framework for Probability-Based Demand and Capacity Factor Design (DCFD) Seismic Formats*. Fatemeh Jalayer and C. Allin Cornell. November 2003.

PEER 2003/07 *Uncertainty Specification and Propagation for Loss Estimation Using FOSM Methods.* Jack W. Baker and C. Allin Cornell. September 2003.

PEER 2003/06 *Performance of Circular Reinforced Concrete Bridge Columns under Bidirectional Earthquake Loading*. Mahmoud M. Hachem, Stephen A. Mahin, and Jack P. Moehle. February 2003.

PEER 2003/05 *Response Assessment for Building-Specific Loss Estimation.* Eduardo Miranda and Shahram Taghavi. September 2003.

PEER 2003/04 *Experimental Assessment of Columns with Short Lap Splices Subjected to Cyclic Loads*. Murat Melek, John W. Wallace, and Joel Conte. April 2003.

PEER 2003/03 *Probabilistic Response Assessment for Building-Specific Loss Estimation.* Eduardo Miranda and Hesameddin Aslani. September 2003.

PEER 2003/02 *Software Framework for Collaborative Development of Nonlinear Dynamic Analysis Program.* Jun Peng and Kincho H. Law. September 2003.

PEER 2003/01 *Shake Table Tests and Analytical Studies on the Gravity Load Collapse of Reinforced Concrete Frames.* Kenneth John Elwood and Jack P. Moehle. November 2003.

PEER 2002/24 *Performance of Beam to Column Bridge Joints Subjected to a Large Velocity Pulse.* Natalie Gibson, André Filiatrault, and Scott A. Ashford. April 2002.

PEER 2002/23 *Effects of Large Velocity Pulses on Reinforced Concrete Bridge Columns.* Greg L. Orozco and Scott A. Ashford. April 2002.

PEER 2002/22 *Characterization of Large Velocity Pulses for Laboratory Testing.* Kenneth E. Cox and Scott A. Ashford. April 2002.

PEER 2002/21 *Fourth U.S.-Japan Workshop on Performance-Based Earthquake Engineering Methodology for Reinforced Concrete Building Structures*. December 2002.

PEER 2002/20 *Barriers to Adoption and Implementation of PBEE Innovations.* Peter J. May. August 2002.

PEER 2002/19 *Economic-Engineered Integrated Models for Earthquakes: Socioeconomic Impacts.* Peter Gordon, James E. Moore II, and Harry W. Richardson. July 2002.

PEER 2002/18 *Assessment of Reinforced Concrete Building Exterior Joints with Substandard Details.* Chris P. Pantelides, Jon Hansen, Justin Nadauld, and Lawrence D. Reaveley. May 2002.

PEER 2002/17 *Structural Characterization and Seismic Response Analysis of a Highway Overcrossing Equipped with Elastomeric Bearings and Fluid Dampers: A Case Study.* Nicos Makris and Jian Zhang. November 2002.

PEER 2002/16 *Estimation of Uncertainty in Geotechnical Properties for Performance-Based Earthquake Engineering.* Allen L. Jones, Steven L. Kramer, and Pedro Arduino. December 2002.

PEER 2002/15 *Seismic Behavior of Bridge Columns Subjected to Various Loading Patterns.* Asadollah Esmaeily-Gh. and Yan Xiao. December 2002.

PEER 2002/14 *Inelastic Seismic Response of Extended Pile Shaft Supported Bridge Structures.* T.C. Hutchinson, R.W. Boulanger, Y.H. Chai, and I.M. Idriss. December 2002.

PEER 2002/13 *Probabilistic Models and Fragility Estimates for Bridge Components and Systems.* Paolo Gardoni, Armen Der Kiureghian, and Khalid M. Mosalam. June 2002.

PEER 2002/12 *Effects of Fault Dip and Slip Rake on Near-Source Ground Motions: Why Chi-Chi Was a Relatively Mild M7.6 Earthquake.* Brad T. Aagaard, John F. Hall, and Thomas H. Heaton. December 2002.

PEER 2002/11 *Analytical and Experimental Study of Fiber-Reinforced Strip Isolators*. James M. Kelly and Shakhzod M. Takhirov. September 2002.

PEER 2002/10 *Centrifuge Modeling of Settlement and Lateral Spreading with Comparisons to Numerical Analyses***.** Sivapalan Gajan and Bruce L. Kutter. January 2003.

PEER 2002/09 *Documentation and Analysis of Field Case Histories of Seismic Compression during the 1994 Northridge, California, Earthquake.* Jonathan P. Stewart, Patrick M. Smith, Daniel H. Whang, and Jonathan D. Bray. October 2002.

PEER 2002/08 *Component Testing, Stability Analysis and Characterization of Buckling-Restrained Unbonded Braces™.* Cameron Black, Nicos Makris, and Ian Aiken. September 2002.

PEER 2002/07 *Seismic Performance of Pile-Wharf Connections.* Charles W. Roeder, Robert Graff, Jennifer Soderstrom, and Jun Han Yoo. December 2001.

PEER 2002/06 *The Use of Benefit-Cost Analysis for Evaluation of Performance-Based Earthquake Engineering Decisions*. Richard O. Zerbe and Anthony Falit-Baiamonte. September 2001.

PEER 2002/05 *Guidelines, Specifications, and Seismic Performance Characterization of Nonstructural Building Components and Equipment*. André Filiatrault, Constantin Christopoulos, and Christopher Stearns. September 2001.

PEER 2002/04 *Consortium of Organizations for Strong-Motion Observation Systems and the Pacific Earthquake Engineering Research Center Lifelines Program: Invited Workshop on Archiving and Web Dissemination of Geotechnical Data, 4–5 October 2001*. September 2002.

PEER 2002/03 *Investigation of Sensitivity of Building Loss Estimates to Major Uncertain Variables for the Van Nuys Testbed.* Keith A. Porter, James L. Beck, and Rustem V. Shaikhutdinov. August 2002.

PEER 2002/02 *The Third U.S.-Japan Workshop on Performance-Based Earthquake Engineering Methodology for Reinforced Concrete Building Structures*. July 2002.

PEER 2002/01 *Nonstructural Loss Estimation: The UC Berkeley Case Study.* Mary C. Comerio and John C. Stallmeyer. December 2001.

PEER 2001/16 *Statistics of SDF-System Estimate of Roof Displacement for Pushover Analysis of Buildings.* Anil K. Chopra, Rakesh K. Goel, and Chatpan Chintanapakdee. December 2001.

PEER 2001/15 *Damage to Bridges during the 2001 Nisqually Earthquake.* R. Tyler Ranf, Marc O. Eberhard, and Michael P. Berry. November 2001.

PEER 2001/14 *Rocking Response of Equipment Anchored to a Base Foundation.* Nicos Makris and Cameron J. Black. September 2001.

PEER 2001/13 *Modeling Soil Liquefaction Hazards for Performance-Based Earthquake Engineering.* Steven L. Kramer and Ahmed-W. Elgamal. February 2001.

PEER 2001/12 *Development of Geotechnical Capabilities in OpenSees.* Boris Jeremi . September 2001.

PEER 2001/11 *Analytical and Experimental Study of Fiber-Reinforced Elastomeric Isolators*. James M. Kelly and Shakhzod M. Takhirov. September 2001.

PEER 2001/10 *Amplification Factors for Spectral Acceleration in Active Regions.* Jonathan P. Stewart, Andrew H. Liu, Yoojoong Choi, and Mehmet B. Baturay. December 2001.

PEER 2001/09 *Ground Motion Evaluation Procedures for Performance-Based Design.* Jonathan P. Stewart, Shyh-Jeng Chiou, Jonathan D. Bray, Robert W. Graves, Paul G. Somerville, and Norman A. Abrahamson. September 2001.

PEER 2001/08 *Experimental and Computational Evaluation of Reinforced Concrete Bridge Beam-Column Connections for Seismic Performance*. Clay J. Naito, Jack P. Moehle, and Khalid M. Mosalam. November 2001.

PEER 2001/07 *The Rocking Spectrum and the Shortcomings of Design Guidelines.* Nicos Makris and Dimitrios Konstantinidis. August 2001.

PEER 2001/06 *Development of an Electrical Substation Equipment Performance Database for Evaluation of Equipment Fragilities*. Thalia Agnanos. April 1999.

PEER 2001/05 *Stiffness Analysis of Fiber-Reinforced Elastomeric Isolators.* Hsiang-Chuan Tsai and James M. Kelly. May 2001.

PEER 2001/04 *Organizational and Societal Considerations for Performance-Based Earthquake Engineering.* Peter J. May. April 2001.

PEER 2001/03 *A Modal Pushover Analysis Procedure to Estimate Seismic Demands for Buildings: Theory and Preliminary Evaluation.* Anil K. Chopra and Rakesh K. Goel. January 2001.

PEER 2001/02 *Seismic Response Analysis of Highway Overcrossings Including Soil-Structure Interaction.* Jian Zhang and Nicos Makris. March 2001.

PEER 2001/01 *Experimental Study of Large Seismic Steel Beam-to-Column Connections.* Egor P. Popov and Shakhzod M. Takhirov. November 2000.

PEER 2000/10 *The Second U.S.-Japan Workshop on Performance-Based Earthquake Engineering Methodology for Reinforced Concrete Building Structures.* March 2000.

PEER 2000/09 *Structural Engineering Reconnaissance of the August 17, 1999 Earthquake: Kocaeli (Izmit), Turkey.* Halil Sezen, Kenneth J. Elwood, Andrew S. Whittaker, Khalid Mosalam, John J. Wallace, and John F. Stanton. December 2000.

PEER 2000/08 *Behavior of Reinforced Concrete Bridge Columns Having Varying Aspect Ratios and Varying Lengths of Confinement.* Anthony J. Calderone, Dawn E. Lehman, and Jack P. Moehle. January 2001.

PEER 2000/07 *Cover-Plate and Flange-Plate Reinforced Steel Moment-Resisting Connections.* Taejin Kim, Andrew S. Whittaker, Amir S. Gilani, Vitelmo V. Bertero, and Shakhzod M. Takhirov. September 2000.

PEER 2000/06 *Seismic Evaluation and Analysis of 230-kV Disconnect Switches.* Amir S. J. Gilani, Andrew S. Whittaker, Gregory L. Fenves, Chun-Hao Chen, Henry Ho, and Eric Fujisaki. July 2000.

PEER 2000/05 *Performance-Based Evaluation of Exterior Reinforced Concrete Building Joints for Seismic Excitation.* Chandra Clyde, Chris P. Pantelides, and Lawrence D. Reaveley. July 2000.

PEER 2000/04 *An Evaluation of Seismic Energy Demand: An Attenuation Approach.* Chung-Che Chou and Chia-Ming Uang. July 1999.

PEER 2000/03 *Framing Earthquake Retrofitting Decisions: The Case of Hillside Homes in Los Angeles.* Detlof von Winterfeldt, Nels Roselund, and Alicia Kitsuse. March 2000.

PEER 2000/02 *U.S.-Japan Workshop on the Effects of Near-Field Earthquake Shaking.* Andrew Whittaker, ed. July 2000.

PEER 2000/01 *Further Studies on Seismic Interaction in Interconnected Electrical Substation Equipment.* Armen Der Kiureghian, Kee-Jeung Hong, and Jerome L. Sackman. November 1999.

PEER 1999/14 *Seismic Evaluation and Retrofit of 230-kV Porcelain Transformer Bushings*. Amir S. Gilani, Andrew S. Whittaker, Gregory L. Fenves, and Eric Fujisaki. December 1999.

PEER 1999/13 *Building Vulnerability Studies: Modeling and Evaluation of Tilt-up and Steel Reinforced Concrete Buildings.* John W. Wallace, Jonathan P. Stewart, and Andrew S. Whittaker, editors. December 1999.

PEER 1999/12 *Rehabilitation of Nonductile RC Frame Building Using Encasement Plates and Energy-Dissipating Devices.* Mehrdad Sasani, Vitelmo V. Bertero, James C. Anderson. December 1999.

PEER 1999/11 *Performance Evaluation Database for Concrete Bridge Components and Systems under Simulated Seismic Loads.* Yael D. Hose and Frieder Seible. November 1999.

PEER 1999/10 *U.S.-Japan Workshop on Performance-Based Earthquake Engineering Methodology for Reinforced Concrete Building Structures.* December 1999.

PEER 1999/09 *Performance Improvement of Long Period Building Structures Subjected to Severe Pulse-Type Ground Motions*. James C. Anderson, Vitelmo V. Bertero, and Raul Bertero. October 1999.

PEER 1999/08 *Envelopes for Seismic Response Vectors.* Charles Menun and Armen Der Kiureghian. July 1999.

PEER 1999/07 *Documentation of Strengths and Weaknesses of Current Computer Analysis Methods for Seismic Performance of Reinforced Concrete Members.* William F. Cofer. November 1999.

PEER 1999/06 *Rocking Response and Overturning of Anchored Equipment under Seismic Excitations.* Nicos Makris and Jian Zhang. November 1999.

PEER 1999/05 *Seismic Evaluation of 550 kV Porcelain Transformer Bushings.* Amir S. Gilani, Andrew S. Whittaker, Gregory L. Fenves, and Eric Fujisaki. October 1999.

PEER 1999/04 *Adoption and Enforcement of Earthquake Risk-Reduction Measures.* Peter J. May, Raymond J. Burby, T. Jens Feeley, and Robert Wood.

PEER 1999/03 *Task 3 Characterization of Site Response General Site Categories*. Adrian Rodriguez-Marek, Jonathan D. Bray, and Norman Abrahamson. February 1999.

PEER 1999/02 *Capacity-Demand-Diagram Methods for Estimating Seismic Deformation of Inelastic Structures: SDF Systems*. Anil K. Chopra and Rakesh Goel. April 1999.

PEER 1999/01 *Interaction in Interconnected Electrical Substation Equipment Subjected to Earthquake Ground Motions.* Armen Der Kiureghian, Jerome L. Sackman, and Kee-Jeung Hong. February 1999.

PEER 1998/08 *Behavior and Failure Analysis of a Multiple-Frame Highway Bridge in the 1994 Northridge Earthquake.* Gregory L. Fenves and Michael Ellery. December 1998.

PEER 1998/07 *Empirical Evaluation of Inertial Soil-Structure Interaction Effects.* Jonathan P. Stewart, Raymond B. Seed, and Gregory L. Fenves. November 1998.

PEER 1998/06 *Effect of Damping Mechanisms on the Response of Seismic Isolated Structures.* Nicos Makris and Shih-Po Chang. November 1998.

PEER 1998/05 *Rocking Response and Overturning of Equipment under Horizontal Pulse-Type Motions.* Nicos Makris and Yiannis Roussos. October 1998.

PEER 1998/04 *Pacific Earthquake Engineering Research Invitational Workshop Proceedings, May 14–15, 1998: Defining the Links between Planning, Policy Analysis, Economics and Earthquake Engineering.* Mary Comerio and Peter Gordon. September 1998.

PEER 1998/03 *Repair/Upgrade Procedures for Welded Beam to Column Connections.* James C. Anderson and Xiaojing Duan. May 1998.

PEER 1998/02 *Seismic Evaluation of 196 kV Porcelain Transformer Bushings.* Amir S. Gilani, Juan W. Chavez, Gregory L. Fenves, and Andrew S. Whittaker. May 1998.

PEER 1998/01 *Seismic Performance of Well-Confined Concrete Bridge Columns.* Dawn E. Lehman and Jack P. Moehle. December 2000.